Cronfa
Swansea University's Research Repository

Swansea University
Prifysgol Abertawe

Development and amelioration of green solvent systems for printed mesoscopic carbon perovskite solar cells

Carys Angharad Worsley

Submitted to Swansea University in fulfilment of the requirements for the degree of Doctor of Philosophy

Swansea University

Department of Materials Engineering

2022

Copyright: The Author, Carys A. Worsley, 2023.

Distributed under the terms of a Creative Commons Attribution-ShareAlike 4.0 International License (CC BY-SA 4.0).

Declarations

This work has not previously been accepted in substance for any degree and is not being concurrently submitted in candidature for any degree.

Signed: [redacted]

Dated: 04-08-22

This thesis is the result of my own investigations, except where otherwise stated. Other sources are acknowledged by footnotes giving explicit references. A bibliography is appended at the end of each section.

Signed: [redacted]

Dated: 04-08-22

I hereby give consent for my thesis, if accepted, to be available for photocopying and for inter-library loan, and for the title and summary to be made available to outside organisati[redacted]

Signed:

Dated: 04-08-22

The university's ethical procedures have been followed for all the work undertaken for this thesis and ethical approval has been granted where appropriate.

Signed: [redacted]

Dated: 04-08-22

Summary

Since their advent in 2009, lead halide perovskite solar cells have rapidly progressed to exhibit power conversion efficiencies of 25.5%, approaching that of commercial monocrystalline silicon devices. Although cheap and amenable to solution processing, commercialization is currently limited by poor device stability under operating conditions, prohibitively expensive or toxic components and manufacturing methods unsuitable for large-scale production.

Highly stable mesoscopic carbon-based perovskite solar cells (CPSCs) make use of easily scaled screen printing and are frequently described as one of the frontrunners for commercialization. However, significant barriers to commercialisation still exist. For example, the most common precursor solvents, dimethylformamide mixtures and γ-butyrolactone, respectively introduce toxicity and legality issues.

This work presents the first application of γ-Valerolactone as a green, non-toxic alternative solvent for CPSC fabrication. Cells fabricated with optimised precursor concentrations and annealing conditions exhibit comparable performance to standard γ-butyrolactone devices, proving that this system is a viable alternative. This will enable continued research in countries where γ-butyrolactone is legally restricted and make large-scale CPSC manufacture more sustainable.

This is then ameliorated with the application of green solvent engineering, wherein methanol (MeOH) is used as a solvent additive to improve the performance and reproducibility of GVL precursors. An optimised MeOH proportion of 10% is found to reduce precursor viscosity and improve wetting, as well as promoting more oriented crystal growth and higher quality absorber layers. Stability is also improved, with an unencapsulated MeOH device exhibiting a T80 of >420 hours at 50°C in ambient humidity under AM1.5 illumination.

Post crystallisation humidity treatments and age-related performance enhancements are then examined. It is revealed that humidity treatments, required for hysteresis reduction in GBL cells, have no significant impact on GVL-MeOH devices. Age-related performance enhancements are instead found to be a consequence of crystal reorganisation due to slow solvent loss after annealing. Introducing an ambient rest period for completed devices and modules prior to encapsulation is therefore important in maximising device efficiency for these systems.

Finally, the factors influencing device infiltration are explored in detail, with the aim of creating a reference resource of methods for targeted infiltration enhancement. A facile, non-destructive method for infiltration analysis is introduced and used to explore the impact of precursor crystallisation, ZrO_2 roughness, ink rheology and carbon mesh marking on stack filling. These methods are then applied in well-performing stacks as a tool for general efficiency enhancement, resulting in a champion efficiency of 15% in a 1 cm^2 device with the new solvent systems.

Acknowledgements

I would first like to thank Professor Trystan Watson, for support and guidance over many years and projects- you have helped me enormously in developing my science-legs and given me invaluable confidence in my work and scientific instinct.

A great deal of thanks also goes to the carbon group and wider SPECIFIC research team throughout this work. The scientific input, technical support and friendship from Simone Meroni, Dimitrios Raptis, Becky Bolton and Sarah-Jane Potts has been indispensable in directing this work and keeping me sane! Special thanks also to Tom Dunlop, whose input, technical expertise and insight has contributed significantly to the quality of this work. Declan, thank you for the emotional support, sitting through multiple rants about carbon cells and the near constant use of your memory stick. Rahul, thank you for sharing your plotting software. My sanity and data records salute you both.

Thanks also to the administrative team for the SUNRISE project; I am positive that herding academics to and from India for collaborative meetings and work has proven difficult at times! Rest assured that your efforts have helped considerably in enabling further work that will have a significant impact in improving people's lives. I am extremely proud to have worked as part of this project, and it has provided me with many great experiences that I will never forget.

Finally, thanks to my parents Maureen and Dave. Your love and support have helped me through even the worst of times. I have no doubt that your support of our interests and encouragement of a curious, questioning, and analytical approach to life has given all three of us the best possible foundation. I am proud of, and grateful for you both.

Contents

Common abbreviations....8
Chapter 1....10
Introduction and literature analysis....10
1.2 Perovskite Solar Cells.... 13
1.2.1 Common Architectures and Materials....13
1.2.2 Hole Conductor Free Devices and Mesoscopic Triple Stacks....16
1.3 Perovskite modifications in CPSCs.... 21
1.3.1 Cation substitution....26
1.3.2 Anion substitution....31
1.3.3 Inorganic additives....34
1.3.4 Organic additives....37
1.3.5 Perovskite processing conditions....43
1.3.6 Solvent engineering in CPSCs....46
1.3.7 A note on CPSC performance and testing protocols....51
1.4 Aims and motivations.... 55
1.5 References.... 56

Chapter 2....65
Experimental Procedures....65
2.1 Sample preparation.... 65
2.1.1 Fabrication of standard CPSCs and modules....65
2.1.2 Fabrication of XRD and PL samples....67
2.1.3 Cross sectional imaging samples....68
2.2 Testing and characterisation methods.... 68
2.2.1 Current-voltage (IV) sweeps and stabilised current measurements....68
2.2.2 Device stability testing....69
2.2.3 X-Ray Diffraction....70
2.2.4 UV-Vis....70
2.2.5 Contact angle measurements....70
2.2.6 Scanning electron microscopy (SEM)....71
2.2.7 Photoluminescence measurements....71
2.2.8 Photoluminescence and photocurrent mapping....71
2.2.9 Viscosity measurements....72
2.3.1 Optical microscopy for infiltration comparison....72

2.3.2 Fourier transform infra-red (FTIR) 72
2.3.3 External quantum efficiency (EQE) 73
2.3.4 Electrochemical impedance measurements.....73
2.3.5 Profilometry.....73
2.3.6 Rheological analysis.....73
2.3.7 Thermogravimetric analysis and Differential scanning calorimetry.....74
2.3.8 Tyndall effect imaging 74
2.4 References 74

Chapter 3 75
γ-Valerolactone: A Non-Toxic Green Solvent for Highly Stable Printed Mesoporous Perovskite Solar Cells 75
3.1 Introduction: GVL and the requirement for green solvents..... 76
3.2 Experimental 78
3.3 Results and discussion..... 79
3.3.1 Initial trials and characterisation.....79
3.3.2 Infiltration optimisation 86
3.3.3 Device and precursor stability.....92
3.3.4 Scale-up and module application 95
3.4 Conclusion 98
3.5 References 99

Chapter 4 GVL Solvent Engineering for improved precursor wetting and device performance 102
4.1 Introduction.....103
4.2 Experimental 104
4.3 Initial trials: Impact of EtOH and MeOH on Device Performance.....105
4.4 GVL-MeOH solvent mixing 107
4.4.1 Precursor Properties and Perovskite Crystallisation.....107
4.3.2 Effect of MeOH on Device Performance and Stability 114
4.3.3 Examining device infiltration 119
4.3.4 Application of GVL-10MeOH precursors to modules 125
4.4 Conclusions.....128
4.7 References 129

Chapter 5 131
Performance evolution and Humidity treatments in GVL-10MeOH devices 131
5.1 Introduction 132
5.2 Experimental 132
5.3.1 Applying humidity treatments to GVL-10MeOH devices 133
5.3.2 Age-related performance changes in high PCE devices. 137
5.3.3 Elucidating age-related performance enhancements 142
5.4 Conclusion 150
5.5 References 150

Chapter 6 Performance and infiltration enhancement in CPSCs 153
6.1 Introduction 153
6.2 Experimental 154
6.3 Analysing the problem and identifying potential causes 155
6.3.1 Determining the mechanisms behind poor infiltration 158
6.3.2 Quantifying stack filling: the relationship between infiltration and performance. 165
6.4 The impact of ambient humidity during infiltration 172
6.5 Paste batches and formulations 177
6.6 Changing printing parameters 183
6.6.1 The influence of layer thickness and mesh selection 183
6.6.2 ZrO_2 printing regimes 190
6.6.3 Adjusting the carbon layer 197
6.7 Summary: Methods for troubleshooting infiltration and performance issues in CPSCs and modules 202
6.9 Conclusion 212
6.8 References 213

Chapter 7 215
Future work and perspectives 215
7.1 Discussion 215
7.2 References 216

Common abbreviations

AVA: 5-aminovaleric acid

CdTe: Cadmium Telluride

CIGS : Copper indium gallium selenide

CPSC: Printed mesoscopic carbon-based perovskite solar cell

CTL: Charge transport layer

DMF: Dimethyl formamide

DMSO: Dimethyl sulfoxide

EIS: Electrochemical impedance spectroscopy

ETL: Electron transport layer

EtOH: Ethanol

FA: Formamidinium

FF: Fill factor

FTO: Fluorine doped tin oxide

GBL: γ-butyrolactone

GVL: γ-valerolactone

GVL-10MeOH: A γ-valerolactone and methanol solvent mix of 10% MeOH by volume

GVL-MeOH: A γ-valerolactone and methanol solvent mix

HOMO: Highest occupied molecular orbital

HT: Humidity treatment/treated

HTL: Hole transport layer

ISOS: International summit on organic photovoltaics stability

ITO: Indium doped tin oxide

IV: Current-voltage measurement

LUMO: Lowest unoccupied molecular orbital

MA: Methylammonium ($[CH_3NH_3]^+$)

MAI: Methylammonium Iodide, CH_3NH_3I

$MAPbI_3$: $CH_3NH_3PbI_3$

MeOH: Methanol

MPP(T): Maximum power point (tracking)

NIR: Near Infra-red

OPV: Organic photovoltaics

Pb-X: Lead-halide

PCBM: [6,6]-phenyl-C61-butyric acid methyl ester

PCE: Power-conversion efficiency

PEDOT-PSS: poly(3,4-ethylenedioxythiophene) polystyrene sulfonate

PL: Photoluminescence

PSC: Perovskite solar cell

PV: Photovoltaic

RH: Relative humidity

SEC: Solvent evaporation-controlled crystallisation

SEM: Scanning electron microscope/microscopy

Spiro-OMeTAD: 2,2',7,7'-Tetrakis-9,9'-spirobifluorene

TiO_2: mesoporous titania layer. Where the compact blocking layer is mentioned, text will say 'blocking layer' or 'c-TiO_2'.

UV: Ultraviolet

XRD: X-ray diffraction

Chapter 1

Introduction and literature analysis

Some parts of this chapter formed the basis of parts of the following published review paper: S. M. P. Meroni, C. Worsley, D. Raptis and T. M. Watson, *Energies*, 2021, *14*, 386

Global energy demand is predicted to rise by over 30% by 2040, and traditional fossil fuel driven energy generation is becoming increasingly unsustainable as the impacts of human driven climate change become clear. While the proportion of energy from renewable sources is predicted to rise over the coming decades, current forecasts indicate that CO_2 emissions due to energy production will also rise.[1] The development and manufacture of cheap renewable energy generation technologies is therefore of great economic and environmental importance.

Solar is the most abundant energy resource on the planet, with more energy reaching the surface of the planet in an average hour than would be required by humanity over the course of a year.[1] However, until relatively recently the use of photovoltaic (PV) devices for energy generation has been limited by the high cost of silicon and a lack of commercially viable alternatives. This has provided incentive for the research and development of alternative light harvesting materials such as CIGS (copper indium gallium selenide), cadmium telluride (CdTe) alloys and dye sensitised TiO_2.[2],[3],[4]

The situation has changed somewhat in recent years. Significant decreases in the price of silicon have resulted in an annual growth of 40% in PV energy generation, with solar energy predicted to account for 11% of total global energy generation by 2050. This proportion may increase dramatically as cheaper alternatives become commercially viable.[1]

Despite the increasing affordability of silicon devices, the development of alternative technologies is still of great importance: the purification and crystallisation of high-quality silicon is energy intensive and produced devices are heavy and inflexible, limiting their application. The availability of a broader range of solar technologies would offer scope for global solar generation to dramatically exceed projected values.

Materials must possess multiple characteristics to be suitable for use as a PV absorber. Absorption coefficients must be high to ensure adequate light absorption and charge generation. Charges must then be quickly separated to avoid recombination and associated energy loss before transport to the device electrodes for collection. This can be achieved through architectural design and careful material selection. For example, minimising absorber layer thickness and using carrier selective electrodes with conduction bands matching that of the absorber layer to minimise interfacial charge build-up significantly improve charge collection.

As well as possessing high absorption, an appropriate light absorber bandgap is required for good charge generation. Wavelengths of lower energy than the material bandgap will not be absorbed, while those of higher energy are absorbed and the excess dissipated (Figure 1.1). High efficiency single junction devices for outdoor use therefore aim to incorporate semiconductor materials with a bandgap close to 1.34 eV, as this represents the point at which a maximum power conversion efficiency (PCE) of 33% may theoretically be obtained (termed the Shockley-Queisser limit, Figure 1.1).

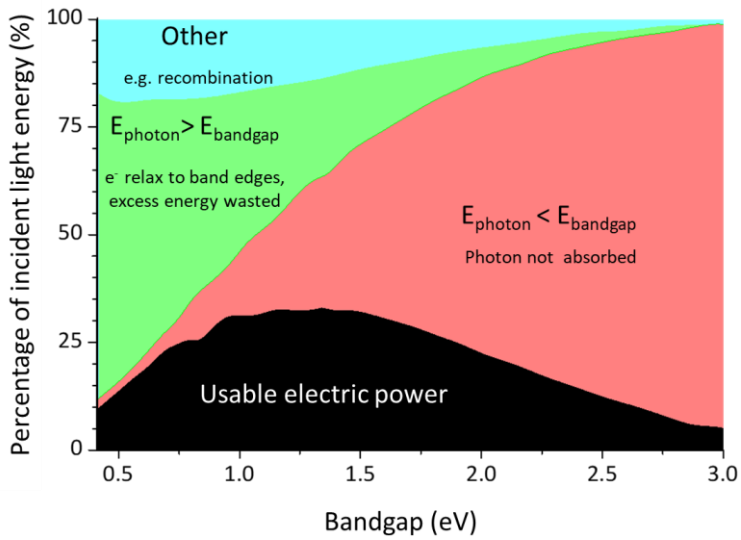

Figure 1.1: Shockley-Queisser plot, showing how photons from the visible spectrum are used in solar devices incorporating semiconductors with different bandgaps.

In practice, devices rarely approach this limit due to energy losses within the cell. Photogenerated carriers can recombine, returning excited electrons to the valence band and releasing absorbed light energy as heat or vibrations. This can occur due to slow charge separation or because of traps- energy states that lie below the conduction band.

As well as sufficient light absorption and a suitable bandgap, a good semiconductor absorber material will possess characteristics that reduce recombination losses, such as low trap densities, long charge lifetimes, high carrier mobility and long diffusion coefficients.

The most promising developments in recent years have been in lead halide perovskite devices. First used in solid state devices in 2012, perovskite efficiencies quickly surpassed those of many other technologies.[9] At the time of writing the highest certified perovskite PCE stands at 26.19%, surpassing that of some commercially available monocrystalline silicon devices.[10],[11] Such rapid development is unprecedented in novel PV technologies.

Perovskites are broad bandgap semiconductors of the general formula ABX_3, where A is generally a monovalent cation, B a bivalent metallic such as Pb^{2+}, and X a monovalent anion (Figure 1.2). Any of the constituent ABX_3 ions may be fully or partially substituted with organic or inorganic species of suitable valence bonding properties and ionic radii, making them highly tuneable.

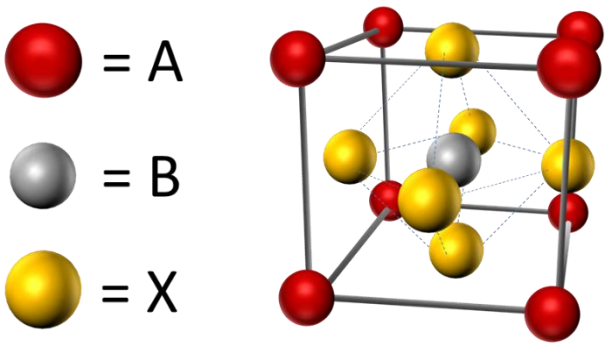

Figure 1.2: Diagrammatic representation of a cubic perovskite crystal structure (ABX_3).

These materials are ideally suited to photovoltaic applications, as they act as both electron and hole transporters, and have high absorption coefficients, long diffusion distances, good carrier mobility, and unusual defect tolerance.[5][6],[7]

Perovskites are also commercially appealing: their tuneable bandgaps and potential for flexible devices enable a variety of device colours and architectures, offering a broader range of technologies than is possible for silicon. Perhaps most attractive from a commercial standpoint, perovskites are amenable to simple solution-based processing. Highly soluble and remarkably tolerant to crystal defects, these materials require less strict process control and lower energy input for high-achieving devices. Both financial and energetic production costs would therefore be far lower than for silicon devices.[8]

Despite this, commercial application is currently hampered by comparatively poor device stability under operative conditions and limited application at larger scale. High efficiency methylammonium iodide based perovskites are particularly sensitive to humidity in many architectures, decomposing to PbI_2 within 24 hours without encapsulation.[12] In many cases a compromise must therefore be made between lifetime and efficiency- the most stable architectures and perovskite formulations are often of comparatively low efficiency. This is also true of cost and production considerations, as champion efficiencies are often achieved with long, energy intense production methods, post treatments and relatively expensive materials, impractical at large scale.

Device efficiency and stability may be manipulated in three ways; changing device architectures, varying deposition techniques to influence layer morphology and altering the chemical components. A brief overview of common perovskite architectures, materials and techniques will be given in the following sections.

1.2 Perovskite Solar Cells

1.2.1 Common Architectures and Materials

Cell architectures may be split into four common categories depending on the type of layers present and their orientation with respect to the light source. Shown in Figure 1.3, classic architectures are exposed to light through a transparent electron transport layer (ETL), whereas light enters inverted architectures through a transparent hole transport layer (HTL). In all cases, light must travel through a transparent charge transport layer (CTL) to reach the perovskite light absorber and generate a charge. Photogenerated holes and electrons must then travel through the perovskite layer to their respective electrodes before collection.

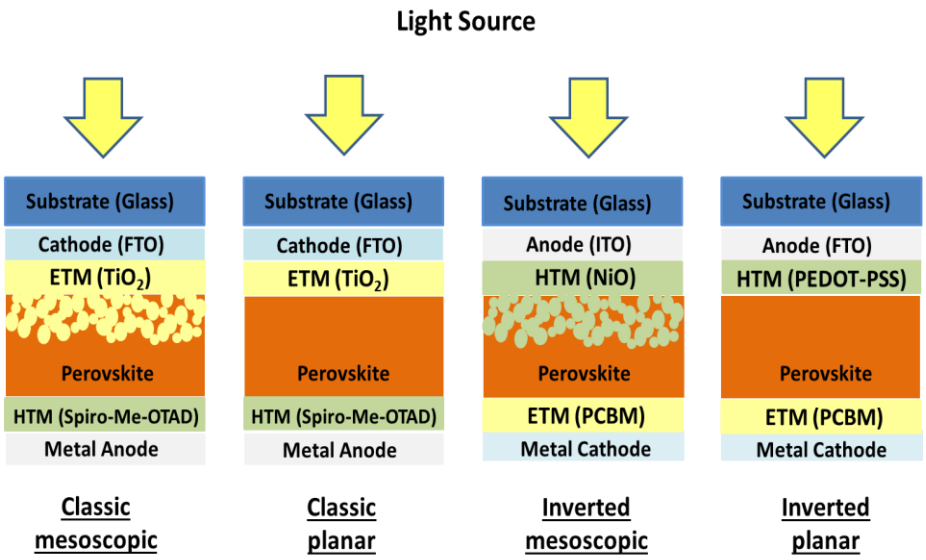

Figure 1.3: Depiction of common types of perovskite device architecture, with labels providing examples of frequently used materials.

Differences in required layer properties and the available materials and processing methods lead to variations in efficiency between different architectures. For example, inverted devices are generally of lower PCE. However, some properties are universal: for all architectures pinholes in any layer can negatively impact on device performance by introducing shorts or recombination centres. The ideal layer is therefore of uniform coverage and thickness: rough layers can produce pinholes in subsequent depositions.

The transparent charge transport layer is most commonly an inorganic semiconductor: usually TiO_2 or SnO_2 in classic devices or NiO_x in inverted devices. Organic conducting polymers such as PEDOT-PSS can also be used for flexible devices, although such layers tend to be of lower conductivity. Compact inorganic CTLs tend to be between 10 and 100 nm thickness. Layers of 10-15 nm provide the best PCEs by increasing the fill factor and decreasing series resistance. However, even at lab scale such thin layers are difficult produce without pinholes on rough FTO with standard spray pyrolysis coating methods, and this becomes increasingly challenging as size increases. Although high-precision methods such as atomic layer deposition (ALD) can be used to this end, they dramatically increase capital cost and are difficult and impractical to scale up.[57] Larger scale projects and demonstrators therefore tend to use layers of around 50 nm deposited by spray pyrolysis.

Mesoscopic devices then incorporate an additional porous charge transport layer (Figure 1.3). Many scalable methods can be used for mesoscopic layer deposition, including bar casting, doctor blading and screen printing. As well as providing a mechanically stabilising scaffold for perovskite crystallisation, a mesoscopic charge transport layer can increase

absorption efficiency by scattering incoming light. Mesoscopic CTLs also provide an extremely large surface area for carrier collection, lowering the required diffusion distance. This is advantageous from a processing perspective as high-performance devices require less stringent crystallisation control. In planar devices carriers much travel much further before collection, making them more vulnerable to trap and defect driven recombination (Figure 1.4). Greater interfacial charge build-up is also observed, and perovskite crystallisation must be carefully controlled to avoid both pinholes and crystal defects. This may be achieved in an inert atmosphere with existing solution-based methods by carefully controlling processing parameters.[58]

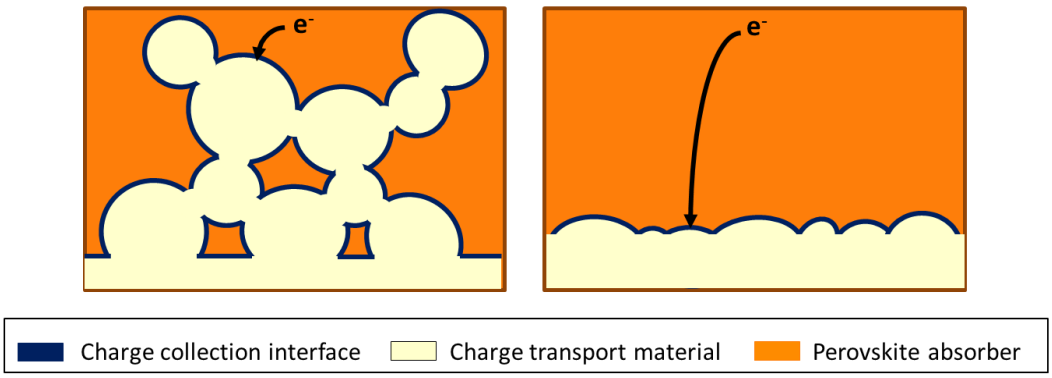

Figure 1.4: Diagrammatic representation of the structural difference between mesoporous (left) and planar (right) charge transport layers to show how carriers must travel further for collection.

However, the mechanical rigidity of inorganic mesoscopic layers makes them unsuitable for use on lightweight flexible substrates. Additionally, the inclusion of a mesoporous layer drastically increases the required processing time as deposited layers must be heated to high temperatures to remove solvents and binders, and in some cases, sinter layers. In the case of mesoporous TiO_2 (a common ETL in classic architectures) this is necessary for efficient charge transport. A typical lab-based mesoporous sintering process at 550°C can exceed two hours in its entirety, as long ramped heating and cooling steps are required to prevent substrate and layer cracking. This introduces significant manufacturing costs and makes roll-to-roll fabrication impractical, introducing the need alternative heating methods such as near-infra-red (NIR), which can successfully reduce annealing times to under a minute.[59]

The perovskite layer is then deposited onto the annealed CTL. Good precursor wetting and controlled nucleation become essential in obtaining high coverage, good quality crystals-especially in planar devices.

The top electrode (HTL in classic structures and ETL in inverted devices) is next deposited onto the annealed perovskite. In classic structures, top electrode is typically a lithium-doped Spiro-OMe-TAD HTL, while PCBM ([6,6]-phenyl-C61-butyric acid methyl ester) is common in inverted devices. Care must be taken so as not to damage the underlying absorber. For example, depositions must be low temperature to prevent perovskite decomposition, and solvents chosen that do not solubilise or react with the layer. Metal contacts are then placed on the dried HTL before encapsulation.

These organic CTLs are highly selective and can produce high PCE devices at lab scale. However, they are also expensive and frequently unstable, and can significantly increase device cost and decrease lifetime.

This has led to many publications on hole conductor-free devices with improved operational stability.[60] Common architectures and materials for such devices will be discussed in the following section.

1.2.2 Hole Conductor Free Devices and Mesoscopic Triple Stacks

To be considered commercially viable, stable, high efficiency devices must be easily and reproducibly attainable at large scale. This is not often the case in the literature; champion efficiencies are commonly achieved on small devices, using expensive charge extraction layers and impractical, energy intense production methods and post treatments.[9] For example, antisolvent-assisted spin coating is used in the fabrication of many record-breaking devices, sacrificing scalability for lab scale efficiency enhancement.[61]

In many cases a compromise must also be made between lifetime and efficiency; the most stable architectures and perovskite formulations are often of comparatively low PCE. The high cost and unstable nature of organic hole extraction materials has led to many publications on hole conductor-free devices with improved operational stability.[60] Architectures replacing traditional HTLs with layers containing conductive carbon allotropes such as graphite and graphene are perhaps the most common, as these materials are thermally stable and extremely cheap.[62],[63]

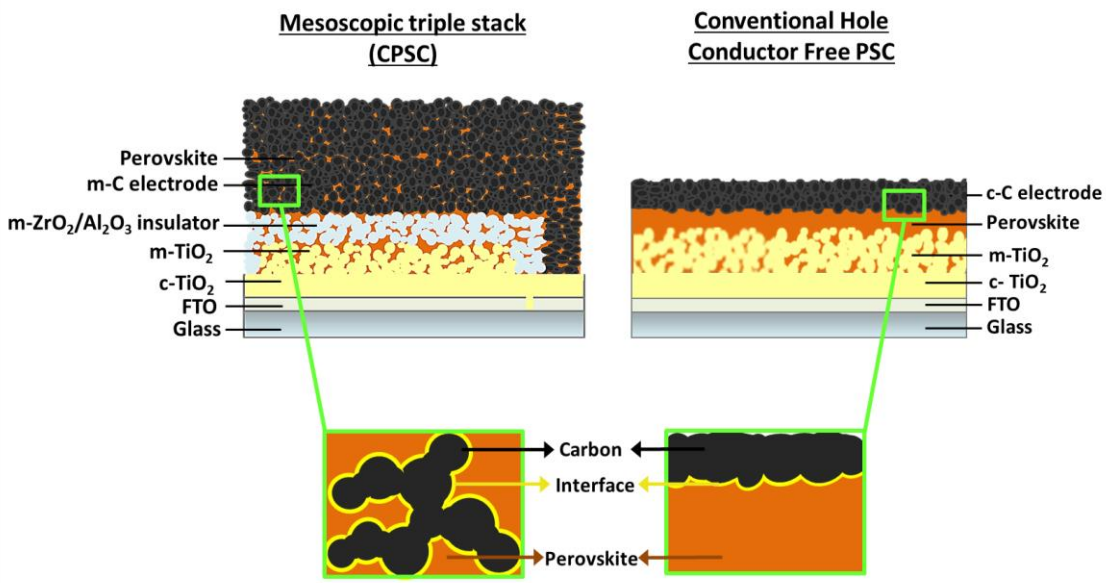

Figure 1.5: Diagrammatic representation of a CPSC and conventional carbon-based PSC to show the difference in the perovskite-carbon interfacial area. Relative layer thicknesses are not to scale and should be used for reference only.

Most carbon HTM-free devices are based on one of two architectures, shown in Figure 1.5. The conventional carbon-based sandwich structure resembles that of the classic mesoscopic device, differing only in the absence of a hole conductor and the compact carbon counter electrode. These conventional hole conductor free devices historically exhibited better PCEs in the literature as the highly crystalline perovskite capping layer above the mesoporous TiO_2 contains large monocrystalline surface grains, improving fill factor and reducing recombination.[63] As a simple modification of classic sandwich devices, the fabrication processes and constituent materials of conventional hole conductor free PSCs are similar to those of classic conventional PSCs: electrode and perovskite layers are commonly deposited by spin coating before subsequent placement of the counter electrode. The materials and fabrication processes developed for producing high-performance sandwich devices with metal electrodes were therefore directly applicable to this architecture.

The mesoporous carbon-based PSC (CPSC, Figure 1.5) is structurally very different, consisting of a screen-printed mesoporous stack which is subsequently infiltrated with perovskite via drop-casting. Stacks typically consist of a compact TiO_2 blocking layer (c-TiO_2) and mesoporous layers of TiO_2, ZrO_2 and C, which respectively act as an ETL, insulating layer and top contact. Although some material variations or additional layers such as Al_2O_3 insulators and NiO HTL have been trialled, most publications work with these three materials.[64]–[66]

Since their introduction in 2013 there has been extensive work into applying and optimising novel fabrication procedures and perovskite formulations to CPSCs, which have emerged as a potential frontrunner for early PSC commercialisation.[67] This is despite a relative lag in PCE: the current highest performing PCE stands at 18.8% for a device using MACl additives with an $MAPbI_3$ perovskite in N-methylformamide (highest certified 17.7% for an $AA_xMA_{(1-x)}PbI_3$ formulation).[68],[69]

The high potential for commercialisation is a consequence of exceptional stability and amenability to low cost, easily scaled manufacturing techniques. The lack of residual binders in the hydrophobic top-contact and all-encompassing scaffold result in improved chemical and mechanical stability. Polyurethane/glass encapsulated devices produced using $AVA_{(x)}MA_{(1-x)}PbI_3$ γ-butyrolactone (GBL) perovskite precursors have recently passed stringent IEC61215:2016 tests, including damp heat tests (85°C at 85% RH, for 1,100 h), thermal cycling tests (-40°C- 85°C for 200 cycles), ultraviolet preconditioning tests (60°C, 50 kWh m^{-2}), and MPPT light soaking tests (55°C, 9,000 h).[70] This is unprecedented for perovskite devices and represents an important step toward commercial viability.

As well as containing much cheaper constituent materials and producing highly stable devices, CPSCs can be manufactured using cheap, easily scaled techniques. The entire stack can be screen-printed, which makes them attractive for large scale batch production of single cells and modules. Modules may be prepared either through a registration, or screen alignment approach, or via mechanical scribing- methods common in industrial manufacture.[71] Additionally, these steps can all be carried out in ambient conditions without the need for expensive atmospheric control equipment, significantly decreasing the set-up and running costs.[72]

Potential bottlenecks to high throughput production include the deposition of compact TiO_2, the ramped heating of each layer and the perovskite infiltration procedure. The mesoporous layers are formed through annealing pastes containing organic binders such as polyethylene glycol or ethyl cellulose, which burn off at high temperatures to leave nanoscale voids in the structure.[66] Annealing processes can be extremely long, significantly increasing production time and decreasing potential commercial throughput. In a laboratory setting, each stack layer is typically annealed separately and requires an excess of two hours due to the ramped heating and cooling required to prevent substrate cracking.[73]

This problem has been addressed by using near infra-red (NIR) to cut each heating step to less than a minute per layer. Combined heating of the ZrO_2 and TiO_2 was then used to further

decrease the heating time. Layers fabricated using this method have been found to exhibit similar porosity, thickness, and surface area to those produced with hot plates, resulting in comparable device performance upon infiltration.[59]

Lab scale infiltration commonly consists of manual drop casting, which is impractical and ineffective at large scale. Deposition techniques such as slot-dye coating and inkjet printing have been used to achieve homogeneous infiltration.[74],[75] However, stringent process controls are required to prevent equipment blockages and non-uniform infiltration. For example, early work on inkjet printing resulted in poor infiltration with thick, inhomogeneous crystal formations at drop boundaries.[76] Novel approaches to mechanised infiltration have also been proposed, including a 'robotic mesh' method, where large precursor droplets are broken up by printing through a patterned mesh.[76]

These advances mean that end-to-end large-scale production of CPSCs is already feasible using established industrial methods. A potential setup for end-to-end stack production using laser etching, rotary screen printing, NIR annealing mechanical scribing is depicted in (Figure 1.6). These techniques have already been used to produce large scale modules of 198 cm^2 active area and over 6% PCE, proving that the production of large-scale devices is feasible with these methods.[77][78] Promisingly, these architectures do not seem to suffer the same level of PCE loss on scale-up as other structures.

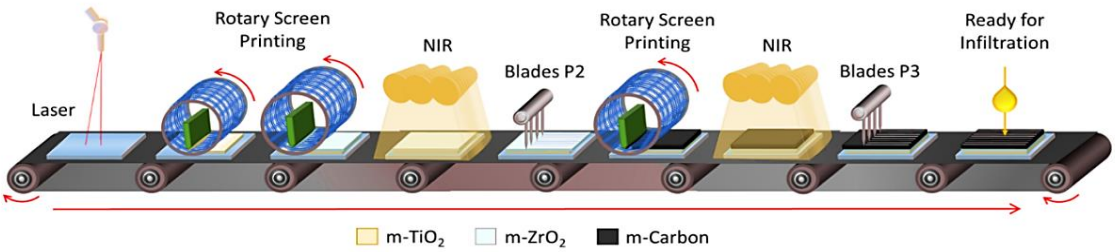

Figure 1.6: Diagrammatic representation of a potential set-up for commercial large-scale end-to-end CPSC fabrication.

These architectures also offer many interesting avenues for fundamental research. In these devices most carriers are produced in the first few hundred nanometres of the TiO_2 layer, meaning photogenerated holes must travel several microns through the ZrO_2 insulator before collection. Additionally, the perovskite crystals transporting the charge are smaller than in other architectures, as grain size is restricted to that of the scaffold pores throughout the stack. Considering the extreme distances, small grain sizes and non-selective nature of the carbon electrode it would be reasonable to expect low current densities due to high levels

of recombination. However, even in large devices current density is generally 22-24 $mAcm^2$ range.

In fact, several studies have found that extremely thick insulating layers can improve device performance: a PCE of 15% was achieved with an insulating layer of 3 µm, far outperforming thinner devices.[60],[79] As yet, the reasons for this behaviour are unclear.

Porosity is also an important factor to consider. With porosity, or the volume fraction of pores in the layer, a balance exists between maximising perovskite infiltration and maintaining a large interfacial area for charge extraction. Small pores maximise the layer surface area but can impede perovskite infiltration. Porosity is determined by nanoparticle size and paste formulation- smaller nanoparticles decrease pore diameters and increase interfacial area, while binders such as ethyl cellulose, or hard and soft templates like polystyrene microbeads and polyethylene glycol can be incorporated to increase pore diameters.[80],[81]

The thickness and porosity of the stack layers clearly have a large influence on device performance. However, optimisation studies have produced mixed results on what stack properties produce the best devices: even just for $AVA_{0.03}MAPbI_3$ devices several different combinations of layer thicknesses and nanoparticle sizes have been presented as optimum.[65],[79],[82] Although this may in some cases represent a lack of rigorous process control between different groups, it is also likely that the optimal device stack varies depending on the perovskite composition or ambient infiltration conditions.[83] Changing the precursor formulation or the ambient temperature and humidity during infiltration can drastically alter its wetting properties, as well as changing crystal growth, packing, and the optoelectronic properties of the annealed absorber. Different layer materials, dopants and perovskite formulations may therefore have different optimal thicknesses and pore sizes. Any change to stack or perovskite composition or deposition therefore requires extensive optimisation of all three layers to achieve maximum performance and reproducibility. Ideally, optimisation should be carried out on any novel systems prior to direct comparison with well-characterised devices.

The non-selective nature and poor conductivity of the carbon electrode limits device performance and can exacerbate hysteresis.[84],[85] The simplest carbon electrodes consist of carbon black/graphite mixtures where the former improves layer porosity, and the latter makes it conductive. For the best devices maximum conductivity must be achieved without impeding perovskite infiltration. This can be difficult, as the properties that improve

conductivity- for example increasing the amount of graphite or layer thickness- often decrease the porosity.

The graphite itself can also be modified to improve selectivity- for example, functionalising with C=O and C-OH groups was found to improve PCE by over 2%.[63] Other works have examined the impact of incorporating different carbon allotropes such as single-walled carbon nanotubes to top contacts or interlayers.[86],[87] Alternatively, other p-type materials can be used. NiO, and WO_3 have been shown to improve charge extraction when incorporated into the carbon top electrode, while CuS, MoO_3, Co_2O_3 and CuO, have been proposed performance enhancing additives.[87]–[90]

Device performance can also be improved by incorporating additional p-type layers to improve charge extraction. As is the case in conventional devices, chosen materials must possess band energies that match with that of the perovskite. However, in the CPSC the added layer must also be porous and be able to withstand the high temperatures required for carbon layer annealing (~400°C). Organic hole transporting materials are generally non-porous and degrade below the carbon annealing temperature, so interlayer materials have thus far been limited to inorganic materials such as NiO and spinel Co_3O_4.[64],[89] NiO was used to produce optimised $Cs_{0.05}(FA_{0.4}MA_{0.6})_{0.95}PbI_{2.8}Br_{0.2}$ TiO_2/Al_2O_3/NiO/carbon devices with 17.02% PCE.[64]

The structural and perovskite requirements of CPSCs are clearly very different to those of other architectures. This is reflected in the literature, where a large variety of processing methods, post treatments, additives, and perovskite substitutions for enhancing CPSC performance have been presented in recent years. However, despite the obvious importance of infiltration to CPSC performance, perovskite crystallisation dynamics within the stack remain poorly understood.

The following chapter will discuss infiltration methods, CPSC perovskite requirements and the variety of perovskite formulations trialled thus far, with the aim to give a detailed overview of current literature and the unique requirements and behaviours of CPSCs

1.3 Perovskite modifications in CPSCs

In any PSC, perovskite layer is of the utmost importance. As any of the component A, B and X ions may theoretically be any ion of suitable charge and radius, many potential perovskite combinations exist. Substitution thus offers a simple route into manipulating physical and optoelectronic properties. Produced materials display varied stabilities to phase transitions,

UV exposure and water-driven decomposition as well as a variety of colours. As well as being advantageous in a commercial setting for potential product aesthetics, this means the absorber materials may be catered toward specific applications: for example, cells for indoor use can use materials with narrower absorption spectra.

The feasibility of a given ionic substitution may be calculated using *Equation 1*, where r terms represent the ionic radii and *t* the extent of lattice distortion from the ideal cubic case ($t = 1$). The greater the deviation from $t = 1$, the more distorted the structure, but if $0.8 \leq t \geq 1$, the cubic crystal structure is stable. Where t falls outside of this range, phase segregation or transitions occur: at $t < 0.8$, orthorhombic structures dominate, while at $t > 1$ hexagonal phases are formed.[15]

$$t = \frac{r_A + r_x}{\sqrt{2}(r_B + r_x)} \qquad \textit{Equation 1}$$

A, B and X substitutions influence chemical and optoelectronic properties different ways. Factors such as size, symmetry and ionic charge density all affect crystallisation kinetics and formed morphologies, which in turn affect the optoelectronic properties and stability of the formed material. For example, changing the X or B ions directly affects valence and conduction band energies as the highest occupied molecular orbitals (HOMOs) and lowest unoccupied molecular orbitals (LUMOs) consist of Pb-X antibonding orbitals. Conversely, changing the 'A' cation indirectly impacts bandgap by influencing crystal packing and unit cell parameters.[13],[14]

Additionally, many performance enhancing additives and processing techniques have been developed for application in classic architectures. These generally focus on increasing capping layer grain size, coverage and crystallinity.

The perovskite requirements in CPSCs are vastly different to classic or planar sandwich, as these devices lack a perovskite capping layer and are 15-20 microns thick (Figure 1.7).

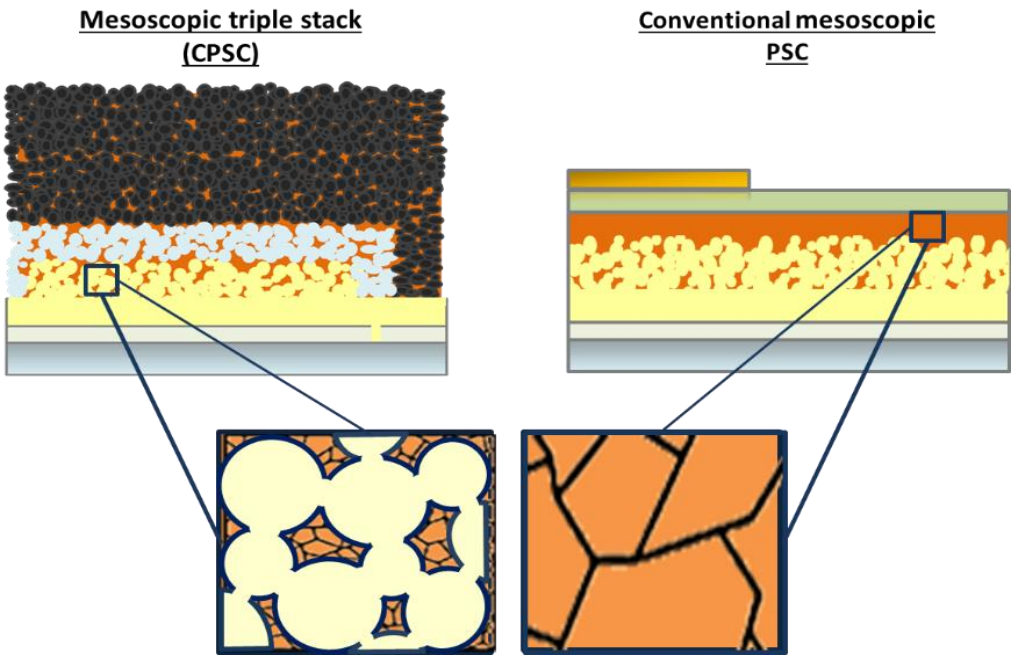

Figure 1.7: Diagram depicting the difference between crystal morphology between an CPSC and a conventional sandwich structure. Perovskite crystals in CPSCs are small, constrained by the mesoporous scaffold, whereas the capping layer in conventional PSCs consists of extremely large surface crystals.

High-performance devices are invariably achieved through maximising infiltration, the extent to which perovskite fills the stack. Full precursor permeation with minimal voids maximises light absorption, conductivity, charge transfer and electrode contact. Additionally, as voids in the scaffold can act as access points for ambient water or oxygen, well-infiltrated devices are also often more stable towards degradation.[95],[96] Unencapsulated $MAPbI_3$ CPSCs exhibit longer lifetimes under ambient conditions than classic mesoscopic devices, with well infiltrated devices produced by two-step infiltrations more resilient to degradation than poorly infiltrated cells.[96],[97]

To achieve this, crystallisation must be relatively slow and carefully controlled; large crystals forming quickly on or near the scaffold surface can prevent precursor accessing the stack.[95] Processes like antisolvent-assisted coating and high-temperature annealing, which improve conventional PSC performance by forcing fast nucleation of large, high coverage surface crystals are therefore unsuitable for CPSCs.

Instead, samples are allowed to rest for some minutes after drop casting to allow the precursor time to percolate the stack before annealing. Annealing tends to be relatively low temperature: from 50°C-100°C depending on the perovskite composition. This step is also much longer than in conventional devices: Annealing procedures of up to 20h have been

presented in the literature.[68] This allows more time for stack filling and produces more densely packed crystals in the scaffold pores.[69],[98],[99].

As depicted in Figure 1.8, infiltration can involve either a one or two-step method. In a one-step deposition a stoichiometric ABX_3 precursor solution is used, which directly forms the desired perovskite upon solvent removal. In a two-step method, the lead halide is infiltrated into the stack and annealed before subsequent reaction with the solvated organic cation (usually in a 2-propanol chemical bath).[100]

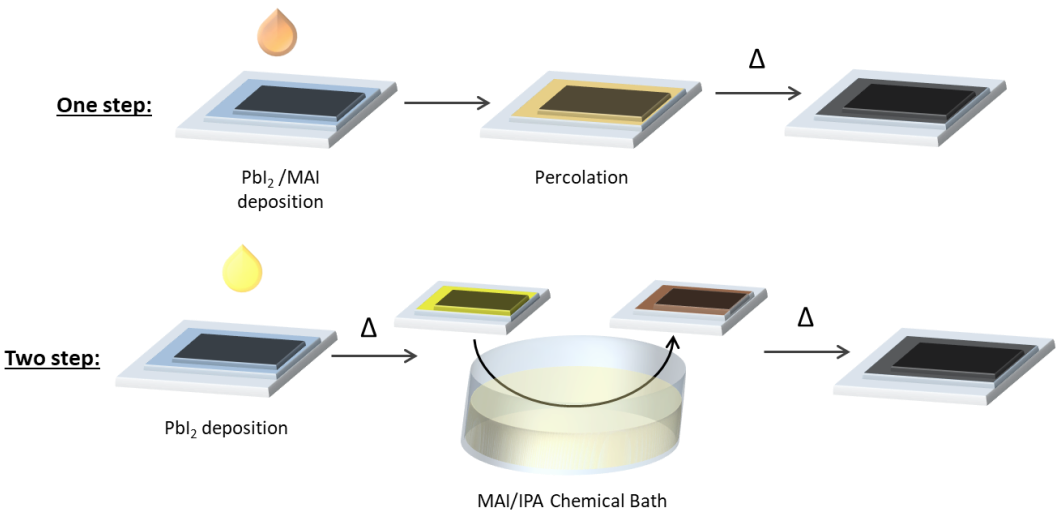

Figure 1.8: One-step (above) and two-step (below) infiltration procedures for CPSC infiltration. The thermal annealing is generally at 50-100°C depending on the perovskite composition. DMF, DMSO and GBL represent the most common solvents.

One-step methods are easier to scale up and involve fewer steps and reagents, especially advantageous when using harmful solvent systems. This method is also less likely to result in PbI_2 islands within the device: In two-step procedures, PbI_2 located deep within the infiltrated stack or at the centre of particularly large crystallites can remain unreacted in the finished device (Figure 1.9). Such crystals can act as recombination centres and catalysts to degradation.[96]

However, reproducible, high-quality infiltration is often easier to obtain using a two-step technique, especially where stoichiometric precursors exhibit poor wetting properties. Poor infiltration via a two-step method is also generally less damaging to device performance. As shown in Figure 1.9, the voids formed by a non-ideal one-step deposition are concentrated mostly in the TiO_2 and ZrO_2 layers at the base of the stack. This un-infiltrated base layer can block or scatter a significant proportion of the incoming light. A poor two-step infiltration can have a similar volume of perovskite-free stack, but performance is less impacted as voids are

more evenly distributed. Such devices therefore have better contact between the perovskite absorber and the ETL, and light absorption is less adversely affected.

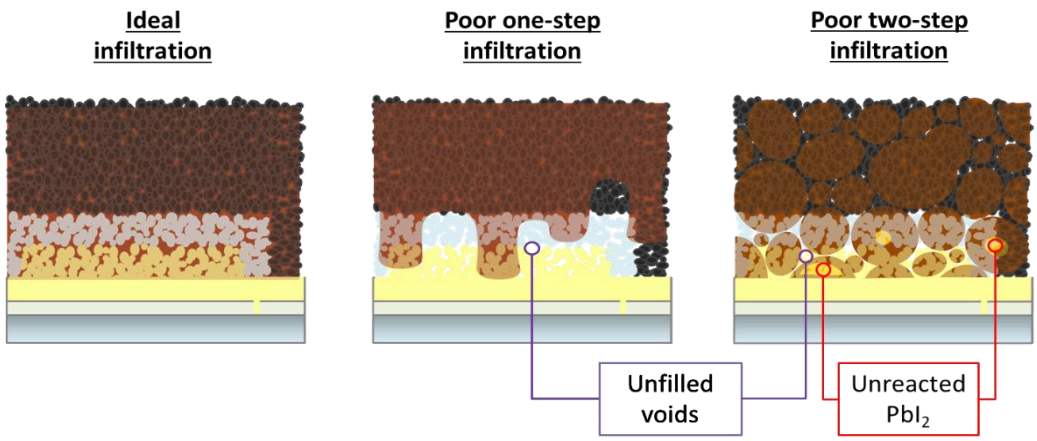

Figure 1.9: Diagram comparing ideal CPSC infiltration to poor infiltration achieved with both one-step (centre) and two-step infiltration (right). The unfilled voids in a poor one-step infiltration are often concentrated in the TiO_2 ETL and ZrO_2 insulator, whereas those in a two-step infiltration are evenly dispersed throughout the stack.

Poor one-step infiltration can be overcome by modifying the perovskite precursor or deposition technique, for example by using vapour assisted annealing or additive and solvent engineering. However, works on novel perovskite applications most frequently rely on two-step methods, which require less stringent process control and optimisation and offer more control over phase formation.[99]–[102] Some device performances achieved with different infiltration methods, using similar perovskite formulations are presented in Table 1.1.

Chemical modification of the perovskite precursors is also common. Two main approaches exist: substitution of component perovskite ions and the introduction of additives. These terms are often used interchangeably, however, in this work substitution refers to an ion that sits within the bulk ABX_3 lattice framework, while 'additives' are species that sit at interfaces or interstitial sites, or are removed during annealing.[103] Some molecules, such as AVA, partially integrate into the lattice at grain boundaries via functional groups.[104] These species, as well as those able to act as both additives and substituents will be included in the 'additives' sections.

*Table 1.1: CPSCs with like perovskite formulations and layer compositions fabricated with one step and two step infiltration methods. **

Perovskite formulation Composition Deposition method Solvent	**PCE (%) (tested area in mm²)**	**V_{oc} (mV) J_{sc} (mA/cm²) FF (%)**	**Inorganic stack Materials, deposition method and thickness of bLayer and porous layers**	**Ref, publication year**
$MAPbI_3$ One-step [(a)] DMF	10.5(7)	914 , 16.92, 68	$TiO_2^{(1)}/TiO_2^{(2)}$-(0.4µm)/ $ZrO_2^{(2)}$-(1.5µm)/$C^{(2)}$-(10µm)	[105], **2016**
$MAPbI_3$ Two-step DMF, IPA	11.4(7)	928, 17.5, 70	$TiO_2^{(1)}$)/$TiO_2^{(2)}$(0.7µm)/ $ZrO_2^{(2)}$-(1.5µm)/$C^{(2)}$-(10µm)	[56],**2014**
$Cs_{0.1}FA_{0.9}PbI_3$ One-step DMF/DMSO	15(10)	920, 23.63, 69	$TiO_2^{(1)}/TiO_2^{(2)}$(1µm)/ $ZrO_2^{(2)}$-(2µm)/$C^{(2)}$-(10µm)	[100], **2019**
$Cs_{0.1}FA_{0.9}PbI_3$ Two-step DMF, IPA	11.72(14.8)	970, 20.91, 58	$TiO_2^{(1)}/TiO_2^{(2)}$(1µm)/ $ZrO_2^{(2)}$-(1.5µm)/$C^{(2)}$-(10µm)	[106], **2019**

*Average PCEs are presented with the measured device area, alongside average photovoltaic parameters parameters ([(i)] Averages are not reported, the champion value is used). All devices were prepared on FTO substrates. Later materials, layer thicknesses are presented deposition methods, labelled as [(1)] spray pyrolysis, [(2)] screen-printing. Where a range of thickness is reported an average is presented. Infiltration methods are labelled are as follows: [(a)] drop casting, [(b)] spin coating. The reported figures show the highest achieving example of a given device formulation, not necessarily the first reported use..

1.3.1 Cation substitution

As previously discussed, the A and B cations may both consist of any ion with appropriate radius and charge. The B cation is almost invariably Pb^{2+}, although some work has begun to focus on alternatives such as Sn^{2+}. However, these formulations have yet to be applied in CPSCs, and will therefore not be discussed in this thesis. The most prevalent organic A cation in the literature is methylammonium, or MA, which produces cubic perovskite structures with broad optical absorption spectra.[16],[17]

Unfortunately, MA can significantly curb operational stability as it is volatile, oxygen sensitive and prone to migration within the crystal structure. Full or partial substitution with alternative cations therefore concurrently improves device stability and performance. This has provided a major driving force for research into alternative cations in multiple device architectures.[18]

Many of the substitutions trialled in conventional architectures were incorporated to enhance operational stability, as the volatile, oxygen sensitive methylammonium ion can be extremely detrimental to device lifetime. However, well-infiltrated $MAPbI_3$ CPSCs are far more stable under ambient conditions than conventional sandwich cells. Such high intrinsic stability may have provided less incentive for work into cation substitution, which could explain the relatively low variety of trialled until recently.[78] Table 1.2 shows the breadth of work into CPSC A cation substitution in the literature at the time of writing.

Incorporating substitutions can also be particularly challenging in CPSCs: small formulation adjustments and minor changes to a precursor's ionic properties can drastically alter crystallisation dynamics, impacting infiltration, device performance and stability. Additionally, perovskite crystallisation processes within the stack remain relatively poorly understood, making targeted modifications to precursor formulations extremely challenging.[95] In these cases, two-step methods offer more control over infiltration and crystal morphology as high quality, reproducible infiltration of lead iodide is more easily achieved.

Additional limitations exist for formulations that are poorly soluble in GBL, as well infiltrating GBL-AVA based precursors cannot be applied. Furthermore, the long, low temperature annealing processes and physical constraint from the mesoporous stack can favour mixed phase formations or solvent retention.[21],[106]

One of the first examples of cation substitution in CPSCs introduced $FAPbI_3$ perovskites to stacks in 2014. Advantageous due to its low bandgap of 1.43 eV and comparatively high thermal stability, α-$FAPbI_3$ can be difficult to crystallise in CPSCs as long, low temperature annealing can result in formation of the yellow *δ*-phase. While one step depositions resulted in almost complete *δ*-phase formation, the two-step method produced the desired α-phase and a device of 11.4% PCE.[21],[137]

Interestingly, recent work has suggested that targeted α-δ phase conversion at device interfaces can be beneficial in $FAPbI_3$ CPSCs. Achieved through controlled humidity exposure, writers suggest that limited δ-formation at the perovskite-carbon interface improves band alignment and perovskite contact, improving charge transfer and significantly reducing recombination. However, significant stability problems due to phase conversion and temperature sensitivity were still present.[138] Indeed, most FA-only devices tend to undergo a gradual phase change to the inactive *δ*-phase, decreasing device performance over time under operative conditions.[131]

FA phase instability can be mitigated through inclusion of a smaller cation such as MA (section 1.3.1) or partial halide substitution (section 1.3.3). This is also true of conventional architectures.[131],[137],[139]

More recently, work emerged examining the impact of Acetamidinium (AA) and Guanidinium (Gu) A-site substituents. When added in molar excess to DMF:DMSO-based $MAPbI_3$ precursors, these ions preferentially replace MA in the perovskite lattice, forming more stabilising hydrogen bonds with the inorganic Pb-I framework. In the case of 15% AA, this resulted in a tenfold improvement in carrier mobility and lower defect density. This led to substantial J_{sc} and V_{oc} improvements and a record certified PCE of 17.7%.[69]

Alternatively, a small inorganic ion may be used, either alone or in conjunction with MA^+. This is most commonly Cs^+. Like FA^+ systems, $CsPbI_3$ forms a black α- phase at high temperatures which reverts to an inactive yellow δ-phase at room temperature. Alternatively, $CsPbBr_3$ may be used to obtain devices of high V_{oc}, although the high material bandgap limits light absorption and device $J_{sc.}$ As of 2020, all inorganic $CsPbBr_3$ CPSCs have achieved 7.52% PCE and a high V_{oc} of 1.46 V. Surprisingly, this system is more stable in CPSCs as the constraining mesoscopic scaffold prevents transition of the desired monoclinic phase to the cubic phase even at 400°C. CPSCs may therefore prove capable of stabilising more, highly stable all-inorganic perovskite phases.

As well as enhancing the phase stability, MA^+ and Cs^+ improve the optoelectronic properties in distinctly different ways: MA^+ increases light absorption and hence the number of generated carriers, while Cs^+ reduces recombination and improves carrier collection. When added to $MA_{0.6}FA_{0.4}PbI_3$ CPSCs, Cs^+ improved V_{oc} and J_{sc} by effectively doubling the carrier diffusion length. In the optimised system, electron and hole carrier diffusion lengths went from 70 nm and 1.9 µm to 140 nm and 0.95 µm for $MA_{0.6}FA_{0.4}PbI_3$ and $Cs_{0.05}(MA_{0.6}FA_{0.4})_{0.95}PbI_3$ systems respectively.[131]

Cs^+ can also be used to stabilise α-$FAPbI_3$ in the absence of MA^+, leading to extremely thermally stable CPSCs. A 2019 paper found that 10% Cs incorporation into the lead solution during the first stage of two step deposition effectively halved CPSC performance loss under thermal stress. $Cs_{0.1}FA_{0.9}PbI_3$ devices kept at 85 at 25% RH retained 70% of initial PCE, compared to 35% for FA-only cells. Cell performance was also enhanced, with $Cs_{0.1}FA_{0.9}PbI_3$ producing devices of >14% PCE compared to 10.8% for $FAPbI_3$.[140]

One-step $Cs_{0.1}FA_{0.9}PbI_3$ infiltration has also been achieved through application of a vapour-controlled crystallisation technique. This method introduced DMSO and ultra-slow annealing in a solvent vapour environment: highly coordinating DMSO reduces precursor colloidal diameters, and a vapour environment slows solvent removal and therefore crystallisation. Produced devices exhibited significant J_{sc} and FF improvements over controls, resulting in PCEs of 15% compared to 10% for $MAPbI_3$. Devices were also found to be stable over 300 hours of dark storage at 50% RH- although it should be noted that such devices have been found in some studies to undergo transitions to the δ-phase over time, with additional mixed halide stabilisation required for long term stability under light.[100],[140]

This vapour-controlled crystallisation method has also been used to incorporate DMF/DMSO-based $Cs_{0.1}Rb_{0.05}FA_{0.85}PbI_3$ precursors into CPSCs. In conventional sandwich PSCs, rubidium has been found to improve performance and alleviate hysteresis through increasing carrier mobility and decreasing bulk recombination. Too small to sit within A lattice sites, Ru^+ instead concentrate at surface defects and within interstitial sites, reducing trap assisted recombination and limiting ion migration within the film. Combined with the V_{oc} enhancement from Cs^+ this produced a champion CPSC with a maximum stabilised PCE of 16.26%.[99]

Although vapour assisted annealing procedures and two-step methods have facilitated the fabrication of high-performance devices, they are not well-suited to scale-up: two-step infiltration takes extra time and materials, while vapour treatments are lengthy and require highly controlled annealing environments. Ideally, a one-step method that does not require additional process control or post treatment is needed to be attractive for application to larger scale modules: hence the continued use of AVA/GBL systems in scale-up projects (Detailed in section 1.3.4).

The work in this thesis therefore focuses on a $MAPbI_3$ system with AVAI additive, to eliminate phase issues while trialling new solvent systems and produce work applicable to recent scale-up initiatives.

Table 2: Table of CPSCs fabricated with different A cations. Rows are grouped by colour to directly compare formulations with similar solvent systems, deposition methods and anion compositions.[*]

Cations	Perovskite formulation Deposition method Solvent system	PCE (%) (aperture area, mm²)	V_{oc} (mV) J_{sc}(mA/cm²) FF (%)	Inorganic stack Material, (deposition method) –(layer thickness)	Ref, Publication year
MA	$MAPbI_3$ One-step[(a)] DMF	13(16)	950, 19.5, 70	$TiO_2^{(1)}/TiO_2^{(2)}$-(0.4µm)/ Al_2O_3 [(2)]-(0.5µm)/$C^{(2)}$-(8µm)	[49], **2017**
Cs, Rb, FA	$Cs_{0.1}Rb_{0.05}FA_{0.85}PbI_3$ One-step DMF	6.42(10.8)	867, 11.12, 66	$TiO_2^{(1)}$-(0.1µm)/$TiO_2^{(2)}$(0.5µm)/$ZrO_2^{(2)}$-(0.75µm)/$C^{(2)}$-(15µm)	[99], **2019**
FA, 40% MACl additive	$FAPbI_3$ One-step DMF:DMSO (4:1)	16.22(10.8)	1029, 21.8, 72.3	$TiO_2^{(1)}$-(n/a)/$TiO_2^{(2)}$(n/a)/$ZrO_2^{(2)}$-(n/a)/$C^{(2)}$-(n/a)	[138], **2022**
MA	$AVA_xMA_{(1-x)}PbI_3$ One-step[(a)] GBL	15.3(16)	869, 21.2, 83	$TiO_2^{(1)}/TiO_2^{(2)}$-(0.5µm)/ $ZrO_2^{(2)}$-(1.5µm)/$C^{(2)}$-(	[91] **2019**
Cs, MA	$CsAVA_{0.05}MA_{0.95}PbI_3$ One-step GBL	12.2(14.8)	893, 20.59, 66	$TiO_2^{(1)}/TiO_2^{(2)}$-(0.5µm)/ $ZrO_2^{(2)}$-(1.4µm)/$C^{(2)}$-(10µm)	[127], **2018**
FA	$FAPbI_3$ Two-Step DMF, IPA	11.9(7)	901, 18.4, 72	$TiO_2^{(1)})/TiO_2^{(2)}$(0.7µm)/ $ZrO_2^{(2)}$-(1.5µm)/$C^{(2)}$-(10µm)	[137], **2014**
FA, MA	$FA_{0.4}MA_{0.6}PbI_3$ Two-step DMF, IPA	12.9(7)	921, 10.9, 67	$TiO_2^{(1)}TiO_2^{(2)}$(0.7µm)/ $ZrO_2^{(2)}$-(1.5µm)/$C^{(2)}$-(10µm)	[137], **2014**
Cs, FA	$Cs_{0.1}FA_{0.9}PbI_3$ Two-step DMF, IPA	11.72(14.8)	970, 20.91, 58	$TiO_2^{(1)}/TiO_2^{(2)}$(1µm)/ $ZrO_2^{(2)}$-(1.5µm)/$C^{(2)}$-(10µm)	[106], **2019**
Cs, FA, MA	$Cs_{0.05}(FA_{0.4}MA_{0.6})_{0.95}PbI_{2.8}Br_{0.2}$ Two-step DMF, IPA	17(12.9)	1008, 23.4, 72	$TiO_2^{(1)}/TiO_2^{(2)}$-(0.46µm)/ Al_2O_3 [(2)]-(0.45µm)/$NiO^{(2)}$-(0.8 µm)/$C^{(2)}$-(10µm)	[131], **2017**
FA, MA	$FA_{0.4}MA_{0.6}PbI_{2.8}Br_{0.2}$ Two-step DMF, IPA	14.88(12.9)	953, 22.31, 70	$TiO_2^{(1)}/TiO_2^{(2)}$-(0.46µm)/ $Al_2O_3^{(2)}$-(0.45µm)/$NiO^{(2)}$-(0.8 µm)/$C^{(2)}$-(10µm)	[131], **2017**
Cs, FA, MA	$Cs_{0.05}(FA_{0.85}MA_{0.15}PbI_{2.55}Br_{0.45})$ One-step[(a), (b)] DMF:DMSO (4:1)	12.1(14.5)	937, 20.4, 66	$TiO_2^{(4)}/TiO_2^{(4)}$-(1.5µm)/ $ZrO_2^{(5),(4)}$-(1.5µm)/$C^{(5)}$-(20µm)	[123]**2021**
FA	$FAPbI_{2.9}Br_{0.1}$ Two-step DMF, IPA	11.53(14.8)	950, 20.29. 59	$TiO_2^{(1)}$-/ $TiO_2^{(2)}$(1µm)/ $ZrO_2^{(2)}$-(1.5µm)/$C^{(2)}$-(10µm)	[106], **2019**
Cs, FA	$Cs_{0.1}FA_{0.9}PbI_{0.9}Br_{0.1}$ Two-step DMF, IPA	14.14(14.8)	1018, 22.16, 63	$TiO_2^{(1)}$/ $TiO_2^{(2)}$(1µm)/ $ZrO_2^{(2)}$-(1.5µm)/$C^{(2)}$-(10µm)	[106], **2019**
Cs	$CsPbBr_3$ Two-step DMF/DMSO/, MeOH	5.33(10)	1330, 5.34, 77	$TiO_2^{(1)}$- $TiO_2^{(2)}$(0.8µm)/ $ZrO_2^{(2)}$-(2µm)/$C^{(2)}$-(15µm)	[141], **2020**
AA	$AA_{0.15}MA_{0.85}PbI_3$ One-step[(a)] NMF	17.78	1006, 24.2, 75	$TiO_2^{(1)}$- $TiO_2^{(2)}$(0.7µm)/ $ZrO_2^{(2)}$-(2.25µm)/$C^{(2)}$-(15µm)	[69], **2021**
Gu	$Gu_{0.2}MA_{0.8}PbI_3$ One-step[(a)] NMF	16.82	998.15, 22.5, 0.74	$TiO_2^{(1)}$- $TiO_2^{(2)}$(0.7µm)/ $ZrO_2^{(2)}$-(2.25µm)/$C^{(2)}$-(15µm)	[69], **2021**

[*]*Average PCEs are presented with measured device area, alongside average PV parameters. Materials and thicknesses are presented with deposition methods labelled as [(1)] spray pyrolysis, [(2)] screen-printing, [(3)]spin coating, [(4)] chemical bath deposition [(5)] doctor blading. Where a range of thickness is reported an average is presented. Infiltration methods are labelled as follows: [(a)] drop casting, [(b)] spin coating. Figures show the highest achieving example, not necessarily the first reported use*

1.3.2 Anion substitution

Changing the X ion directly affects valence and conduction band energies, as the highest occupied molecular orbitals (HOMO) and lowest unoccupied molecular orbitals (LUMO) of the perovskite absorber consist of Pb-X antibonding orbitals.[6] Like with cation substitution, differences in the ionic radii of substituted ions also cause changes to unit cell size and shape, affecting properties such as charge transfer and phase stability.[14]

The X^- anion is generally a halide or combination thereof.[39] Precise ratio control is most easily achieved by changing the molar ratios of precursor components. Alternatively, deposited perovskite layers may be exposed to HX or other gaseous halide species. Ion substitution at surface grains then produces a layer or halide gradient, which homogenises within hours to form the final film.[47] A table citing recent works applying X substitutions to CPSCs can be found at the end of this section (Table 1.3).

Partial substitution of I^- with Br^- is common in conventional architectures for stability enhancement, bandgap tuning and increased V_{oc}.[42] However, these V_{oc} and stability gains are often accompanied by lower absorption efficiency, which can lead to lower overall PCE. In conventional devices with high performance and low stability, such losses are an acceptable trade for improved device longevity. However, less incentive exists to apply methods that improve stability to the detriment of performance in $MAPbI_3$ CPSCs, where Br ratios must be very carefully controlled to avoid large J_{sc} losses.[97],[109]

For example, $MAPbBr_3$ produces high V_{oc} CPSCs: up to 1.33 V, while typical $MAPbI_3$ devices are usually ~0.9 V. However, current densities of under 7 $mAcm^{-2}$ resulted in a comparatively low PCE of 7.11%, compared to 12% for $MAPbI_3$.[142] To maintain high enough J_{sc} for good performance requires lower Br^- proportions. For example, depositing $MAPbI_2Br$ using a two-step method resulted in open circuit voltages of over 1 V and 11.0% PCE compared to 0.9 V and 10.5% for $MAPbI_3$. In this case, the substantial V_{oc} improvement outweighed J_{sc} losses from the bandgap increase. Devices were also more stable to photodegradation under operative conditions.[143] Optimised performance can be achieved with even lower proportions: optimised bromide substitutions of 10% can obtain average PCEs of 12.76%.[144]

Bromide substitutions have also been used improve the phase stability of mixed cation CPSCs. Interestingly, the performance enhancements of Br^- and Cs^+ substitution were found to be additive, with performance optimised $Cs_{0.1}FA_{0.9}PbI_{0.9}Br_{0.1}$ layers exhibiting higher optical absorption, longer carrier lifetimes and better performance than either substituent in

isolation.[131],[140] The combined systems were also more stable, showing negligible conversion to the δ-phase over time despite little change in the material bandgap.[106]

Halide alternatives include large anions of lower charge density such as BF_4^- or SCN^-, both of which have been shown to improve thermal stability and moisture tolerance of perovskite layers.[13],[145] The BF_4^- has been used to produce planar devices of over 20% PCE, with extremely high carrier lifetimes and low defect density.[55] In $MAPbI_3$ CPSCs prepared by one-step DMF depositions a 5% BF_4^- substitution increased PCE from 9.65% to 12.24%, with significant improvements to all device parameters.[105] The high charge density of the fluoride anions results in stronger intermolecular interactions, enhancing layer conductivity, hole mobility and overall stability. A similar level of improvement is seen in one-step GBL depositions, which achieved a champion PCE of 15.5% with BF_4^- compared to the 13.4% AVA-$MAPbI_3$ champion control.[56] These 'pseudohalide' substituents can substantially improve performance and lack the segregation issues observed in mixed halide perovskites and could therefore offer an alternative route to anion substitution in CPSCs. However, other alternatives such as SCN^- have yet to be thoroughly investigated in these devices.

Perhaps the greatest issue with these materials is light-induced segregation, where iodine rich areas form under constant illumination.[52]–[54] Caused by halide ion migration within the lattice, these areas form hole traps that increase the rate of recombination, negatively affecting lifetime and efficiency under operative conditions. Halide migration can theoretically be reduced by using large hydrogen-bonding organic cations such as formamidinium to increase intermolecular attraction within the lattice, but this introduces phase issues when annealing at low temperature.[53] Phase stability can vary greatly depending on the precursor solvent system. To avoid potential phase and stability issues, I^- only systems are examined in this thesis. Application of these solvents with alternative ion formulations represents an avenue for potential future work.

Table 1.3: Table of CPSCs fabricated with different X anions. Rows are grouped by colour to directly compare formulations with similar solvent systems, deposition methods and cation compositions.[*]

Anions	Perovskite formulation Chemical formula Deposition method Solvent system	PCE (%) (aperture area, mm²),	V_{oc} (mV) J_{sc} (mA/cm²) FF (%)	Inorganic stack Material, (deposition method) – (layer thickness)	Ref, Publication year
I_3	$AVA_xMA_{(1-x)}PbI_3$ One-step[(a)] GBL	15.3(16)	869, 21.2, 83	TiO_2[(1)]/TiO_2[(2)]-(0.5µm)/ ZrO_2[(2)]-(1.5µm)/C[(2)]-(20µm)	[91] **2019**
$I_{2.95}$, $(BF_4)_{0.05}$	$AVA_xMA_{(1-x)}PbI_{2.95}(BF_4)_{0.05}$ One-step[(a)] GBL	15.5(10)	970, 24.37, 66	TiO_2[(1)]/TiO_2[(2)]-(0.6µm)/ ZrO_2[(2)]-(2.5µm)/C[(2)]-(12µm)	[56], **2018**
I_3	$MAPbI_3$ One-step[(a)] DMF	13(16)	950, 19.5, 70	TiO_2[(1)]/TiO_2[(2)]-(0.4µm)/ Al_2O_3 [(2)]-(0.5µm)/C[(2)]-(8µm)	[49], **2017**
$I_{2.95}$, $(BF_4)_{0.05}$	$MAPbI_{2.95}(BF_4)_{0.05}$ One-step[(a)] DMF	13.24(7)	957, 18.15, 76	TiO_2[(1)]/TiO_2[(2)]-(0.4µm)/ ZrO_2[(2)]-(1.5µm)/C[(2)]-(10µm)	[105], **2016**
$I_{2.7}Br_{0.03}$	$MAPbI_{2.7}Br_{0.03}$ Two-step DMF, IPA	13.49	1010, 18.93, 71	TiO_2[(1)]/TiO_2[(2)]-(0.4µm)/ Al_2O_3 [(2)]-(1.2µm)/C[(2)]-(10µm)	[46] , **2016**
I_2Br	$MAPbI_2Br$ Two-step DMF, IPA	11.03(16)	1040, 15.37, 69	TiO_2[(1)]/TiO_2[(2)]-(0.4µm)/ Al_2O_3 [(2)]-(0.6µm)/C[(2)]-(10µm)	[143], **2015**
I_3	$FAPbI_3$ Two-Step DMF, IPA	11.9(7)	901, 18.4, 72	TiO_2[(1)]-(0.1µm)/TiO_2[(2)](0.7µm)/ ZrO_2[(2)]-(1.5µm)/C[(2)]-(10µm)	[137], **2014**
$I_{2.9}$, $Br_{0.1}$	$FAPbI_{2.9}Br_{0.1}$ Two-step DMF, IPA	11.53(14.8)	950, 20.29. 59	TiO_2[(1)]-(0.1µm)/TiO_2[(2)](1µm)/ ZrO_2[(2)]-(1.5µm)/C[(2)]-(10µm)	[106], **2019**
I_3	$FA_{0.4}MA_{0.6}PbI_3$ Two-step DMF, IPA	12.9(7)	921, 10.9, 67	TiO_2[(1)]-(0.1µm)/TiO_2[(2)](0.7µm)/ZrO_2[(2)]-(1.5µm)/C[(2)]-(10µm)	[137],**2014**
$I_{2.8}$, $Br_{0.2}$	$FA_{0.4}MA_{0.6}PbI_{2.8}Br_{0.2}$ Two-step DMF, IPA	14.88(12.9)	953, 22.31, 70	TiO_2[(1)]/TiO_2[(2)]-(0.46µm)/ Al_2O_3 [(2)]-(0.45µm)/NiO[(2)]-(0.8 µm)/C[(2)]-(10µm)	[131], **2017**
I_3	$Cs_{0.1}FA_{0.9}PbI_3$ Two-step DMF, IPA	11.72(14.8)	970, 20.91, 58	TiO_2[(1)]-(0.1µm)/TiO_2[(2)](1µm)/ ZrO_2[(2)]-(1.5µm)/C[(2)]-(10µm)	[106], **2019**
$I_{0.9}Br_{0.1}$	$Cs_{0.1}FA_{0.9}PbI_{0.9}Br_{0.1}$ Two-step DMF, IPA	14.14(14.8)	1018, 22.16, 63	TiO_2[(1)]-(0.1µm)/TiO_2[(2)](1µm)/ ZrO_2[(2)]-(1.5µm)/C[(2)]-(10µm)	[106], **2019**
Br_3	$CsPbBr_3$ Two-step DMF/DMSO/, MeOH	5.33(10)	1330, 5.34, 77	TiO_2[(1)]- TiO_2[(2)](0.8µm)/ ZrO_2[(2)]-(2µm)/C[(2)]-(15µm)	[141], **2020**

Average PCEs are presented with the measured device area, alongside average PV parameters. Reported figures show the highest achieving example of a given formulation, not necessarily the first reported use. Materials and thicknesses are presented with deposition methods labelled as [(1)] spray pyrolysis, [(2)] screen-printing, [(3)] spin coating, [(4)] chemical bath deposition [(5)] doctor blading. Where a range of thickness is reported an average is used. Infiltration methods are labelled as follows: [(a)] drop casting, [(b)] spin coating.

1.3.3 Inorganic additives

Depending on the ionic radius and valence bonding properties of the relevant ion, inorganic additives sit either at grain boundaries and interfaces or in interstitial sites in the perovskite lattice. Depending on the dopant concentration and the radius of the metal ion, the dopant can incorporate in different ways. At low molar concentrations (generally < 2% depending on the dopant), the metal ions sit within the interstitial lattice sites to produce a more 'n' type layer. At more typical high dopant concentrations of >5%, ions do not incorporate into the lattice, accumulating at grain boundaries and interfaces.[103] Interestingly, at high concentration, none of the added metal ions appear to incorporate into the lattice. In other words, once the dopant concentration surpasses the upper low-doping limit all the added metal ions gather at grain surfaces.[103] Instead of actively passivating pre-existing defects, interstitial ion incorporation prevents the formation of bulk defects by inhibiting halide migration, and hence the formation of 'Frenkel' defects.[40] Low-concentration doping can therefore also be used in mixed halide systems to combat migration-induced phase segregation and the associated performance and stability losses. These two distinct doping regimes allow targeted passivation of specific defects, using high dopant concentrations to selectively passivate surface defects and vice versa.[103]

A large variety of metal salts have been incorporated to precursors for conventional devices in recent years, ranging from main group species like Mg^{2+} to transition and rare earth metal salts. A broad range of properties may be influenced in this way, including trap state densities, photoluminescence quantum yields and band positions.[20],[128]–[131] The different doping regimes also affect the semiconductor properties of the perovskite absorber, with high concentrations producing more 'n type' layers and vice versa.[103]

Due to smaller grain sizes, CPSCs likely have higher surface defect density per unit active area than other architectures. It follows that incorporating high concentrations of metal salts for targeted surface defect passivation could therefore be particularly beneficial in these devices. However, despite an abundance of work on metal doping in other architectures relatively few have been applied in CPSCs at the time of writing. A table comparing additives applied in CPSCs thus far is presented at the end of this section (Table 1.4).

This may be due to the relatively poor solubility of many such salts in GBL, one of the more common solvents for one-step depositions. Currently, the only inorganic additive added to GBL-based systems thus far is CuSCN. Although this was not found significantly to affect PCE,

its presence reduced hysteresis and improved device response time, which may result in improved stability under operative conditions.[91]

The other solvent commonly used for one-step infiltrations is DMF, which solvates a wider variety of salts, but can form non-uniform, poorly infiltrated films with large needle-like crystals in the absence of vapour treatments.[132] Where metal salts have been used for performance enhancement, optimal dopant concentrations appear to coincide with those that suppress the formation of these large needle-like crystals. The optimum concentrations for CPSC performance of LiCl and $SrCl_2$ additives were also those where needle-like crystal formation was completely suppressed.[49],[133] A 30% LiCl addition to $MAPbI_3$ in DMF completely prevents the formation of such structures resulting in high quality infiltration and ~4% average PCE improvement. Recombination and film resistivity was also decreased, a consequence of surface defect passivation and Li^+ doping of the TiO_2 interface.[133]

Similarly, 0.1 molar excess of $SrCl_2$ produces small, densely packed and highly crystalline layers. Concentrated at grain boundaries, this additive acted as an effective defect inhibitor in the annealed film, producing an impressive PCE of 16%.[49] Interestingly, the annealed devices also retained almost all the added Cl^-, unusual as added chloride ions are often difficult to detect post-crystallisation.[50]

The smaller crystals observed in additive-enhanced devices are likely indicative of crystal growth inhibition during the early stages of infiltration, which benefits infiltration through preventing the formation of blockages. Therefore, although many additives result in small crystal sizes, the formation of smaller crystals is not itself essential to high CPSC performance.

Increasing the size of grains within the stack can be in fact be beneficial if the mechanism by which grain size is increased does not impede infiltration. For example, adding PW_{12} polyoxymetallates to AVA-$MAPbI_3$ precursors facilitates the growth of 30-50 µm crystals by Otswald ripening during thermal annealing. The additive therefore decreases defect density within the annealed film, as well as acting as an electro acceptor to improve charge transfer. A concentration of 15 mg/ml of PW_{12} was therefore found to enhance device PCE by over 2%, from 9.17% to 11.35%.[134]

In other architectures, improved crystallinity and device stability can also be achieved through incorporating excess PbI_2. Excess PbI_2 collects at grain boundaries, to reduce defect concentrations and the associated performance losses.[135] However, this is not the case in CPSCs; AVA-$MAPbI_3$. devices with excess PbI_2 showed no significant performance

enhancement and degraded significantly faster than stoichiometric devices.[136] It is possible that the long CPSC annealing times cause more MAI loss, resulting a slight excess of PbI_2 at grain boundaries from stoichiometric precursors. A molar excess in the precursor solution could therefore result in a detrimental surplus of PbI_2. Alternatively, AVA alone may provide sufficient surface passivation, rendering excess PbI_2 obsolete in this case.

Much work remains to be done on the effects of inorganic additives in these systems, with scope for applying other dopants as well as unravelling the underlying mechanisms behind CPSC performance enhancement.

*Table 1.4: Table of CPSCs fabricated with various inorganic additives for different perovskite formulations.**

Inorganic additive	Perovskite formulation Chemical formula Deposition method Solvent system	PCE (%) (aperture area, mm^2), publication year	V_{oc} (mV) J_{sc} (mA/cm^2) FF (%)	Inorganic stack Material, (deposition method) – (layer thickness)	Ref, publication year
CuSCN, 0.04M	$AVA_xMA_{(1-x)}PbI_3$ One-step GBL	15[(i)](16)	888, 21.9, 77	TiO_2[(1)]/TiO_2[(2)]-(1µm)/ ZrO_2[(2)]-(2.2µm)/C[(2)]-(20µm)	[91],**2019**
CsAVA, 5% Molar excess	$CsAVA_{0.05}MA_{0.95}PbI_3$ One-step GBL	12.2(14.8)	893, 20.59, 66	TiO_2[(1)]/TiO_2[(2)]-(0.5µm)/ ZrO_2[(2)]-(1.4µm)/C[(2)]-(10µm)	[127],**2018**
LiCl, 30% Molar excess	$MAPbI_3$.0.3LiCl One-step [(a)] DMF	14.5(10)	927, 20.2, 77	TiO_2[(1)]/TiO_2[(2)]-(0.5µm)/ ZrO_2[(2)]-(2µm)/C[(2)]-(10µm)	[133],**2016**
$SrCl_2$, 10% Molar excess	$MAPbI_3$.0.1$SrCl_2$ One-step[(a)] DMF	15.9(16)	1050, 20.15, 75	TiO_2[(1)]/TiO_2[(2)]-(0.4µm)/ Al_2O_3 [(2)]-(0.5µm)/C[(2)]-(8µm)	[49],**2017**
PW_{12}	$(5\text{-}AVA)_x(MA)_{1-x}PbI_3/PW_{12}$ One-step[(a)] DMF	11.35(7)	800, 22.57, 57	TiO_2[(1)]/TiO_2[(2)]-(0.4µm)/ ZrO_2[(2)]-(1.5µm)/C[(5)]-(10µm)	[134],**2017**

*Average PCEs are presented with the measured device area, alongside average photovoltaic parameters ([(i)] Averages are not reported, the champion value is used). All devices were prepared on FTO substrates. Layer materials and thicknesses are presented with deposition methods, labelled as [(1)] spray pyrolysis, [(2)] screen-printing, [(3)] spin coating, [(4)] chemical bath deposition [(5)] doctor blading. Where a range of thickness is reported an average is presented. Infiltration methods are labelled as follows: [(a)] drop casting, [(b)] spin coating.

1.3.4 Organic additives

By far the most conspicuous additive is 5-aminovaleric acid (AVA). This molecule can be added in molar ratio or excess.[96],[101] First presented in 2014 to improve infiltration, cross-sectional analysis has since shown that 3% AVA added to $MAPbI_3$-GBL precursors can improve the infiltration of a one-step deposition by 94%.[107] This is achieved by a templating effect, where AVA adsorbs to the metal oxide surface via carboxyl groups, improving precursor wetting and introducing crystal nucleation points. The resultant crystals are small and densely packed, which enhances light absorption. The AVA templating effect also boosts charge collection through improving the perovskite-TiO_2 interfacial contact. Produced devices show correspondingly high J_{sc} and PCE values.[96],[101]

Better scaffold infiltration can enhance the stability of $MAPbI_3$ CPSCs.[96] However, the extent to which AVA enhances stability far outstrips that usually observed with improved infiltration. The light-exposed lifetime of unencapsulated $MAPbI_3$ devices increases by a factor of 40 with 3-5% AVA addition, extending the time taken for 50% initial performance loss from ~2 h to ~80 h.[108] In a separate study, hermetically sealed $AVA_{0.03}MAPbI_3$ devices and modules passed IEC61646 qualifications with 9000h operational tracking, undergoing thermal cycling (70 cycles from -40°C to 85°C) and 50 h damp heat tests (85°C, 85% RH). This is unprecedented for PSCs and represents an exciting step towards commercially viable stability.[70]

Multiple factors contribute to this lifetime enhancement. As well as improving wetting, AVA induces a 2D/3D hybrid phase at the perovskite-TiO_2 interface.[104] As shown in Figure 1.10, the amine group sits at grain boundary "A" sites as the large organic sections cannot incorporate into the lattice. Produced crystals therefore have a bulk internal 3D structure with a 2D surface phase, which acts as a barrier to electron recombination and passivates surface defects. The large organic tails further enhance stability by providing a physical barrier that prevents water access, inhibits MAI loss and reduces irreversible ion migration at device interfaces.[70]

Further work has proven that incorporation is not limited to the metal oxide interface, with AVA double layers present at grain boundaries (Figure 1.10).[108] Consequently, even glass-based films are more resistant to degradation. In particular, superoxide and humidity driven degradation pathways are inhibited, as AVA blocks access to surface defects (Figure 1.10).[108],[109] Indeed, while conventional architectures experience rapid degradation

to PbI_2 in humid conditions, 70% humidity exposure actually improves $AVA_{0.03}MAPbI_3$ CPSC performance by up to 45% by enhancing crystallinity.[104],[109],[110]

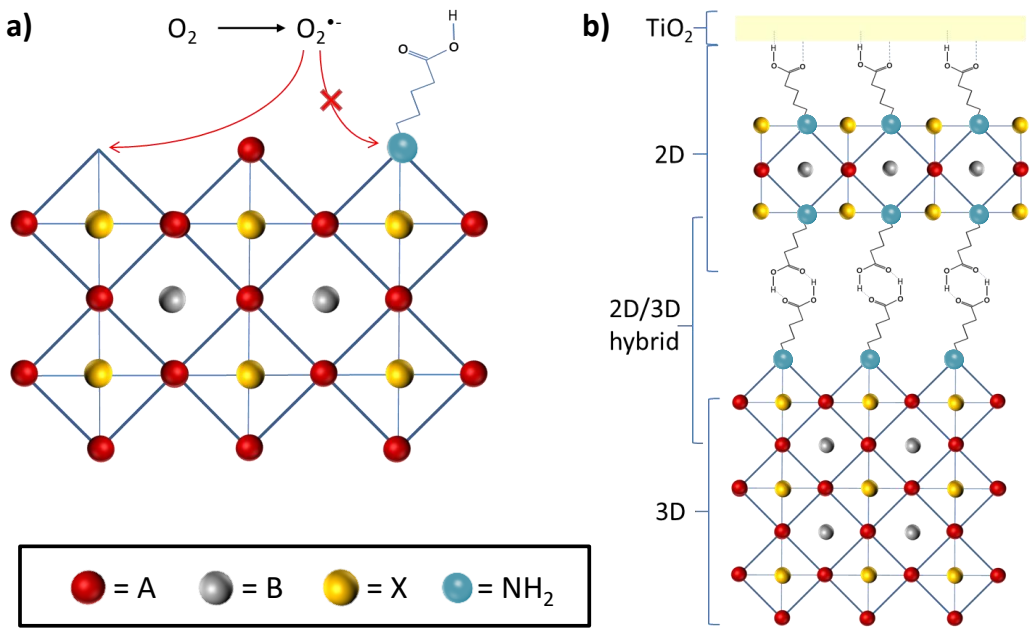

Figure 1.10: Diagrammatic representation of mechanisms by which AVA enhances stability: (a) Superoxide formation and photodegradation under illumination is prevented where defects are passivated by AVA (b) the crystal structure of the 2D/3D hybrid phase found at the perovskite/TiO_2 interface in $MAPbI_3$-AVA films.

The physical and chemical structure of AVA is intrinsic to its performance-enhancing properties. For example, the carboxyl is key to both the templating effect and the formation of 2D/3D phases: structurally similar additives lacking this group, such as benzylamine do not improve infiltration and form single phases.[111]–[113] The amine group is then necessary for interaction with the Pb ions in solution and incorporation to the perovskite surface structure: FTIR analysis of PbI_2/AVA crystallised from GBL have shown no evidence of carboxyl-lead interactions.[111] Additionally, the aliphatic chain is long enough to prevent interfacial recombination, short enough not to act as a significant barrier to electron transport, and lacks disorganised side chains that can introduce crystal growth variation.[104] Even small changes in the aliphatic chain length can result in poor devices: despite possessing the same functional groups as AVA, recent works found alternative molecules 4-aminobutyric acid and 7-aminoheptanoic acid (respectively shorter and longer than AVA) to be ineffective for improving device performance.[112]

Although several organic additives have appeared in the literature, the combination of performance enhancement and lifetime extension offered by AVA is hard to match. For

example, 4-(aminomethyl) benzoic acid hydroiodide (AB, Figure 1.11) enhanced carrier lifetime and PCEs with an average of ~15.0% PCE compared to ~13.5% using AVA. However, AB did not improve device lifetimes to the same extent as AVAI, losing over 10% PCE over 100 hours of light soaking.[77],[111]

Scope may exist for combined additive approaches. For example, thiourea has been shown to improve $MAPbI_3$ stability via a different mechanism to AVA, through catalysed $I_2 \rightarrow 2I^-$ reduction in the annealed film.[114] Guanidinium (Gu), and similar analogues improve $MAPbI_3$ scaffold contact and infiltration through similar crosslinking and hydrogen bonding-mediated changes in crystallisation dynamics.[115] Combined use with AVA or other surface passivating additives could therefore offer avenues into further lifetime enhancement.[114]

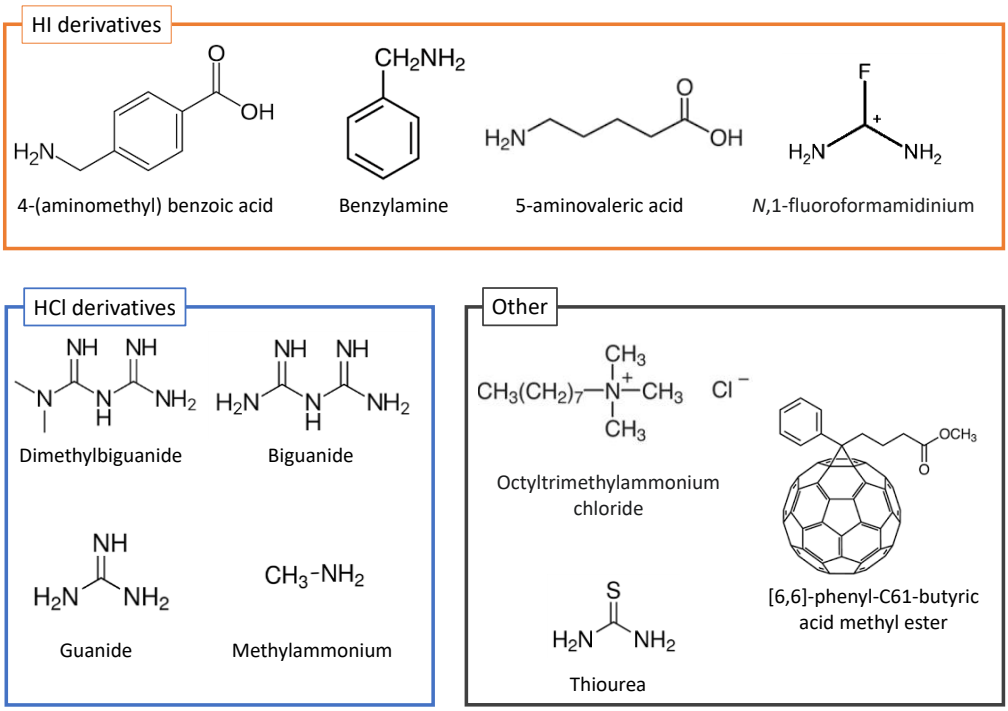

Figure 1.11: Examples of organic molecules used as additives in CPSCs in recent years.[84],[111],[114],[117]–[120]

This is realised in recent work incorporating 6% ethylene carbonate (EC) in $AVA_{0.03}MAPbI_3$ devices. Enhanced performance and stability were achieved through grain boundary passivation; electron rich carbonyl groups in the EC additive interact with Pb^{2+} centres, passivating ion vacancy defects. This increased PCE from 12.99% to 15.26% and improved ambient dark storage lifetimes.[116]

Despite its many advantages, AVA presents some potential limitations. Drastically reducing grain size and introducing a bilayer of organic molecules at each boundary has been found to reduce inter-grain charge transport.[68],[70] This may present a limit to the PCEs that can be

obtained with this additive. Additionally, AVAI produces exceptionally slow device responses, taking several hundreds of seconds in many devices to reach stabilise performance. As slow or unstable power output is undesirable in a practical setting, this could also limit the commercial viability and practicality of AVA formulations. The avenue towards commercial-level PCEs may therefore lie elsewhere. Recent works on improving CPSC performance have therefore moved away from AVA to focus on additives and crystallisation methods that increase grain size, maximising carrier lifetime and charge transport.

For example, *N*,1-fluoroformamidinium iodide (FFAI) added to $MAPbI_3$ precursors in N-Methyl formamide (NMF) produced a champion device of 17.01% PCE by significantly improving device V_{oc} and FF.[121] As well as inducing micron sized grains and a 2D hybrid at the perovskite surface, the additive fluoride substituents introduced an electron withdrawing effect, increasing the strength of Pb-I interactions within the structure and inducing a downshift in the fermi level. This decreased ion migration, reduced the number of surface defects and provided superior band matching between the perovskite and device electrodes.[121]

Similar results have been obtained using octyl trimethylammonium chloride (OTAC), which upshifts the Fermi level of TiO_2 and passivate trap states in bulk $MAPbI_3$ when added in a 10% molar excess. This enhances V_{oc} to 1007 mV and produced a PCE of 16.53%.

Interestingly, despite the initial focus on AVAI, many more recent publications focus instead on chloride salts.[120] Unlike Bromide and iodide, Cl^- is rarely found in large quantities in the final film as it forms volatile MACl and evaporates during annealing. Organic chloride additives may therefore be included in MA-containing precursors without impacting the halide content of the annealed film.[50] Instead, Cl^- influences device performance by changing the crystallisation dynamics, slowing nucleation, promoting directional crystal growth, and improving coverage and crystallinity. In CPSCs this corresponds to hysteresis alleviation, better infiltration and enhanced J_{sc}.[68]

For example, a study comparing one-step DMF/DMSO based depositions doped with GuCl, Biguanide Hydrochloride (BCl) and Dimethylbiguanide hydrochloride (DCl). A 30% molar addition of BCl resulted in a champion device of 16.35% PCE compared to a control device of 9.65% due to highly oriented crystal growth and packing and a favourable shift in perovskite band edges.[117]

More recently an impressive PCE of 18.82 % was achieved by adding 15% excess MACl to $MAPbI_3$ precursors in N-methylformamide, where it acted to decrease colloidal diameters and hence slow nucleation.[68] This represents the highest PCE achieved at the time of writing, and implies that for ultra-high performance, suppressing colloidal formation and fast nucleation are key.

The above additives all influence both nucleation and crystal growth dynamics, as evidenced by the observed changes in crystal size and shape.[111] Increasing the number of nucleation points effectively reduces crystal size without affecting shape. Other additives, such as PCBM ([6,6]-phenyl-C61-butyric acid methyl ester, Figure 1.11) and carbon quantum dots solely influence nucleation, or influence device performance solely through changing the optoelectronic properties of the annealed material. This can be advantageous: with little effect on crystal growth dynamics post-nucleation, there is less risk of these additives resulting in unwanted phase formation.[118],[122] Such additives can drastically improve infiltration, J_{sc} and PCE. For example, when 0.25 mg/ml of PCBM added to one-step DMF $MAPbI_3$ precursors, PCEs of over 11% were obtained: a similar PCE improvement to that observed in the first GBL/AVA trials.[118]

It should be noted that relatively little exists on additive enhancement of non-MA based perovskites, as until recently few formulations had been applied in CPSCs. However, 10 % urea was recently found to improve the performance of $Cs_{0.05}(FA_{0.85}MA_{0.15}PbI_{2.55}Br_{0.45})$, applied to CPSCs using DMF-DMSO based precursors.[123] Varied perovskite formulations are now beginning appearing in the literature, and it follows that work on additive based amelioration of these perovskites will soon emerge.[69],[99],[124] A summary of trialled additives thus far is provided in Table 1.5 at the end of this section.

These recent works prove that high performing, well infiltrated devices can be obtained without the presence of AVA or a similar bifunctional molecule and offer alternatives to those looking to scale up these technologies. However, many years after its initial appearance in the literature, AVA-$MAPbI_3$ formulations still dominate in large-scale module and scale-up trials.[71],[75] Especially at larger scale, its wetting enhancing properties are extremely beneficial, producing good infiltration over large areas without the need for lengthy annealing procedures to slow solvent removal. Guaranteeing reproducible infiltration without such long fabrication steps still makes AVA one of the most attractive options for large scale applications and development. AVA systems with therefore be used for devices and modules in this thesis, so as to be directly applicable to ongoing scale-up work.

*Table 1.5: Table of CPSCs fabricated with organic additives used in different perovskite formulations.**

Additive: concentration	**Perovskite formula Deposition method Solvent system**	**Avg PCE (%) (aperture area, mm²)**	**V_{oc}(mV) J_{sc}(mA/cm²) FF (%)**	**Inorganic stack Material, (deposition method) – (thickness)**	Ref**, year**
5-Aminovaleric acid hydroiodide (AVAI) 3-5% molar ratio	$AVA_xMA_{(1-x)}PbI_3$ One-step[(a)] GBL	15.3(16)	869, 21.2, 83	TiO_2[(1)]/TiO_2[(2)]-(0.5µm)/ ZrO_2[(2)]-(1.5µm)/C[(2)]-(20µm)	[110], **2019**
AVAI, Phenethylammonium iodide (PEAI) 3-5% molar ratio (both)	$AVA_xMA_{(1-x)}PbI_3$ One-step, DMF	6.72	875, 15.8, 49	TiO_2[(1)]/TiO_2[(3)]-(2µm)/ ZrO_2[(2)]-(1.8µm)/C[(5)]-(24µm)	[125],**2020**
D-Leucine (D-L) 3-5% molar ratio	$(D\text{-}L)_xMA_{(1-x)}PbI_3$ One-step[(a)], DMF	9.0	838, 24.2, 45	TiO_2[(4)]/TiO_2[(3)]-(0.5µm)/ ZrO_2[(3)]-(1.5µm)/C[(3)]-(13µm)	[113], **2020**
Aminobenzoic acid hydroiodide (AB) 3% molar ratio	$ABxMA_{(1-x)}PbI_3$ One-step[(a)] GBL: ethanol	15.6(12.6)	940, 23.4, 71	TiO_2[(1)]/TiO_2[(2)]-(0.5µm)/ ZrO_2[(2)]-(2µm)/C[(2)]-(15µm)	[111] ,**2018**
4-aminobutyric acid (ABA)	$ABAxMA_{(1-x)}PbI_3$ One-step[(a)] GBL	6.56(10.2)	859, 12.91, 62	TiO_2[(1)]/TiO_2[(2)]-(n/a)/ ZrO_2[(2)]-(n/a)/C[(2)]-(n/a)	[112],**2022**
7-aminoheptanoic acid (AHA)	$ABAxMA_{(1-x)}PbI_3$ One-step[(a)], GBL	7.55(10.2)	806, 14.76, 63	TiO_2[(1)]/TiO_2[(2)]-(n/a)/ ZrO_2[(2)]-(n/a)/C[(2)]-(n/a)	[112],**2022**
Melamine hydroiodide (MLAI) 2 wt%	$MAPbI_3$ One-step DMF/DMSO 4:1	13.86(10)	940, 20.34, 72	TiO_2[(1)]/TiO_2[(2)]-(0.5µm)/ ZrO_2[(2)]-(2µm)/C[(2)]-(15µm)	[126],**2020**
Thiourea 15 $mgml^{-1}$	$MAPbI_3$ One-step[(a)], DMF	13.0	910, 22.39, 64	TiO_2[(1)]/TiO_2[(2)]/ ZrO_2[(2)]-/C[(2)]	[114], **2019**
Cesium-5-aminovaleric acetate 5% molar ratio	$CsAVA_{0.05}MA_{0.95}PbI_3$ One-step, GBL	12.2(14.8)	893, 20.59, 66	TiO_2[(1)]/TiO_2[(2)]-(0.5µm)/ ZrO_2[(2)]-(1.4µm)/C[(2)]-(10µm)	[127], **2018**
Methlammonium chloride (MACl) 45% molar excess	$MAPbI_3$ One-step DMF	14.5(14.8)	1033, 20.14, 70	TiO_2[(1)]/TiO_2[(2)]-(1µm)/ ZrO_2[(2)]-(1.6µm)/C[(2)]-(11µm)	[84], **2018**
Guanidinium Chloride 25% molar excess	$MAPbI_3$ One-step[(a)], DMF	14.35(12.6)	1000, 19.31, 74	TiO_2[(1)]/TiO_2[(2)]-(0.5µm)/ZrO_2[(2)]-(0.5µm)/C[(2)]-(10µm)	[115], **2017**
[6,6]-phenyl-C61-butyric acid methyl ester (PCBM) 25$mgml^{-1}$ molar excess	$MAPbI_3$, One-step[(a)] DMF	12.36	930, 20.26, 66	TiO_2[(1)]/TiO_2[(2)]-(0.6µm)/ ZrO_2[(2)]-(2µm)/C[(2)]-(12µm)	[118], **2018**
PCBM 25$mgml^{-1}$ molar excess	$MAPbI_{2.95}(BF_4)_{0.05}$, One-step[(a)] DMF	14.26	990, 20.55, 70	TiO_2[(1)]/TiO_2[(2)]-(0.6µm)/ ZrO_2[(2)]-(2µm)/C[(2)]-(12µm)	[118], **2018**
MACl 15% molar excess	$MAPbI_3$, One-step, NMF	18.82[(i)](10)	1025, 22.82, 80	TiO_2[(1)]/TiO_2[(2)]-(0.8µm)/ ZrO_2[(2)]-(2.5µm)/C[(2)]-(25µm)	[68], **2021**
Biguanide hydrochloride (BH) 30% molar excess	$MAPbI_3$ One-step[(a)] DMF/DMSO	14.4(10)	910, 23, 68	TiO_2[(1)]/TiO_2[(2)]-(0.5µm)/ ZrO_2[(2)]-(3µm)/C[(2)]-(15µm)	[117], **2020**
Octyltrimethylammonium Chloride (OTAC) 10% molar excess	$MAPbI_3$, One-step[(a)] DMF/DMSO	16.53(10)	1007, 23.56, 62	TiO_2[(1)]/TiO_2[(2)]-(0.5µm)/ ZrO_2[(2)]-(2.5µm)/C[(2)]-(15µm)	[120], **2021**
Urea	$Cs_{0.05}(FA_{0.85}MA_{0.15}PbI_{2.55}Br_{0.45})$ One-step[(a), (b)] DMF:DMSO (4:1)	12.1(14.5)	937, 20.4, 66	TiO_2[(4)]/TiO_2[(4)]-(1.5µm)/ ZrO_2[(5),(4)]-(1.5µm)/C[(5)]-(20µm)	[123], **2021**
Ethylene carbonate	$AVA_xMA_{(1-x)}PbI_3$ One-step[(a)] , GBL	15.02(N/A)	930, 24.14, 67	TiO_2[(1)]/TiO_2[(2)]-(0.5µm)/ZrO_2[(2)]-(2-2.5µm)/C[(2)]-(10µm)	[116], **2022**

**Average PCEs are presented with aperture area, alongside average PV parameters ([(i)] Averages not reported, champion value used). Materials and thicknesses are presented with deposition methods, labelled as [(1)] spray pyrolysis, [(2)] screen-printing, [(3)] spin coating, [(4)] chemical bath deposition [(5)] doctor blading. Where a range of thickness is reported an average is presented. Infiltration methods are labelled as: [(a)] drop casting, [(b)] spin coating. Reported figures show the highest achieving example of a given formulation, not necessarily the first reported use.*

1.3.5 Perovskite processing conditions

Changing processing environments also offers a valid route to infiltration improvement and can impact the perovskite through changing crystal quality. In some cases, treatments can also alter the chemical composition of the perovskite by incorporating at the grain surface to form hybrid structures at the metal oxide interface. This can take several forms, including pre-treating stacks, changing the external environment during infiltration or annealing, and applying treatments to the crystallised layer. A summary table comparing notable processing changes in CPSCs is presented at the end of this section (Table 6).

A notable recent example of pre-treating involved 2-phenyl-5-benzimidazole alkali metal salts: Stacks treated with 3.5 µl of 0.05 M salt in GBL/ethanol and annealed at 100°C before infiltration exhibited average PCEs of 15.76 ± 0.44%, compared to control devices of 13.91 ± 0.38%.[146] While the organic component acted to improve wetting and interfacial stack/perovskite contact, changing the metal ion modified the ETL conduction band. Of trialled $Na^{=}$, Li^{+} and K^{+} salts, Na^{+} provided the best band-matching and therefore the highest PCE.[146] Similarly, stacks have been treated with organic silanes before infiltration, which form a monolayer at the metal oxide surface before infiltration. This improves wetting, band alignment and charge extraction, and results in an average PCE improvement of nearly 2%. Unlike with AVAI, these species are found only at the perovskite: metal oxide interfaces.[147]

In classic sandwich structures, alkali metal salts have also been shown to improve charge extraction when applied as a pre-treatment. For example, treatment of $mTiO_2$ with 30 mmol LiCl was found to improve charge extraction and V_{oc} in planar $MAPbBr_3$ cells through introducing a barrier to recombination at the TiO_2 surface.[148] This may be applicable CPSCs, although perhaps only in AVA-free devices, as AVA already prevents TiO_2-perovskite recombination to some extent.[104]

The external environment during annealing can also impact on the quality of the formed perovskite. Although CPSCs are generally less sensitive to environmental conditions and can be annealed in ambient, the temperature, humidity and solvent composition of the perovskite annealing environment can all impact the perovskite crystallisation kinetics.[99],[102],[110],[149],[150] For example, maintaining a solvent vapour environment around the stack during annealing slows the rate of crystal growth, allowing more time for infiltration and producing larger crystals.[99],[100] These solvent evaporation-controlled crystallisation (SEC) treatments have also been shown to improve α-phase formation in mixed FA^{+}/Cs^{+}

formulations, which are prone to detrimental δ-phase formation (section 1.3.1).[82] At the time of writing, such treatments have been confined to improving the infiltration of mixed cation DMF/DMSO precursors in CPSCs.

By far the most common example of post-treatment is the humidity treatment (HT) commonly applied to $AVA_{0.03}MAPbI_3$ devices, wherein the completed cells are exposed to 70% humidity at 40°C for several hours.[78],[110] HT have been found to improve initial $AVA_{0.03}MAPbI_3$ device performance by up to 45% through inducing recrystallisation. During HT, crystal grain sizes increase, and layers become more oriented and better connected to the TiO_2 ETL. Treated devices therefore exhibit reduced hysteresis and more reproducible PCEs.[78],[110] The impact of HT on GVL-MeOH devices is explored in Chapter 5.

In other architectures, exposure to such conditions can result in rapid degradation to PbI_2.[151] However, in CPSCs the presence of the hydrophobic carbon top-contact prevents of large droplets entering the stack, only allowing a limited amount of water vapour to access the perovskite. Additionally, the presence of AVAI at perovskite crystal grain boundaries reduces defect density and prevents water molecules accessing the surface, inhibiting water-induced degradation and preventing volatile MAI escaping the structure.[70],[108] Humidity assisted perovskite crystal rearrangements in the ZrO_2 and TiO_2 layers can therefore occur.[70]

Similar treatments can be applied in tandem with ammonium chloride (NH_2CHO, NH_4Cl) in $MAPbI_3$ formulations. When incorporated into the perovskite precursor, these additives significantly slow crystallisation, resulting in dense infiltration and large grains.[99],[149] NH_4Cl forms a crystalline NH_4PbI_3 intermediate, which must then be removed with a humidity treatment to form the desired $MAPbI_3$ perovskite structure. All device parameters were improved, effectively doubling the average PCE from 6.77% to 13.92%. The cells were also relatively stable, maintaining performance over 130 days in dark storage.[149] MACl vapour treatments have also been applied in other architectures post- perovskite annealing to improve perovskite crystal quality, passivate surface defects and improve performance and stability, although this has yet to be applied in CPSCs at the time of writing.[47]

More recently, work has been presented on alternative organic post treatments that improve perovskite-carbon band alignment and interfacial hole transfer.[152]–[154]. For example, $AVA_{0.03}MAPbI_3$ and $Cs_{0.05}FA_{0.95}PbI_3$ devices exposed to 10 $mgml^{-1}$ pentafluorophenylethylammonium iodide (5-PEAI) in isopropanol recently achieved respective PCEs of 16.24% and 17.47%.[124] P-type molecule 2,3,5,6-tetrafluoro-7,7,8,8-

tetracyanoquinodimethane (F4TCNQ) was found to have a similar effect, achieving a champion PCE of 18.05%. [153]

Performance enhancements were found to be a consequence of improved device V_{oc} due to selective formation of 2D phases at the perovskite-carbon interface. Not only did these layers reduce defect density and associated recombination losses, but their wide bandgaps improved band alignment and hole selectivity at the carbon electrode.[124]

Perhaps most interesting is that the above post treatment was applicable to multiple perovskite formulations, showing that this is a broad approach that could potentially be applied to many different perovskite structures or device architectures in the coming years. It also provides a useful example of performance amelioration in highly stable $AVA_{0.03}MAPbI_3$ systems, which are currently considered the most commercially applicable and recently passed stringent IEC2016 photovoltaic stability tests.[70],[124]

Table 1.6: Table of CPSCs fabricated using pre- or post- infiltration treatments for performance enhancement.

Treatment	**Perovskite formula Deposition method Solvent system**	**Inorganic stack Material, (deposition method) –(thickness)**	**PCE (%) (aperture area, mm²),**	**V_{oc} (mV) J_{sc} (mA/cm²) FF (%)**	**Ref, year**
Highly controlled solvent environment during annealing	$MAPbI_3$ One-step(a) NMP	$TiO_2^{(1)}/TiO_2^{(2)}$-(1µm)/ $Al_2O_3^{(2)}$-(1µm)/$C^{(2)}$-(10µm)	15(9)	893, 22.43, 75	[155], **2017**
5 day humidity treatment	$AVA_xMA_{(1-x)}PbI_3$ One-step(a) GBL	$TiO_2^{(1)}/TiO_2^{(2)}$-(0.5µm)/$ZrO_2^{(2)}$-(1.5µm)/$C^{(2)}$-(20µm)	15.3(16)	869, 21.2, 83	[91] [110], **2019**
5 day humidity treatment	$AVA_xMA_{(1-x)}PbI_3$ 0.04CuSCN One-step GBL	$TiO_2^{(1)}/TiO_2^{(2)}$-(1µm)/ $ZrO_2^{(2)}$-(2.2µm)/$C^{(2)}$-(20µm)	15(16)	888, 21.9, 77	[91], **2019**
Humidity exposure required for perovskite formation	$MAPbI_3$, 53.3mg/ml NH4Cl One-step DMF	$TiO_2^{(1)}/TiO_2^{(2)}$-(1µm)/ $ZrO_2^{(2)}$-(1µm)/$C^{(2)}$-(10µm)	15.6(12.6)	940, 21.45, 77	[149], **2017**
Solvent vapour assisted crystallisation. (SAC)	$Cs_{0.1}FA_{0.9}PbI_3$ One-step DMF/DMSO	$TiO_2^{(1)}/TiO_2^{(2)}$(1µm)/ $ZrO_2^{(2)}$-(2µm)/$C^{(2)}$-(10µm)	15(10)	920, 23.63, 69	[100], **2019**
2 h SAC.	$Cs_{0.1}Rb_{0.05}FA_{0.85}PbI_3$ One-step DMF/DMSO/5% Formamide	$TiO_2^{(1)}/TiO_2^{(2)}$(0.5µm)/ $ZrO_2^{(2)}$-(0.75µm)/$C^{(2)}$-(15µm)	16.21(10.8)	909, 22.69, 79	[99], **2019**
2 h SAC Average device values.	$Cs_{0.1}Rb_{0.05}FA_{0.85}PbI_3$ One step DMF/DMSO	$TiO_2^{(1)}/TiO_2^{(2)}$(0.5µm)/ $ZrO_2^{(2)}$-(0.75µm)/$C^{(2)}$-(15µm)	14.59(10.8)	888, 22.56, 72	[99], **2019**
2 h SAC Average device values.	$Cs_{0.1}Rb_{0.05}FA_{0.85}PbI_3$ One-step DMF	$TiO_2^{(1)}/TiO_2^{(2)}$(0.5µm)/ $ZrO_2^{(2)}$-(0.75µm)/$C^{(2)}$-(15µm)	6.42(10.8)	867, 11.12, 66	[99], **2019**
Immersion in 2-Phenyl-5-benzimidazole sulfonate-Na in	$AVA_xMA_{(1-x)}PbI_3$ One-step(a) GBL	$TiO_2^{(1)}/TiO_2^{(2)}$(0.55µm) / $ZrO_2^{(2)}$-(2µm)/$C^{(2)}$-(12.5µm)	15.76(10)	1000, 22.89, 69	[146], **2020**

GBL/EtOH prior to infiltration					
Stacks immersed in aminopropyltrimethoxysilane (0.05mM) in 2- propanol for hours prior to infiltration	$MAPbI_3$ Two-step DMF, IPA	$TiO_2^{(1)}/TiO_2^{(2)}$(2µm)/ $ZrO_2^{(2)}$-(1µm)/$C^{(2)}$-(9µm)	11.7 (13)	833, 19.6, 72	[147], **2015**
3 minute immersion of full cells in pentafluorophenylethylammonium (PTFA)/IPA (10 mg/ml)	$AVA_xMA_{(1-x)}PbI_3$ One-step[(a)] GBL	$TiO_2^{(1)}/TiO_2^{(2)}$(0.5µm)/ $ZrO_2^{(2)}$-(1.5µm)/$C^{(2)}$-(10µm)	16.24 (10)	981, 23.3, 70	[124],**2021**
3 minute immersion of full cells in PTFA/IPA (10 mg/ml)	$Cs_{0.05}FA_{0.95}PbI_3$, excess MACl 35% One-step DMF/DMSO	$TiO_2^{(1)}/TiO_2^{(2)}$(0.5µm)/ $ZrO_2^{(2)}$-(1.5µm)/$C^{(2)}$-(10µm)	17.47 (10)	1023, 22.3, 77	[124],**2021**
3ul of 0.1M 2-Bromo-6-fluoronaphthalene dropped onto full cell	$Cs_{0.05}FA_{0.80}MA_{0.15}PbI_{2.85}Br_{0.15}$ One-step, NMF	$TiO_2^{(1)}/TiO_2^{(2)}$(>0.5µm) / $ZrO_2^{(2)}$-(n/a)/$C^{(2)}$-(n/a)	16.45(10)	950, 22.25, 77	[154],**2022**
Drop cast 3ul saturated F4TCNQ/ IPA to full cells, anneal at 50°C, 3 min.	$Cs_{0.05}FA_{0.95}PbI_3$, One-step DMF/DMSO	$TiO_2^{(1)}/TiO_2^{(2)}$(0.5µm)/ $ZrO_2^{(2)}$-(1.5µm)/$C^{(2)}$-(10µm)	17.35(10.8)	1045, 21.87, 75	[153],**2022**

Average PCEs are presented with the measured device area, alongside average photovoltaic parameters. All devices were prepared on FTO substrates. Layer materials and thicknesses are presented with deposition methods, labelled as [(1)] spray pyrolysis, [(2)] screen-printing, [(3)] spin coating, [(4)] chemical bath deposition [(5)] doctor blading. Where a range of thickness is reported an average is presented. Infiltration methods are labelled as follows: [(a)] drop casting, [(b)] spin coating.

1.3.6 Solvent engineering in CPSCs

Solvent-based manipulation of perovskite crystallisation kinetics is also common in conventional devices.[156]–[158] In conventional architectures, DMF/DMSO mixtures are used to obtain large, high coverage surface grains through increased lead-solvent coordination.[158] Unlike the additives mentioned thus far, solvents are invariably removed during annealing and therefore affect performance solely through impacting crystal formation.

Solvent systems can impact the quality of the formed layer in two distinct ways: through their influence on precursor wetting properties and by changing the colloidal composition and crystallisation kinetics of the system. Again, the requirement for high-quality infiltration introduces additional requirements of the solvent systems used in these devices: those systems optimised for their crystallisation properties in conventional mesoscopic devices may not sufficiently wet the triple stack, hence producing poor devices.

A very limited number of solvent systems have so far been used in these devices, with relatively few examples of solvent additives for targeted infiltration improvement. Most published work on one-step depositions focuses solely on standard one-step DMF or GBL based solvent systems, and formulations that are insoluble or infiltrate poorly with these solvents are generally applied using two-step methods.[78]

GBL systems are somewhat limited in that the comparatively low solvent polarity results in a poorly wetting precursor that requires AVA to aid with wetting. As a bifunctional molecule that reduces grain size and interacts with the perovskite framework, this can cause problems with poor perovskite quality and undesirable phase formation.

Conversely, DMF/DMSO mixtures are more polar, less viscous, and do not require AVA mediated wetting improvements. This has meant that the majority of novel CPSC perovskite additives and substitutions have relied on precursors produced using DMF or DMF/DMSO. A few exceptions exist: Some work exists using *N*-methyl-2-pyrrolidone (NMP), and but as this is highly toxic it is unsuitable for scale-up.[155],[159]

Several recent publications have presented N-methyl formamide (NMF)- based precursors. NMF based $MAPbI_3$ devices of up to 16.8% PCE have been obtained, rising to 18.8% with the addition of 15% molar excess MACl.

This work is perhaps most notable in that it presents a potential framework of how to design solvent systems that can obtain large, oriented grains within the mesoporous scaffold. From this work, it would appear that maximising PbI_2 solubility while maintaining low to moderate solvent coordination with the solubilised Pb^{2+} and I^- is key to limiting colloidal size, random nucleation and the formation of intermediate solvent adducts. Decreased colloidal size in particular was highlighted as the main contribution of MACl additives in enhancing device performance, as it allowed for even lower nucleation rates and larger grain formation.

This presents an interesting contradiction: several publications have observed enhanced CPSC performance in precursors with larger colloidal diameters, fast crystal growth and resultant small grains.[49],[101],[133] However, this work suggests that to obtain the highest device performance, the opposite may be true.

It is possible that some additives improve infiltration to the extent that this counteracts any performance lost due to smaller grains- any PCE lost due to increased grain boundaries is regained due to enhanced electrode contact and additive-mediated defect passivation. It may also be true that the control devices in these studies do not possess large enough grains

to provide the enhanced carrier lifetimes observed in the NMF study. This would mean that the control devices in previous studies already contain grains far below the optimal size. Negative effects due to further size decreases would therefore be negligible compared to the positive impact of adding a surface defect passivator.

All these solvent systems present significant problems when considering large-scale production. Although less toxic than NMP, mixtures of DMF and DMSO present significant health and environmental hazards- particularly in the presence of solubilised lead.[160],[161] The 30 mgm^{-1} short-term exposure limit (STEL) of these mixtures, coupled with a flash point within the perovskite processing window, mean large-scale production would require expensive vapour handling and solvent recovery systems.[161] Thermogravimetric analyses have shown that residual DMF is retained in perovskite films post-annealing, which could introduce issues with device lifetimes and complicate end-of-life disposal or recycling procedures.[162] This is especially relevant to CPSCs, where devices contain larger amounts of perovskite and the mesoporous scaffold could impede solvent removal.[68]

Additionally, long-term reliance on DMF as a solvent for large-scale manufacture is potentially unviable: European Registration, Evaluation, Authorisation and Restriction of Chemicals (REACH) regulations classify DMF as a 'Substance of very high concern' a precursor to introducing usage restrictions.[163]

DMSO is significantly less toxic and more sustainable than DMF, but issues emerge when considering its use in combination with solubilised Pb^{2+}: the use of a skin permeable solvent in conjunction with these highly toxic ionic species presents a significant health and safety risk.[161],[164] This is also true of NMF: a very skin-permeable category 4 acute dermal toxin with potential reproductive toxicity, large volumes would require specialist handling.[165] Additionally the 20 h annealing procedures required for high-quality infiltration and large crystal growth would introduce significant production delays.[68]

There has perhaps been less drive to find alternative non-hazardous solvent systems for CPSCs, as one of the most common, GBL, is of relatively low toxicity. However, GBL is a legally restricted psychoactive.[166] Despite relatively low oral toxicity the doses for psychoactive effects can be close to lethal amounts, introducing a significant health risk for users.[167],[168] As such, GBL is subject to legal restrictions in many countries, which introduces legislative costs at large scale and can hamper lab-scale research where access is prohibited.

Scope therefore exists for exploring alternative solvents or solvent engineering to improve the toxicity and sustainability of perovskite precursors. As these technologies get closer to commercialisation, this issue will become increasingly important. Current work on non-toxic, safe and sustainable alternative solvents is therefore essential to avoid problems with safety, regulation or pollution in any future scale-up endeavours. Ensuring sustainability developing these novel technologies using 'green' solvents is particularly pertinent, to ensure that future large-scale manufacture and energy production do not make renewable technologies a source of environmental damage. Chapter 3 explores γ-valerolactone as a potential green solvent for CPSCs.

Table 1.7: CPSCs fabricated with solvent systems. Rows are grouped by colour to directly compare devices using like perovskite formulations.[*]

Solvent system **Perovskite formula** **Deposition method**	**PCE (%) (aperture area, mm²)**	**V_{oc} (mV)** **J_{sc} (mA/cm²)** **FF (%)**	**Inorganic stack Material, (deposition method) –(layer thickness)**	**Ref, publication year**	**Comments**
DMF $MAPbI_3$ One-step[(a)]	13(16)	950, 19.5, 70	$TiO_2^{(1)}/TiO_2^{(2)}$-(0.4µm)/ $Al_2O_3^{(2)}$-(0.5µm)/$C^{(2)}$-(8µm)	[49], **2017**	
DMF, IPA $MAPbI_3$ Two-step	11.4(7)	928, 17.5, 70	$TiO_2^{(1)}$-(0.1µm)/$TiO_2^{(2)}$(0.7µm) / $ZrO_2^{(2)}$-(1.5µm)/$C^{(2)}$-(10µm)	[137][56], **2014**	Average cell values
NMP $MAPbI_3$ One-step[(a)]	15(9)	893, 22.43, 75	$TiO_2^{(1)}/TiO_2^{(2)}$-(1µm)/ $Al_2O_3^{(2)}$-(1µm)/$C^{(2)}$-(10µm)	[155], **2017**	Highly controlled solvent evaporation crystallisation(SEC)
GBL $MAPbI_3$ One-step[(a)]	6.6(12.5)	878, 12.4, 61	$TiO_2^{(1)}/TiO_2^{(2)}$-(1µm)/ $ZrO_2^{(2)}$-(1µm)/$C^{(2)}$-(10µm)	[97], **2013**	With Spheroidal graphite
NMF $MAPbI_3$ One-step[(a)]	16.8[(i)](10)	970, 21.78, 80	$TiO_2^{(1)}/TiO_2^{(2)}$-(0.7µm)/ $ZrO_2^{(2)}$-(2.5µm)/$C^{(2)}$-(25µm)	[155], **2021**	Ultra-long 20 h SEC
$AVA_xMA_{(1-x)}PbI_3$ One-step[(a)] GBL	15.3(16)	869, 21.2, 83	$TiO_2^{(1)}/TiO_2^{(2)}$-(0.5µm)/ $ZrO_2^{(2)}$-(1.5µm)/$C^{(2)}$-(20µm)	[91], **2019**	30 min ambient infiltration time, 5 day humidity treatment
$AVA_xMA_{(1-x)}PbI_3$ One-step[(a)] GBL/Ethanol	15.1(10)	900, 23.58, 71	$TiO_2^{(1)}/TiO_2^{(2)}$-(0.5µm)/ $ZrO_2^{(2)}$-(3µm)/$C^{(2)}$-(10µm)	[169], **2019**	
$AVA_xMA_{(1-x)}PbI_3$ One-step DMF	9.1	848, 23.8, 45	$TiO_2^{(3)}/TiO_2^{(3)}$-(0.5µm)/ $ZrO_2^{(3)}$-(1.5µm)/$C^{(3)}$-(13µm)	[113], **2020**	
$Cs_{0.1}Rb_{0.05}FA_{0.85}PbI_3$ One-step DMF/DMSO/5% Formamide	16.21(10.8)	909, 22.69, 79	$TiO_2^{(1)})/TiO_2^{(2)}$(0.5µm)/ $ZrO_2^{(2)}$-(0.75µm)/$C^{(2)}$-(15µm)	[99], **2019**	2 h SEC
$Cs_{0.1}Rb_{0.05}FA_{0.85}PbI_3$ One step DMF/DMSO	14.59(10.8)	888, 22.56, 72	$TiO_2^{(1)}/TiO_2^{(2)}$(0.5µm)/ $ZrO_2^{(2)}$-(0.75µm)/$C^{(2)}$-(15µm)	[99], **2019**	2 h SEC Average device values.
$Cs_{0.1}Rb_{0.05}FA_{0.85}PbI_3$ One-step DMF	6.42(10.8)	867, 11.12, 66	$TiO_2^{(1}/TiO_2^{(2)}$(0.5µm)/ $ZrO_2^{(2)}$-(0.75µm)/$C^{(2)}$-(15µm)	[99], **2019**	2 h SEC. Average device values.

Where possible, average PCEs are presented with the measured device area, alongside average photovoltaic parameters ([(i)] Averages are not reported, the champion value is used). All devices were prepared on FTO. Layer materials and thicknesses are presented with deposition methods labelled as [(1)] spray pyrolysis, [(2)] screen-printing, [(3)] spin coating, [(4)] chemical bath deposition [(5)] doctor blading. Where a range of thickness is reported an average is presented. Infiltration methods are labelled as follows: [(a)] drop casting, [(b)] spin coating. The reported figures show the highest achieving example of a given device formulation, not necessarily the first reported use.

1.3.7 A note on CPSC performance and testing protocols

Perovskite device performance is most commonly measured using current/voltage (IV) scans on a solar simulator. Devices are placed under a light source of measured intensity with a spectrum approximating that of solar irradiation and placed under a bias voltage. Depending on the chosen start value, this voltage is stepped incrementally up or down towards a designated end point and the generated photocurrent measured at each interval to produce an IV curve (Figure 1.12). This reveals the short circuit current (J_{sc}) and open circuit voltage (V_{oc}) of the device, which respectively represent the light-generated carrier density at bias voltage V=0 and the applied voltage required to produce net zero photocurrent.

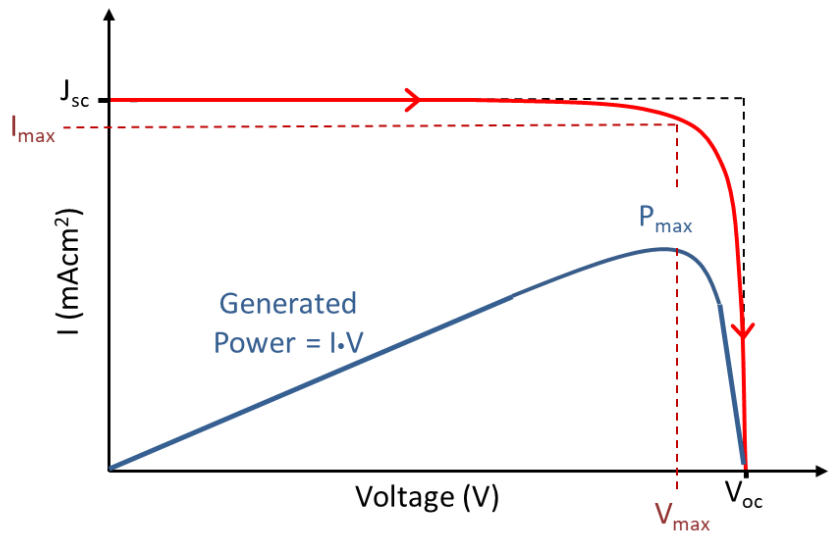

Figure 1.12: Representative current/voltage (IV) (red) and generated power (blue) curves. Open circuit voltage (V_{oc}) and short circuit current (J_{sc}) labelled. V_{max} and I_{max} represent the bias voltage and output current at the point of maximum power output. Fill Factor is the area ratio between the red and blue squares.

Multiplying the generated photocurrent (I_L) by the relevant bias voltage reveals the power produced at each condition. As shown in Figure 1.12, there exists a point of maximum power output (P_{max}) at V_{max}, I_{max}. This is the point of applied bias at which the device is most effective at converting incoming light to useable power.

These values can then be used to calculate other important parameters, such as percentage cell efficiency (PCE) and fill factor. PCE represents the proportion of input energy (P_{in}) converted to electrical power at the point of maximum power output (Equation 2). The proportion of generated power that is successfully collected is represented by the fill factor, calculated using equation 3. In an ideal device with no recombination or resistive losses the

Equation 2

IV curve is square and $V_{max}.J_{max}=V_{oc}.J_{sc}$: i.e the two squares outlined in Figure 1.12 would have the same area.

$$PCE = \frac{P_{max}}{P_{in}} = \frac{I_{max} \cdot V_{max}}{P_{in}} \qquad \textit{Equation 2}$$

$$FF = \frac{I_{max} \cdot V_{max}}{V_{oc} \cdot J_{sc}} = \frac{P_{max}}{V_{oc} \cdot J_{sc}} \qquad \textit{Equation 3}$$

$$P_{max} = I_{max} \cdot V_{max} = J_{sc} \cdot FF \qquad \textit{Equation 4}$$

As the maximum power output is calculated using (FF), short circuit current (I_{sc}) and open circuit voltage (V_{oc}), both absorption efficiency and recombination rates are accounted for in this value.

These photovoltaic parameters are dependent on external conditions such as the light spectrum, intensity, and temperature, as well as being affected by intrinsic device properties such as crystallinity and layer thicknesses. These properties can be changed in several ways, such as varying layer orientations, changing processing methods and manipulating the chemical composition of individual components. Common PSC architectures and materials are outlined in section 1.2.1.

Standard practice is to measure device performance with two voltage sweeps, stepping the bias voltage from low to high values (a forward measurement) and vice versa (reverse measurement). This is particularly important in thin film photovoltaics such as perovskites and organic photovoltaic (OPV) devices, where the IV curves and associated device parameters can vary widely with scan direction, rate and voltage range (Figure 1.13). Termed hysteresis, a variety of factors have been found to contribute to this phenomenon, including ion diffusion, interfacial charge build-up and trap density.[85],[91] A multi-faceted approach is often therefore required for hysteresis mitigation.

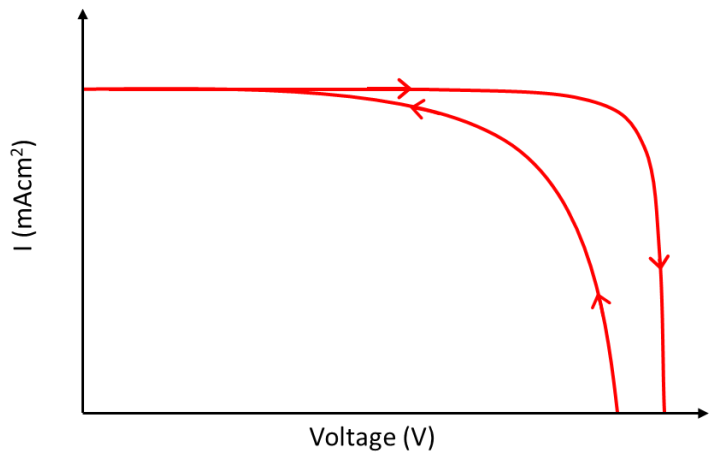

Figure 1.13: Depiction of device hysteresis, or the variation between IV curves generated from reverse (V = 0.2 → 1.0) and forward (V = 1.1 → -0.2) voltage sweeps.

Hysteresis is often particularly pronounced in CPSCs, a consequence of the large distance holes must travel to reach the carbon electrode. In CPSCs, the vast majority of carriers are generated in the first few hundred nanometres of the TiO_2 layer.[92] Electrons are therefore extracted quickly while holes must travel several micrometres before collection, leading to interfacial charge build-up and imbalanced charge extraction.[91] This can in turn lead to slow device stabilisation, high levels of hysteresis and abnormally shaped IV curves.[85]

To overcome this issue, a light soaking procedure is usually applied, wherein the device is exposed to 1 sun at zero bias for 3-10 minutes prior to IV sweeps.[42],[91] Additionally, a slower scan rate of 100 mVs^{-1} is used to allow devices to adjust during sweeps and avoid PCE overestimation.

IV measurements are often presented in conjunction with other complementary techniques, such as stabilised current measurements and maximum power point tracking. This can be challenging in CPSCs, as slow response times require long measurement periods to achieve stabilisation or maximum power. Additionally, stabilised current measurements frequently produce lower PCE values than IV curves in CPSCs due to imbalanced charge extraction at device electrodes.[42] This is exacerbated in cases where perovskite infiltration is poor, as low stack filling reduces electrode contact and further decreases charge collection efficiency.[42] In other words, poorly infiltrated samples tend to exhibit larger differences between PCEs calculated from IV curves and those from stabilised current measurements.

Measured IV CPSC performance is also impacted by the device active area and mask aperture.[93] While lab scale devices are typically around 0.8-1 cm^2 active area, cells are masked during IV testing to maintain the accuracy of PCE calculations and maintain a known

light exposed area. The aperture area and the ratio between illuminated area and total active area have both been found to contribute to differences in PCEs obtained from IV curves.[93] When aperture area is decreased, diffuse light entering the masked area contributes more to J_{sc}, resulting in J_{sc} and PCE overestimations: apertures of 0.05-0.020 cm^2 produce ~3.5% PCE overestimation due to artificially enhanced photocurrent, while those of 0.28-0.50 cm^2 overestimate by <1%. The opposite trend can be observed for V_{oc}, which is underestimated by ~2.6% when using 0.05-0.020 cm^2 apertures and ~1.0% for larger 0.28-0.50 cm^2 masks.[93] Additionally, decreasing the aperture size somewhat mitigates the negative impact of the resistive carbon top contact. [93] Smaller aperture masks therefore produce higher PCEs, but such results are not necessarily representative of the true device performance at larger scale. To provide PCEs representative of true device performance, the aperture areas of masks used to obtain PCEs in all following work are 0.49 cm^2 or 0.16 cm^2 on a device of 1 cm^2 active area unless otherwise stated.* Additionally, devices were measured in the centre of the active area (as shown in Figure 1.14) to ensure the same area was examined during consecutive measurements.

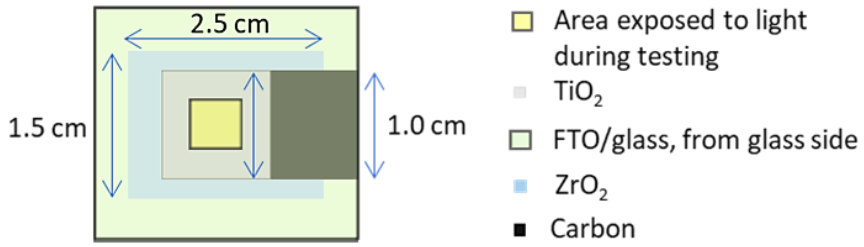

Figure 1.14: Diagrammatic representation of a CPSC from the glass side, with corresponding measurements for each printed layer and depiction of the area illuminated during IV testing (0.49 cm^2 unless otherwise stated)

More established technologies such as silicon and OPV have clear published guidelines for performance, lifetime, and stability testing.[94] Developed specifically for industrial testing of silicon modules, standard silicon testing regimes tend to be unsuitable for less environmentally stable OPV and perovskite technologies.

OPV specific performance and stability testing procedures exist in the form of ISOS (International Summit on Organic Photovoltaic Stability) consensus protocols. These guidelines were developed in 2011 for clear and reproducible reporting of lab based OPV

* Results from 0.16 cm^2 and 0.49 cm^2 masks are never directly compared in this work. However, some chapters contain results from both masks: standard testing was changed to use 0.16 cm^2 masks in early 2021 to bring our testing procedures in line with that of other groups, who use 0.1-0.2 cm^2 as standard for CPSCs. [78],[93] Where results from two mask sizes are used in the same chapter, each figure will specify the aperture used and data is discussed separately.

performance and degradation studies. When applied properly, such standardised testing procedures can enable direct comparisons between results from different laboratories.[94]

As PSC performance and stability are heavily impacted by ambient conditions and testing environments, accurate reporting of testing and storage environments is vital when comparing results from different laboratories.[94] The lack of standardised testing thus far has resulted in a broad variety of different testing methods and inconsistent reporting of environmental conditions before, during and after testing- particularly important in PSC analysis, as devices are so sensitive to ambient conditions.[94] This lack of consistency in the reporting of testing conditions prevents meaningful data comparison between different laboratories and has likely impeded progress in the identification of the operational processes underlying PSC performance and stability.

1.4 Aims and motivations

The large number of recent studies covered in this chapter shows the versatility of CPSCs, and how quickly the field is currently advancing. Performance has advanced to a champion of 18.8% PCE since their advent in 2013. [67][68] Although the record PCEs for lab-scale devices still currently lag behind those of more conventional spin coated planar devices, their low cost, inherently higher stability and ease of processing offer a significant advantage when considering scale-up initiatives. Indeed, modules of up to 198cm^2 of over 6% PCE have already been fabricated in ambient conditions in the literature. [77][78]

Considering the considerable ongoing work into both CPSC scale-up and performance enhancement, it is feasible that commercially viable CPSC modules could soon become a reality.

Works examining CPSC scale-up have focussed mainly on the $AVA_{0.03}MAPbI_3$ system, as it is well-infiltrating, highly stable and can be quickly annealed in ambient conditions. [71], [75], [77]

However, there exist some significant drawbacks. As discussed in section 1.3.6, $AVA_{0.03}MAPbI_3$ devices and modules are generally produced using GBL as the perovskite precursor solvent. Although of relatively low toxicity, GBL is a psychoactive substance banned in several countries, which could limit scaled production or introduce significant legislative costs.[166] Other formulations rely overwhelmingly on toxic DMF-DMSO mixtures, introducing their own issues for scaled production.[161]-[164]

This thesis will explore γ-valerolactone (GVL) as a potential alternative to GBL for CPSC device and module fabrication. Compared to GVL is not subject to legal restrictions, significantly less toxic, biodegradable and can be obtained from sustainable lignocellulosic feedstocks.[170]-[172] This makes GVL much more suited to scaled use than the GBL or DMF-DMSO systems currently used in these devices.

Once applied, the system will be optimised and applied to large modules to evaluate its performance at scale. Performance evolution will then be examined, to evaluate the optimum time at which to encapsulate for peak performance.

Another significant issue with CPSCs (and arguably, perovskite devices in general) is a lack of reproducibility. Although seldom discussed in detail in the literature, CPSCs frequently exhibit significant batch-to-batch performance variation due to changes in infiltration (the extent to which the device stack is filled with perovskite). The reasons for these variations have not been analysed in depth, and as such, there is a lack of understanding across the field as to the precise causes of these issues. This can slow research significantly and could be catastrophic to production at an industrial scale.

The final section of this work will therefore focus on determining the causes of poor infiltration, with the aim of producing a reference resource of methods for troubleshooting infiltration issues in these devices.

1.5 References

[1] IEA (2021), Net Zero by 2050, *IEA*, https://www.iea.org/reports/net-zero-by-2050 (accessed July 2022)

[2] T. Baines, PhD Thesis, University of Liverpool, 2019

[3] J. Gong, K. Sumathy, Q. Qiao and Z. Zhou, *Renew. Sustain. Energy Rev*., 2017, **68**, 234–246

[4] J. Ramanujam and U. P. Singh, *Energy Environ. Sci.,* 2017, **10**, 1306–1319

[5] D. Zhou, T. Zhou, Y. Tian, X. Zhu and Y. Tu, *J. Nanomater*., 2018, **vol. 2018**, 1–15

[6] A. Walsh, *J. Phys. Chem. C*, 2015, **119**, 5755–5760

[7] W. Zhang, S. Pathak, N. Sakai, T. Stergiopoulos, P. K. Nayak, N. K. Noel, A. A. Haghighirad, V. M. Burlakov, D. W. deQuilettes, A. Sadhanala, W. Li, L. Wang, D. S. Ginger, R. H. Friend and H. J. Snaith, *Nat. Commun.,* 2015, **6**, 10030

[8] M. Grätzel, *Acc. Chem. Res*., 2017, **50**, 487–491

[9] K. Li, H. Chen, H. Liu, Y. Yuan, Y. Gao, B. Yang and C. Zhou*, Org. Electron*., 2018, **62**, 298–303

[10] W. S. Yang, B.-W. Park, E. H. Jung, N. J. Jeon, Y. C. Kim, D. U. Lee, S. S. Shin, J. Seo, E. K. Kim, J. H. Noh and S. Il Seok, *Science*, 2017, **356**, 1376–1379

[11] J. Yang and T. L. Kelly, Inorg. Chem., 2017, **56**, 92–101

[12] S. Nagane, U. Bansode, O. Game, S. Chhatre and S. Ogale, *Chem. Commun.,* 2014, **50**, 9741

[13] L.-Q. Xie, L. Chen, Z.-A. Nan, H.-X. Lin, T. Wang, D.-P. Zhan, J.-W. Yan, B.-W. Mao and Z.-Q. Tian, *J. Am. Chem. Soc.,* 2017, **139**, 3320–3323

[14] Z. Li, M. Yang, J.-S. Park, S.-H. Wei, J. J. Berry and K. Zhu, *Chem. Mater.,* 2016, **28**, 284–292

[15] N. J. Jeon, J. H. Noh, W. S. Yang, Y. C. Kim, S. Ryu, J. Seo and S. Il Seok, *Nature*, 2015, **517**, 476–480

[16] C. Yi, J. Luo, S. Meloni, A. Boziki, N. Ashari-Astani, C. Grä, S. M. Zakeeruddin, U. Rö and M. Grä, *Energy Environ. Sci*, 2016, **9**, 656

[17] S.-H. Turren-Cruz, A. Hagfeldt and M. Saliba, *Science,* 2018, **362**, 449–453

[18] G. E. Eperon, S. D. Stranks, C. Menelaou, M. B. Johnston, L. M. Herz and H. J. Snaith, *Energy Environ. Sci.,* 2014, **7**, 982

[19] T. M. Koh, K. Fu, Y. Fang, S. Chen, T. C. Sum, N. Mathews, S. G. Mhaisalkar, P. P. Boix and T. Baikie*, J. Phys. Chem. C,* 2014, **118**, 16458–16462

[20] O. J. Weber, D. Ghosh, S. Gaines, P. F. Henry, A. B. Walker, M. S. Islam and M. T. Weller, *Chem. Mater.,* 2018, **30**, 3768–3778

[21] M. Saliba, T. Matsui, J.-Y. Seo, K. Domanski, J.-P. Correa-Baena, M. K. Nazeeruddin, S. M. Zakeeruddin, W. Tress, A. Abate, A. Hagfeldt and M. Grätzel, *Energy Environ. Sci*., 2016, **9,** 1989–1997

[22] S. Masi, C. Echeverría-Arrondo, K. M. M. Salim, T. T. Ngo, P. F. Mendez, E. López-Fraguas, D. F. Macias-Pinilla, J. Planelles, J. I. Climente and I. Mora-Seró, *ACS Energy Lett.,* 2020, **5**,418–427

[23] E. L. Unger, E. T. Hoke, C. D. Bailie, W. H. Nguyen, A. R. Bowring, T. Heumüller, M. G. Christoforo and M. D. McGehee, *Energy Environ. Sci.,* 2014, **7**, 3690–3698

[24] T. Zhang, M. Long, K. Yan, M. Qin, X. Lu, X. Zeng, C. M. Cheng, K. S. Wong, P. Liu, W. Xie and J. Xu, *Adv. Energy Mater*., 2017, 7, 1700118

[25] D. W. Ferdani, S. R. Pering, D. Ghosh, P. Kubiak, A. B. Walker, S. E. Lewis, A. L. Johnson, P. J. Baker, M. S. Islam and P. J. Cameron, *Energy Environ. Sci.,* 2019, **12**, 2264-2272

[26] R. E. Beal, D. J. Slotcavage, T. Leijtens, A. R. Bowring, R. A. Belisle, W. H. Nguyen, G. F. Burkhard, E. T. Hoke and M. D. McGehee, *J. Phys. Chem. Lett*., 2016, **7**, 746–751

[27] Q. Wang, X. Zheng, Y. Deng, J. Zhao, Z. Chen and J. Huang, Joule, 2017, 1, 371–382

[28] Y. Hu, E. M. Hutter, P. Rieder, I. Grill, J. Hanisch, M. F. Aygüler, A. G. Hufnagel, M. Handloser, T. Bein, A. Hartschuh, K. Tvingstedt, V. Dyakonov, A. Baumann, T. J. Savenije, M. L. Petrus and P. Docampo, *Adv. Energy Mater.,* 2018, **8**, 1703057

[29] W. Rehman, D. P. McMeekin, J. B. Patel, R. L. Milot, M. B. Johnston, H. J. Snaith and L. M. Herz, *Energy Environ. Sci*., 2017, **10**, 361-369

[30] J.-W. Lee, D.-H. Kim, H.-S. Kim, S.-W. Seo, S. M. Cho and N.-G. Park, *Adv. Energy Mater.,* 2015, **5**, 1501310

[31] P. Gao, A. Rashid, B. M. Yusoff and M. K. Nazeeruddin, *Nat. Comm*., 2018, **9**, 5028

[32] I. B. Koutselas, L. Ducasse and G. C. Papavassiliou, *J. Phys.: Condens. Matter*, 1996, **8**, 1217

[33] Y. Liu, S. Akin, L. Pan, R. Uchida, N. Arora, J. V. Milić, A. Hinderhofer, F. Schreiber, A. R. Uhl, S.

M. Zakeeruddin, A. Hagfeldt, M. Ibrahim Dar and M. Grätzel, *Sci. Adv.*, 2019, **5**, 2543

[34] I. Poli, S. Eslava and P. Cameron, *J. Mater. Chem. A*, 2017, *5*, 22325–22333

[35] Z. Zhao, F. Gu, Y. Li, W. Sun, S. Ye, H. Rao, Z. Liu, Z. Bian and C. Huang, *Adv. Sci.*, 2017, **4**, 1700204

[36] F. Hao, C. C. Stoumpos, D. H. Cao, R. P. H. Chang and M. G. Kanatzidis, *Nat. Photonics*, 2014, **8**, 489–494

[37] J. Liang, P. Zhao, C. Wang, Y. Wang, Y. Hu, G. Zhu, L. Ma, J. Liu and Z. Jin, *J. Am. Chem. Soc.*, 2017, **139**, 14009–14012

[38] Z. Zhang, Y. Zhou, Y. Cai, H. Liu, Q. Qin, X. Lu, X. Gao, L. Shui, S. Wu and J.-M. Liu, *J. Power Sources*, 2018, **377**, 52–58

[39] Y. Zhou, J. Chen, O. M. Bakr and H.-T. Sun, *Chem. Mater.*, 2018, **30**, 6589-6613

[40] G. P. Nagabhushana, R. Shivaramaiah and A. Navrotsky, *Proc. Natl. Acad. Sci. U. S. A.*, 2016, **113**, 7717–21

[41] H. F. Zarick, N. Soetan, W. R. Erwin and R. Bardhan, *J. Mater. Chem. A*, 2018, **6**, 5507–5537

[42] J. Chae, Q. Dong, J. Huang and A. Centrone, *Nano Lett.*, 2015, *15*, 8114–8121

[43] M. Kim, B. J. Kim, D.-Y. Son, N.-G. Park, H. S. Jung and M. Choi, *Nano Lett.*, 2016, **16**, 5756–5763

[44] L. K. Ono, E. J. Juarez-Perez and Y. Qi, *ACS Appl. Mater. Interfaces*, 2017, *9*, 30197–30246

[45] K. Cao, H. Li, S. Liu, J. Cui, Y. Shen and M. Wang, *Nanoscale*, 2016, **8**, 8839–8846

[46] D. B. Khadka, Y. Shirai, M. Yanagida, T. Masuda and K. Miyano, *Sustain. Energy Fuels*, 2017, **1**, 755–766

[47] S. Colella, E. Mosconi, P. Fedeli, A. Listorti, F. Gazza, F. Orlandi, P. Ferro, T. Besagni, A. Rizzo, G. Calestani, G. Gigli, F. De Angelis and R. Mosca, *Chem. Mater.*, 2013, **25**, 4613–4618

[48] H. Zhang, H. Wang, S. T. Williams, D. Xiong, W. Zhang, C.-C. Chueh, W. Chen and A. K.-Y. Jen, *Adv. Mater.*, 2017, **29**, 1606608

[49] S. Colella, E. Mosconi, G. Pellegrino, A. Alberti, V. L. P. Guerra, S. Masi, A. Listorti, A. Rizzo, G. G. Condorelli, F. De Angelis and G. Gigli, *J. Phys. Chem. Lett.*, 2014, **5**, 3532–3538

[50] M. I. Dar, N. Arora, P. Gao, S. Ahmad, M. Grätzel and M. K. Nazeeruddin, *Nano Lett.*, 2014, *14*, 6991–6996

[51] E. T. Hoke, D. J. Slotcavage, E. R. Dohner, A. R. Bowring, H. I. Karunadasa and M. D. McGehee, *Chem. Sci.*, 2015, **6**, 613–617

[52] A. J. Barker, A. Sadhanala, F. Deschler, M. Gandini, S. P. Senanayak, P. M. Pearce, E. Mosconi, A. J. Pearson, Y. Wu, A. R. Srimath Kandada, T. Leijtens, F. De Angelis, S. E. Dutton, A. Petrozza and R. H. Friend, *ACS Energy Lett.*, 2017, **2**, 1416–1424

[53] A. Aziz, N. Aristidou, X. Bu, R. J. E. Westbrook, S. A. Haque and M. Saiful Islam, *Chem. Mater*, 2020, **32**, 400–409

[54] J. Zhang, S. Wu, T. Liu, Z. Zhu and A. K. -Y. Jen, *Adv. Funct. Mater.*, 2019, **29**, 1808833

[55] Y. Sheng, A. Mei, S. Liu, M. Duan, P. Jiang, C. Tian, Y. Xiong, Y. Rong, H. Han and Y. Hu, *J. Mater. Chem. A*, 2018, **6**, 2360–2364

[56] A. Guerrero, G. Garcia-Belmonte, I. Mora-Sero, J. Bisquert, Y. S. Kang, T. J. Jacobsson, J. P. Correa-Baena and A. Hagfeldt, *J. Phys. Chem. C*, 2016, **120**, 8023–8032

[57] G. E. Eperon, V. M. Burlakov, P. Docampo, A. Goriely and H. J. Snaith, *Adv. Funct. Mater.*, 2014, **24**, 151–157

[58] J. Baker, K. Hooper, S. Meroni, A. Pockett, J. McGettrick, Z. Wei, R. Escalante, G. Oskam, M. Carnie and T. Watson, *J. Mater. Chem. A*, 2017, **5**, 18643–18650

[59] A. Priyadarshi, A. Bashir, J. T. Gunawan, L. J. Haur, A. Bruno, Z. Akhter, N. Mathews and S. G. Mhaisalkar, *Energy Technol.*, 2017, **5**, 1866-1872

[60] https://www.nrel.gov/pv/assets/pdfs/pv-efficiency-chart.20181221.pdf, (accessed July 2022)

[61] A. D. Taylor, Q. Sun, K. P. Goetz, Q. An, T. Schramm, Y. Hofstetter, M. Litterst, F. Paulus and Y. Vaynzof, *Nat. Commun. 2021 121*, 2021, **12**, 1–11

[62] H. Chen and S. Yang, *J. Mater. Chem. A*, 2019, **7**, 15476–15490

[63] L. Fagiolari and F. Bella, *Energy Environ. Sci.*, 2019, **12**, 3437–3472

[64] S. Liu, W. Huang, P. Liao, N. Pootrakulchote, H. Li, J. Lu, J. Li, F. Huang, X. Shai, X. Zhao, Y. Shen, Y. B. Cheng and M. Wang, *J. Mater. Chem. A*, 2017, **5**, 22952–22958

[65] J. Barichello, L. Vesce, F. Matteocci, E. Lamanna and A. Di Carlo, *Sol. Energy Mater. Sol. Cells*, 2019, **197**, 76–83

[66] Z. Meng, D. Guo and K. Fan, *Appl. Surf. Sci.*, 2018, *430*, 632–638

[67] Z. Ku, Y. Rong, M. Xu, T. Liu and H. Han, *Sci. Rep.*, 2013, **3**, 1–5

[68] S. Liu, Y. Sheng, D. Zhang, W. Zhang, Z. Qin, M. Qin, S. Li, Y. Wang, C. Gao, Q. Wang, Y. Ming, C. Liu, K. Yang, Q. Huang, J. Qi, Q. Gao, K. Chen, Y. Hu, Y. Rong, X. Lu, A. Mei and H. Han, *Fundam. Res.*, 2022, **2**, 276-283

[69] X. Xiao, Y. Chu, C. Zhang, Z. Zhang, Z. Qiu, C. Qiu, H. Wang, A. Mei, Y. Rong, G. Xu, Y. Hu and H. Han, *Fundam. Res*., 2021, **1**, 385-392

[70] A. Mei, Y. Sheng, Y. Ming, Y. Hu, Y. Rong, W. Zhang, S. Luo, G. Na, C. Tian, X. Hou, Y. Xiong, Z. Zhang, S. Liu, S. Uchida, T.-W. Kim, Y. Yuan, L. Zhang, Y. Zhou and H. Han, *Joule*, 2020, **4**, 2646–2660

[71] S. M. P. Meroni, K. E. A. Hooper, T. Dunlop, J. A. Baker, D. Worsley, C. Charbonneau and T. M. Watson, *Energies,* 2020, **13**, 1589

[72] H. Chen and S. Yang, *Adv. Mater*., 2017, **29**, 1603994

[73] D. Raptis, V. Stoichkov, S. M. P. Meroni, A. Pockett, C. A. Worsley, M. Carnie, D. A. Worsley and T. Watson, Curr. Appl. Phys., 2020, **20**, 619–627

[74] S. G. Hashmi, D. Martineau, X. Li, M. Ozkan, A. Tiihonen, M. I. Dar, T. Sarikka, S. M. Zakeeruddin, J. Paltakari, P. D. Lund and M. Grätzel, *Adv. Mater. Technol.,* 2017, **2**, 1600183

[75] A. Verma, D. Martineau, S. Abdolhosseinzadeh, J. Heier and F. Nüesch, *Mater. Adv.,* 2020, **1**, 153–160

[76] S. M. P. Meroni, Y. Mouhamad, F. De Rossi, A. Pockett, J. Baker, R. Escalante, J. Searle, M. J. Carnie, E. Jewell, G. Oskam and T. M. Watson, *Sci. Technol. Adv. Mater.*, 2018, **19**, 1–9

[77] F. De Rossi, J. A. Baker, D. Beynon, K. E. A. Hooper, S. M. P. Meroni, D. Williams, Z. Wei, A. Yasin, C. Charbonneau, E. H. Jewell and T. M. Watson, *Adv. Mater. Technol.*, 2018, **3**, 1800156

[78] S. M. P. Meroni, C. Worsley, D. Raptis and T. M. Watson, *Energies,* 2021, **14**, 386

[79] G. Syrrokostas, G. Leftheriotis, S. N. Yannopoulos and Jianbo Yin, *J. Nanomater.,* 2019, **vol. 2019**, 8348237

[80] X. Sun, J. Xu, L. Xiao, J. Chen, B. Zhang, J. Yao and S. Dai, *Int. J. Photoenergy*, 2017, **vol. 2017**, 4935265

[81] Z. hui Liu, S. Bi, G. liang Hou, C. zhan Ying and X. jia Su, *J. Power Sources*, 2019, **430**, 12–19

[82] T. Liu, L. Liu, M. Hu, Y. Yang, L. Zhang, A. Mei and H. Han, *J. Power Sources*, 2015, **293**, 533–538

[83] Y. Rong, X. Hou, Y. Hu, A. Mei, L. Liu, P. Wang and H. Han, *Nat. Commun.,* 2017, **8**, 14555

[84] H. Jiang, X. Liu, N. Chai, F. Huang, Y. Peng, J. Zhong, Q. Zhang, Z. Ku and Y. Cheng, *RSC Adv.*, 2018, **8**, 35157–35161

[85] A. Pockett, D. Raptis, S. M. P. Meroni, J. Baker, T. Watson and M. Carnie, *J. Phys. Chem. C*, 2019, **123**, 11414–11421

[86] H. Li, K. Cao, J. Cui, S. Liu, X. Qiao, Y. Shen and M. Wang, *Nanoscale*, 2016, **8**, 6379–6385

[87] L. Zhou, Y. Zuo, T. K. Mallick and S. Sundaram, *Sci. Rep*., 2019, **9**, 8778

[88] P. Jiang, Y. Xiong, M. Xu, A. Mei, Y. Sheng, L. Hong, T. W. Jones, G. J. Wilson, S. Xiong, D. Li, Y. Hu, Y. Rong and H. Han, *J. Phys. Chem. C*, 2018, **122**, 16481–16487

[89] A. Bashir, S. Shukla, J. H. Lew, S. Shukla, A. Bruno, D. Gupta, T. Baikie, R. Patidar, Z. Akhter, A. Priyadarshi, N. Mathews and S. G. Mhaisalkar, *Nanoscale*, 2018, **10**, 2341–2350

[90] R. Hu, R. Zhang, Y. Ma, W. Liu, L. Chu, W. Mao, J. Zhang, J. Yang, Y. Pu and X. Li, Appl. Surf. Sci., 2018, **462**, 840–846

[91] I. Zimmermann, P. Gratia, D. Martineau, G. Grancini, J.-N. N. Audinot, T. Wirtz and M. K. Nazeeruddin, *J. Mater. Chem*. *A*, 2019, **7**, 8073–8077

[92] R. Kerremans, O. J. Sandberg, S. Meroni, T. Watson, A. Armin and P. Meredith, *Sol. RRL*, 2019, **4**, 1900221

[93] C. Tong, W. Ji, D. Li, A. Mei, Y. Hu, Y. Rong and H. Han, *J. Mater. Chem. A*, 2019, **7**, 10942–10948

[94] M. V. Khenkin, E. A. Katz, A. Abate, G. Bardizza, J. J. Berry, C. Brabec, F. Brunetti, V. Bulović, Q. Burlingame, A. Di Carlo, R. Cheacharoen, Y. B. Cheng, A. Colsmann, S. Cros, K. Domanski, M. Dusza, C. J. Fell, S. R. Forrest, Y. Galagan, D. Di Girolamo, M. Grätzel, A. Hagfeldt, E. von Hauff, H. Hoppe, J. Kettle, H. Köbler, M. S. Leite, S. (Frank) Liu, Y. L. Loo, J. M. Luther, C. Q. Ma, M. Madsen, M. Manceau, M. Matheron, M. McGehee, R. Meitzner, M. K. Nazeeruddin, A. F. Nogueira, Ç. Odabaşı, A. Osherov, N. G. Park, M. O. Reese, F. De Rossi, M. Saliba, U. S. Schubert, H. J. Snaith, S. D. Stranks, W. Tress, P. A. Troshin, V. Turkovic, S. Veenstra, I. Visoly-Fisher, A. Walsh, T. Watson, H. Xie, R. Yıldırım, S. M. Zakeeruddin, K. Zhu and M. Lira-Cantu, *Nat. Energy*, 2020, **5**, 35–49

[95] O. Filonik, M. E. Thordardottir, J. Lebert, S. Pröller, S. Weiß, L. J. Haur, A. Priyadarshi, P. Fontaine, P. Müller-Buschbaum, N. Mathews and E. M. Herzig, *Energy Technol*., 2019, **7**, 1900343

[96] H. Lakhiani, T. Dunlop, F. De Rossi, S. Dimitrov, R. Kerremans, C. Charbonneau, T. Watson, J. Barbé and W. C. Tsoi, *Adv. Funct. Mater.,* 2019, **29**, 1900885

[97] Z. Ku, Y. Rong, M. Xu, T. Liu and H. Han, *Sci. Rep.*, 2013, **3**, 3132

[98] C. Worsley, D. Raptis, S. Meroni, A. Doolin, R. Garcia, M. Davies and T. Watson, *Energy Technol.,* 2021, **9**, 202100312

[99] Q. Wang, W. Zhang, Z. Zhang, S. Liu, J. Wu, Y. Guan, A. Mei, Y. Rong, Y. Hu and H. Han, *Adv. Energy Mater.,* 2020, **10**, 1903092

[100] X. Hou, M. Xu, C. Tong, W. Ji, Z. Fu, Z. Wan, F. Hao, Y. Ming, S. Liu, Y. Hu, H. Han, Y. Rong and Y. Yao, *J. Power Sources,* 2019, **415**, 105–111

[101] A. Mei, X. Li, L. Liu, Z. Ku, T. Liu, Y. Rong, M. Xu, M. Hu, J. Chen, Y. Yang, M. Grätzel and H. Han, *Science,* 2014, **345,** 295–298

[102] X. Hou, M. Xu, C. Tong, W. Ji, Z. Fu, Z. Wan, F. Hao, Y. Ming, S. Liu, Y. Hu, H. Han, Y. Rong and Y. Yao, *J. Power Sources,* 2019, **415**, 105–111

[103] N. Phung, R. Félix, D. Meggiolaro, A. Al-Ashouri, G. Sousa E Silva, C. Hartmann, J. Hidalgo, H. Köbler, E. Mosconi, B. Lai, R. Gunder, M. Li, K. L. Wang, Z. K. Wang, K. Nie, E. Handick, R. G. Wilks, J. A. Marquez, B. Rech, T. Unold, J. P. Correa-Baena, S. Albrecht, F. De Angelis, M. Bär and A. Abate, *J. Am. Chem. Soc.*, 2020, **142**, 2364–2374

[104] G. Grancini, C. Roldán-Carmona, I. Zimmermann, E. Mosconi, X. Lee, D. Martineau, S. Narbey, F. Oswald, F. De Angelis, M. Graetzel and M. K. Nazeeruddin, *Nat. Commun.*, 2017, **8**, 15684

[105] J. Chen, Y. Rong, A. Mei, Y. Xiong, T. Liu, Y. Sheng, P. Jiang, L. Hong, Y. Guan, X. Zhu, X. Hou, M. Duan, J. Zhao, X. Li and H. Han, *Adv. Energy Mater.*, 2016, **6**, 1502009

[106] P. Wang, N. Chai, C. Wang, J. Hua, F. Huang, Y. Peng, J. Zhong, Z. Ku and Y. B. Cheng, *RSC Adv.*, 2019, **9**, 11877–11881

[107] Y. Rong, Z. Ku, A. Mei, T. Liu, M. Xu, S. Ko, X. Li and H. Han, *J. Phys. Chem. Lett.*, 2014, **5**, 2160–2164

[108] C.-T. Lin, F. De Rossi, J. Kim, J. Baker, J. Ngiam, B. Xu, S. Pont, N. Aristidou, S. A. Haque, T. Watson, M. A. McLachlan and J. R. Durrant, *J. Mater. Chem. A*, 2019, **7**, 3006–3011

[109] E. V. Péan, C. S. De Castro, S. Dimitrov, F. De Rossi, S. Meroni, J. Baker, T. Watson and M. L. Davies, *Adv. Funct. Mater.*, 2020, **30**, 1909839

[110] S. G. Hashmi, D. Martineau, M. I. Dar, T. T. T. Myllymäki, T. Sarikka, V. Ulla, S. M. Zakeeruddin and M. Grätzel, *J. Mater. Chem. A*, 2017, **5**, 12060–12067

[111] Y. Hu, Z. Zhang, A. Mei, Y. Jiang, X. Hou, Q. Wang, K. Du, Y. Rong, Y. Zhou, G. Xu and H. Han, *Adv. Mater.*, 2018, **30**, 1705786

[112] W. Zhang, J. Du, W. Zhang, Y. Chu, A. Mei, Y. Rong, X. Gao, H. Han and Y. Hu, *J. Energy Chem.*, 2022, **69**, 253–260

[113] A. Karavioti, E. Vitoratos and E. Stathatos, *J. Mater. Sci. Mater. Electron.*, 2020, **31**, 6109–6117

[114] S. G. Ko, G. Il Ryu, B. Kim, G. J. Cha, J. H. Ri, G. S. Sonu and U. C. Kim, *Sol. Energy Mater. Sol. Cells*, 2019, **196**, 105–110

[115] X. Hou, Y. Hu, H. Liu, A. Mei, X. Li, M. Duan, G. Zhang, Y. Rong and H. Han, *J. Mater. Chem. A*, 2017, **5**, 73–78

[116] K. Chen, Z. Zhang, J. Liu, Y. Huang, D. Wang, B. She, B. Liu, X. Zhang and J. Zhang, *Adv. Mater. Interfaces*, 2022, **9**, 2100395

[117] J. Wu, W. Zhang, Q. Wang, S. Liu, J. Du, A. Mei, Y. Rong, Y. Hu and H. Han, *J. Mater. Chem. A*, 2020, **8**, 11148-11154

[118] Y. Guan, A. Mei, Y. Rong, M. Duan, X. Hou, Y. Hu and H. Han, *Org. Electron.*, 2018, **62**, 653–659

[119] X. Hou, Y. Hu, H. Liu, A. Mei, X. Li, M. Duan, G. Zhang, Y. Rong and H. Han, *J. Mater. Chem. A*, 2017, **5**, 73–78

[120] K. Yang, S. Liu, J. Du, W. Zhang, Q. Huang, W. Zhang, W. Hu, Y. Hu, Y. Rong, A. Mei and H. Han, *Sol. RRL*, 2021, **5**, 2000825

[121] C. Liu, S. Liu, Y. Wang, Y. Chu, K. Yang, X. Wang, C. Gao, Q. Wang, J. Du, S. Li, Y. Hu, Y. Rong, L. Guo, A. Mei and H. Han, *Adv. Funct. Mater.*, 2021, **31**, 2010603

[122] H. Zou, D. Guo, B. He, J. Yu and K. Fan, *Appl. Surf. Sci.*, 2018, **430**, 625–631

[123] M. Bidikoudi, C. Simal and E. Stathatos, *ACS Appl. Energy Mater.*, 2021, **4**, 8810-8823

[124] X. Chen, Y. Xia, Q. Huang, Z. Li, A. Mei, Y. Hu, T. Wang, R. Cheacharoen, Y. Rong and H. Han, *Adv. Energy Mater.*, 2021, **11**, 2100292

[125] D. Papadatos, D. Sygkridou and E. Stathatos, *Mater. Lett.*, 2020, **268**, 127621

[126] J. Liu, D. Wang, K. Chen, J. Kang, J. Yang, J. Zhang and H. Zhang, *Sol. Energy*, 2020, **206**, 548–554

[127] X. Liu, Y. Zhang, J. Hua, Y. Peng, F. Huang, J. Zhong, W. Li, Z. Ku and Y. B. Cheng, *RSC Adv.*, 2018, **8**, 14991–14994

[128] Z. Tang, T. Bessho, F. Awai, T. Kinoshita, M. M. Maitani, R. Jono, T. N. Murakami, H. Wang, T. Kubo, S. Uchida and H. Segawa, *Sci. Rep.*, 2017, **7**, 12183

[129] M. Abdi-Jalebi, Z. Andaji-Garmaroudi, S. Cacovich, C. Stavrakas, B. Philippe, J. M. Richter, M. Alsari, E. P. Booker, E. M. Hutter, A. J. Pearson, S. Lilliu, T. J. Savenije, H. Rensmo, G. Divitini, C. Ducati, R. H. Friend and S. D. Stranks, *Nature*, 2018, **555**, 497–501

[130] F. Yang, M. A. Kamarudin, G. Kapil, D. Hirotani, P. Zhang, C. H. Ng, T. Ma and S. Hayase, *ACS Appl. Mater. Interfaces*, 2018, **10**, 24543–24548

[131] S. Liu, W. Huang, P. Liao, N. Pootrakulchote, H. Li, J. Lu, J. Li, F. Huang, X. Shai, X. Zhao, Y. Shen, Y.-B. Cheng and M. Wang, *J. Mater. Chem. A*, 2017, **5**, 22952–22958

[132] P. P. Khlyabich and Y.-L. Loo, *Chem. Mater.*, 2016, **28**, 9041–9048

[133] Y. Sheng, Y. Hu, A. Mei, P. Jiang, X. Hou, M. Duan, L. Hong, Y. Guan, Y. Rong, Y. Xiong and H. Han, *J. Mater. Chem. A*, 2016, **4**, 16731–16736

[134] Y. Zhang, Y. Wang, Z. Sun, F. Li, R. Tao, Z. Jin and L. Xu, *Chem. Commun.*, 2017, **53**, 2290–2293

[135] B. wook Park, N. Kedem, M. Kulbak, D. Y. Lee, W. S. Yang, N. J. Jeon, J. Seo, G. Kim, K. J. Kim, T. J. Shin, G. Hodes, D. Cahen and S. Il Seok, *Nat. Commun.*, 2018, **9**, 3301

[136] V. Kapoor, A. Bashir, L. J. Haur, A. Bruno, S. Shukla, A. Priyadarshi, N. Mathews and S. Mhaisalkar, *Energy Technol.*, 2017, **5**, 1880–1886

[137] M. Hu, L. Liu, A. Mei, Y. Yang, T. Liu and H. Han, *J. Mater. Chem. A*, 2014, **2**, 17115–17121

[138] X. Chen, Y. Xia, Z. Zheng, X. Xiao, C. Ling, M. Xia, Y. Hu, A. Mei, R. Cheacharoen, Y. Rong and H. Han, *Chem. Mater.*, 2022, **34**, 728–735

[139] N. Pellet, P. Gao, G. Gregori, T.-Y. Yang, M. K. Nazeeruddin, J. Maier and M. Grätzel, *Angew. Chemie Int. Ed.*, 2014, **53**, 3151–3157

[140] P. Wang, N. Chai, C. Wang, J. Hua, F. Huang, Y. Peng, J. Zhong, Z. Ku and Y. Cheng, *RSC Adv.*, 2019, **9**, 11877–11881

[141] S. Wang, W. Shen, Y. Chu, W. Zhang, L. Hong, A. Mei, Y. Rong, Y. Tang, Y. Hu and H. Han, *J. Phys. Chem. Lett.*, 2020, **11**, 9689–9695

[142] J. Song, F. Huang, J. Chen, S. Liu, K. Cao and M. Wang, *Chem. Eng. Transactions* 2017, **62**, 1147

[143] K. Cao, J. Cui, H. Zhang, H. Li, J. Song, Y. Shen, Y. Cheng and M. Wang, *J. Mater. Chem. A*, 2015, **3**, 9116–9122

[144] K. Cao, H. Li, S. Liu, J. Cui, Y. Shen and M. Wang, *Nanoscale*, 2016, **8**, 8839–8846

[145] Q. Jiang, D. Rebollar, J. Gong, E. L. Piacentino, C. Zheng and T. Xu, *Angew. Chemie Int. Ed.*, 2015, **54**, 7617–7620

[146] Y. Sheng, W. Ji, Y. Chu, Y. Ming, A. Mei, Y. Hu, Y. Rong and H. Han, *Sol. RRL*, 2020, **4**, 2000185

[147] L. Liu, A. Mei, T. Liu, P. Jiang, Y. Sheng, L. Zhang and H. Han, *J. Am. Chem. Soc.*, 2015, **137**, 1790–1793

[148] C. Aranda, A. Guerrero and J. Bisquert, *ACS Energy Lett.*, 2019, **4**, 741–746

[149] Y. Rong, X. Hou, Y. Hu, A. Mei, L. Liu, P. Wang and H. Han, *Nat. Commun.*, 2017, **8**, 14555

[150] C. Liu, K. Wang, C. Yi, X. Shi, A. W. Smith, X. Gong and A. J. Heeger, *Adv. Funct. Mater.*, 2016, **26**, 101–110

[151] Q. Wali, F. J. Iftikhar, M. E. Khan, A. Ullah, Y. Iqbal and R. Jose, *Org. Electron.*, 2020, **78**, 105590

[152] X. Chen, Y. Xia, Q. Huang, Z. Li, A. Mei, Y. Hu, T. Wang, R. Cheacharoen, Y. Rong and H. Han, *Adv. Energy Mater.*, 2021, **11**, 2100292

[153] Y. Xia, X. Chen, Z. Zheng, X. Xiao, C. Ling, M. Xia, J. Gong, L. Gao, J. Xiang, Y. Hu, A. Mei, Y. Rong and H. Han, *J. Phys. Chem. Lett.*, 2022, **13**, 2144–2149

[154] D. Zhang, P. Jiang, D. Li, S. Li, J. Qi, X. Wang, Y. Hu, Y. Rong, A. Mei and H. Han, *Sol. RRL*, 2022, **6**, 2100851

[155] C. M. Tsai, G. W. Wu, S. Narra, H. M. Chang, N. Mohanta, H. P. Wu, C. L. Wang and E. W. G. Diau, *J. Mater. Chem. A*, 2017, **5**, 739–747

[156] H.-B. Kim, H. Choi, J. Jeong, S. Kim, B. Walker, S. Song and J. Y. Kim, *Nanoscale*, 2014, **6**, 6679

[157] C.-H. Chiang, M. K. Nazeeruddin, M. Grätzel and C.-G. Wu, *Energy Environ. Sci.*, 2017, **10**, 808–817

[158] J. C. Hamill, J. Schwartz and Y.-L. Loo, *ACS Energy Lett.*, 2018, **3**, 92–97

[159] C. Y. Chan, Y. Wang, G. W. Wu and E. Wei-Guang Diau, *J. Mater. Chem. A*, 2016, **4**, 3872–3878

[160] MSDS - 227056, https://www.sigmaaldrich.com/MSDS/MSDS/DisplayMSDSPage.do?country=GB&language=en&productNumber=227056, (accessed 16 March 2022)

[161] MSDS - M81802, https://www.sigmaaldrich.com/MSDS/MSDS/DisplayMSDSPage.do?country=GB&language=en&productNumber=M81802, (accessed 16 March 2022)

[162] A. E. Williams, P. J. Holliman, M. J. Carnie, M. L. Davies, D. A. Worsley and T. M. Watson, *J. Mater. Chem. A*, 2014, **2**, 19338–19346

[163] Candidate List of substances of very high concern for Authorisation - ECHA, https://echa.europa.eu/candidate-list-table, (accessed 16 March 2021)

[164] F. P. Byrne, S. Jin, G. Paggiola, T. H. M. Petchey, J. H. Clark, T. J. Farmer, A. J. Hunt, C. Robert McElroy and J. Sherwood, *Sustain. Chem. Process.*, 2016, **4**, 7

[165] NMF Msds, https://www.sigmaaldrich.com/GB/en/sds/aldrich/473936, (accessed 3 November 2021)

[166] R. B. Palmer, *Toxicol. Rev.*, 2004, **23**, 21–31

[167] GBL MSDS - B103608, https://www.sigmaaldrich.com/MSDS/MSDS/DisplayMSDSPage.do?country=GB&language=en&productNumber=B103608, (accessed 16 March 2020)

[168] K. Knudsen, J. Greter and M. Verdicchio, *Clin. Toxicol.*, 2008, **46**, 187–192

[169] Y. Ming, M. Xu, S. Liu, D. Li, Q. Wang, X. Hou, Y. Hu, Y. Rong and H. Han, *J. Power Sources*, 2019, **424**, 261–267

[170] A. Osatiashtiani, A. F. Lee and K. Wilson, J. Chem. Technol. Biotechnol., 2017, 92, 1125–1135

[171] I. T. Horváth, H. Mehdi, V. Fábos, L. Boda and L. T. Mika, Green Chem., 2008, 10, 238–

[172] S. G. Wettstein, D. M. Alonso, Y. Chong and J. A. Dumesic, Energy Environ. Sci., 2012, 5, 8199–8203

Chapter 2

Experimental Procedures

The following sections detail methods, materials and measurement techniques common to each chapter. Where different procedures for sample preparation or measurement were used, this is detailed in the relevant chapter.

2.1 Sample preparation

2.1.1 Fabrication of standard CPSCs and modules

Materials: Titanium diisopropoxide bis (acetylacetonate) (TAA, 75% in IPA, Sigma-Aldrich), anhydrous 2-propanol (IPA, 99.5%, Sigma Aldrich), TiO_2 paste (30NR-D, GreatCell Solar)), ZrO_2 paste (GreatCell Solar), Carbon paste (Gwent electronic materials) and terpineol (95%, Sigma-Aldrich) were used as received. Precursor materials PbI_2 (99%, Sigma-Aldrich), MAI (CH_3NH_3I, anhydrous, Dyesol), 5-ammonium valeric acid iodide (5-AVAI, Dyesol), γ-butyrolactone (GBL, Sigma Aldrich), γ-valerolactone (GVL, Sigma Aldrich) and anhydrous MeOH (99%, Sigma Aldrich) were used as received. Additive and dopant materials are named in the experimental section of each relevant chapter.

Device fabrication: Device structure and dimensions are depicted in Figure 2.1.

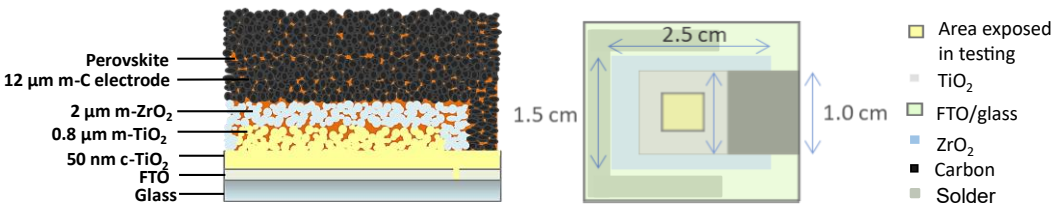

Figure 2.1: Depiction of 1cm^2 device cross section (left) and print dimensions via the glass substrate (right).

FTO substrates were patterned with a Nb:YVO_4 laser (532 nm) before cleaning with ~2% Hellmanex in deionised water, rinsing with acetone and IPA and drying with N_2. Substrates were then placed in a Nano plasma system (Diener Electronics) and plasma cleaned for five minutes in an O_2 environment. The substrate was heated to 300°C on a hot plate and a compact TiO_2 blocking layer deposited by spray pyrolysis of 0.2 M titanium di-isopropoxide-bis(acetylacetonate) in IPA.

To form the mesoporous TiO_2 layer, the titania paste (30NRD) was diluted 1:1 by weight in terpineol, screen printed and sintered at 550°C for 30 minutes after a slow ramp. Next, ZrO_2 and carbon were printed and annealed at 400°C for 30 minutes each.[†] Unless otherwise specified, layer thicknesses were 600-800 nm, ~2 µm and ~12-17 µm for TiO_2, ZrO_2 and carbon respectively. All layers were printed and annealed in ambient conditions.

All precursors and solvent mixes were fabricated in an N_2 glove box to the specified concentration. GBL solutions were dispersed through stirring at 60°C for 1-4 hours on a hot plate, while GVL precursors and other solvent mixes were stirred at room temperature until dissolved. Once fabricated, precursors were stored in dark ambient conditions (~18°C, 30-60% RH).

Unless specified, devices were cooled to room temperature in ambient conditions (30-50% RH, 18-21°C) before drop casting of 18-20 µl room temperature precursor onto the stack surface. Devices were left for ten to fifteen minutes (22.5 minutes Chapter 3 onwards) in ambient conditions after drop casting precursor to ensure adequate infiltration, before annealing on a hot plate for 1h at 50°C or 45°C unless otherwise stated. Contacts were applied with an ultrasonic solder at 190°C.

Where relevant (for all samples in Chapter 3, and humidity treatment samples in Chapter 5) humidity treatments were applied: 16 hours in a humidity oven at 25°C and 70% RH and a subsequent 4-10 hours under vacuum before measuring.

Module fabrication: Module fabrication was carried out following previously established scribe method[1] with scribe widths of 50 nm, 0.60 mm and 0.20 mm for P1, P2 and P3, respectively, resulting in an active area of 220 cm^2 over 22 cells and geometric fill factor of 80%. Scribe P1 was created via a $Nd:YVO_4$ laser, and the triple mesoporous layers were deposited via screen printing. The measured mesoporous layer thicknesses were 0.8, 1.9 and 12 µm for TiO_2, ZrO_2 and carbon, respectively. P2 and P3 scribes were created mechanically with a steel blade under 0.54 N/mm pressure. Precursor solutions were deposited into the module shells via the Robotic Mesh (RbM) method, using a 30 ga blunt end needle tip with a deposition speed of 12 m/s.[2] The wet devices were kept in a low

[†] All devices in Chapter 3 were prepared with one layer of ZrO_2. Unless specified, all devices thereafter were prepared with two printed ZrO_2 layers, to maintain layer thickness with previous samples after a paste formulation change by Solaronix.

humidity atmosphere for 10 minutes at room temperature prior to curing at 45°C in a low humidity oven for 1 hour.

Encapsulation: Unless specified, all device data throughout this thesis is for unencapsulated devices. Any encapsulated devices were encapsulated after 4-7 days of ambient storage to allow PCE to settle or perform humidity treatments where necessary.[‡] To encapsulate, one sided hot melt polyurethane was cut to size and placed melt side down onto the completed device. The device was placed between cushioned pads to prevent cracking and placed in a hot press at 125°C for 45 seconds.

Next, electric wires were soldered onto the already soldered device electrodes before application of a 1:1 marine epoxy and placement of cover glass. Devices were left to cure in ambient conditions for at least 24 hours prior to testing.

2.1.2 Fabrication of XRD and PL samples

Glass substrates were first cleaned with ethanol and IPA before screen printing of ~1.6 µm ZrO_2 paste and subsequent annealing on a hot plate at 400°C for 30 minutes. A carbon layer was then printed onto the cooled ZrO_2 and annealed on a hot plate at 400°C for 30 minutes. 20 µl of the relevant precursor was drop cast onto the cooled substrates and left at room temperature for 15 minutes to maximise infiltration. Samples were annealed at 45°C on a hot plate in ambient conditions for 1.5 h. Sample dimensions and measurement positions are presented in Figure 2.2. Chapter 3 and 4 samples were humidity treated (section 2.1.1) before testing. XRD and PL measurement protocols are presented in sections 2.2.3 and 2.2.7 respectively.

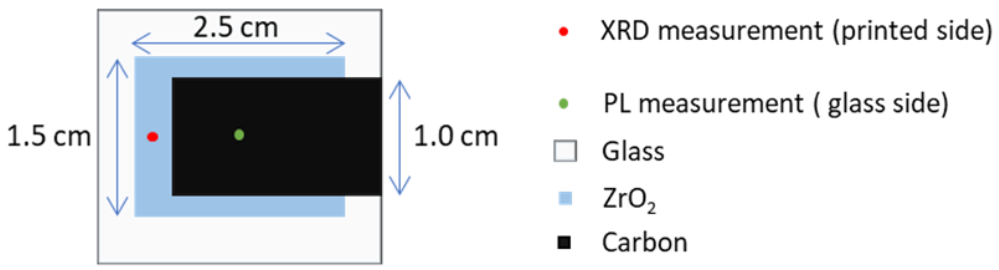

Figure 2.2: Diagram showing dimensions and areas tested of PL and XRD samples produced for this work. Annealed perovskite is present across the entire sample surface.

[‡] PCE evolution during the week following fabrication is discussed in detail in Chapter 5.

2.1.3 Cross sectional imaging samples

Cross sectional samples were prepared by snapping fully fabricated devices after scribing on the glass substrate base. Each section was then mounted onto a conductive metal substrate with conductive carbon/silver tape before sputtering with 5-10 nm Pt on a rotating stage. Copper strips were then applied to maximise electrical contact with the device surface and conductive substrate (Figure 2.3). This was then attached to the SEM stage using conductive carbon/silver tape and copper tape. Images were obtained using a JSM-7800F Field Emission SEM at 12 kV (probe current 8) using secondary electron imaging.

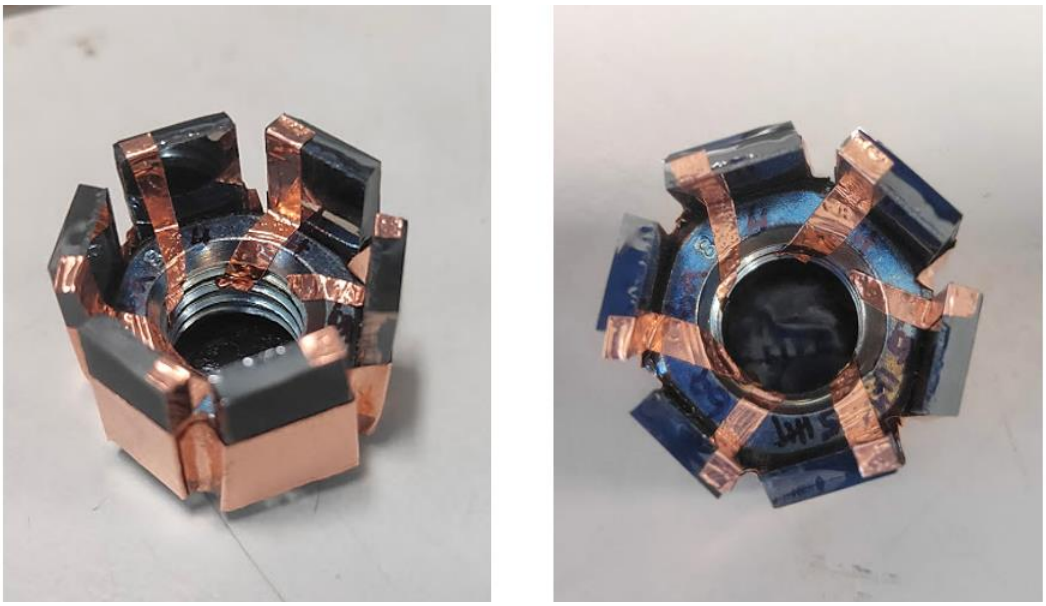

Figure 2.3: Photos of prepared samples for cross sectional analysis (side and top profiles).

2.2 Testing and characterisation methods

2.2.1 Current-voltage (IV) sweeps and stabilised current measurements

Devices: The 1 cm^2 devices were masked to 0.49 cm^2 (Chapter 3) or 0.16 cm^2 as shown in Figure 2.4, and placed under a fan for testing. Where chapters contain results from two different masking regimes, the relevant mask size will be specified in the figure heading.[§]

A Keithley 2400 source meter and class AAA solar simulator (Newport Oriel Sol3A) at 1 sun were used for *J-V* measurements (calibrated against a KG5 filtered silicon reference cell, Newport Oriel 91150-KG5). Devices were scanned at a rate of 0.126 Vs^{-1} from V_{oc} to J_{sc} and

[§] Results from 0.16 cm^2 and 0.49 cm^2 masks are never directly compared in this work. However, some chapters contain results from both masks: standard testing was changed to use 0.16 cm^2 masks in early 2021 to bring our testing procedures in line with that of other groups, who use 0.1-0.2 cm^2 as standard for CPSCs. [3],[4] Where results from two mask sizes are used in the same chapter, each figure will specify the aperture used and data is discussed separately.

vice-versa after a light soaking period of 180 s. For stabilised current measurements, devices were held at the maximum power point (as determined by the preceding IV scan) for a period of 200-250 s to account for slow device response times and allow devices to stabilise.

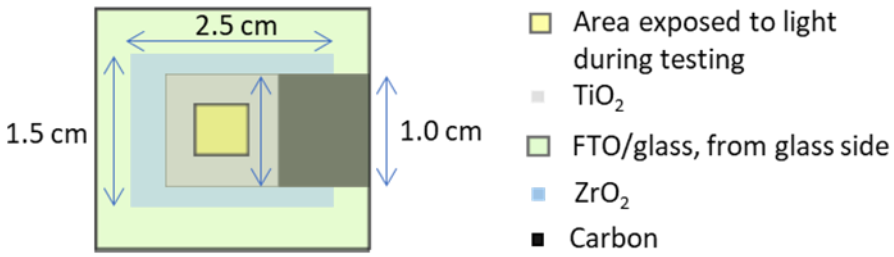

Figure 2.4: Diagram showing dimensions of standard CPSCs produced for this work. The yellow square corresponds to 0.49 cm^2 mask placement, but 0.16 cm^2 masks were similarly placed at the centre of the active area.

Modules: Modules were tested using a Solaronix Solixon A-20 in tandem with in-house developed software, a Keithley 2400 source meter under AM1.5 illuminations from a Lumixo-S lamp calibrated at 1 sun using a KG5 filtered silicon reference cell (Newport Oriel 91150-KG5). The devices were scanned at a rate of 70 mV/s between -0.1 V and 20 V in forward and reverse directions over the full area.

Outdoor testing was performed with the above setup on epoxy encapsulated modules, with an adjacent pyranometer and reference Silicon module to monitor irradiance. Modules were subject to forward and reverse IV sweeps at five-minute intervals and held at maximum power between tests. Testing was done from 8 am- 7 pm and devices held at open circuit overnight.

2.2.2 Device stability testing

Unless otherwise stated, stability measurements were carried out under 1 Sun AM 1.5G illumination. The source was a plasma bulb in a Lumartix SA instrument (Luxim-S). The devices were masked at 0.49 cm^2 and measured periodically after a resting time under illumination in open circuit (specific resting times and scan frequencies detailed in the experimental section of each chapter). The substrates were heated by the IR component of the light spectrum leading to a temperature of 50-55°C when under fan-cooling, or 60-65°C in the absence of a fan.

2.2.3 X-Ray Diffraction

Unless otherwise stated, standard single scan samples were prepared as described in section 2.1.1 and 2.1.2. A Bruker D8 discover diffractometer with Bragg–Brentano geometry and a Cu kα radiation X-ray source was used. 2θ scans between 5° and 65° were collected using a step size of 0.03°.

The in-situ crystallisation measurements were carried out on full device stacks. The diffractometer was used in a divergent beam set-up with a Ni filter. An Anton-Paar DHS1100 thermal stage run using Nambicon software was used for temperature control. Empty stacks were placed on a thermal stage at 25°C in the XRD equipment directly after cooling to room temperature post carbon-annealing. 20 µl of the relevant perovskite precursor was drop cast onto the stack and XRD measurements started immediately. Samples were held at 25°C for 15 minutes then heated to the desired temperature with a ramp rate of 15°C/min and held for 40 minutes to 1 hour or complete crystallisation. XRD measurements were continued while samples cooled to room temperature (a further 5-10 minutes). Tests were conducted as a PSD fixed scan using a 2.26° opening on a Lynxeye 1D detector, covering the 2θ range of 13.00-15.26° with a time per step of 15 seconds for the duration.

2.2.4 UV-Vis

Precursors were diluted before measurements, as specified in the main text of each chapter.

The diluted precursor was well mixed and placed in a clean quartz cuvette of 1 cm path length for measurement. Samples were measured from 300-500 nm at a rate of 90 $nmmin^{-1}$ on a Perkin Elmer Lambda 9 UV/VIS/NIR Spectrophotometer.

2.2.5 Contact angle measurements

Samples were prepared by screen printing ~600 nm TiO_2 paste (Greatcell solar, 30 NRD, diluted 1:1 with terpineol) onto FTO. Layers were annealed at 550°C for 30 minutes and cooled to room temperature in ambient conditions (20°C, 30% RH) before contact angle testing.

A 1 ml syringe with a blunt end needle (Metcal 22-gauge precision dispenser needle) was used to drop cast one droplet of room temperature perovskite precursor or solvent onto the substrate. Dynamic contact angle measurements were taken using a Nikon camera and analysed using FTA-32 software, with images obtained every 0.1 s for the duration. Timing

was started from t=0, when the droplet first came into contact with the substrate. Spreading distance and droplet height were measured using FTA-32 software.

2.2.6 Scanning electron microscopy (SEM)

Cross sectional samples were prepared by snapping fully fabricated devices. Each section was then sputtered with ~5 nm Pt before mounting onto a conductive metal substrate with conductive carbon/silver tape. This was attached to the SEM stage using conductive carbon/silver tape and copper tape to ensure adequate contact. Images were obtained using a JSM-7800F Field Emission SEM at 12 kV (probe current 8) using secondary electron imaging.

2.2.7 Photoluminescence measurements

The PL spectra in Chapter 1 were obtained using an OceanOptics USB2000+ spectrometer with an excitation wavelength of 450 nm and a 490 nm longpass filter in the emission pathway. Samples were measured from λ=600-850 nm with a step size of 0.5 nm and dwell time of 0.2 s. The excitation and emission bandwidths were each 3 nm.

The photoluminescence quantum yield (PLQY) measurements in Chapter 3 were performed on an FS5 Spectrofluorometer (Edinburgh Instruments) with an SC-30 Integrating sphere module. All measurements were made through the glass side of the sample (prepared as detailed in section 2.1.2). Each scattering peak was obtained with a 410-490 nm range (peak at 450 nm) using a step size of 0.1 nm and dwell time of 0.2 s. Five measurements were taken for each scattering (excitation) peak. The excitation and emission bandwidths were 5 nm and a neutral density filter with an optical density of 3 was used. Emission peaks were measured from 600-850 nm, and no filter was used. All other measuring conditions were the same as detailed for the excitation peaks.

2.2.8 Photoluminescence and photocurrent mapping

Samples were prepared as described above.

Photoluminescence mapping measurements were done using Renishaw InVia confocal Raman microscope in a backscattering configuration. Light was shone from the glass side on to the directly mounted samples on an *X*–*Y* scanning stage with a minimum step size of 100 nm. Measurement was done using 532 nm laser excitation source, the power of the which was adjusted to 300 nW using 1 OD neutral density filter to 0.0075 µW ((NA: 0.50, spot size ~ 1 µm). Photoluminescence spectra was recorded at every 250 µm step using 50 x objective lens with an acquisition time of 25 ms (Chapter 4) or 1s (Chapter 5).

Photocurrent mapping measurements were carried out using a Renishaw InVia confocal Raman microscope in backscattering configuration by measuring the samples through the glass substrates. All measurements were performed in an electrical chamber (LTS420E, Linkam Scientific Instrument) mounted directly to a X–Y scanning stage (100 nm minimum step size). Utilizing the scanning stage, maps were produced with individual spectra at each region. All measurements were conducted with a 50 × objective lens (NA = 0.50). A 532 nm laser excitation source was used (spot size ≈ 1 µm). PL and photocurrent (laser beam–induced current) data were acquired simultaneously at short circuit: for the large photoluminescence–photocurrent map (4000 × 500 µm), 0.3 µW laser power ($3x10^4$ $mWcm^{-2}$) and 1 s acquisition time were used. To acquire the photocurrent, the device electrodes were connected to a lock-in amplifier (Stanford Research SR830) with a chopper cutting the laser beam at 73 Hz.

2.2.9 Viscosity measurements

1.25 ml of each precursor at the specified concentration and solvent mix was prepared for each sample. Measurements were performed at ~18°C on a Rheosense microvisc with an internal chip of 4-600 cP sensitivity. 10-12 measurements were obtained for each sample and a mean value calculated.

2.3.1 Optical microscopy for infiltration comparison

The tested area of each device was marked with permanent marker before IV testing and optical analysis, to ensure the imaged and tested area were identical. Images were taken through the glass substrate of completed devices using a Zeiss Observer inverted compound microscope. For quantitative image analysis, images were brightness and contrast equalised before a contrast lookup table was applied to maximise the contrast between infiltrated and uninfiltrated areas and remove any glass reflections. Pixels were then binned according to colour and data used to calculate % uninfiltrated area. To obtain data for the entire 4x4 mm tested area, uninfiltrated area was calculated for each image and an average obtained.

2.3.2 Fourier transform infra-red (FTIR)

Presented in Chapter 5 as evidence of GVL retention on dried PbI_2. ZrO_2 layers were screen printed on glass and annealed at 400°C for 30 minutes. Once cooled, 7 µl of the relevant precursor was drop cast onto the cooled layer. After ten minutes of percolation time, samples were annealed for one hour at 45°C. Where stated, some samples were prepared on glass only, without a supporting ZrO_2 scaffold.

Samples were scraped off onto the ATR crystal of a Perkin Element Frontier FTIR and spectra measured between 1000 and 4000 cm^{-1}. Spectra were obtained and analysed using spectrum V10 software.

2.3.3 External quantum efficiency (EQE)

Presented to compare absorption across the visible spectrum for samples produced using different solvent systems. External quantum efficiency (EQE) measurements in Chapters 3 and 7 were obtained using a QE X10 system (PV Measurements) from 300 and 850 nm in direct current mode with a light spot of less than 10 mm^2. Wavelengths were stepped up in increments of ten, and three readings obtained for each wavelength. A 30-35 s delay was used at each filter change to allow for slow device responses.

The measurements in Chapter 4 were carried out using a custom-built system consisting of Xenon arc and Quartz halogen white light sources (Bentham) and a Bentham TMc300 monochromator controlled by Labview software. The cell photocurrent was measured using a transimpedance amplifier (Femto), with the incident light intensity calibrated using a silicon reference photodiode (Newport).

2.3.4 Electrochemical impedance measurements

Measurements were performed on unmasked devices using a Zahner CIMPS-X photoelectrochemical workstation. Measurements were performed over the frequency range 10 MHz to 1 Hz at open circuit under illumination from a red LED (630 nm) at intensities from 1 to 0.01 Sun equivalent intensity.

2.3.5 Profilometry

Thickness measurements and surface roughness values were obtained using a Dektak D150 profilometer with a 12.5 µm stylus diameter and force of 3 mg. Samples were measured across the whole printed area, and step height obtained for both edges of the print when possible. All presented average values include data from 3 or more such measurements.

2.3.6 Rheological analysis

Rheological evaluation was carried out using a combination of shear and viscoelastic measurements. Shear viscosity measurements were carried out on a Malvern Bohlin rotational rheometer (Gemini Bohlin Nano, Malvern Instruments, Malvern Panalytical Ltd, Malvern, UK) with a 2° 20 mm stainless steel cone and a parallel plate held at 25°C. Ink viscosity was measured as the shear rate was gradually increased to 300 s^{-1} and then reduced back to 1 s^{-1}. Viscoelastic measurements were carried out on a Malvern Kinexus Pro

Rheometer (Malvern Instruments, Malvern Panalytical Ltd., Malvern, UK) with a 1° 50 mm stainless steel cone and parallel plate. Amplitude (strain) sweep measurements were conducted to establish the linear viscoelastic range at 0.1, 1, and 10 Hz. Then using a stress within the established linear viscoelastic region, a frequency sweep from 0.1 to 10 Hz was conducted.

2.3.7 Thermogravimetric analysis and Differential scanning calorimetry.

TGA was performed on a Perkin Elmer Pyris 1 instrument and accompanying Pyris software. Perovskite samples were prepared on plain glass or in ZrO_2 /TiO_2 scaffolds as state. After annealing, samples were stored as films on glass in a dry ambient environment. To measure, 8-12 mg was placed in a Pt basket, in an Al pan with partial Al lid. Samples were placed under an N_2 flow and heated to 40°C for one minute before ramping to 250°C or 400°C as stated, at a rate of 5°C per minute (Chapter 5) or 20°C per minute (Chapter 6).

DSC were carried out using a Perkin Elmer DSC 4000 with Al pan and reference pan. 8-12 mg was placed in the Al basket before application of N_2 flow, heating to 40°C for one minute and ramping to 250°C or 400°C as stated, at a rate of 5°C per minute. Data were processed using Pyris software.

The masses used for concurrently presented TGA and DSC traces were kept as similar as possible, to ensure comparable data were obtained for TGA and DSC of each sample.

2.3.8 Tyndall effect imaging

The presence of colloids in precursors was examined by looking for evidence of the Tyndall effect, wherein colloidal particles scatter aligned light. Precursor vials were placed in a dark cupboard on a dark background and a red laser pointer shone through the liquid. Samples were observed perpendicular to the laser pointer for evidence of a visible line of scattered light. Photographs were obtained from this angle, perpendicular to the laser pointer and parallel to the sample vial.

2.4 References

[1] S. M. P. Meroni, C. Worsley, D. Raptis and T. M. Watson, *Energies*, 2021, **14**, 386

[2] C. Tong, W. Ji, D. Li, A. Mei, Y. Hu, Y. Rong and H. Han, *J. Mater. Chem. A*, 2019, **7**, 10942–10948

Chapter 3

γ-Valerolactone: A Non-Toxic Green Solvent for Highly Stable Printed Mesoporous Perovskite Solar Cells

Sections of work in the followng chapter form the basis of the following publication: C. Worsley, D. Raptis, S. Meroni, A. Doolin, R. Garcia, M. Davies and T. Watson, *Energy Technol.*, 2021, ente.202100312

Unless specified, all sample preparation, measurement and data analysis was performed by C. Worsley.

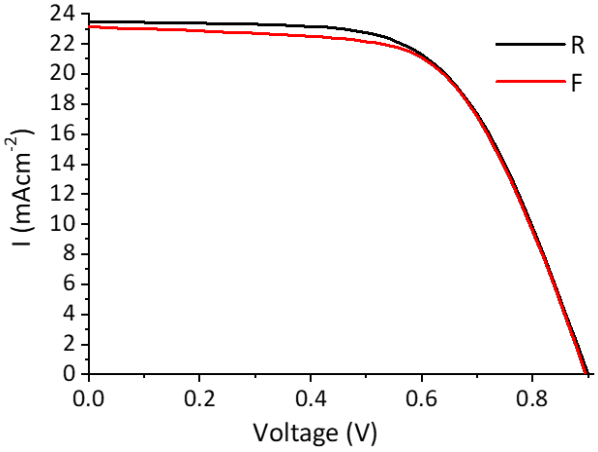

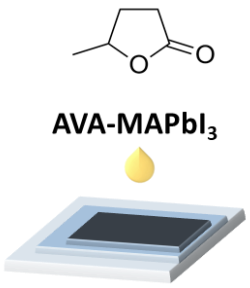

	PCE (%)	V_{oc} (mV)	FF (%)	J_{sc} (mA/cm^{-2})
Rev	12.81	0.89	62	23.12
Fwd	12.91	0.9	61	23.42

In this chapter, γ-Valerolactone (GVL) is presented as a non-toxic, biodegradable, green alternative to GBL for CPSC fabrication. Cells fabricated with a precursor concentration of 1.1 M and annealed at 45°C exhibit comparable performance to standard GBL devices, achieving a champion PCE of 12.91% in a device of 1 cm^2 active area. This work proves that GVL is a viable alternative to GBL for CPSCs, and could enable research in countries where GBL is legally restricted while helping make large-scale CPSC manufacture more sustainable.

3.1 Introduction: GVL and the requirement for green solvents

The impressive stability of CPSCs, combined with the use of scalable deposition techniques, make them attractive for commercial development, and they are considered one of the frontrunners for PSC commercialisation. Manufacturing bottlenecks for CPSCs are already being addressed in the scientific literature, for example using near-infra red annealing and robotic infiltration methods to drastically reduce heating times and automate infiltration.[1],[2]

However, to be considered commercially viable, stable, high efficiency devices must be easily and reproducibly attainable at large scale and low cost. Additionally, the toxicity of device components becomes increasingly important when manufacturing at large scale. This is a particularly relevant issue for perovskite devices, which require copious amounts of water-soluble lead and frequently require large volumes of toxic solvents. This is exacerbated in conventional sandwich devices, which often rely on antisolvent-assisted spin coating to obtain high quality perovskite layers at lab scale.

Notably, the most common precursor solvents for CPSCs; dimethylformamide (DMF)-dimethylsulfoxide (DMSO) mixtures and γ-butyrolactone (GBL), could represent significant barriers to CPSC commercialisation, as they respectively introduce toxicity and legality issues.[3]–[10]

Toxic mixtures of DMF and DMSO present significant health and environmental hazards, particularly in the presence of solubilised lead.[11],[12] The 30 mgm^{-1} short-term exposure limit (STEL) of these mixtures coupled with a flash point within the perovskite processing window mean large-scale production would require expensive vapour handling and solvent recovery systems.[12] Long-term reliance on DMF as a solvent for large-scale manufacture is also potentially unviable: European Registration, Evaluation, Authorisation and Restriction of Chemicals (REACH) regulations classify DMF as a 'Substance of very high concern', a precursor to introducing usage restrictions.[13] Additionally, thermogravimetric analyses have shown that residual DMF is retained in perovskite films post-annealing, which has unknown impact on device lifetimes and could complicate end-of-life disposal or recycling procedures. This is especially relevant to CPSCs, where devices contain larger amounts of perovskite and the mesoporous scaffold could impede solvent removal.[14]

Although much less toxic than DMF/DMSO systems, GBL is a legally restricted psychoactive.[15] Despite relatively low oral toxicity, the doses for psychoactive effects can be close to lethal amounts, introducing a significant health risk for users.[16],[17] As such, GBL is

subject to legal restrictions in many countries. This introduces legislative costs at large scale and can hamper lab-scale research where access to solvents is prohibited.

It is clear that a greener, non-hazardous solvent would improve the commercial viability of CPSCs. The requirement for less harmful solvents in PSCs has been recognised, leading to several publications on alternative perovskite precursor formulations. However, these works do not apply to CPSCs, having been applied mostly in planar devices.[18]–[21] Developed for R2R, blade coating or spin coating, the properties of these systems are often unsuitable for CPSCs, which require high boiling point solvents of low vapour pressure for suitable infiltration. Many traditional polar aprotic solvents are not therefore suitable, somewhat limiting the options to more novel alternatives. Such compounds often have limited safety information, making environmental, health and safety (EHS) screening far more difficult.

Often, lifecycle impact assessment (LCIA) data is also lacking- particularly for emerging solvents of limited industrial application.[22] This can be problematic when conducting lifecycle assessments (LCA), which are necessary to determine the true environmental impact of a given chemical. Emerging solvents can also be more costly, as limited demand results in specialist, small batch production.[22] The combination of high cost and low availability can easily result in potential alternative solvents being written off as too expensive for large-scale manufacture.

Fully biodegradable, readily available from sustainable lignocellulosic biomass feedstocks and frequently used as a food and perfume additive, γ-valerolactone (GVL) is already well studied. Additionally, recent price drops in Europe and the emergence of biodegradability and toxicity studies indicate that industrial GVL application is likely to increase in the coming years.[23]

This work presents GVL as a non-toxic GBL alternative for fabricating highly stable CPSCs. Although chemically similar to GBL, GVL is over five times less toxic (GVL LD_{50} oral-rat =8800mg/kg, GBL LD_{50} oral-rat = 1540-1800 mg/kg).[24]–[26] Furthermore, the legal restrictions that impact GBL availability in certain counties do not apply, making GVL well suited to large scale sustainable production. This work could therefore provide an avenue towards more commercially viable CPSCs and enable continued CPSC research in countries where GBL is prohibited.

3.2 Experimental

Unless specified below, all materials, sample preparation and measurement procedures were performed as detailed in Chapter 2.

Device and module testing

Testing was carried out 3-4 days after device or module completion in all cases.

Testing and Characterisation

UV Vis

UV Vis samples were prepared by diluting precursors to 250 mmol with GVL before measurement, as detailed in section 2.2.4.

XRD

Glass substrates were first cleaned with ethanol and IPA before bar casting of ~5 µm TiO_2 paste (Greatcell Solar, 30-NRD) and subsequent annealing on a hot plate at 550°C for 30 minutes. 5 µl of the relevant precursor was drop cast onto the cooled layer and left at room temperature for ten minutes to maximise infiltration. Samples were annealed at 50°C in a fan assisted oven for one hour. Measurements were then performed as detailed in section 2.2.3.

Contact angle testing

Samples were prepared by screen printing ~600 nm TiO_2 paste (Greatcell solar, 30 NRD, diluted 1:1 with terpineol) onto FTO. Layers were annealed at 550°C for 30 minutes and cooled to room temperature before contact angle testing as detailed in section 2.2.5.

Photoluminescence

Glass and FTO substrates (for ZrO_2 and TiO_2 samples respectively) were cleaned a solution of 2.4% Hellmanex in deionised water before rinsing with ethanol and IPA and plasma cleaning in an O_2 environment for 5 minutes. ZrO_2 samples were prepared on glass substrates as detailed in section 2.1.2. For the TiO_2 samples, a c-TiO_2 blocking layer was sprayed onto the FTO as described above, before screen printing of ~600 nm mesoporous TiO_2 using 1:1 30NRD: terpineol. Samples were annealed at 550°C for 30 minutes before screen printing of

~15 um carbon paste. Samples were annealed at 400°C for a further 30 minutes and infiltrated immediately after cooling to room temperature, as detailed in section 2.1.2.

Samples were humidity treated at 70% RH and 25°C for 14-16 hours and placed under vacuum for ≥4 hours before PL measurements (section 2.2.7). The ZrO_2 /C samples were also used for PLQY (section 2.2.7).

Device Testing

Standard device and module testing was performed as detailed in section 2.2.1.

Stability tests were performed using a Solaronix Solixon A-20 a.m. 1.5G AAA solar simulator. Devices were kept under continuous 0.85 AM irradiation at 38-43°C and 40-50% relative humidity. IV curves were measured between at a rate of 0.126 Vs^{-1} from V_{oc} to J_{sc} and vice-versa every 30 minutes for the duration.

SEM

Cross sectional samples and images were prepared as detailed in section 2.2.3. Surface SEM images were obtained using a HITACHI desktop scanning electron microscope in composition mode.

3.3 Results and discussion

3.3.1 Initial trials and characterisation

In CPSCs, the perovskite precursor is generally incorporated into the mesoscopic triple stack via drop-casting through the top electrode, before approximately ten minutes percolation time and subsequent annealing. Significant precursor penetration of the base TiO_2 layer can even be observed during the first minute following drop casting of GBL precursors, although ten minutes percolation time is generally allowed.[27],[28] Conventional $AVA_{0.03}MAPbI_3$-GBL devices are generally then annealed for an hour at 50°C in ambient conditions.[4],[27]–[30]

Solvent systems heavily impact solvent-metal coordination, the quality of infiltration and the crystallinity of annealed perovskite. Precursors utilising different solvents can thus require different annealing conditions for quality $MAPbI_3$ formation and stack infiltration. Therefore, XRD of infiltrated ZrO_2 scaffolds and UV-vis analysis of precursor solutions were performed before initial device trials, to compare the precursor absorption characteristics and confirm

that the GVL solutions formed $MAPbI_3$ without degradation under standard GBL annealing conditions.

As shown in Figure 3.1a, both XRD samples showed identical peak positions. This indicates that the $MAPbI_3$ unit cells are the same size and that the phase composition of both samples is similar. Additionally, the lack of a PbI_2 peak at 2θ~ 12.5° suggests that complete conversion to $MAPbI_3$ with no subsequent degradation occurred with the standard GBL annealing procedure. Interestingly, the relative intensity of the 2θ = 14.13° peak is higher in the GVL samples. This can be indicative of improved crystallinity.

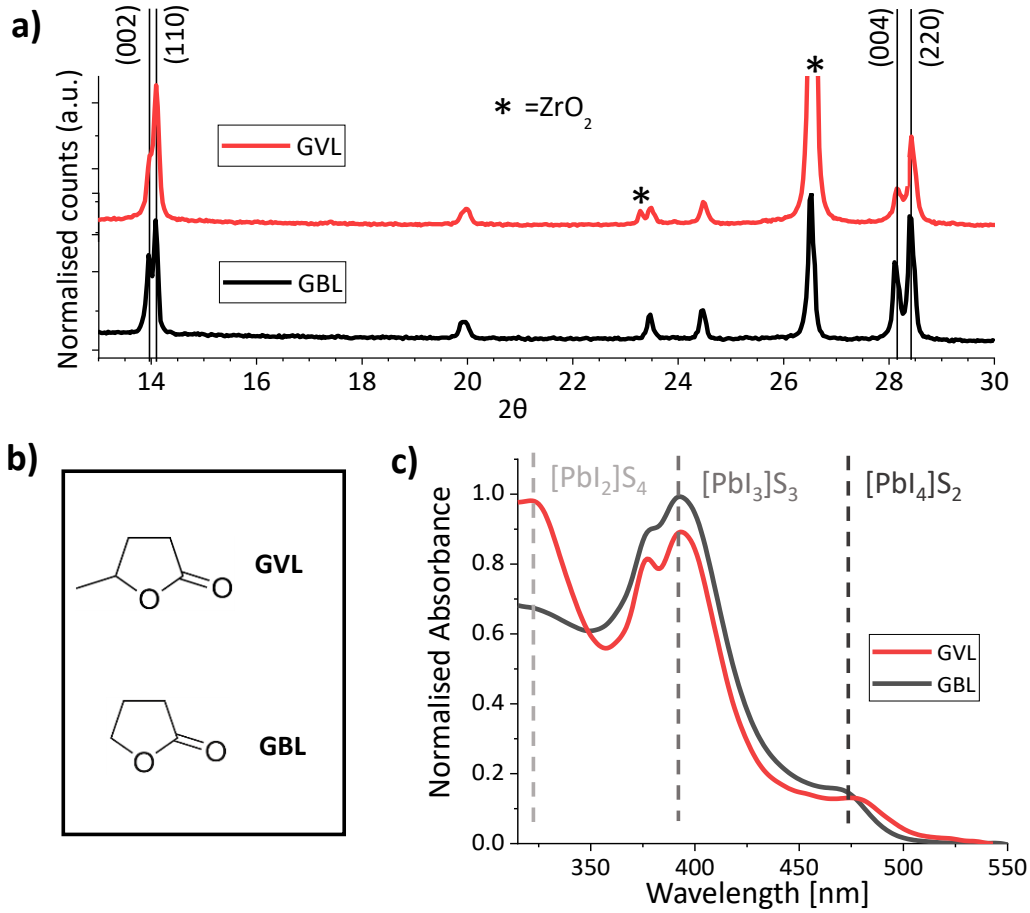

Figure 3.1: a) XRD of $AVA_{0.03}MAPbI_3$ perovskites on mesoporous TiO_2/FTO/glass, annealed from GVL (red) and GBL (black) precursors. TiO_2 signals have been subtracted for clarity b) Chemical structures of the solvents., c) UV-vis spectra of 175 mmol $AVA_{0.03}MAPbI_3$ precursors in GVL and GBL.

Improved crystallinity is suggestive of coordination changes. As a more viscous solvent of slightly different chemical structure, the behaviour of GVL precursors may be different to that of GBL (Figure 3.1b).[31]–[33] Solvents of lower Gutman donor numbers (D_n) coordinate

less easily to Pb^{2+} centres, leading to increased Pb-I interactions and correspondingly larger crystal sizes.

Solvent coordination to Pb^{2+} centres can be probed by comparing the UV-vis absorption of diluted precursors. When solvent-Pb^{2+} coordination is less favourable, greater proportions of I^- interact with the metal ions and the relative concentration of highly coordinated iodoplumbates increases.[31]–[33] In a dilute precursor this changes the relative absorption intensities of solvated PbI_2, PbI_3^- and PbI_4^{2-}. This has been shown to correspond with changes in crystal diameter, with greater solvent-Pb coordination linked to decreased colloidal diameters or complete solute dissolution.[31],[33],[34]

As shown in Figure 3.1c, UV-vis spectra of GVL precursors diluted to 175 mmol showed a higher relative PbI_2 absorbance peak at ~320 nm whereas the $[PbI_3]^-$ peak at ~380 nm was much more pronounced in the GBL solutions. This suggests that the GVL coordinates more readily to the Pb^{2+} centres than GBL and could explain the superior stability of GVL precursors towards room temperature precipitation.[31],[33],[34]

A significant increase in solvent coordination could even produce a non-colloidal precursor. This can easily be examined using the Tyndall effect, where a laser is shone through the solution to observe whether a visible beam appears perpendicular to the laser direction. In a colloidal solution aligned light will be scattered, becoming visible from a perpendicular angle. Non colloidal solutions will lack a visible beam.

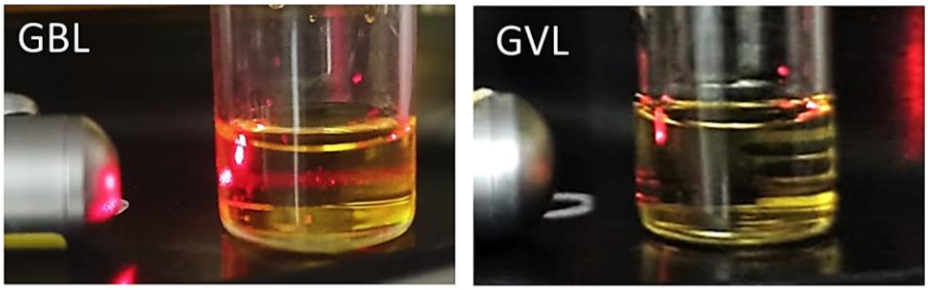

Figure 3.2: Photographs of laser beam shone through a GBL (left) and a GVL (right) precursor.

As shown in Figure 3.2, a clear scattered beam was observed in the GBL precursor, whereas the GVL formulation showed no beam scattering. It appears that the increased GVL coordination has resulted in a non-colloidal precursor.

In fast crystallising solutions, increased colloidal diameter can improve the crystallinity of formed perovskite.[32] Alternatively, some work has suggested that non colloidal solutions produce superior perovskite in CPSCs by enabling slower crystal growth.[35] Upon examining surface growth it appeared that GBL precursors produced larger crystals, but ones of varied quality, with areas where crystals appeared rough and poorly formed (Figure 3.3). Conversely, the GVL solutions produced smaller crystals with a more even size distribution and well-formed smooth grains. However, these surface crystals may not reflect crystallinity within the stack.

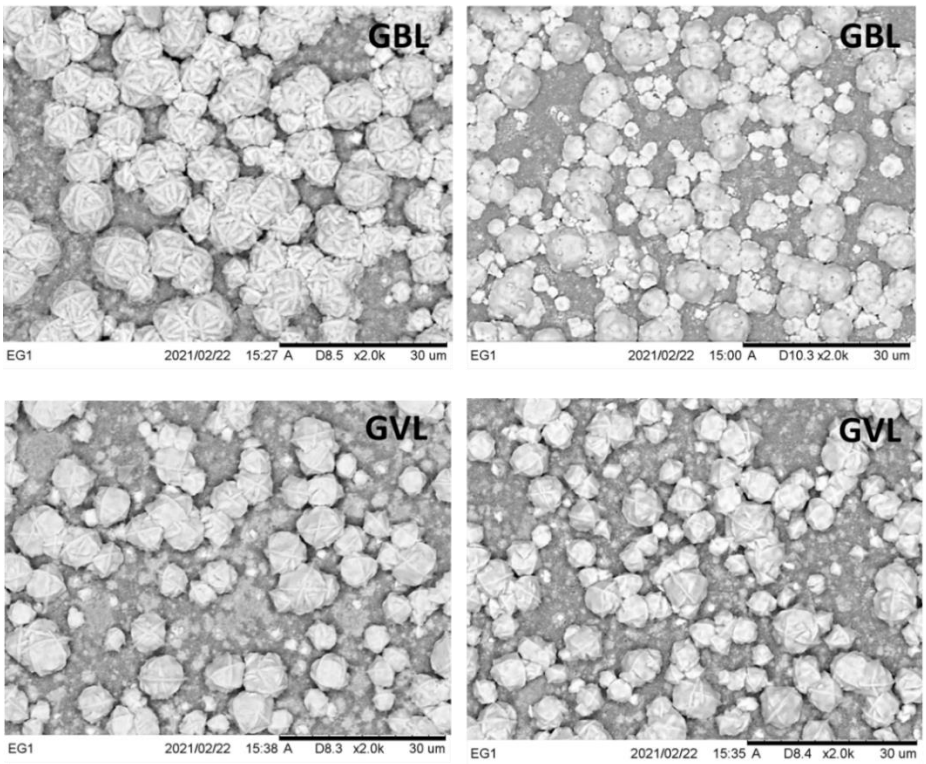

Figure 3.3: Surface SEM images of $AVA_{-0.03}MAPbI_3$ crystals on the surface of an infiltrated ZrO_2 scaffold, crystallised from 0.95 M GBL (top) and GVL (bottom) precursors at 50°C.

Changing the precursor solvent can also impact on wetting, which greatly impacts device performance by influencing pore filling. GBL devices are typically infiltrated at room temperature. However, as a slightly more viscous solvent (1.9 CP vs 1.7 CP for GBL), GVL may not spread well on the TiO_2 ETL at room temperature and could require gentle heating prior to infiltration. To compare room temperature precursors before initial device trials, viscosity measurements and contact angle tests were carried out for 0.95M GVL and GBL solutions.

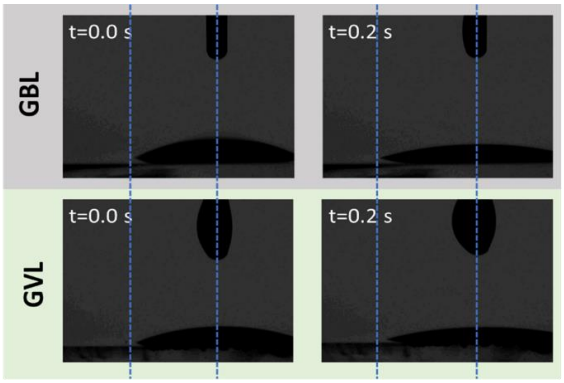

Solvent	[$AVA_{0.03}MAPbI_3$], moldm^{-3}	Viscosity (~18°C), cP	Density (~18°C), gcm^{-3}
GBL	0.95	5.198	1.519
GVL	0.95	6.431	1.439

Figure 3.4: Left; Contact angles of 0.95 M $AVA_{0.03}MAPbI_3$ in GBL and GVL on room temperature $mTiO_2$. Right; Viscosity and density of 0.95 M GBL and GVL precursors at 18°C. Viscosities are average values from 10-12 measurements.

Surprisingly, the GVL precursor was found to be much more viscous than that produced using GBL: the GVL solution measured at 6.431 cP, whereas the standard GBL precursor was nearly 24% less viscous at 5.198 cP (Figure 3.4). However, this change did not significantly change the precursor wetting in contact angle measurements- as shown in Figure 3.4 the GVL solution had spread almost as far as the GBL by t = 0.2 s.

As both precursors exhibited similar wetting, crystal phase formation and no significant degradation, the 50°C GBL annealing procedure was deemed suitable for initial GVL device trials.

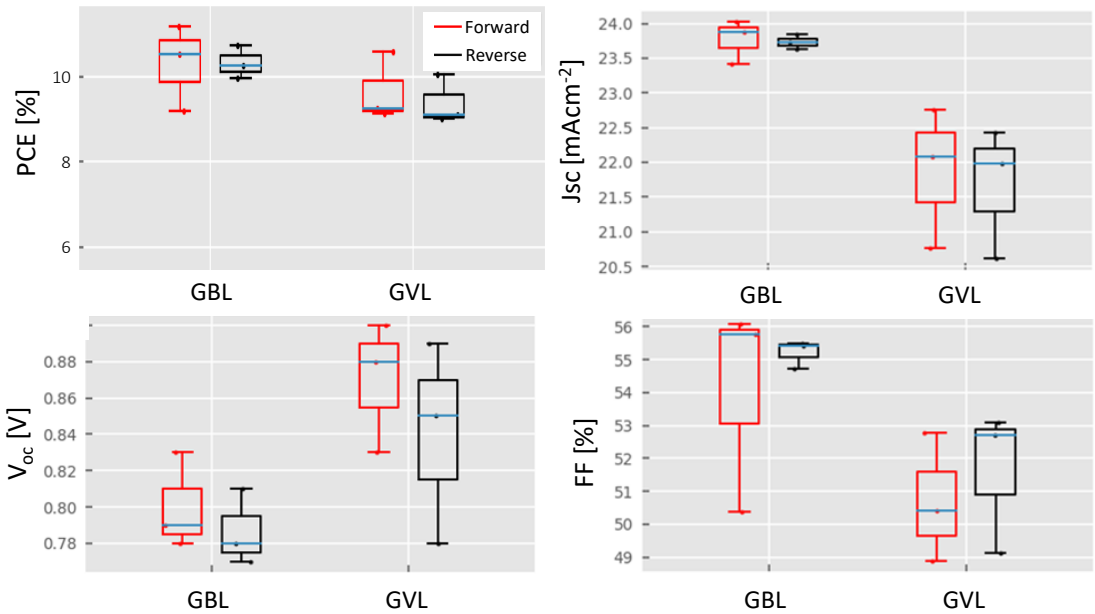

Figure 3.5: Box plots of photovoltaic parameters obtained during initial device trials.

As shown in Figure 3.5, the $AVA_{0.03}MAPbI_3$-GVL cells annealed at 50°C exhibited an average PCE of 9.9%, only slightly lower than the average GBL PCE of 10.3%. Although GVL devices exhibited slightly lower J_{sc} and FF values, this was counteracted by consistently higher V_{oc}.

Decreased J_{sc} accompanied by V_{oc} increases can be indicative of an increased perovskite bandgap, although this is unlikely here given the same perovskite formulation is present in both samples. The increased V_{oc} values are therefore more likely a consequence of higher crystallinity: higher quality perovskite crystals have fewer shallow traps near the band edge, so less non-radiative recombination occurs under illumination.[36] In this case, the lower J_{sc} and FF values could also correspond to poor perovskite infiltration, as insufficient perovskite contact with charge extraction layers impedes carrier collection. Photoluminescence (PL), external quantum efficiency (EQE) and photoluminescence quantum yield analyses were therefore performed to compare the absorption spectra, optical bandgaps, emissivity, and levels of recombination in GVL and GBL-based samples.

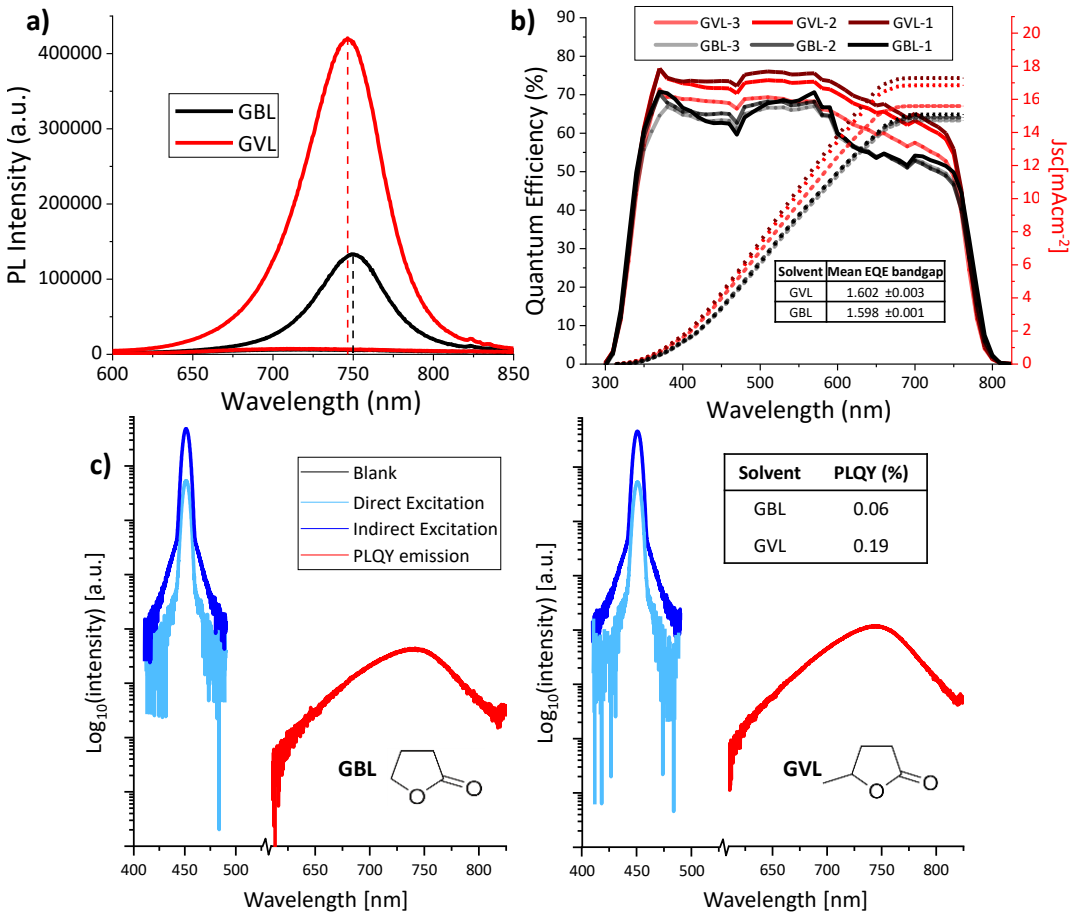

Figure 3.6: a) SSPL emission of 0.95 M $AVA_{0.03}MAPbI_3$ in ZrO_2/Carbon scaffolds. b) EQE of three GBL and three GVL devices with inlaid table of average calculated bandgaps. c) PLQY excitation data and corresponding corrected emission of a GBL (right) and GVL (left) sample, with table showing calculated external PLQY. PL and PLQY measurements by Dr. R. Garciarodruigez.

As shown in Figure 3.6a, the PL emission intensity of GVL perovskites in ZrO_2 scaffolds was far higher than that of the GBL samples. PLQY was also significantly higher. This indicates that the GVL precursors result in higher quality perovskite layers with lower levels of non-radiative recombination and could explain the higher V_{oc} observed in GVL devices. The observed increases in the PL of GVL samples are therefore most likely due to higher quality perovskite crystals with fewer defects. This is corroborated by the earlier XRD analysis, where the higher intensity (110) peak of GVL samples indicated more oriented crystal growth.

A slight blue-shift in the emission peak of the GVL samples was also apparent, with samples experiencing some photodarkening during the initial measurements. This can be caused by several factors, including decreased grain sizes, shifts in the band edge or sample degradation.[37],[38] Sample degradation is often accompanied by blue-shifting of the emission peak over time due to degradation producing shallow trap states.[36],[38] In this case the emission peak position did not change over multiple measurements and the photodarkening behavior stabilised within ten measurements. The slightly lower performance of GVL devices annealed at 50°C is therefore unlikely to be a consequence of changes in the material bandgap or instability, and the observed PL blue-shift is likely a consequence of smaller crystals.[36]

This is further supported by the EQE measurements, where the calculated material bandgaps were comparable between both sets; GVL samples showed improved absorption intensity in the 600-800 nm range (Figure 3.6b). Longer wavelengths are absorbed deeper in the stack, and such improved absorption could therefore suggest that the GVL samples have a higher proportion of perovskite in the ZrO_2 layer.[39]

Although the GVL EQE intensities are also less consistent than those of the GBL samples, it should be noted that EQE intensities are often highly variable in CPSCs as inconsistencies in infiltration can lead to changes in absorption efficiency across the active area. Mismatches between the IV J_{sc} and EQE photocurrent are also common as IV curves are obtained after long light soaking periods.[40] EQE photocurrents are therefore not representative of device performance or photocurrents after light soaking, and variations in EQE intensity between sample sets should not be used to compare infiltration.[5] However, when observed in conjunction with increased absorption of higher wavelength light and lower J_{sc} and FF values, highly variable EQE intensities can be an indication of poor perovskite infiltration.

The next section will detail the work undertaken in optimising device performance and infiltration.

3.3.2 Infiltration optimisation

Poor infiltration can be a consequence of poor solvent wetting. Alternatively, this can be a consequence of detrimentally fast perovskite crystallisation: If nucleation occurs too fast, growing crystals can form blockages, leading to voids in the annealed stack. Such devices typically present as uneven or grey in colour due to poor TiO_2 filling (Figure 3.7a).

Recent work has shown that CPSC infiltration may be improved through vapour-assisted crystallisation, where devices are kept in a closed solvent vapour environment during some or all of the annealing process. This solvent evaporation controlled (SEC) crystallisation allows more time for precursor percolation and allows the solvent to warm within the stack, reducing its viscosity and improving wetting. The technique also reduces the rate of crystal growth to form larger, more densely packed crystals.[10],[41] A one-hour SEC treatment at 50°C was therefore applied to devices infiltrated with GVL and GBL- based $AVA_{0.03}MAPbI_3$ precursors before standard annealing at 50°C.

As shown in Figure 3.7, SEC treated GBL devices were more reproducible, likely due to improved infiltration quality. However, SEC treatment of GVL devices resulted in visibly poor infiltration (Figure 3.7a) and low J_{sc} and FF (Figure 3.7b). Consequently, GVL-SEC devices exhibited much lower average PCE (7.7%) than controls (9.4%).**

It was hypothesized that for the GVL system, the small amount of solvent loss from the stack during the SEC treatment resulted in highly saturated, poorly wetting solution within the scaffold, or even crystal nucleation, which then annealed extremely fast upon removal of the petri dish. This suggests that GVL systems are more sensitive to detrimentally fast crystal growth.

** Although GVL device performance is lower here than for GBL, this was not the case in all batches. GVL reproducibility and performance is improved during the rest of this Chapter, before further enhancement in Chapter 4.

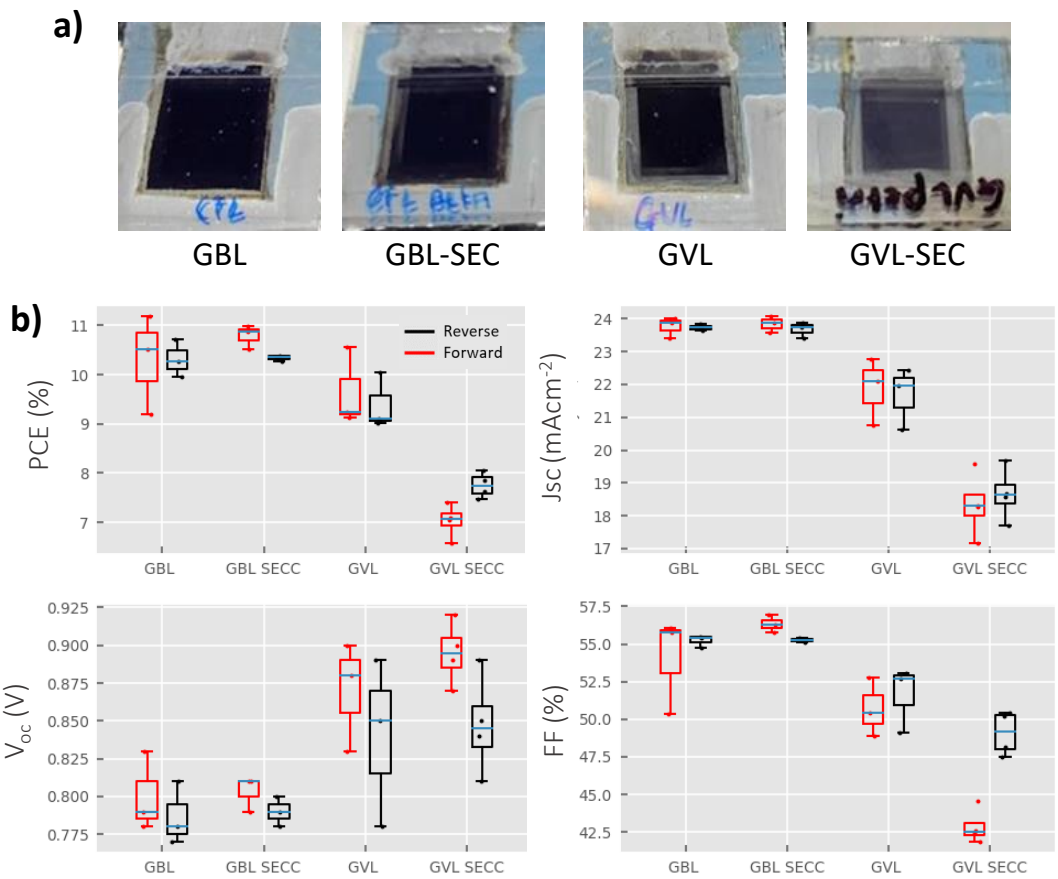

Figure 3.7: a) Diagrammatic representation of SEC treatments. b) Photograph of standard and SEC (solvent evaporation crystallised) devices infiltrated with GBL and GVL precursors. Right; Device parameters for standard and SEC devices with GBL and GVL precursors

This was investigated by performing in-situ XRD tests, wherein annealed stacks were placed on a thermal stage within the XRD, before drop casting of perovskite precursor and in-situ annealing. To accurately imitate the standard infiltration procedure, stacks were left at room temperature for ten minutes prior to heating of the thermal stage. Devices were then annealed at 50°C for one hour before being cooled to room temperature. XRD snapshots from 2θ = 13.0- 14.5° were obtained at 15 s intervals from the point of drop casting until room temperature cooling, to monitor the evolution of the peak at 2θ = 14.1°.

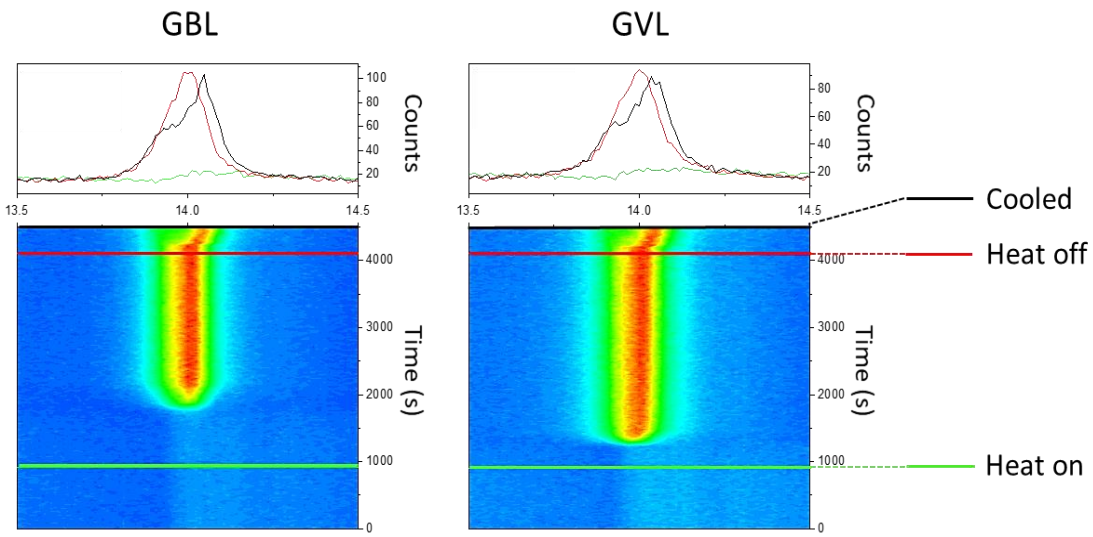

Figure 3.8: Contour maps showing the evolution of the peak at 2θ = 14.1° over time in GBL and GVL $AVA_{0.03}MAPbI_3$ precursors (0.95 M) drop cast into stacks and annealed at 50°C. Single plots shown above display the single XRD traces obtained at the onset of heating (green), end of annealing (red) and after cooling (black). Measurement by Dr. T. Dunlop and C. Worsley.

As shown in Figure 3.8, the GVL precursor crystallised far faster than the GBL system and formed an intense final peak much more rapidly. Specifically, the GVL system began crystallising at 1235 s (335 s (6 min 35 s) after heating onset) and had formed an intense peak by 1470 s (570 s (9 min 30 s) after heating onset). Apart from some very slight broadening this peak remained unchanged for the rest of the heated period. The crystallisation process therefore occurred in 235 s (4 min 55 s) after peak evolution began.

Conversely, no peak evolution was observed in the GBL sample until 1710 s (810 s or 13 min 30 s) after heat onset. Peak evolution also occurred more slowly, reaching the highest intensity at 2115 s (1215 s, or 20 min 15 s after heat onset). The crystallisation process therefore occurred in 405 s (6 min 45 s) after peak evolution began.

This data reveals that both nucleation and crystal growth occurred much faster in the GVL systems. This could be problematic, as the fast formation of large crystals early in the heating process could impede stack infiltration by forming blockages, which could explain the poor performance of devices exposed to SEC treatments.

In GBL devices, the presence of the petri dish during SEC prevents crystallite nucleation and warms precursor within the stack. This gives precursors more time to reach the smallest pores deep within the stack and could promote faster infiltration of small pores through reducing solution viscosity. Conversely in GVL solutions, the small solvent loss during SEC

treatments could be enough to induce crystallite formation, blocking further infiltration or encouraging increased crystal growth at the stack surface.

It was postulated that a lower annealing temperature could mitigate this problem by slowing the rate of solvent removal, crystal growth and nucleation- without the need for additives or additional annealing steps. Devices were therefore fabricated with a range of annealing temperatures (40, 45, 50 and 60°C).

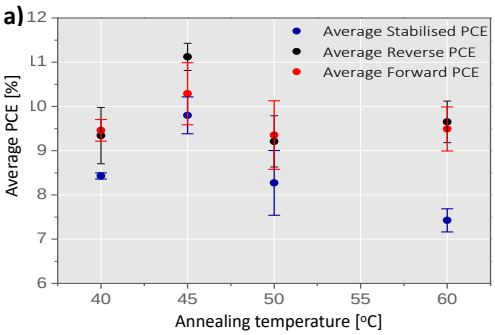

b)

Anneal temp (°C)	Scan	PCE (%)	V_{oc} (mV)	J_{sc} (mAcm^{-2})	FF(%)
40	r	9.34 ± 0.64	824 ± 36	23.2 ± 0.1	49 ± 2
	f	9.46 ± 0.25	823 ± 16	23.2 ± 0.1	50 ± 1
45	r	11.12 ± 0.31	919 ± 4	21.4 ± 0.3	57 ± 1
	f	10.29 ± 0.70	914 ± 2	21.5 ± 0.0	53 ± 3
50	r	9.21 ± 0.58	815 ± 56	22.2 ± 1.0	51 ± 2
	f	9.35 ± 0.78	838 ± 54	22.4 ± 1.0	50 ± 2
60	r	9.65 ± 0.47	834 ± 31	23.1 ± 0.5	50 ± 1
	f	9.49 ± 0.50	825 ± 21	23.2 ± 0.5	50 ± 2

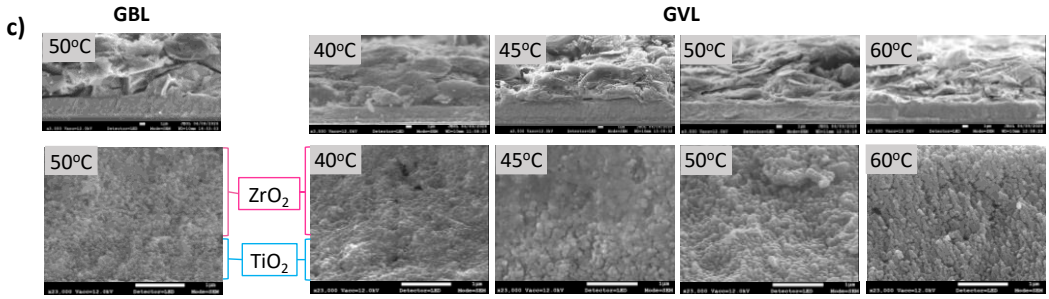

Figure 3.9: a) Average forward (red), reverse (black) and stabilised (blue) PCEs and b) table of PV parameters of GVL devices annealed at different temperatures. Three devices in each set. c) Cross-sectional SEMs of corresponding CPSCs. Above: 3500x magnification. Below: 23000x magnification.

As shown in Figure 3.9, an annealing temperature of 45°C produced the best devices, with the champion device exhibiting a J_{sc} of 21.6 mAcm^2, V_{oc} of 916 mV, FF of 58% and PCE of 11.4%. This is reflected in the stabilised current measurements, where devices annealed at 45°C far outperformed those prepared at other temperatures, with an average stabilised PCE of 9.80 ± 0.42% and champion stabilised PCE of 10.2% (Figure 3.9a).

As highlighted in Chapter 2, discrepancy between stabilised and IV PCEs is common in CPSCs due to imbalanced charge extraction at device electrodes.[42] Although these problems have here been mitigated by long light-soaking procedures and a slow scan rate, the IV PCEs are still higher than those from the stabilised current measurements.

Poorly infiltrated samples tend to exhibit larger differences between PCEs calculated from IV curves and those from stabilised current measurements due to poor perovskite-electrode contact.[42] This is clearly the case in the 60°C samples, where there is a marked discrepancy between the IV (9.65 ± 0.47%) and stabilised (7.42 ± 0.26%) PCEs, and many perovskite-free voids are visible in the TiO_2 layer (Figure 3.9c). Conversely, the optimum 45°C sample shows particularly dense ZrO_2 infiltration with larger, more continuous perovskite crystals and much more comparable IV and stabilised PCE values.

However, despite improving the device infiltration, even the optimised 45°C device exhibited larger perovskite free voids than the standard GBL device (Figure 3.9c).

Precursor concentration is also known to impact infiltration. Concentrated precursors can experience detrimental nucleation during the initial infiltration stages and prevent complete precursor penetration, whereas the volume contraction experienced by dilute solutions during solvent evaporation can result in poor pore-filling. The optimal concentration of a given precursor is highly dependent on solvent properties such as polarity and coordination.[34] As dilute GVL precursors exhibited lower PbI_3^- absorption in the UV-Vis analysis, it was hypothesised that the increased solvent-Pb^{2+} interactions could be resulting in less Pb-I interaction and thus less continuous crystal formation (Figure 3.7). GVL precursors may therefore require higher concentrations for optimal performance. Devices were therefore fabricated with 0.7 M, 0.95 M, 1.1 M, and 1.25 M $AVA_{0.03}MAPbI_3$ GVL precursors at the optimised 45°C annealing temperature.

As shown in Figure 3.10a, the 0.70 M precursors produced highly variable devices. This is likely a consequence of the poor infiltration and sparse perovskite formation seen here. The highest quality infiltration was achieved with a 1.10 M concentration, where dense perovskite formation was observed throughout the ZrO_2 and TiO_2 across the entire active area (Figure 3.10b). Performance was correspondingly higher in these devices with consistently higher device PCEs due to superior V_{oc}.

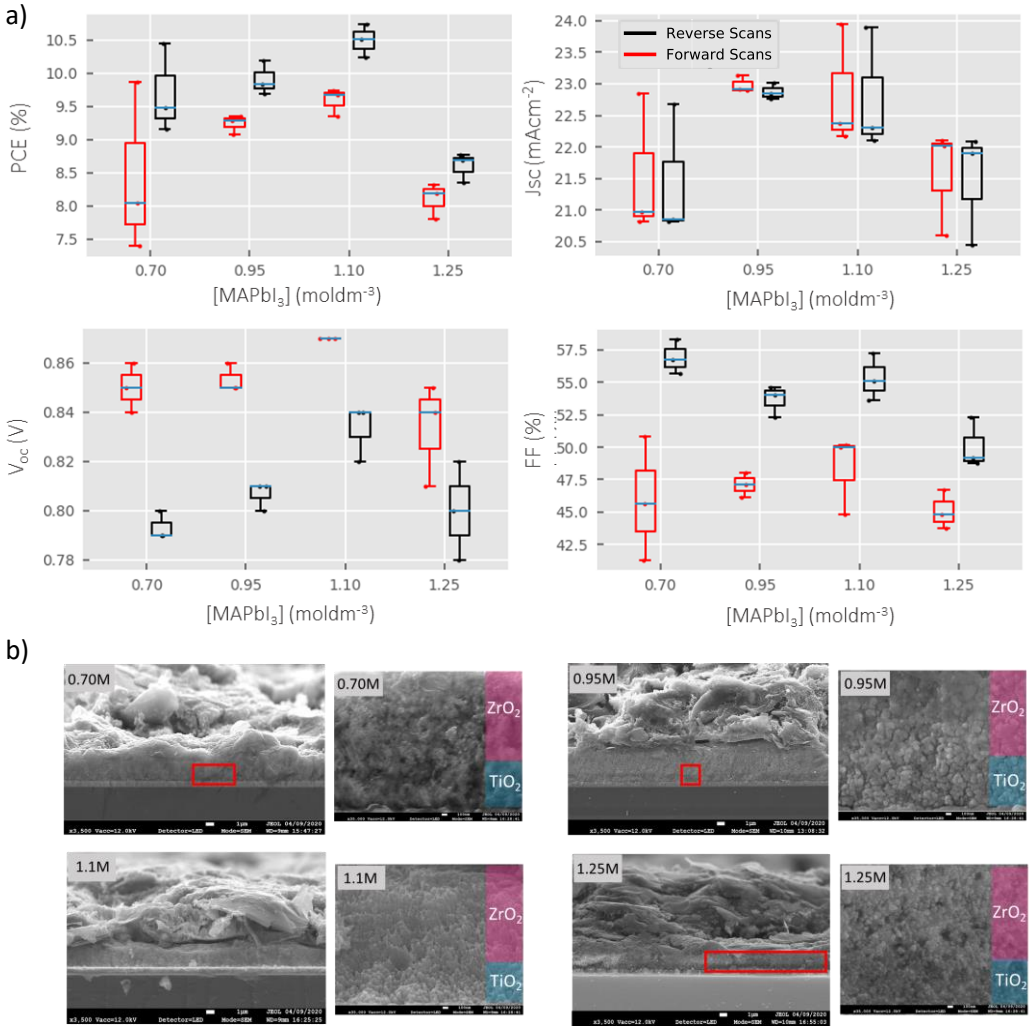

Figure 3.10: a) PV parameters of devices made using 0.70, 0.95, 1.10 and 1.25 M $MAPbI_3$ GVL precursors during optimisation. b) Corresponding cross-sectional SEM images of GVL devices. Red boxes highlight large areas with minimal perovskite infiltration. Three devices in each set.

The photovoltaic parameters for a batch of GVL devices fabricated with the optimised precursor (1.1 M) and annealing conditions (45°C) is presented in Figure 3.11 alongside standard GBL devices. The GVL devices exhibited an average PCE of 12.44 ± 0.56% (champion PCE 12.91%, 11.3% stabilised), higher than that of the GBL control devices at 11.67 ± 0.40%. All the IV parameters are higher on average in the GVL devices, with notably high and reproducible V_{oc} (0.90 ± 0.01 V and 0.82 ± 0.02 V for GVL and GBL respectively). There was also reduced hysteresis in the GVL devices, although it should be noted that this was not the case for every batch. From cross sectional SEM analysis, it is clear that the optimised annealing procedure and precursor concentration produced similar (if not improved) small pore filling to GBL (Figure 3.11b).

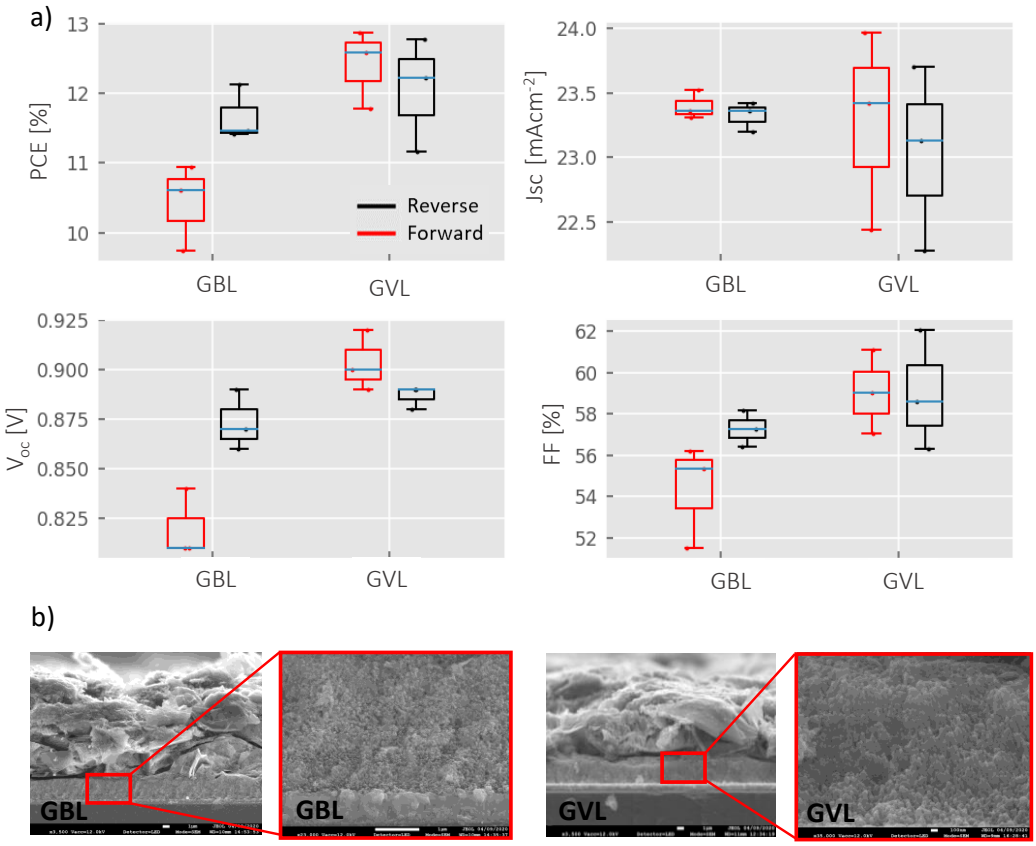

Figure 3.11: a) PV parameters of GBL devices compared to the optimised GVL system. b) Cross-sectional SEM images of devices made using standard GBL (0.95 M) and optimised GVL (1.1 M) precursors. Three devices in each set.

3.3.3 Device and precursor stability

One of the major advantages of GBL- based $AVA_{0.03}MAPbI_3$ CPSCs is their inherent stability. Any potential GBL replacement must therefore produce devices of similar longevity to be considered a viable alternative. Unencapsulated devices were therefore subjected to long term light exposure at 0.85 sun, elevated temperature (~40°C) and ambient humidity (40-70%).

As presented in Figure 3.12, minimal performance loss was observed in both devices over 550 hours of continuous illumination: the GVL device performance fell 7.8%, from 10.87% to 10.02%, while the GBL device fell 8.9% (from 9.08% to 8.27% PCE). The comparable stability of the two samples proves that GVL is a viable replacement for GBL in the fabrication of highly stable $AVA_{0.03}MAPbI_3$ devices.

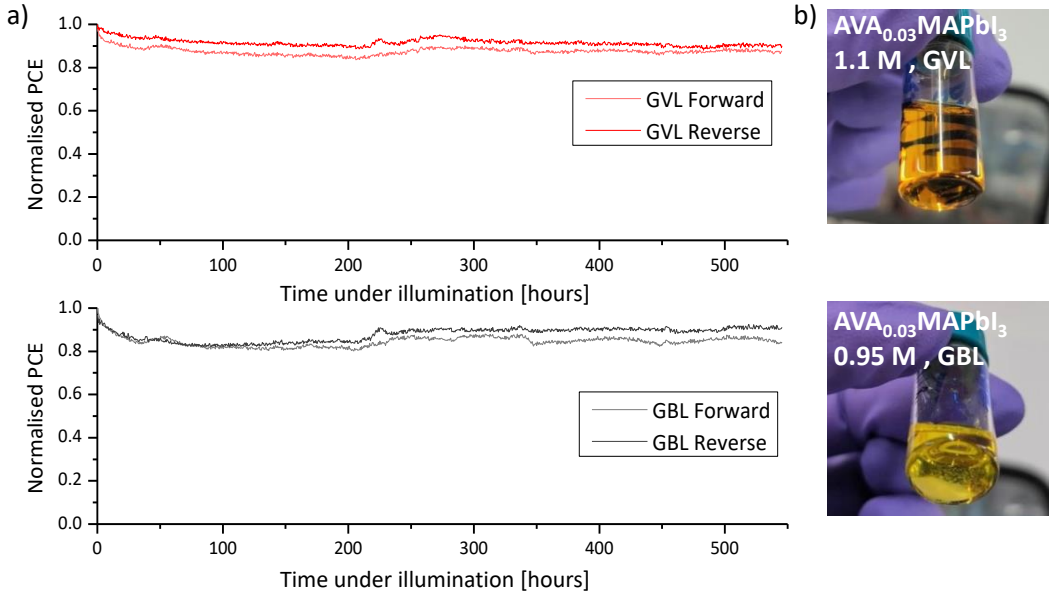

Figure 3.12: a) Normalised PCEs of GVL and GBL devices over time. Devices were kept under an illumination of 0.85 sun at ~40°C and ambient humidity (50-70%) and measured every 30 minutes for the duration. b) Photographs of 0.95M GBL and 1.1M GVL precursors after 1 week of room temperature storage. The GBL precursor has experienced significant precipitation.

Standard 0.95 M $AVA_{0.03}MAPbI_3$ in GBL precipitate when stored at room temperature (Figure 3.12). However, even the more concentrated GVL precursors were stable towards room temperature precipitation. This removes the need for redissolution prior to manufacture, saving energy and time. It potentially also makes these precursors much more suitable for large-scale industrial deposition techniques such as inkjet printing, where precipitation can clog printer nozzles and damage equipment. This added stability may be because GVL precursors do not form colloids (section 3.3.1).

Although the GVL precursors were observed to be stable towards precipitation, it was not known whether stored solutions would continue to produce high quality devices after storage. In a lab environment, CPSC precursors are generally made in small volumes and used within 3 days. This would not be the case at larger scale. As a hygroscopic solvent, precursors could feasibly incorporate some ambient water over time, as well as undergoing degradation processes such as I_2 formation.

A long-term experiment was therefore performed, wherein devices from the same printing batch were periodically annealed and infiltrated with the same batch of precursor over a period of several weeks. The 1.1 M $AVA_{0.03}MAPbI_3$ precursor was stored in a sealed vial in ambient conditions between uses (18-19°C, 30-40% RH), and all devices were prepared in an

ambient environment according to the previously optimised annealing procedure. It should be noted that device performance is less than that of the previously presented champion device sets as stacks contained a sub-optimal thin ZrO_2 layer of around 1 µm (optimal ~2 µm). This was due to a change in ZrO_2 paste formulation.* However, the devices were deemed good enough for simple comparison between sets, and were of sufficiently high and reproducible PCE for the purposes of this test.

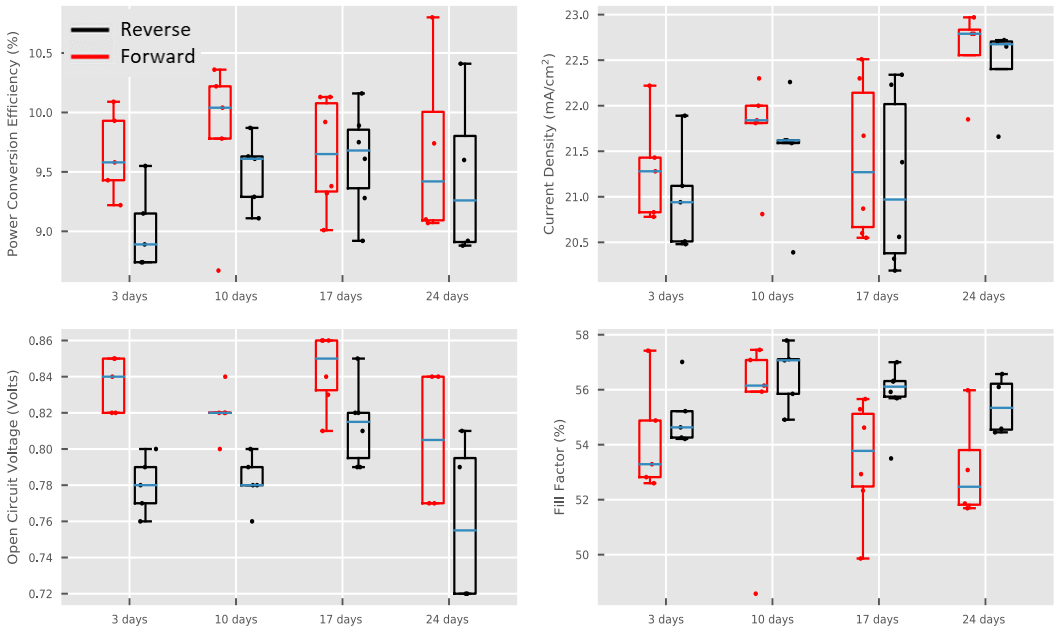

Figure 3.13: PV parameters of $AVA_{0.03}MAPbI_3$ devices fabricated from the same GVL precursor solution and printing batch over a period of 24 days. Note that performance is less than that of champion sets as stacks contained a sub-optimal thin ZrO_2 layer of around 1 µm (optimal ~2 µm).[††] *5 devices in each batch.*

As presented in Figure 3.13, no significant change in device performance was observed over time. Devices produced after 3 days exhibited an average PCE of 9.58 ± 0.39% (forward sweep), whereas those produced after 24 days storage were at 9.69 ± 0.79% PCE. Additionally, the champion device across the whole experiment was achieved after 24 days storage, with a PCE of 10.81% (V_{oc} = 0.84, J_{sc} = 23.0 mAcm^{-2}, FF = 56%). A slight increase in average J_{sc} can be observed over time, however this was not a statistically significant change.

Clearly, GVL precursors are stable during ambient storage. This would be extremely useful in commercial applications or scale-up initiatives, allowing offsite large-batch precursor

[††] This was due to a supplier formulation change. The impacts of this change and other stack properties on infiltration are discussed in detail in Chapter 6.

fabrication for modules. The next section will apply GVL precursors to modules, to assess their viability at scale.

3.3.4 Scale-up and module application

A variety of scalable techniques have been applied to obtain large area precursor infiltration, including inkjet printing and robotic mesh infiltration.[4],[43],[44] GBL-based precursors have been applied in modules of up to 198 cm^2 active area in the literature, achieving a maximum PCE of 6.6% via a scribing method with this size of module.[45] To be truly comparable to GBL, GVL must also be amenable to these techniques and produce large scale modules of comparable performance to GBL. It was hypothesised that GVL precursors would be more amenable to automated infiltration methods, as the lack of room temperature precipitation could prevent mesh and nozzle clogging- a problem often encountered with GBL solutions. Such issues can result in uneven infiltration across the module area and could significantly impact throughput in an industrial setting.

GVL and GBL $AVA_{0.03}MAPbI_3$ precursors were therefore applied in modules of 220 cm^2 active area and 80% geometric fill factor, prepared via a scribing method and robotic mesh infiltration.[45],[46]

As shown in Figures 3.14 and 3.15, both GBL and GVL precursors far outperformed those in previous publications, achieving champion PCEs of 8.14% and 8.12% respectively (Figure 3.14, 3.15). While the champion GVL module has superior V_{oc} and I_{sc}, slightly lower FF lowered its PCE to be comparable to that of the best GBL module.

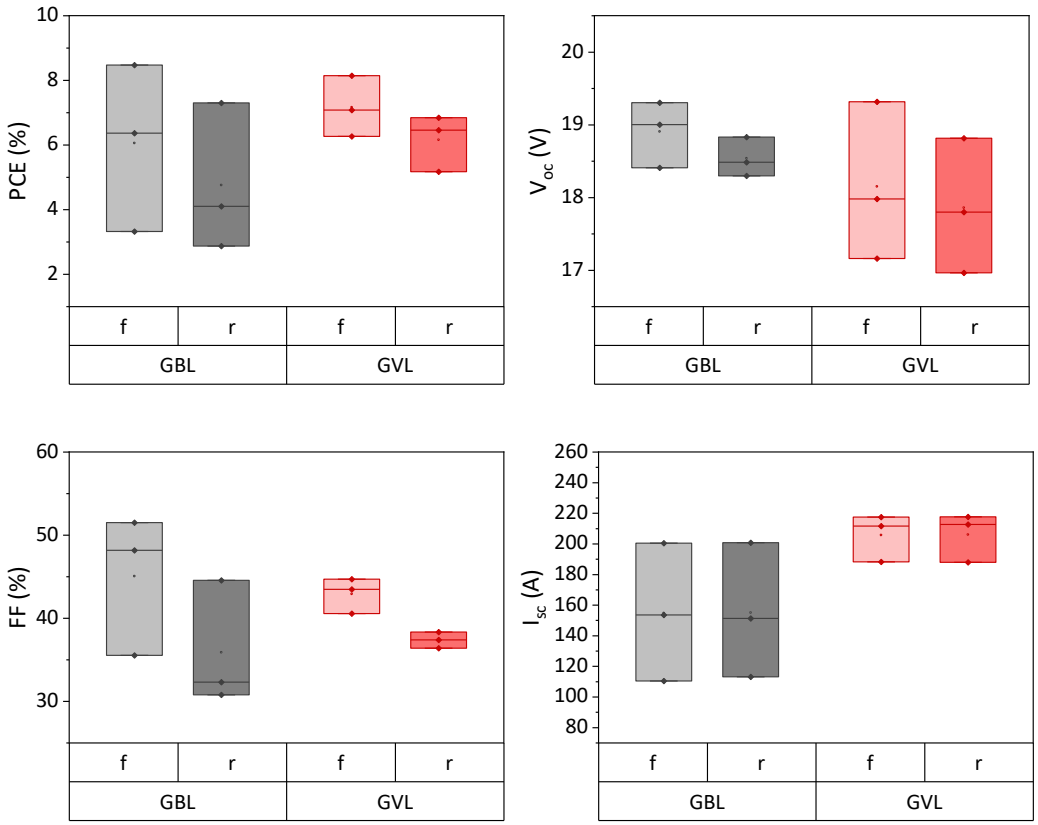

Figure 3.14: Box plots of photovoltaic parameters of 220 cm² modules fabricated via a scribing method using GBL or GVL precursors. Three tested for each solvent. Module preparation and testing by Dr. R. Bolton and Dr S. Potts. Analysis by C. Worsley.

However, the GVL devices exhibited much lower hysteresis, with a reverse PCE 1.4% higher than that obtained for the champion GBL module (Figure 3.15a, b). This is likely a consequence of improved perovskite crystallinity with GVL solutions. Reproducibility was also improved: While the GBL batch had an average PCE of 6.05 ± 2.59% (forward) and 4.76 ± 2.28% (reverse), three GVL modules from the same printing batch exhibited averages of 6.72 ± 0.41% and 6.59 ± 1.49% for forward and reverse sweeps respectively.

This was due to inconsistent infiltration in GBL modules. As shown in Figure 3.15c, GBL modules had pale bands of poor infiltration at the centre of multiple cells across the module area. Such areas have limited light absorption, poor perovskite-electrode contact and experience high levels of recombination.[43],[47],[48] As the performance of a module is limited to that of the lowest performing cell, any infiltration issues across the module area can have a significant detrimental effect on performance.[45]

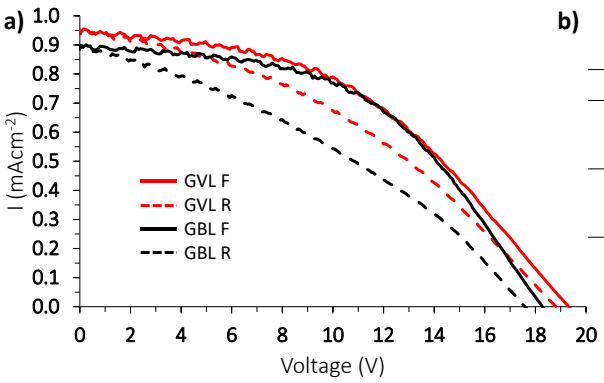

b)

		PCE (%)	V_{OC} (V)	FF (%)	J_{SC} (mA/cm^{-2})
GBL	R	5.44	17.6	34.7	0.89
	F	**8.12**	**18.3**	**49.5**	**0.90**
GVL	R	6.84	18.8	38.3	0.95
	F	8.14	19.3	44.7	0.94

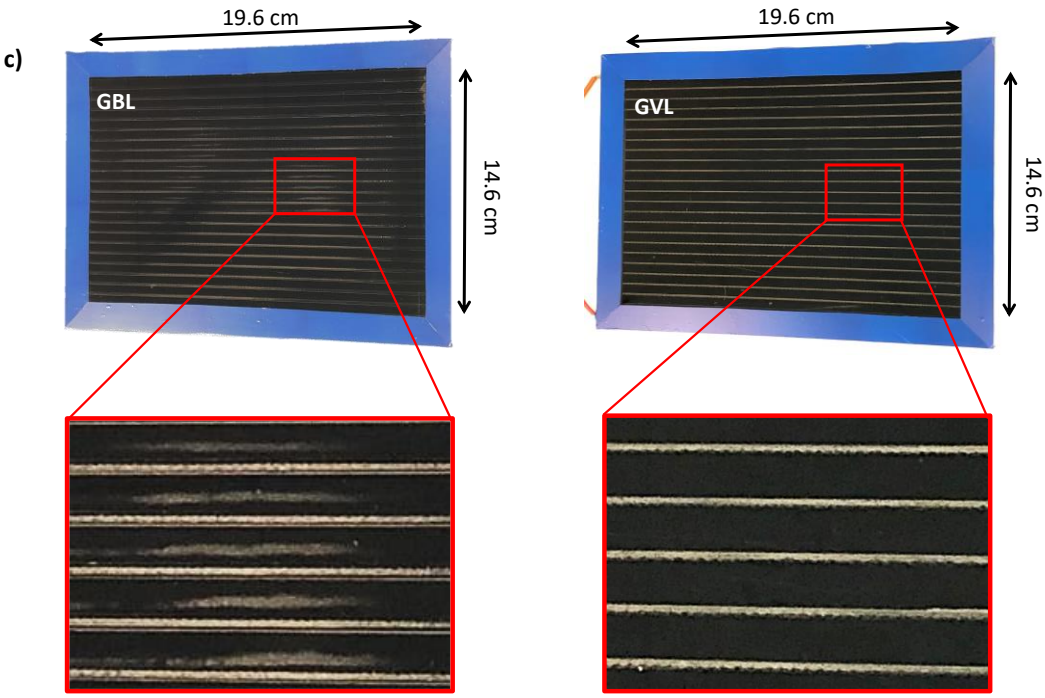

Figure 3.15: a) IV curves of modules fabricated with GBL and GVL precursors, b) table showing measured photovoltaic parameters, c) Photograph of the modules with dimensions labelled. Close up sections to compare visual infiltration quality. Module preparation and testing by Dr. R. Bolton and Dr S. Potts.

These infiltration issues were likely a consequence of GBL precipitation. Consistent mesh infiltration of the GBL precursors proved difficult, as crystal formation on the screen during infiltration prevented easy access to the underlying module. To prevent this issue, and to avoid nozzle blockages, the robotic dispenser and screens required thorough cleaning between every deposition, and GBL precursors were heated before each use. Even after taking these steps, achieving adequate infiltration over large areas proved challenging, as room temperature crystallisation of GBL inks atop the electrode also prevented successful infiltration in some places (shown in Figure 3.15c).

The enhanced stability of GVL precursors towards precipitation was therefore extremely advantageous at scale, resulting in large improvements in module reproducibility and drastically reducing the number of long cleaning steps required. This result confirms that green GVL precursors are well-suited to scale-up and proves that these green systems are a viable, superior alternative to GBL for CPSC module production.

3.4 Conclusion

Printable $AVA_{0.03}$-$MAPbI_3$ CPSCs are frequently cited as a potential forerunner for perovskite commercialisation. However, the DMF or GBL-based solvent systems used in these devices represent a significant barrier to scale up and commercial viability: DMF is highly toxic and GBL a psychoactive that is restricted in many countries. Consequently, neither solvent system is well-suited for application in large-scale CPSC manufacture.

This work presents GVL as a sustainable, nontoxic novel solvent for CPSC fabrication. Five times less toxic than GBL, GVL is completely biodegradable, and can be sourced from renewable lignocellulosic biomass feedstocks. Furthermore, the legal restrictions that impact GBL availability in certain counties do not apply, making GVL well suited to large scale sustainable production. A recent price drop in Europe and the recent emergence of biodegradability and toxicity studies indicate that industrial GVL application is likely to increase in the coming years.[23]

In this study, a low optimized annealing temperature of 45°C and optimized precursor concentration of 1.1 M are shown to improve GVL precursor infiltration and produce CPSCs of comparable efficiency to those fabricated with standard GBL precursors, achieving a champion PCE of 12.91% in a 1 cm^2 device (11.33% stabilized). GVL precursors were also found to improve the reproducibility of large-scale modules, producing a champion PCE of 8.12% in a module of 220 cm^2 active area.

Perhaps most interesting from a scaling perspective, GVL precursors were found to be extremely stable towards room temperature precipitation. While GBL precursors are prone to significant precipitation at room temperature and require heating after storage, GVL solutions were found to produce high quality devices over a month in ambient conditions, with no heating steps required. At scale this helped prevent equipment blockages, improved the quality of automated robotic mesh infiltration, and reduced the number of long cleaning steps required between depositions. This work could therefore improve the commercial

viability of CPSCs, as well as allowing continued CPSC research in countries where GBL access is prohibited.

Although this work aids in improving the reproducibility of large-scale modules through preventing precipitation induced equipment blockages, inter-batch performance variation was still significant. Device performance and the quality of infiltration of devices produced from different prints on different days was still somewhat variable. In a commercial setting, this could significantly impact throughput and the quality of produced modules.

Variation could be a consequence of high precursor viscosity- GVL is more viscous than GBL (1.9 cP compared to 1.7 cP), and the optimised precursor concentration of 1.1 M is higher. This could limit precursor percolation into the stack or make GVL precursors more sensitive to slight ambient changes. The next chapter will therefore examine a mixed solvent system, to analyse how precursor viscosity influences performance and attempt to improve reproducibility.

3.5 References

[1] Y. Cai, L. Liang and P. Gao, *Chinese Phys. B*, 2018, **27**, 018805

[2] M. Duan, Y. Hu, A. Mei, Y. Rong and H. Han, *Mater. Today Energy*, 2018, **7**, 221–231

[3] J. Baker, K. Hooper, S. Meroni, A. Pockett, J. McGettrick, Z. Wei, R. Escalante, G. Oskam, M. Carnie and T. Watson, *J. Mater. Chem. A*, 2017, **5**, 18643–18650

[4] S. M. P. Meroni, Y. Mouhamad, F. De Rossi, A. Pockett, J. Baker, R. Escalante, J. Searle, M. J. Carnie, E. Jewell, G. Oskam and T. M. Watson, *Sci. Technol. Adv. Mater.*, 2018, **19**, 1–9

[5] A. Mei, X. Li, L. Liu, Z. Ku, T. Liu, Y. Rong, M. Xu, M. Hu, J. Chen, Y. Yang, M. Grätzel and H. Han, *Science*, 2014, **345**, 295–298

[6] G. Grancini, C. Roldán-Carmona, I. Zimmermann, E. Mosconi, X. Lee, D. Martineau, S. Narbey, F. Oswald, F. De Angelis, M. Graetzel and M. K. Nazeeruddin, *Nat. Commun.*, 2017, **8**, 15684

[7] Y. Sheng, Y. Hu, A. Mei, P. Jiang, X. Hou, M. Duan, L. Hong, Y. Guan, Y. Rong, Y. Xiong and H. Han, *J. Mater. Chem. A*, 2016, **4**, 16731–16736

[8] H. Zhang, H. Wang, S. T. Williams, D. Xiong, W. Zhang, C.-C. Chueh, W. Chen and A. K.-Y. Jen, *Adv. Mater.*, 2017, **29**, 1606608

[9] Y. Hu, Z. Zhang, A. Mei, Y. Jiang, X. Hou, Q. Wang, K. Du, Y. Rong, Y. Zhou, G. Xu and H. Han, *Adv. Mater.*, 2018, **30**, 1705786

[10] X. Hou, M. Xu, C. Tong, W. Ji, Z. Fu, Z. Wan, F. Hao, Y. Ming, S. Liu, Y. Hu, H. Han, Y. Rong and Y. Yao, *J. Power Sources*, 2019, **415**, 105–111

[11] MSDS - 227056, https://www.sigmaaldrich.com/MSDS/MSDS/DisplayMSDSPage.do?country=GB&language=en&productNumber=227056, (accessed 16 March 2020)

[12] MSDS - M81802, https://www.sigmaaldrich.com/MSDS/MSDS/DisplayMSDSPage.do?country=GB&language=en&productNumber=M81802, (accessed 16 March 2020)

[13] Candidate List of substances of very high concern for Authorisation - ECHA, https://echa.europa.eu/candidate-list-table?, (accessed 16 March 2020)

[14] A. E. Williams, P. J. Holliman, M. J. Carnie, M. L. Davies, D. A. Worsley and T. M. Watson, *J. Mater. Chem. A*, 2014, **2**, 19338–19346

[15] R. B. Palmer, *Toxicol. Rev.*, 2004, **23**, 21–31

[16] GBL MSDS - B103608, https://www.sigmaaldrich.com/MSDS/MSDS/DisplayMSDSPage.do?country=GB&language=en&productNumber=B103608, (accessed 16 March 2020)

[17] K. Knudsen, J. Greter and M. Verdicchio, *Clin. Toxicol.*, 2008, **46**, 187–192

[18] K. L. Gardner, J. G. Tait, T. Merckx, W. Qiu, U. W. Paetzold, L. Kootstra, M. Jaysankar, R. Gehlhaar, D. Cheyns, P. Heremans and J. Poortmans, *Adv. Energy Mater.*, 2016, **6**, 1600386

[19] N. K. Noel, S. N. Habisreutinger, B. Wenger, M. T. Klug, M. T. Hörantner, M. B. Johnston, R. J. Nicholas, D. T. Moore and H. J. Snaith, *Energy Environ. Sci.*, 2017, **10**, 145–152

[20] Q. Liu, Y. Zhao, Y. Ma, X. Sun, W. Ge, Z. Fang, H. Bai, Q. Tian, B. Fan and T. Zhang, *J. Mater. Chem. A*, 2019, **7**, 18275–18284

[21] K. H. Hendriks, J. J. Van Franeker, B. J. Bruijnaers, J. A. Anta, M. M. Wienk and R. A. J. Janssen, *J. Mater. Chem. A*, 2017, **5**, 2346–2354

[22] S. Jin, F. Byrne, C. R. McElroy, J. Sherwood, J. H. Clark and A. J. Hunt, *Faraday Discuss.*, 2017, **202**, 157–173

[23] F. Kerkel, M. Markiewicz, S. Stolte, E. Müller and W. Kunz, *Green Chem.*, 2021, **23**, 2962–2976

[24] A. Osatiashtiani, A. F. Lee and K. Wilson, *J. Chem. Technol. Biotechnol.*, 2017, **92**, 1125–1135

[25] I. T. Horváth, H. Mehdi, V. Fábos, L. Boda and L. T. Mika, *Green Chem.*, 2008, **10**, 238–242

[26] S. G. Wettstein, D. M. Alonso, Y. Chong and J. A. Dumesic, *Energy Environ. Sci.*, 2012, **5**, 8199–8203

[27] E. V. Péan, C. S. De Castro, S. Dimitrov, F. De Rossi, S. Meroni, J. Baker, T. Watson and M. L. Davies, *Adv. Funct. Mater.*, 2020, **30**, 1909839

[28] A. Mei, Y. Sheng, Y. Ming, Y. Hu, Y. Rong, W. Zhang, S. Luo, G. Na, C. Tian, X. Hou, Y. Xiong, Z. Zhang, S. Liu, S. Uchida, T.-W. Kim, Y. Yuan, L. Zhang, Y. Zhou and H. Han, *Joule*, 2020, **4**, 2646–2660

[29] M. Duan, Y. Rong, A. Mei, Y. Hu, Y. Sheng, Y. Guan and H. Han, *Carbon N. Y.*, 2017, **120**, 71–76

[30] S. Jiang, Y. Sheng, Y. Hu, Y. Rong, A. Mei and H. Han, *Front. Optoelectron.*, 2020, **13**, 256-264

[31] J. C. Hamill, J. Schwartz and Y.-L. Loo, *ACS Energy Lett.*, 2018, **3**, 92–97

[32] J. Kim, B. W. Park, J. Baek, J. S. Yun, H. W. Kwon, J. Seidel, H. Min, S. Coelho, S. Lim, S. Huang, K. Gaus, M. A. Green, T. J. Shin, A. W. Y. Ho-Baillie, M. G. Kim and S. Il Seok, *J. Am. Chem. Soc.*, 2020, **142**, 6251–6260

[33] K. Yan, M. Long, T. Zhang, Z. Wei, H. Chen, S. Yang and J. Xu, *J. Am. Chem. Soc.*, 2015, **137**,

4460–4468

[34] Y. Ming, M. Xu, S. Liu, D. Li, Q. Wang, X. Hou, Y. Hu, Y. Rong and H. Han, *J. Power Sources*, 2019, **424**, 261–267

[35] S. Liu, Y. Sheng, D. Zhang, W. Zhang, Z. Qin, M. Qin, S. Li, Y. Wang, C. Gao, Q. Wang, Y. Ming, C. Liu, K. Yang, Q. Huang, J. Qi, Q. Gao, K. Chen, Y. Hu, Y. Rong, X. Lu, A. Mei and H. Han, *Fundam. Res.*, 2022, **2**, 276-283

[36] K. P. Goetz, A. D. Taylor, F. Paulus and Y. Vaynzof, *Adv. Funct. Mater.*, 2020, **30**, 1910004

[37] W. Nie, H. Tsai, R. Asadpour, J. C. Blancon, A. J. Neukirch, G. Gupta, J. J. Crochet, M. Chhowalla, S. Tretiak, M. A. Alam, H. L. Wang and A. D. Mohite, *Science*, 2015, **347**, 522–525

[38] E. V. Péan, C. S. De Castro and M. L. Davies, *Mater. Lett.*, 2019, **243**, 191–194

[39] R. Kerremans, O. J. Sandberg, S. Meroni, T. Watson, A. Armin and P. Meredith, *Sol. RRL*, 2019, **4**, 1900221

[40] A. Pockett, D. Raptis, S. M. P. Meroni, J. Baker, T. Watson and M. Carnie, *J. Phys. Chem. C*, 2019, **123**, 11414–11421

[41] Q. Wang, W. Zhang, Z. Zhang, S. Liu, J. Wu, Y. Guan, A. Mei, Y. Rong, Y. Hu and H. Han, *Adv. Energy Mater.*, 2020, **10**, 1–7

[42] I. Zimmermann, P. Gratia, D. Martineau, G. Grancini, J.-N. N. Audinot, T. Wirtz and M. K. Nazeeruddin, *J. Mater. Chem. A*, 2019, **7**, 8073–8077

[43] S. G. Hashmi, D. Martineau, X. Li, M. Ozkan, A. Tiihonen, M. I. Dar, T. Sarikka, S. M. Zakeeruddin, J. Paltakari, P. D. Lund and M. Grätzel, *Adv. Mater. Technol.*, 2017, **2**, 1600183

[44] A. Verma, D. Martineau, S. Abdolhosseinzadeh, J. Heier and F. Nüesch, *Mater. Adv.*, 2020, **1**, 153–160

[45] F. De Rossi, J. A. Baker, D. Beynon, K. E. A. Hooper, S. M. P. Meroni, D. Williams, Z. Wei, A. Yasin, C. Charbonneau, E. H. Jewell and T. M. Watson, *Adv. Mater. Technol.*, 2018, **3**, 1800156

[46] S. M. P. Meroni, K. E. A. Hooper, T. Dunlop, J. A. Baker, D. Worsley, C. Charbonneau and T. M. Watson, *Energies*, 2020, **13**, 1589

[47] A. Priyadarshi, L. J. Haur, P. Murray, D. Fu, S. Kulkarni, G. Xing, T. C. Sum, N. Mathews and S. G. Mhaisalkar, *Energy Environ. Sci.*, 2016, **9**, 3687–3692

[48] H. Lakhiani, T. Dunlop, F. De Rossi, S. Dimitrov, R. Kerremans, C. Charbonneau, T. Watson, J. Barbé and W. C. Tsoi, *Adv. Funct. Mater.*, 2019, **29**, 1900885

Chapter 4

GVL Solvent Engineering for improved precursor wetting and device performance

The work in this chapter formed the basis of the following publication: C. Worsley, D. Raptis, S. M. P. Meroni, R. Patidar, A. Pockett, T. Dunlop, S. J. Potts, R. Bolton, C. M. E. Charbonneau, M. Carnie, E. Jewell and T. Watson, Mater. Adv., 2022,3, 1125

Unless specified, all sample preparation, measurement and data analysis was performed by C. Worsley.

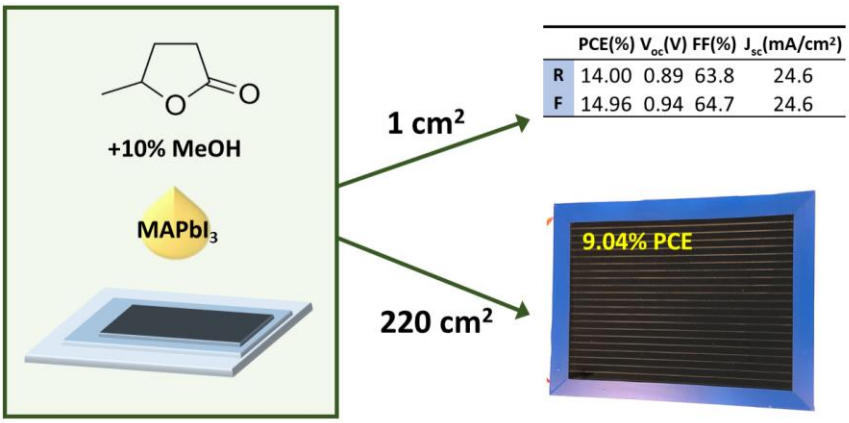

	PCE(%)	V_{oc}(V)	FF(%)	J_{sc}(mA/cm²)
R	14.00	0.89	63.8	24.6
F	14.96	0.94	64.7	24.6

Chapter 3 established GVL as a viable green alternative to GBL, with optimised devices demonstrating comparable performance. In this work, methanol (MeOH) is used to enhance PCE and infiltration by improving electrode wetting, infiltration and perovskite crystal quality. Precursors incorporating 10% MeOH achieved 14.96% PCE in a 1 cm^2 device and 9.04% in a 220 cm^2 module fabricated in ambient conditions. Stability was also enhanced, with an unencapsulated device exhibiting a T80 of >420 hours at 50°C in ambient humidity under AM1.5 illumination. Improved precursor quality also enabled production of large 517.7 cm^2 modules. This could make GVL-based precursors more commercially attractive and provides an example of how green solvent engineering can be applied in the development, amelioration and scale-up of novel renewable technologies.

4.1 Introduction

In the previous chapter, GVL was introduced as a non-toxic biodegradable alternative to GBL for CPSC fabrication. With an optimised annealing temperature of 45°C and precursor concentration of 1.1 M, GVL solutions were found to produce devices of comparable performance to standard GBL procedures. Additionally, GVL precursors were found to be more stable towards room temperature precipitation: 0.95 M GBL precursors undergo significant precipitation in ambient storage, while more concentrated 1.1 M GVL alternatives remain in solution. This would be advantageous in a commercial setting, where ink precipitation could cause printer blockages and other equipment issues. However, a slight increase in batch variation was noted, with more instances of visually poor infiltration in some batches.

Even in GBL $AVA_{0.03}MAPbI_3$ precursors, complete infiltration can be difficult to obtain.[1] Both GVL and GBL are relatively viscous: while DMF has a viscosity of 0.92 CP at 25°C, those of GBL and GVL are 1.7 CP and 1.9 CP respectively. [1]–[3] This can limit infiltration of small pores deep within the stack. The TiO_2 layer in particular can experience wetting problems, leading to poor perovskite/electrode contact and decreased device performance.[4],[5]

High viscosity and associated wetting issues are potentially a greater issue in GVL systems as GVL is slightly more viscous than GBL and the optimised precursor concentration is higher (1.1 M and 0.95 M for GVL and GBL respectively, Chapter 3).[1],[2] Differences in the solvent coordination and resultant changes to colloidal composition could also impact viscosity. This would therefore make GVL precursor infiltration more sensitive towards slight changes in ambient temperature or stack thickness could explain why batches of GVL devices fabricated at room temperature more frequently exhibit a wide spread of results.

Viscosity can easily be reduced by heating- GBL precursors are often heated prior to infiltration to remove precipitates and reduce viscosity. However, heating GVL precursors to 60°C to improve infiltration is not viable, as this can induce perovskite crystal formation within the solution and loss of volatile MA species. Any heating must therefore be limited to shorter times at lower temperatures to maintain the integrity of the precursor. Heating would also be impractical at large scale and maintaining precursors at temperature would increase the energetic cost of fabrication. Therefore, a different approach is required for GVL-based precursors.

The main advantages of GVL-based solvent systems are the low toxicity, biodegradability, and lack of legal restrictions on access. Compared to more common DMF/DMSO solutions, these systems are far less environmentally harmful, and can be sourced from sustainable, renewable sources.[6] To maintain these advantages, any solvent additions to GVL-based precursors should be similarly sustainable and present a relatively low toxicity risk. Small molecule alcohols such as ethanol and MeOH fit this profile, are already mass-produced at low cost and have been applied in similar GBL systems to improve device performance and reproducibility.[4]

Small additions of highly polar solvents have been used in many architectures to improve perovskite crystal quality and coverage. For example, addition of highly coordinating DMSO to DMF-based precursors has been shown to improve grain size, coverage and crystallinity in conventional sandwich architectures with NIP and PIN architectures.[7] In CPSCs, GBL devices have been found to reproducibly exhibit improved performance when diluted with 15% ethanol due to reductions in viscosity and improved precursor wetting: Dilution with 15 volume % of ethanol produced devices of 14.95 ± 0.27% PCE compared to 13.66 ± 0.41% in the undiluted case.[4]

The following sections will look at the impact of using mixed GVL: alcohol solvent systems on formed perovskite, solution properties and resultant device performance.

4.2 Experimental

Unless specified below, all materials, sample preparation and measurement procedures were performed as detailed in Chapter 2.

Precursors

All precursors and solvent mixes were fabricated in an N_2 glove box to a concentration of 1.1 M. To ensure comparable concentration between precursors of different solvent ratios, precursors were prepared by dilution of a 1.25 M $AVA_{0.03}MAPbI_3$ / GVL stock solution. The stock solution was stirred at room temperature overnight to ensure complete dissolution of the components before separation to different vials and dilution with the appropriate volumes of GVL and MeOH.

Contact angle testing

Samples were prepared by screen printing ~600 nm TiO_2 paste (Greatcell solar, 30 NRD, diluted 1:1 with terpineol) onto FTO. Layers were annealed at 550°C for 30 minutes and cooled to room temperature in ambient conditions (20°C, 30% RH) before contact angle testing (as described in Chapter 2.25)

UV Vis

UV Vis samples were prepared by diluting precursors to 250 mmol with GVL/MeOH in the appropriate solvent ratio (0, 5, 10 or 15% MeOH in GVL as specified) immediately before measuring as detailed in Chapter 2.2.4.

Stability measurements

Measurements were carried out under 1 Sun AM 1.5G illumination. The source was a plasma bulb in a Lumartix SA instrument (Luxim-S). The unencapsulated devices were masked at 0.49 cm^2 and measured every 4h after a resting time in open circuit. The substrates were heated by the IR component of the light spectrum leading to a temperature of around 50°C.

SEM

Cross sectional samples were prepared as described in Chapter 2.1.3. Images were obtained using a JSM-7800F Field Emission SEM at 15 kV using secondary electron imaging. **PL**

PL

Samples were prepared as described in Chapter 2.1.2. Samples were humidity treated at 25°C and 70% RH for 14-18 hours and then placed under a vacuum for ≥4 hours before testing. Mapping was done as described in section 2.2.8.

4.3 Initial trials: Impact of EtOH and MeOH on Device Performance

As 15% ethanol has proven optimal in GBL solvent systems, initial trials on mixed GVL systems compared the previously optimised 1.1 M $AVA_{0.03}MAPbI_3$ GVL system to those incorporating 15% ethanol or MeOH.[4] Both initial trials yielded promising results, with the mixed systems producing devices of higher stabilised PCE than GVL-only precursors (Figure 4.2).

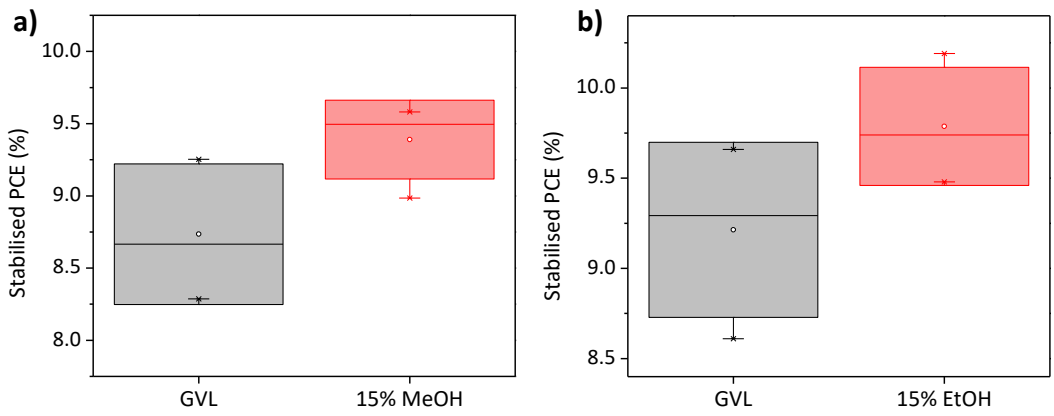

Figure 4.2: Box plots of stabilised current data obtained from initial trials testing GVL-only precursors against precursors incorporating a) 15% MeOH or b) 15% EtOH [‡‡]

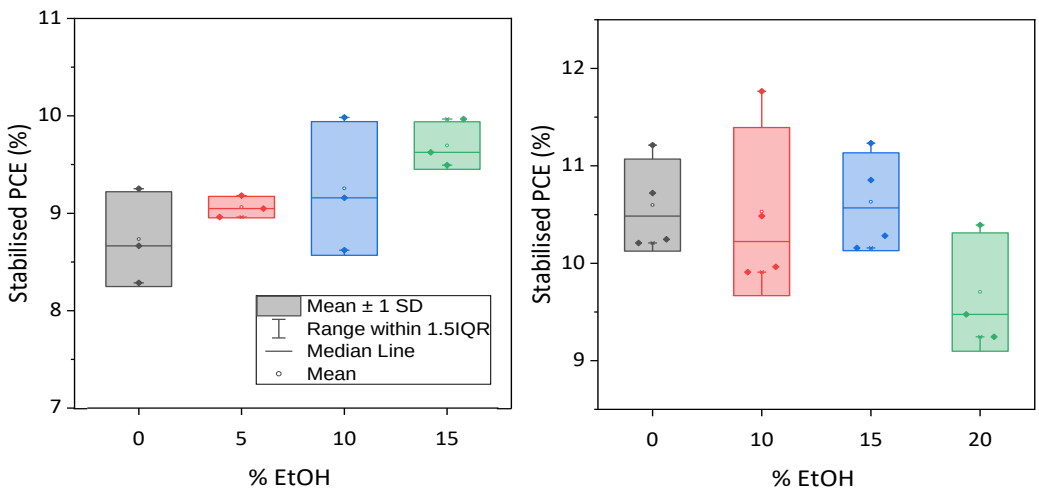

Figure 4.3: Stabilised current PCEs from two batches of devices identically fabricated with $AVA_{0.03}MAPbI_3$ devices using GVL: EtOH mixed solvents (with 0, 5, 10, 15 and 20 % EtOH as specified). 4-6 devices in each set.

Further trials were performed on both systems. However, despite having proven successful in improving device performance for GBL $AVA_{0.03}MAPbI_3$ devices, EtOH optimisation trials produced mixed results in a variety of batches (Figure 4.3).[4] No significant difference in performance was observed with EtOH addition in the second round of tests, with 10% EtOH producing a wider spread of results than the GVL-only formula and 20% resulting in an

[‡‡] Although in this example EtOH appears to outperform MeOH, this was not consistently the case due to high batch to batch EtOH variability (Figure 4.3). Examples of higher MeOH consistency and performance are shown throughout this Chapter.

average PCE drop of over 1% (Figure 4.3). Continued work therefore focused on MeOH additives, which will be the focus of the remainder of this chapter.[§§]

4.4 GVL-MeOH solvent mixing

CPSCs are unique in that precursors must percolate through over 15 µm of mesoscopic material to produce a functional device. The lack of a crystalline perovskite capping layer introduces the need for dense, high quality perovskite formation throughout the three layers: for a high performing device, consistent infiltration with minimal perovskite-free voids is essential. Precursor infiltration can be influenced by several factors, including viscosity, wetting, colloidal diameters and crystallisation dynamics.[4],[8]–[10] Observed performance enhancements with MeOH addition could therefore be a consequence of several concurrent changes in precursor behaviour. The following section will therefore examine the impact of MeOH addition on precursor viscosity, wetting, colloidal composition, and the resultant $MAPbI_3$ crystal properties before continuing to assess the impact of MeOH on device and module performance.

4.4.1 Precursor Properties and Perovskite Crystallisation

At 1.9 CP, GVL is slightly more viscous and less dense at room temperature than GBL (GBL:1/13 gcm^{-3}, GVL:1.05 gcm^{-3}). Additionally, the optimised precursor concentration of 1.1 M is higher than the 0.95 M used for standard GBL solutions (Chapter 2). This could make GVL-based precursors more sensitive to slight environmental changes during infiltration and annealing, reducing potential processing windows and overall device reproducibility.

As a low viscosity solvent (0.54 cP)[11] with high polarity, MeOH incorporation could drastically change precursor viscosity and its wetting of mesoporous oxide layers. To ascertain how GBL and GVL systems differ and examine the effect of MeOH addition, the viscosities of various GBL, GVL and GVL-MeOH mixed solutions were measured (Figure 4.4a). Additionally, contact angle analysis of different GVL-MeOH precursors on mesoporous TiO_2 was performed to investigate the impact of MeOH incorporation on electrode wetting (Figure 4.4b, c).

As shown in Figure 4.4, even 0.95 M GVL precursors were found to be over 24% more viscous than those made using GBL: the 0.95 M GVL precursor had a viscosity of 6.43 cP compared

[§§] Although in this example EtOH appears to outperform MeOH, this was not consistently the case due to high batch to batch EtOH device variability. Examples of higher MeOH consistency and performance are shown throughout this Chapter.

to 5.20 cP for GBL. The previously optimised 1.1 M GVL precursor viscosity was higher again at 7.96 cP, a more than 53% increase compared to the standard 0.95 M GBL solution. This increase could account for the higher inter-batch variation observed for GVL samples: small changes in ambient temperature, humidity or stack thickness that can impede infiltration will have a more significant impact when using highly viscous solutions. GVL-based precursors may therefore benefit more from solvent mixing than conventional GBL formulations, as such high viscosities could easily impede access to smaller pores within the stack.[12]

MeOH addition significantly reduced precursor viscosity in all samples, with a linear reduction observed up to 10% MeOH (GVL-10MeOH, Figure 4.4a). This could positively impact performance: Previous works have found that diluting GBL precursors with ethanol to reduce viscosity improves device infiltration, performance and reproducibility.[4]

a)

Solvent	[$MAPbI_3$] moldm^{-3}	Viscosity, cP (~18°C)
GBL	0.95	5.198
GVL	0.95	6.431
	1.1	7.961
5% MeOH	1.1	6.777
10% MeOH	1.1	5.809
15% MeOH	1.1	5.311

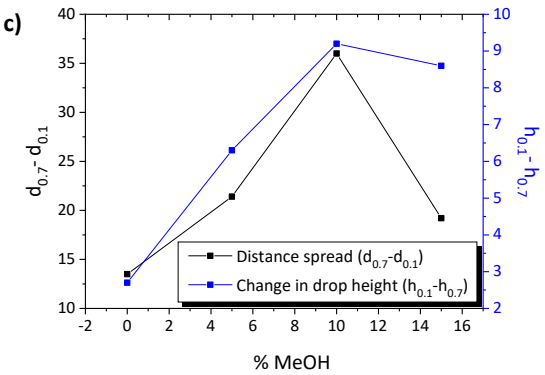

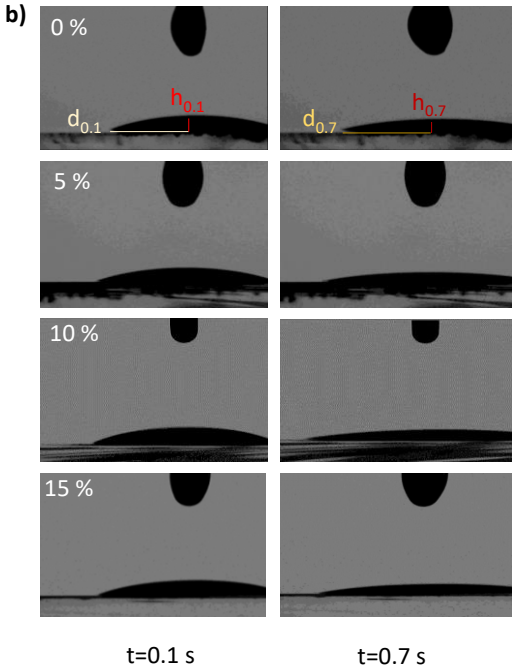

Figure 4.4: a) Viscosities of GBL, GVL and GVL-MeOH precursors at 18°C (average values from 10-12 measurements). b) GVL $AVA_{0.03}MAPbI_3$ precursors with different volume % MeOH at t=0.1 s and t=0.7 s after deposition onto TiO_2 (~800 nm). Examples of horizontal distance (d) and height (h) measurements are shown on the 0% samples. c) Δd and Δh between t=0.1 s and t=0.7 s.

The viscosity change is reflected in the contact angle analysis, where MeOH increased the rate of droplet spread and height reduction, greatly improving TiO_2 surface wetting (Figure 4.4b, c). The flatter shape of the GVL-MeOH droplets after 0.6 s could also suggest that more precursor entered the mesoporous layer in these samples. This is especially true of the 10% system (GVL-10MeOH), which exhibited the greatest change in both measures. Interestingly, increasing the solvent ratio from 10-15% MeOH had little impact on viscosity,

and the contact angle sample experienced a smaller change in droplet spread and height. As the fastest-wetting formulation, GVL-10MeOH was considered most likely to improve device infiltration. This will be compared in section 4.3.4.

Precursor viscosity clearly impacts the rate of electrode wetting. However, changing the solvent composition of a precursor can also impact crystallisation dynamics and the quality of formed perovskite.[9],[12] Less polar aprotic solvents of lower Gutman donor numbers (D_n) such as GBL or GVL coordinate less easily to Pb^{2+} centres, leading to increased Pb-I interactions, impacting perovskite crystallinity and increased chance of forming colloidal networks.[13],[14] Simply using MeOH to tune precursor viscosity to match that of standard GBL precursors may not therefore provide optimum performance. Given the insolubility of $MAPbI_3$ in MeOH, its high polarity and low boiling point, it is possible that it could have a negative influence on precursor or crystallised perovskite properties. To obtain high quality perovskite layers and devices it is therefore key to understand the influence of MeOH on solvent-Pb coordination and the properties of the annealed film.

Although GVL precursors were found not to form colloids in chapter 3, MeOH addition may change this. Lower solvent-solute coordination for MeOH systems is logical in this case, as both PbI_2 and $MAPbI_3$ are insoluble in MeOH: polar protic solvents like IPA and Ethanol are often used for chemical bath conversion of PbI_2 to $MAPbI_3$, and MeOH has been used as an antisolvent additive to improve spin coated $MAPbI_3$ crystal quality.[15]

UV-vis absorption of diluted precursors can be used to compare solvent coordination to Pb^{2+} centres, which has been shown to correlate to changes in the colloidal diameters of more concentrated solutions. Where Pb^{2+}-solvent coordination is less favourable, more I^- interact with the metal ions, increasing the relative concentration of highly coordinated iodoplumbates and changing the relative absorption intensities of solvated PbI_2, PbI_3^- and PbI_4^{2-}.[4],[13],[16] Increased relative absorption of the PbI_3^- and PbI_4^{2-} peaks have been shown to correspond with increased colloidal diameters in GBL, GBL: Ethanol and DMF: DMSO based perovskite precursors. [4],[13],[16]

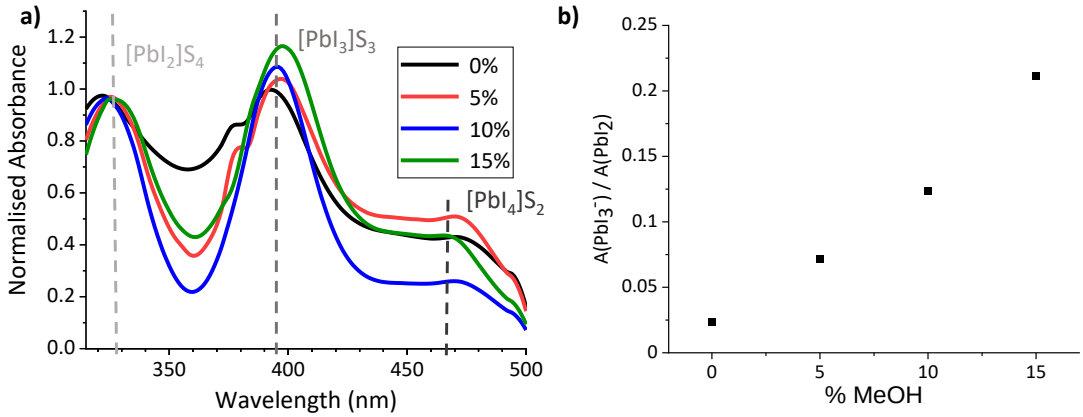

Figure 4.5: a) UV-vis absorption spectra of $AVA_{0.03}MAPbI_3$ in GVL-MeOH mixtures with 0, 5, 10 and 15% MeOH. b) Change in height ratio of the PbI_2 and PbI_3^- peaks with % MeOH. The shoulder at ~375 nm is the result of an equipment artefact.

As shown in Figure 4.5, the relative intensity of the PbI_3^- peak increased linearly with the MeOH proportion, suggesting that solvent-Pb^{2+} is indeed less favourable in the mixed systems. MeOH mixed precursors may therefore be more likely to form colloids.

The 10% precursor was thus examined for evidence of colloid formation using the Tyndall effect, as discussed in Chapter 3, Figure 3.2. Shown in Figure 4.6, this is not evident in either sample, indicating that MeOH inclusion up to 10% does not induce colloid formation. This may occur at higher ratios however, as solutions containing over 20% formed yellow precipitates during storage.

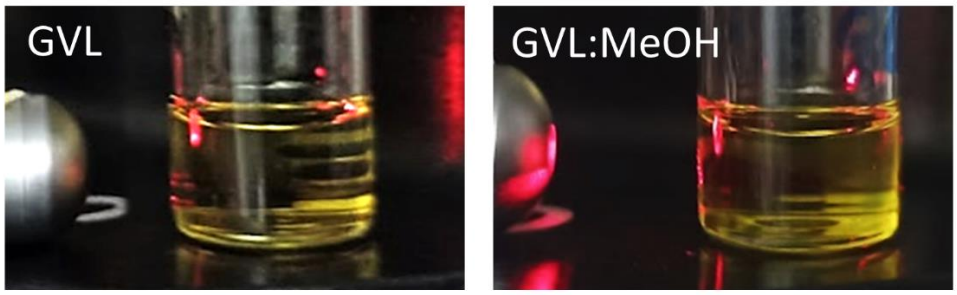

Figure 6: Photographs of GVL and GVL-10MeOH precursors examined with a laser beam for evidence of light scattering (the Tyndall effect).

Including a more volatile solvent in the precursor formulation could also induce fast nucleation of less crystalline perovskite.[8],[13],[16] Introducing volatile MeOH (b.p. 64.7°C, GVL b.p. 208°C) is likely to affect the rate of solvent removal and hence crystallisation- known to impact infiltration, grain size and crystallinity. [5], [17],[18]

To observe whether MeOH impacted crystallisation dynamics, GVL and GVL-10MeOH precursors were monitored during initial stack infiltration and annealing (Figure 4.7). Precursors were drop cast to freshly annealed stacks on an XRD thermal stage. Evolution of the 2θ =14.13° peak was then monitored using PSD fixed scans from 2θ = 13-15.26° every fifteen seconds during room temperature percolation and subsequent 45°C annealing. This can effectively monitor nucleation and the rate of crystal growth.[17]

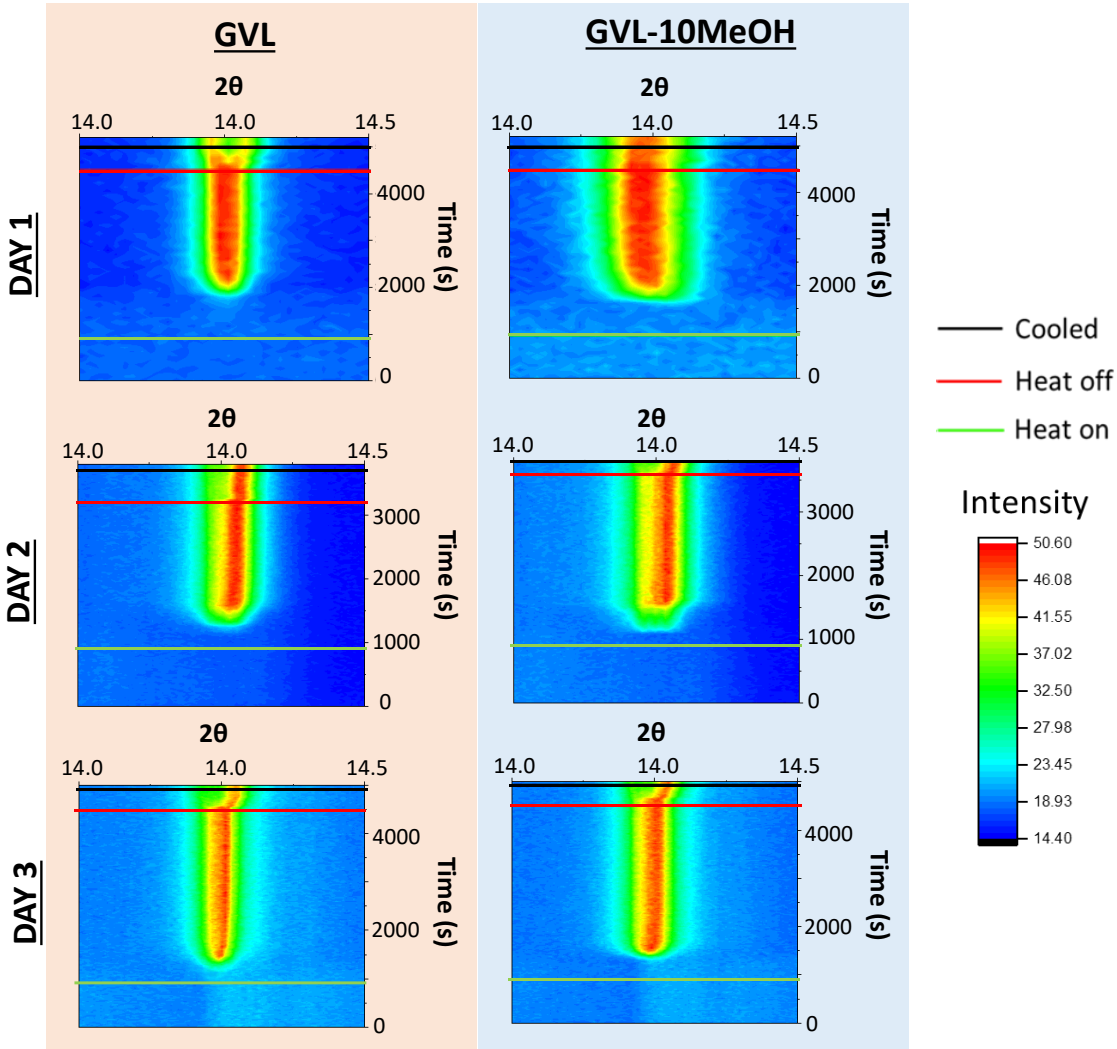

Figure 4.7: 2D contour maps and monitoring the evolution of the 2θ=14.3° peak over time during stack infiltration and annealing at 45°C of GVL and GVL-10MeOH precursors. Heat onset in green, heat removal in red and cooled sample in green. Measurements by Dr. T. Dunlop and C. Worsley, sample preparation and graphs by C. Worsley.

Slight variation in crystallisation onset time, annealing duration and peak evolution was apparent in each batch, but no consistent differences were observed between the two solvent systems (Figure 4.7). Indeed, the variation observed between batches was far greater than that observed between samples from the same testing batch, suggesting that that both

systems exhibit similar crystallisation behaviour during annealing regardless of the environmental conditions on a given day.

For example, on day 3 crystallisation onset occurred at 1174 s and 1275 s for GVL and GVL-10MeOH respectively (Figure 4.7). Samples generally formed a single peak at 2θ ≈ 14° during annealing, which separated to two overlapping peaks at 2θ ≈ 13.9° and 2θ ≈ 14.1° (Figure 4.8). This is consistent with a heat induced cubic to tetragonal phase transition, commonly observed in $MAPbI_3$ systems.[19] Interestingly, while standard γ-butyrolactone (GBL)-based precursors have been found to form stable crystallite populations during the initial infiltration and annealing stages, this was not the case for either solvent here: once initiated, crystallisation progressed rapidly to completion in both samples during all three measurements.[17]

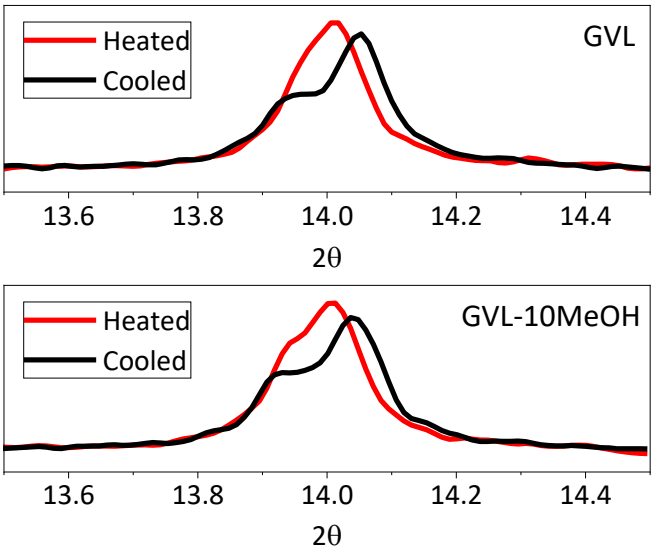

Figure 4.8: Individual plots from in-situ crystallisation monitoring XRD. Plots show the ~14° diffraction signals of $AVA_{0.03}MAPbI_3$ after complete crystallisation from GVL or GVL-10MeOH precursors, while heated (red) and after cooling to room temperature (black). Measurements by Dr. T. Dunlop and C. Worsley.

Crystallinity and orientation can be compared by analysing the relative peak breadths and intensity of XRD peaks.[20] For example, in $AVA_{0.03}MAPbI_3$ perovskites an increase in the relative intensity of the 2θ =14.13° peak indicates preferential (110) orientation, while decrease of the full width at half maximum (FWHM) occurs with improved crystallinity.[21]

XRD were therefore performed on $AVA_{0.03}MAPbI_3$ crystallised from GVL only and GVL-MeOH mixed precursors in ZrO_2 scaffolds. Mesoporous scaffolds were used over glass substrates to provide the most accurate representation of infiltrated CPSCs: precursors crystallised in the

absence of a scaffold exhibit much larger crystals and can have different morphology and orientation.

As shown in Figure 4.9a, all three MeOH samples exhibited significantly narrower peaks. MeOH incorporation therefore produces higher quality crystals during device annealing. Interestingly, the 10% samples also consistently showed a particularly intense 2D peak at ~5.8° (Figure 4.9c), although there was no significant trend observed between ~5.8° peak height and MeOH content.[***]

The increased crystallinity is likely a consequence of lower solvent-Pb^{2+} coordination leading to decreased nucleation and larger resultant crystals (Figure 4.5).[22] Such crystallinity enhancements improve device performance and stability, as crystals with fewer defects experience less carrier recombination and have fewer sites for ambient O_2 or water to bind.[23] GVL-MeOH cells may therefore exhibit superior stability to those made using GVL-only (examined in section 4.3.2).

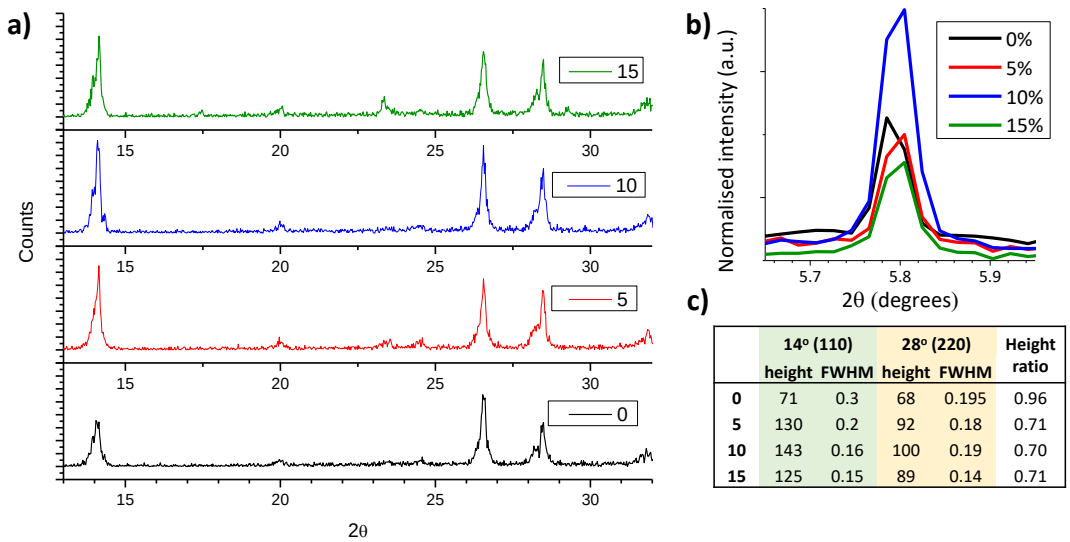

	14° (110)		28° (220)		Height ratio
	height	FWHM	height	FWHM	
0	71	0.3	68	0.195	0.96
5	130	0.2	92	0.18	0.71
10	143	0.16	100	0.19	0.70
15	125	0.15	89	0.14	0.71

Figure 4.9: a) XRD $AVA_{0.03}MAPbI_3$ annealed from different GVL-MeOH solvent mixtures in m-ZrO_2. obtained the day after fabrication. ZrO_2 signals have been removed for clarity. b) Magnified 2D peak at 5.8°, obtained 5 days after fabrication. c) Table showing peak heights, widths, and height ratios of the 14° (110) and 28° (220) signals.

A repeat measurement was performed after 5 days of ambient storage to ascertain that no significant degradation had occurred. No PbI_2 peak at ~12.5° emerged during the 5 days of ambient storage, proving that no significant degradation to PbI_2 occurred during this period.

[***] These peaks were no longer observed after changes to the solaronix ZrO_2 paste (described as a nanoparticle supplier change) and are thus not discussed in detail in this thesis.

Interestingly, the crystallinity of all four samples significantly improved: relative intensity of the 2θ =14.13° peaks increased, and the FWHMs decreased, indicating that significant crystal rearrangement occurred during this period. This will be further examined in Chapter 5.

4.3.2 Effect of MeOH on Device Performance and Stability

To determine the optimal solvent mix, $AVA_{0.03}MAPbI_3$ devices were fabricated with GVL: MeOH mixes of 0, 5, 10 and 15% MeOH. As shown in Figure 4.10, both 5 and 10% MeOH ratios improved reproducibility, with the optimal 10% (henceforth GVL-10MeOH) also improving V_{oc} and FF. GVL-10MeOH devices exhibited average V_{oc} of 0.91 V and FF of 59%, compared to 0.88 V and 50% for GVL only. Consequently, an average PCE of 12.8 ± 0.5% and champion result of 13.8% was achieved with GVL-10MeOH, compared to 11.4 ± 0.8% and 12.6% for GVL only.

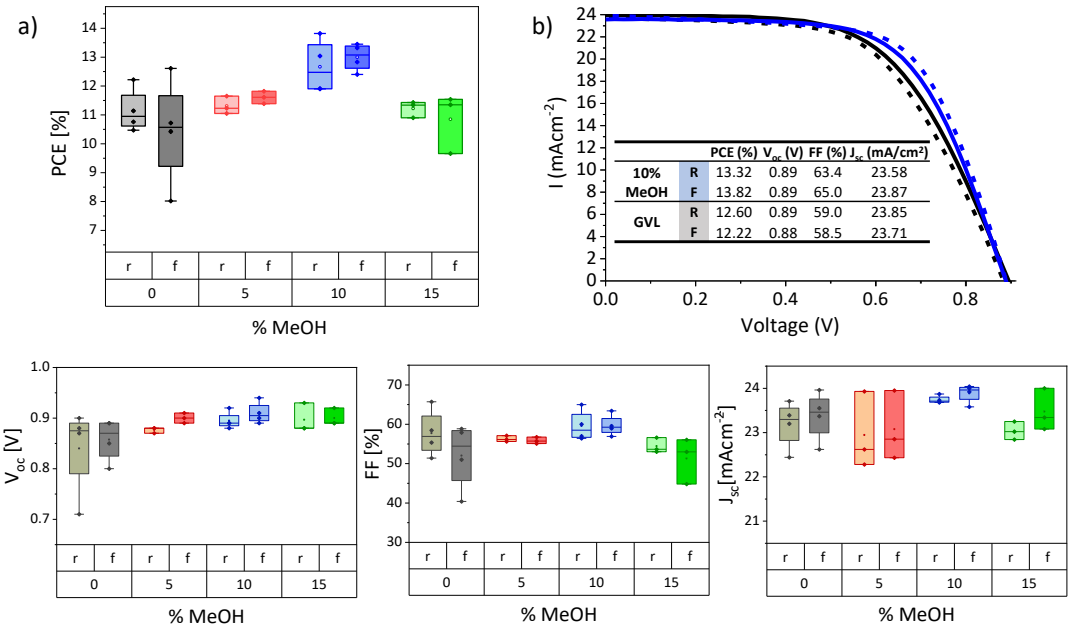

Figure 4.10: a) PV device parameters from devices made using $AVA_{0.03}MAPbI_3$ precursors in GVL with 0, 5, 10 and 15% MeOH. Four devices in each set. b) IV curves of the champion GVL-10MeOH and GVL only devices with inlaid table showing IV parameters.

It should be noted that although the hysteresis in this set flipped with MeOH addition, this was not the case in all batches. Similarly, although reverse PCE in GVL only devices are most often higher than the forward, this was not always the case. Differences in hysteresis between batches could have many contributing causes- for example, slight variations in layer

thicknesses, roughness and perovskite infiltration. Optimisation tests should therefore always be carried out using devices from the same printing batches to minimise printing-associated device variation. Stabilised PCEs should also be obtained, as significant hysteresis can mask trends in device performance.

Average stabilised current data for the best performing batch is presented in Figure 4.11b. These results produced a much clearer trend, confirming that the GVL-10MeOH devices exhibited significantly enhanced performance. The stabilised current results for several different batches were also normalised, with the resultant plot presented in Figure 4.11a. It is clear from the normalised plot that the trend was reproducible between batches, and that the GVL-10MeOH mix produced both the highest performing devices and the most consistent result spread.

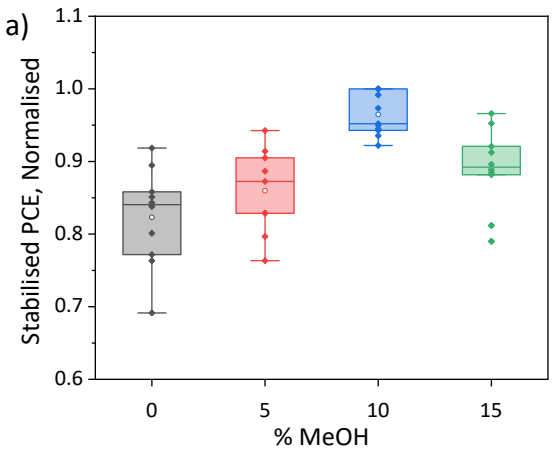

b)

% MeOH	Mean Stabilised PCE (%)
0	9.60 ± 0.53
5	9.76 ± 0.46
10	11.50 ± 0.45
15	10.36 ± 0.67

Figure 4.11: a) Box plot of normalised stabilised current data from 3 batches (10-12 devices for each %), d) Table showing average stabilised current data obtained from the highest performing batch (four samples for each %)

Improvements in V_{oc} with MeOH addition contributed significantly to performance enhancements. However, unlike J_{sc} and FF improvements, these increases are unlikely to be a consequence of improved infiltration. Instead, this is likely caused by the improved perovskite quality observed in section 4.3.1.[23]

One of the major advantages of CPSCs is their inherent stability. GBL-based precursors have been used to produce CPSCs with predicted stability of >20 years under accelerated testing conditions.[24] GVL-only devices were shown to have comparable unencapsulated stability to GBL cells in Chapter 3. Any new solvent systems must therefore produce similarly stable devices to be considered a viable alternative.[25]

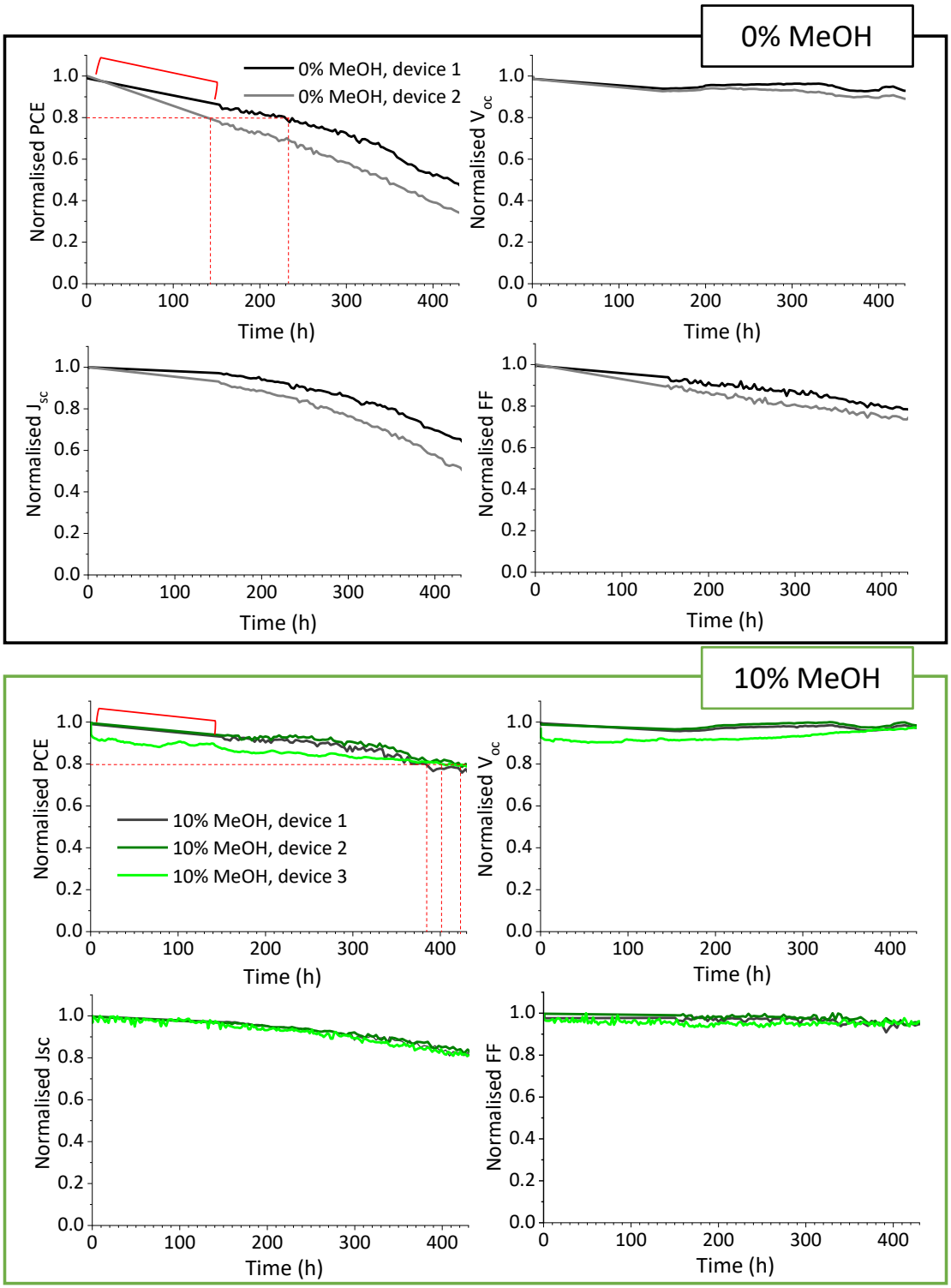

Figure 4.12: Normalised PV parameters of two GVL and three GVL-10MeOH devices (unencapsulated) over 430 hours, held at V_{oc} under AM1.5 at 50°C in ambient conditions and tested every four hours. The red bracket highlights extrapolated data between hours 12 and 136, where a software glitch prevented data collection. Red dashes highlight device T80 lifetimes.

Figure 4.12 shows the performance over time of unencapsulated GVL and GVL-10MeOH devices placed under AM 1.5 illumination, at 50°C and ambient humidity, held at V_{oc} and tested every four hours. All three GVL-10MeOH devices significantly outperformed the GVL controls, with the best performing device demonstrating a T80 of over 420 hours. Another device maintained 75% of initial PCE even after 500 h exposure in these conditions. Performance loss was due to a gradual J_{sc} decrease in all cases. Conversely, the GVL-only devices exhibited a maximum T80 of ~230 hours and experienced more significant FF and J_{sc} losses over the measurement period.

Such enhanced stability can be a consequence of multiple factors. Better infiltration of MeOH precursors produces fewer voids within the stack, helping limit moisture and O_2 access and preventing the escape of volatile MA species at temperature.[5] The more oriented growth observed in Figure 4.9 is indicative higher quality perovskite. This may also contribute to stability improvements: more crystalline perovskite grains with fewer defects can enhance device lifetime through decreasing trap density and providing fewer sites for degradation.[8]

These stability enhancements, coupled with the improvements in device performance make GVL-10MeOH precursors a superior candidate for scale-up than GVL-only systems. However, precursor stability is also an important consideration: any commercial precursors should ideally be stable in ambient storage to minimise storage costs. Any mixed solvent system should ideally exhibit similar stability to GVL under ambient storage to be considered a commercially viable alternative. As both GVL and MeOH are hygroscopic solvents, precursors could feasibly incorporate some ambient water over time, as well as undergoing degradation processes such as I_2 formation during storage. In a lab environment, CPSC precursors are generally made in small volumes and used within 3 days, which does not represent what would occur during large-scale production.

A long-term experiment was therefore performed, wherein devices from the same printing batch were periodically annealed and infiltrated with the same batch of 1.1 M GVL only or GVL-10MeOH precursor over a period of several weeks. Precursors were stored in sealed vials in ambient conditions between uses (18-19°C, 30-40% RH).

As presented in Figure 4.13, no significant change in device performance was observed over time for either precursor, with no significant performance change in any photovoltaic parameter over time in either case. Additionally, the champion performance for each precursor was achieved after 17 and 24 days storage for the GVL-10MeOH and GVL only

solutions respectively. Both precursor formulations were stable towards room temperature precipitation during storage. This would be beneficial in a commercial setting and represents a significant advantage of these formulations over conventional GBL solutions.

Figure 4.13: PV parameters of GVL or GVL-10MeOH devices from the same printing batch fabricated over a period of 24 days. Device performance is below that of champion sets as stacks contained sub-optimally thin ZrO_2 due to a change in paste formulation (discussed in Chapter 6). 5-6 devices in each batch.

It should be noted that these devices underperform compared to the previously presented champion sets as they were obtained using stacks with sub-optimal ZrO_2 thickness. A change in ink formulations by Solaronix resulted in layers of below 1 µm (optimal ~2 µm), which in turn impacted performance by decreasing J_{sc} and V_{oc} values. This will be discussed in Chapter 5.

4.3.3 Examining device infiltration

The device and module data presented in sections 4.3.2 and 4.3.4 show significant performance enhancements with the use of GVL-10MeOH precursors. These improvements are down to consistent FF improvement with MeOH addition. Devices also exhibited improvements in average V_{oc} and current reproducibility. Concurrent FF and J_{sc} improvements are suggestive of improved perovskite-electrode contact due to superior infiltration, whereas V_{oc} enhancements are likely due to the increased perovskite crystallinity observed in section 4.3.1.

To visually gauge the quality of infiltration, devices were optically examined and cross sectional SEM images taken (Figures 4.14, 4.15). Optical examination can be used for comparing infiltration and identifying large uninfiltrated µm-scale defects at the base of the TiO_2 layer,[†††] while cross sectional imaging can show nanometre vacancies and the extent of perovskite filling deeper within the stack.[5] As printing defects or thickness changes can significantly impact infiltration, devices were compared within the same printing batch to maintain similarity between stacks.

[†††] This method is introduced and discussed in detail in Chapter 6.

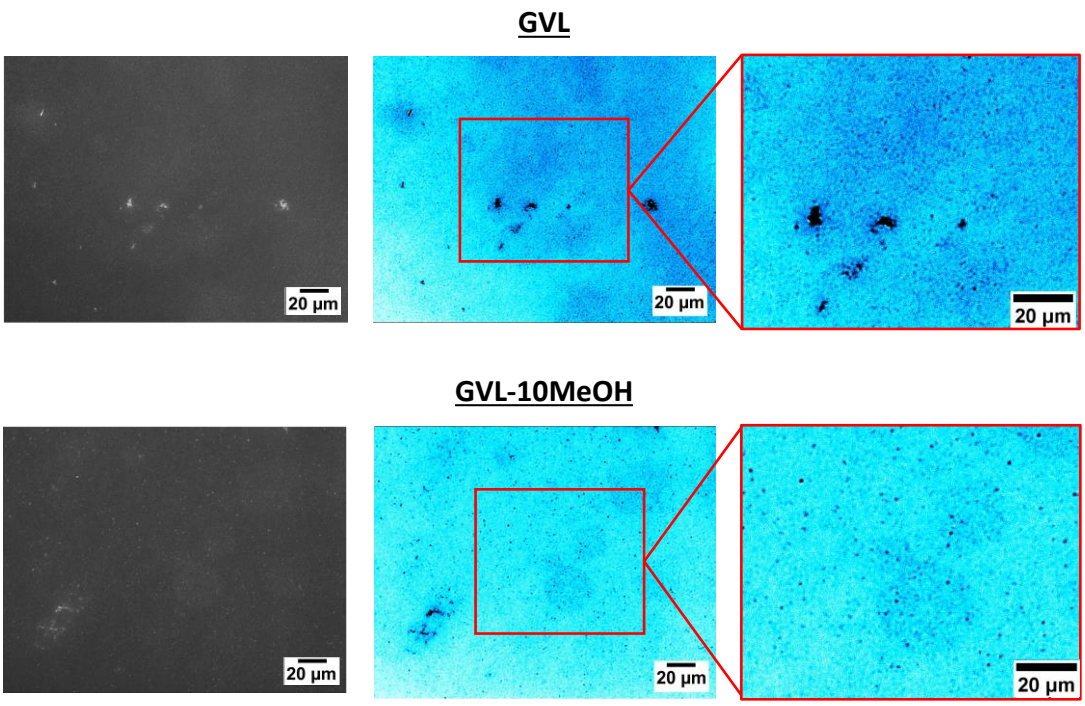

Figure 4.14: Optical images of the infiltrated TiO_2 layer in devices prepared with GVL only and GVL-10MeOH precursors. Blue images more clearly show the differences in infiltration between the two samples, with darker colour representing areas of poor infiltration. Optical images obtained by Dr. T. Dunlop, editing and sample preparation by C.Worsley.

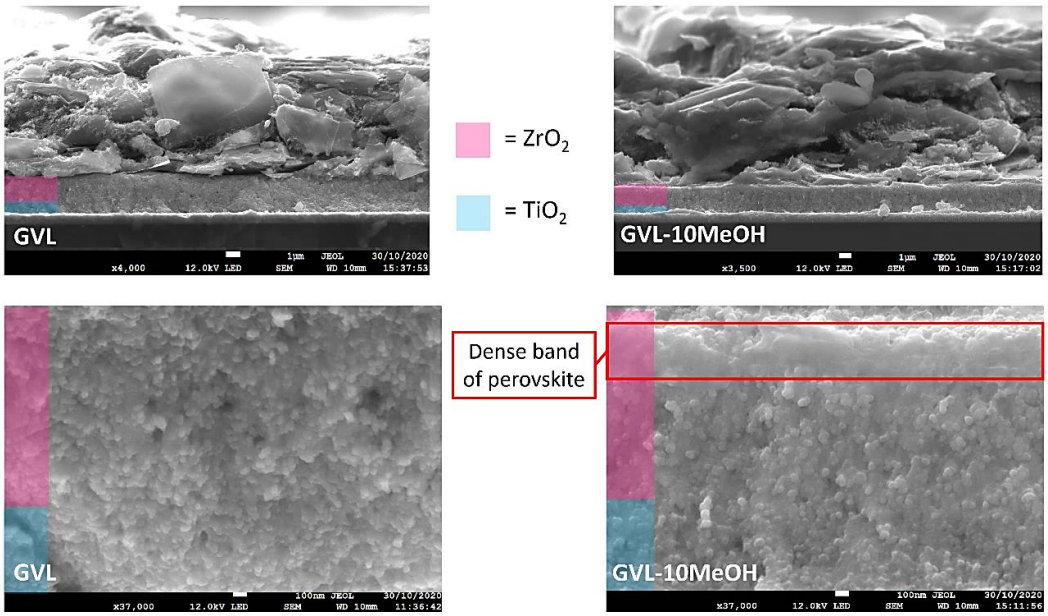

Figure 4.15: a) Cross sectional images of devices made using GVL only or GVL-10MeOH. A dense band of perovskite is present at the ZrO_2/C interface in the 10% samples (red box)

As shown in Figure 4.14, GVL-10MeOH devices present as darker and more even under optical examination, with fewer uninfiltrated µm-scale defects when compared with GVL only cells. Such large defects are commonly caused by large horizontal graphite flakes in the carbon electrode, which block precursor from accessing the underlying stack.[5] Alternatively, printing flaws such as mesh marks or bubbles can also cause such artefacts. The lower viscosity and increased TiO_2 wetting of GVL-10MeOH precursors may facilitate filling of such areas during percolation time, resulting in fewer, smaller perovskite-free voids.

Cross sectional imaging showed some areas with perovskite-free holes of similar size and distribution in both samples (Figure 4.15). However, a dense band of perovskite at the ZrO_2/carbon interface was present in the GVL-10MeOH samples, and GVL-10MeOH presented some areas of particularly dense ZrO_2 and TiO_2 infiltration (Figure 4.15). This could be due to the improved wetting of GVL-MeOH precursors observed in Figure 4.3 and could improve devices by improving absorption of long-wave (~500-600nm) light deep in the ZrO_2 layer, as well as increasing contact and charge extraction at the ZrO_2/C interface.[31] These, along with the areas of dense infiltration and improved electrode contact could explain the observed FF improvements in GVL-10MeOH samples.

The infiltration of GVL-10MeOH precursors is clearly superior to GVL-only formulations. However, infiltration is not the sole factor in determining device performance. The quality of perovskite deep within the stack also plays an important role. This can be examined through PL mapping: comparing the variation and intensity of PL signals across a given area can provide information on both infiltration and perovskite crystal quality.[5]

In other architectures, standard steady state photoluminescence (SSPL) is more commonly applied to compare perovskite quality. However, in the case of CPSCs, mapping provides a more accurate representation of PL as peak positions and signal intensity can vary over the device area due to incomplete infiltration. Therefore, values obtained using SSPL do not necessarily provide a good representation of the sample, and unless the SSPL intensities of two infiltrated mesoscopic samples are extremely different, maps or multiple measurements should be obtained.

Different information may be extracted depending on the mesoscopic scaffold used in sample preparation. For example, in electron extracting TiO_2 layers, PL intensity is reduced and red shifted in areas of good infiltration due to improved charge extraction. Peak shifting and reduction may therefore be linked to areas of improved perovskite-TiO_2 contact. Conversely, in inert ZrO_2 layers increased PL intensities are found in well infiltrated areas, and

areas of significant peak shifting and photodarkening can correspond to poor perovskite crystal quality. In ZrO_2 scaffolds, areas with reduced PL can therefore be indicative of either infiltration or, when accompanied by significant blue-shift and photodarkening, poor crystal quality.[5],[26]

Although the XRD measurements presented in section 4.3.1 show improved crystallinity in ZrO_2 scaffolds, they only probe the quality of crystals near the scaffold surface. PL mapping of samples from the glass substrate side allows for comparison of crystal quality at the base of the stack. To compare the and infiltration and perovskite quality of GVL-only and GVL-10MeOH precursors at the base of the mesoporous scaffolds, ZrO_2/Carbon layers on glass were prepared and infiltrated for PL mapping.

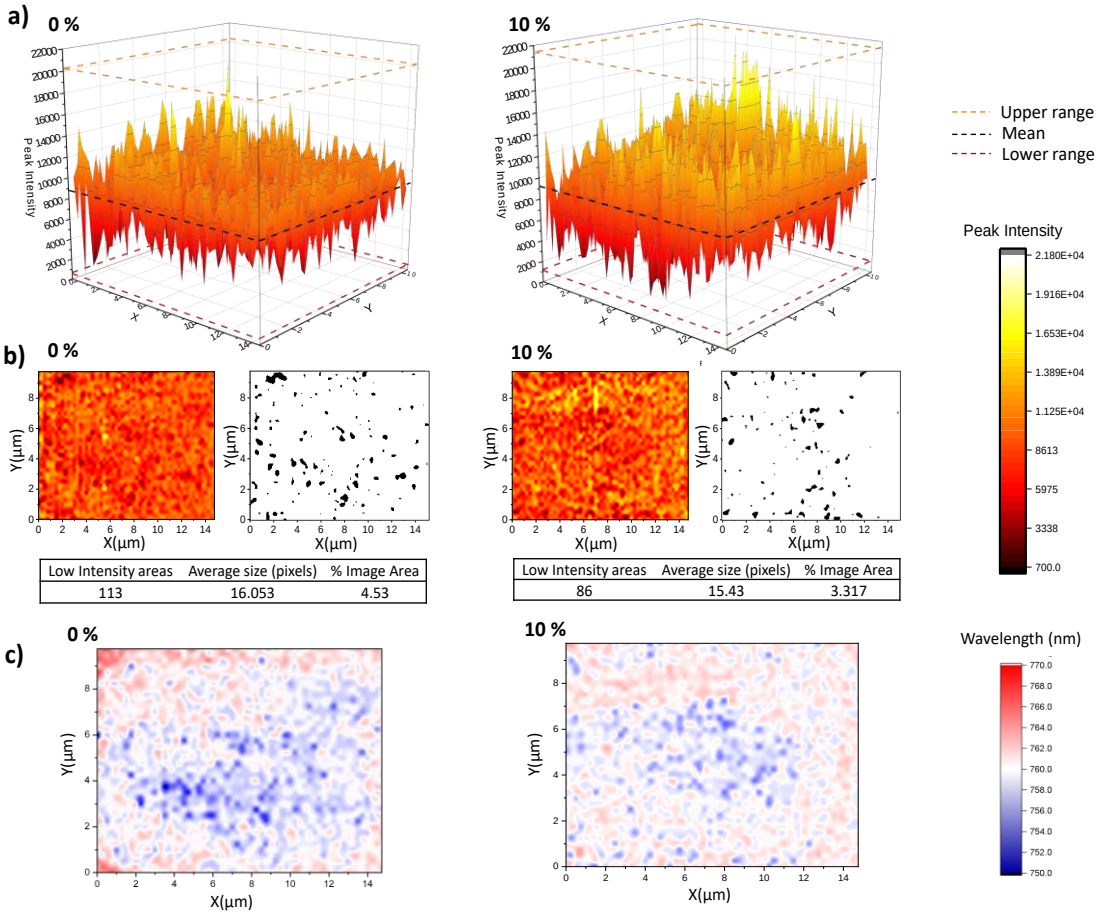

Figure 4.16: a) 200 µm² 3D PL intensity maps of $AVA_{0.03}MAPbI_3$ in m-ZrO_2 from GVL only and GVL-10MeOH. Pixel size 0.083 µm². b) 2D maps, with monochrome images highlighting pixels in the bottom 10% of the intensity range. Tables detail quantity, mean size and % coverage of low intensity regions, c) 2D maps of PL peak shifting. Measurements by R. Patidar, sample preparation and data analysis by C. Worsley.

As shown in Figure 4.16, the GVL-10MeOH sample exhibited a greater proportion of high intensity areas and fewer areas in the bottom 10% of the range. The decrease in the number and range of low intensity areas is evidence for superior infiltration at the base of the GVL-10MeOH infiltrated stacks. Additionally, the increased incidence of highly emissive areas suggests that the GVL-10MeOH precursors are forming higher quality perovskite.

This is corroborated when considering the peak position maps, where the GVL-10MeOH samples exhibit less peak shifting over the measured area. Compared to the GVL-10MeOH case, the GVL only maps show a much greater range in peak shifts with a larger proportion of peaks moving to lower wavelengths. Such shifts have been associated with poorer crystal quality and correspondingly higher defect concentrations, which introduce shallow traps near the band edge.[26],[27]

These results confirm that GVL-10MeOH precursors produce better infiltrated perovskite layers of improved crystallinity: The decrease in the number of low intensity areas is typical of more consistent infiltration, while the increased frequency of high intensity areas and decreased peak shifting are suggestive of improved crystal quality.[5],[27]

Improved infiltration can also impact EQE and EIS measurements. Improved infiltration results in enhanced perovskite-TiO_2 contact, which can causes greater charge accumulation in the electrode and resultant increases in measured charge at each given V_{oc} during EIS-although it should be noted that in the absence of improved device performance and PL increases this can also be indicative of increased trap density.[28]–[30] EQE increases in the 300-450 nm range can be linked to improved infiltration at the base of the stack, as this is where the majority of short wavelength light is absorbed in CPSCs.[31] These analyses were therefore performed on devices infiltrated with GVL and GVL-MeOH mixed $AVA_{0.03}MAPbI_3$ precursors.

Shown in Figure 4.17, EQE increased in the 300-450 nm range for all the MeOH mixed samples, especially once MeOH content exceeded 5%.

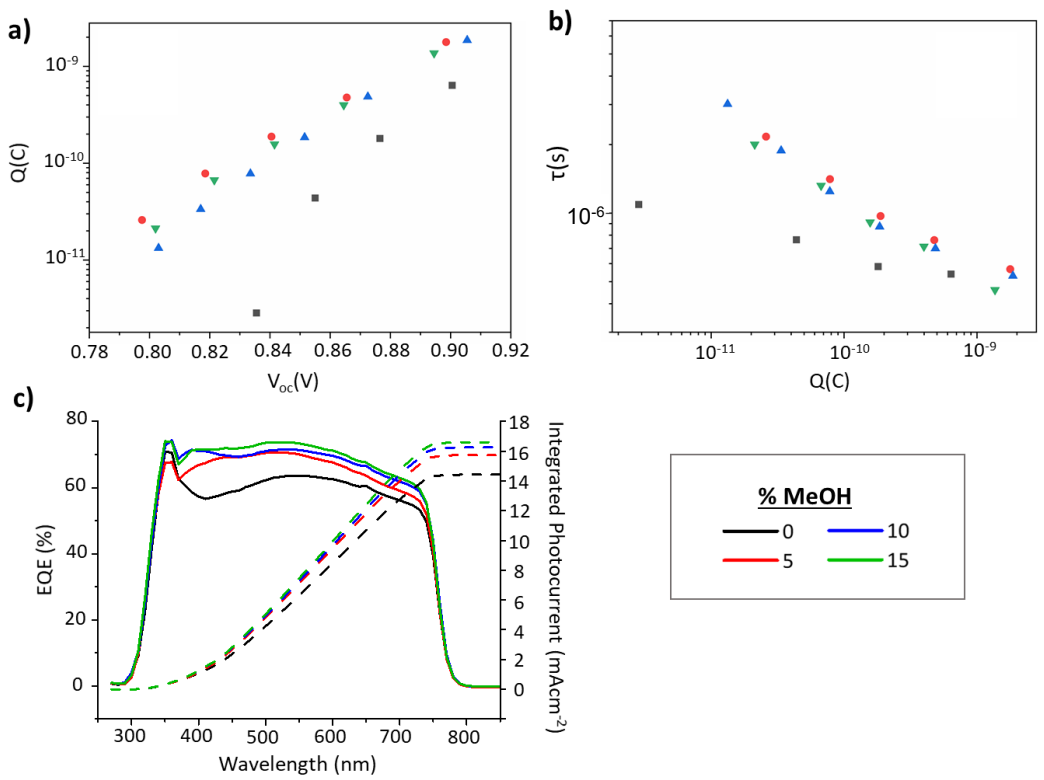

Figure 4.17: a) Variance in measured charge with applied voltage for GVL and GVL-MeOH devices, obtained from EIS measurement b) EIS data showing variance of carrier lifetime with Q, c) EQE plots from the highest performing device from each MeOH %. EIS by Dr. A. Pockett. EQE and sample preparation by C. Worsley.

EIS measurements revealed increased charge accumulation in MeOH samples, which can be linked to improved charge extraction due to increased perovskite-TiO_2 contact. This was observed as a clear increase in the chemical capacitance for GVL-MeOH devices. Many reports have shown that a chemical capacitance related to photogenerated charge accumulation is not commonly observed in perovskite devices.[28]–[30] The presence of such a capacitance in these devices suggests charge is more efficiently injected into the TiO_2, in which charges accumulate. Although such accumulation can also be indicative of increased trap density this was considered unlikely as MeOH samples also exhibited significantly increased charge carrier lifetimes. Coupled with increased PL intensity and more oriented crystal growth, this enhanced carrier lifetime suggests that the MeOH precursors form devices with higher quality perovskites of lower trap density. It could also contribute to the observed V_{oc} enhancements.

4.3.4 Application of GVL-10MeOH precursors to modules

Infiltration inconsistencies can result in significant performance loss on device scale-up, introducing poorly conductive areas of high recombination. For a stable, high-performance module, all contributing devices must exhibit consistently high PCE across the active area. GVL precursors have already been proven superior to GBL for large-scale 220 cm^2 module fabrication (Chapter 3), producing more consistent performance data and highly reproducible infiltration across large areas. Previous published works have cited a champion PCE of 6.6% for scribed modules of this size using GBL precursors, while GVL precursors produced modules of over 8% PCE.[32]

The performance enhancements observed with GVL in the previous chapter were due to enhanced infiltration over large areas. Consequently, the improved infiltration and enhanced reproducibility of small scale GVL-10MeOH devices compared to GVL could translate to further improvements at scale. GVL only and GVL-10MeOH precursors were therefore used to infiltrate 220 cm^2 active area modules (fabricated by screen printing and scribing method).[32],[33]

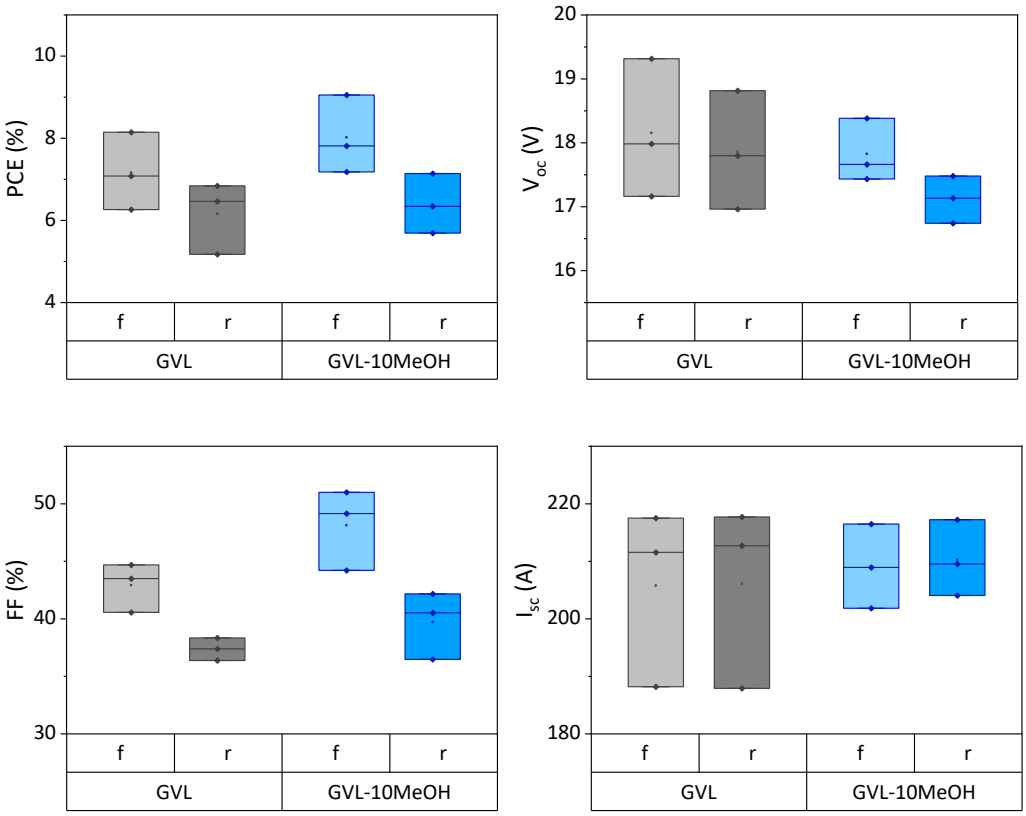

Figure 4.18: Box plots of photovoltaic parameters of 220 cm^2 modules fabricated via a scribing method using GBL or GVL $AVA_{0.03}MAPbI_3$ precursors. Three modules tested for each solvent.

As shown in Figure 4.18, both GVL-only and GVL-10MeOH precursors performed well, achieving champion PCEs of 8.14% and 9.05% respectively (Figure 4.19). GVL-10MeOH modules also performed better across the batch, exhibiting an average PCE of 8.1 ± 0.95% compared to 6.73 ± 0.42% for the GVL only system. Performance enhancement is mostly due to a large improvement in the FF of GVL-10MeOH modules, which rose from 44.7% with GVL only to 51.0% in the GVL-10MeOH system. This is likely a consequence of better, more reproducible infiltration across the active area leading to improved perovskite-electrode contact and better charge extraction.

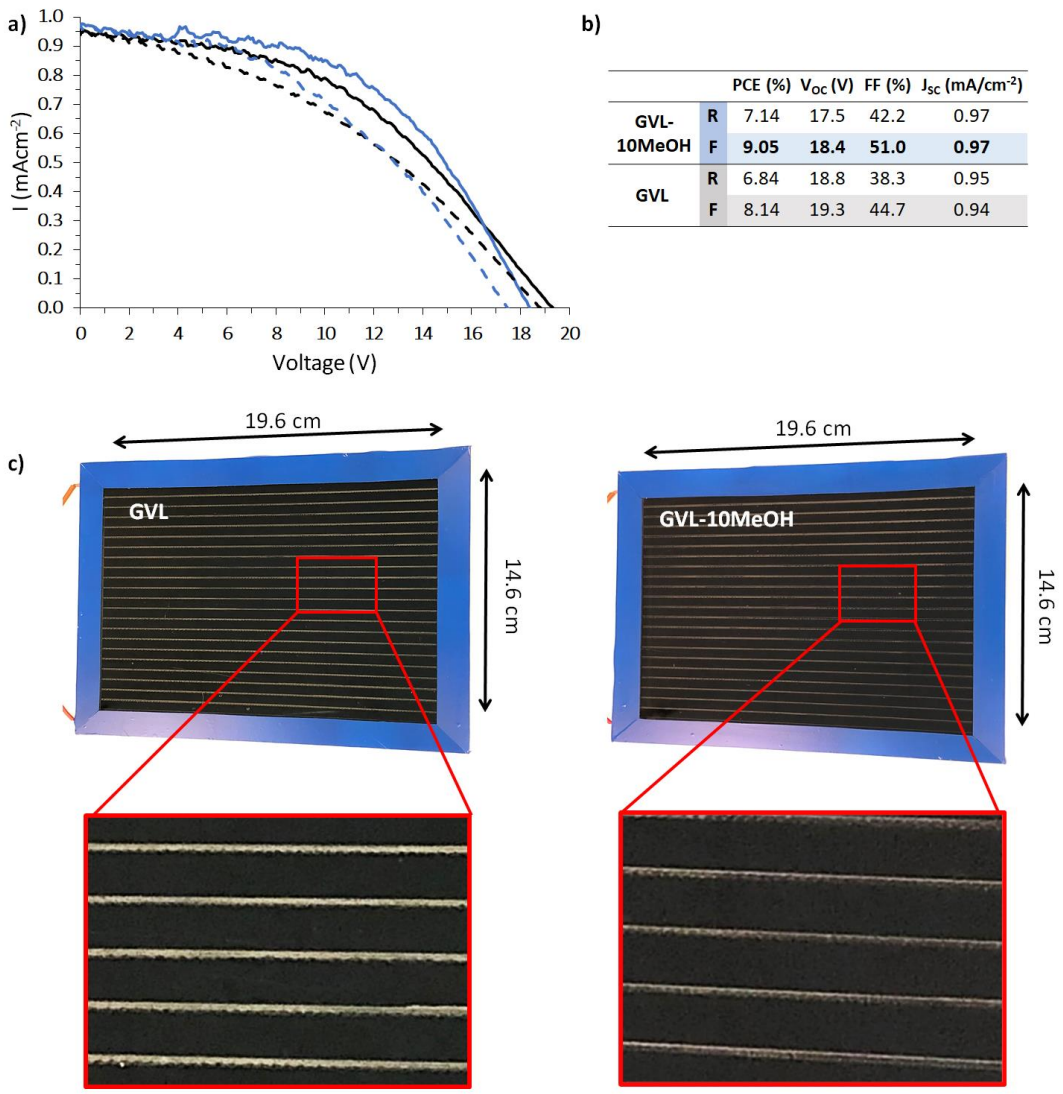

		PCE (%)	V_{OC} (V)	FF (%)	J_{SC} (mA/cm^{-2})
GVL-10MeOH	R	7.14	17.5	42.2	0.97
	F	**9.05**	**18.4**	**51.0**	**0.97**
GVL	R	6.84	18.8	38.3	0.95
	F	8.14	19.3	44.7	0.94

Figure 4.19: a) IV curves of modules fabricated with GVL only and GVL-10MeOH precursors, b) table showing measured photovoltaic parameters, c) Photograph of the GVL-10MeOH module with dimensions labelled. Close up sections to compare visual infiltration quality. Module preparation and testing by Dr. R. Bolton and Dr. S. Potts.

The improved performance of these systems later enabled successful infiltration of even larger modules, with 517.7 cm^2 active area and 80% geometric fill factor (Figure 4.19). Limited by the capability of available equipment, these devices were not tested using a solar simulator, and instead encapsulated and placed for outdoor IV testing with an accompanying pyranometer (Figure 4.20). Six modules were encapsulated and placed outdoors, where they were IV tested every 5 minutes during daylight hours.

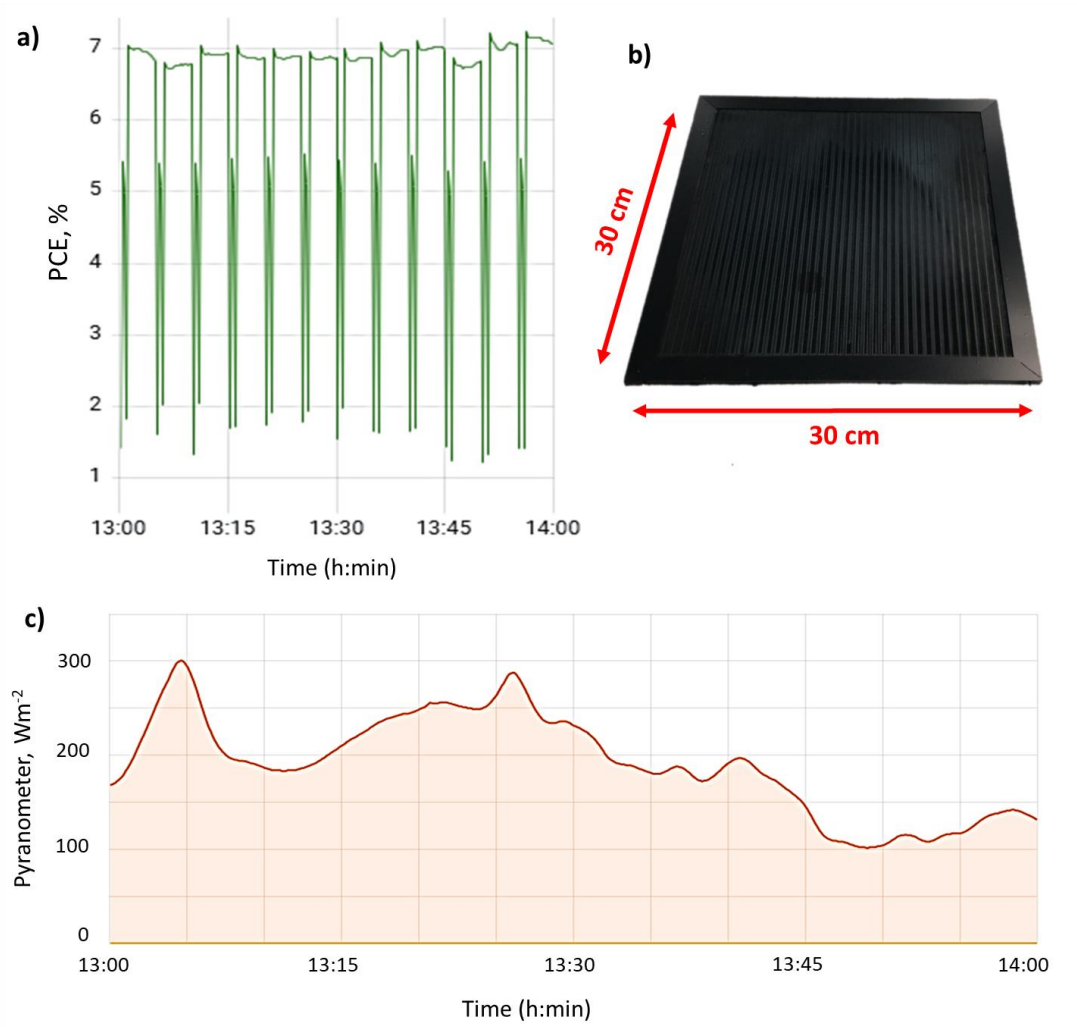

Figure 4.20: a) PCE data from outdoor testing of a 517.7 cm^2 active area encapsulated module (depicted in b), fabricated by Dr R. Bolton). Relevant pyranometer data from the same period in c). Data from mid-May 2022, modules

The data presented in Figure 4.20 is from a module after four months of continuous testing and outdoor exposure (method outlined in Chapter 2). Performance did not decrease significantly during this time, indicating that the modules are stable under operating conditions. It should be noted that these modules were part of an initial trial fabrication.

With further process optimisation, it is likely that power output and PCE will increase. Nevertheless, this result proves that GVL-10MeOH precursor is suited for large-scale fabrication.

4.4 Conclusions

Printable $AVA_{0.03}$-$MAPbI_3$ CPSCs are frequently cited as the most commercially viable perovskite architecture. Previous work has presented GVL as a non-toxic green solvent for CPSC fabrication. However, GVL precursors are much more viscous than standard GBL formulations, which can limit device infiltration.

In this work, methanol (MeOH) is used as a solvent additive to improve the performance and reproducibility of GVL-based $AVA_{0.03}MAPbI_3$ precursors. To maintain the advantages of GVL, any solvent additions to GVL-based precursors should be similarly sustainable and present a relatively low toxicity risk. MeOH fits this profile and is sustainable and already mass-produced at low cost.

An optimised MeOH proportion of 10% is found to reduce precursor viscosity and improve wetting, as well as promoting more oriented perovskite growth and higher quality absorber layers. Precursors incorporating 10% MeOH are found to enhance reproducibility and performance, achieving a champion PCE of 13.82% in a 1 cm^2 device and 9.05% in a 220 cm^2 module fabricated in ambient conditions. This represents a significant improvement compared to GVL-only systems, which produced a champion module of 8.12% PCE. These results confirm that green GVL-10MeOH precursors are well-suited to scale-up and proves that these green systems are a viable for CPSC module production.

Stability is also improved, with an unencapsulated MeOH device exhibiting a T80 of >420 hours at 50°C in ambient humidity under AM1.5 illumination, nearly twice that of the best GVL device. The precursors are found to be stable towards room temperature precipitation and produce consistent devices over a month of storage. This would be highly advantageous in an industrial setting, preventing equipment blockages and ensuring reproducible performance over time.

This work builds on that presented in Chapter 3, improving upon the performance and stability of devices made using green GVL-based precursors and providing an example of how green solvent engineering can be applied in the development and amelioration of novel renewable technologies.

However, although reproducibility and performance have been improved, significant inter-batch performance and infiltration variation was still observed. The following Chapters will more closely examine performance evolution during the week following fabrication, and the factors influencing infiltration in these devices.

4.7 References

[1] GVL MSDS, https://www.sigmaaldrich.com/MSDS/MSDS/DisplayMSDSPage.do?country=GB&language=en&productNumber=V403, (accessed 14 January 2021)

[2] GBL MSDS - B103608, https://www.sigmaaldrich.com/MSDS/MSDS/DisplayMSDSPage.do?country=GB&language=en&productNumber=B103608, (accessed 16 March 2020)

[3] MSDS - 227056, https://www.sigmaaldrich.com/MSDS/MSDS/DisplayMSDSPage.do?country=GB&language=en&productNumber=227056, (accessed 16 March 2020)

[4] Y. Ming, M. Xu, S. Liu, D. Li, Q. Wang, X. Hou, Y. Hu, Y. Rong and H. Han, *J. Power Sources*, 2019, **424**, 261–267

[5] H. Lakhiani, T. Dunlop, F. De Rossi, S. Dimitrov, R. Kerremans, C. Charbonneau, T. Watson, J. Barbé and W. C. Tsoi, *Adv. Funct. Mater.*, 2019, **243**, 1900885

[6] F. Kerkel, M. Markiewicz, S. Stolte, E. Müller and W. Kunz, *Green Chem.*, 2021, **23**, 2962–2976

[7] Y. K. Ren, S. D. Liu, B. Duan, Y. F. Xu, Z. Q. Li, Y. Huang, L. H. Hu, J. Zhu and S. Y. Dai, *J. Alloys Compd.*, 2017, **705**, 205–210

[8] J. Kim, B. W. Park, J. Baek, J. S. Yun, H. W. Kwon, J. Seidel, H. Min, S. Coelho, S. Lim, S. Huang, K. Gaus, M. A. Green, T. J. Shin, A. W. Y. Ho-Baillie, M. G. Kim and S. Il Seok, *J. Am. Chem. Soc.*, 2020, **142**, 6251–6260

[9] M. Xu, W. Ji, Y. Sheng, Y. Wu, H. Cheng, J. Meng, Z. Yan, J. Xu, A. Mei, Y. Hu, Y. Rong and H. Han, *Nano Energy*, 2020, **74**, 104842

[10] S. M. P. Meroni, C. Worsley, D. Raptis and T. M. Watson, *Energies*, 2021, **14**, 386

[11] MeOH MSDS - 322415, https://www.sigmaaldrich.com/MSDS/MSDS/DisplayMSDSPage.do?country=GB&language=en&productNumber=322415, (accessed 8 April 2021)

[12] S. M. P. Meroni, Y. Mouhamad, F. De Rossi, A. Pockett, J. Baker, R. Escalante, J. Searle, M. J. Carnie, E. Jewell, G. Oskam and T. M. Watson, *Sci. Technol. Adv. Mater.*, 2018, **19**, 1–9

[13] J. C. Hamill, J. Schwartz and Y.-L. Loo, *ACS Energy Lett.*, 2018, **3**, 92–97

[14] A. Kumar, A. Sharma, B. G. de la Torre and F. Albericio, *Molecules*, 2019, **24**, 4004

[15] F. Yang, M. A. Kamarudin, P. Zhang, G. Kapil, T. Ma and S. Hayase, *ChemSusChem*, 2018, **11**, 2348–2357

[16] K. Yan, M. Long, T. Zhang, Z. Wei, H. Chen, S. Yang and J. Xu, *J. Am. Chem. Soc.*, 2015, **137**, 4460–4468

[17] O. Filonik, M. E. Thordardottir, J. Lebert, S. Pröller, S. Weiß, L. J. Haur, A. Priyadarshi, P. Fontaine, P. Müller-Buschbaum, N. Mathews and E. M. Herzig, *Energy Technol.*, 2019, **7**, 1900343

[18] P. P. Khlyabich and Y.-L. Loo, *Chem. Mater.*, 2016, **28**, 9041–9048

[19] P. S. Whitfield, N. Herron, W. E. Guise, K. Page, Y. Q. Cheng, I. Milas and M. K. Crawford, *Sci. Rep.*, 2016, **6**, 1–16

[20] T. Du, J. Kim, J. Ngiam, S. Xu, P. R. F. Barnes, J. R. Durrant and M. A. McLachlan, *Adv. Funct. Mater.*, 2018, **28**, 1801808

[21] G. Grancini, C. Roldán-Carmona, I. Zimmermann, E. Mosconi, X. Lee, D. Martineau, S. Narbey, F. Oswald, F. De Angelis, M. Graetzel and M. K. Nazeeruddin, *Nat. Commun.*, 2017, **8**, 15684

[22] K. Yan, M. Long, T. Zhang, Z. Wei, H. Chen, S. Yang and J. Xu, *J. Am. Chem. Soc.*, 2015, **137**, 4460–4468

[23] W. Rehman, D. P. McMeekin, J. B. Patel, R. L. Milot, M. B. Johnston, H. J. Snaith and L. M. Herz, *Energy Environ. Sci.*, 2017, **10**, 361–369

[24] E. Kobayashi, R. Tsuji, D. Martineau, A. Hinsch and S. Ito, *Cell Reports Phys. Sci.*, 2021, **2**, 100648

[25] C. Worsley, D. Raptis, S. Meroni, A. Doolin, R. Garcia, M. Davies and T. Watson, *Energy Technol.*, 2021, **9**,202100312

[26] K. P. Goetz, A. D. Taylor, F. Paulus and Y. Vaynzof, *Adv. Funct. Mater.*, 2020, **30**, 1910004

[27] E. V. Péan, C. S. De Castro and M. L. Davies, *Mater. Lett.*, 2019, **243**, 191–194

[28] A. Pockett, G. E. Eperon, T. Peltola, H. J. Snaith, A. Walker, L. M. Peter and P. J. Cameron, *J. Phys. Chem. C*, 2015, **119**, 3456–3465

[29] A. Guerrero, G. Garcia-Belmonte, I. Mora-Sero, J. Bisquert, Y. S. Kang, T. J. Jacobsson, J. P. Correa-Baena and A. Hagfeldt, *J. Phys. Chem. C*, 2016, **120**, 8023–8032

[30] A. Riquelme, L. J. Bennett, N. E. Courtier, M. J. Wolf, L. Contreras-Bernal, A. B. Walker, G. Richardson and J. A. Anta, *Nanoscale*, 2020, **12**, 17385–17398

[31] R. Kerremans, O. J. Sandberg, S. Meroni, T. Watson, A. Armin and P. Meredith, *Sol. RRL*, 2019, **4**, 1900221

[32] F. De Rossi, J. A. Baker, D. Beynon, K. E. A. Hooper, S. M. P. Meroni, D. Williams, Z. Wei, A. Yasin, C. Charbonneau, E. H. Jewell and T. M. Watson, *Adv. Mater. Technol.*, 2018, **3**, 1800156

[33] S. M. P. Meroni, K. E. A. Hooper, T. Dunlop, J. A. Baker, D. Worsley, C. Charbonneau and T. M. Watson, *Energies*, 2020, **13**, 1589

Chapter 5

Performance evolution and Humidity treatments in GVL-10MeOH devices

Unless specified, all sample preparation, measurement and data analysis was performed by C. Worsley.

The last chapter presented GVL-10MeOH precursors as a route to improving infiltration and performance in devices and modules. During device measurements, it was observed that devices exhibit significant performance improvement over the week following perovskite annealing. The following chapter aims to quantify the extent of performance enhancements and elucidate the mechanisms behind this phenomenon.

Humidity treatments (HT) of 70% RH, essential for performance enhancement and hysteresis elimination in GBL devices, were trialled. However,78% of untreated GVL-MeOH devices were found to improve over time regardless of HT, which had no significant impact on the extent or speed of GVL-10MeOH device PCE increase. This eliminates a significant step from the fabrication process.

Performance improvements are instead found to be a consequence of slow residual solvent loss. This is evidenced by time dependent crystal rearrangements and accompanying increases in photocurrent and photoluminescence response. It appears that slow removal is essential, as early device encapsulation and extended heating were found to both decrease initial performance and prevent time related PCE increases. Consequently, devices and modules should be left unencapsulated for 4-7 days after fabrication to achieve peak power output. This may help future scale-up endeavours in designing fabrication processes for high performance, large-scale modules.

5.1 Introduction

As presented in Chapter 4, CPSCs fabricated with mixed precursors of 9:1 GVL:MeOH exhibit improved performance as compared to GVL-only formulations. Introducing a lower viscosity polar solvent enabled greater infiltration of the base TiO_2 layer, as well as improving perovskite crystallinity. As well as improving performance, devices also exhibited increased lifetimes, with the best device demonstrating a T80 of over 420 hours unencapsulated under AM1.5 illumination. When applied in 220cm^2 modules this resulted in a champion PCE of 9.05%, compared to 8.14% for the GVL-only solution.

In similar GBL devices, there is an additional step after device infiltration wherein cells are kept in 70% RH for several hours prior to testing. This 'humidity treatment' is known to improve performance by inducing crystal reorganisation in the 110 plane (or 2θ = 14° XRD peak).[1] Resultant devices and modules typically exhibit improved PCE, large hysteresis reduction and improved lifetime.[1]–[4]

As the GVL and GVL-10MeOH perovskites presented in this work have shown superior initial crystallinity to GBL, it was hypothesised that devices may not benefit from humidity treatments to the same extent. This could reduce fabrication time and potential future manufacturing costs through removing a lengthy and highly controlled step from the production process. Additionally, understanding any changes in performance in the days following fabrication could help inform how best to treat, encapsulate or test devices to maximise performance and module power output.

5.2 Experimental

Unless specified, all sample preparation, encapsulation and experimental analyses were performed as detailed in Chapter 2.

IV Testing: Tests were performed as detailed in section 2.2.1, on devices 24 hours and 7-8 days after perovskite annealing. HT samples were tested at 24 hours (prior to treatment), and then again immediately following humidity exposure. Devices were then stored in dark ambient conditions between tests. Encapsulation samples were tested prior to encapsulation on day 1, encapsulated immediately and then retested on day 7 as usual.

EL measurements: EL was performed on completed devices, 24 hours and 7 days after perovskite annealing. EL tests were performed before IV testing on each day. An FS5 Spectrofluorometer (Edinburgh Instruments) with Keithley 2401 Source Meter Unit were used for all measurements. All samples were measured under 3V applied bias to obtain high

emission. Applied voltage was begun 10 seconds before each measurement. All samples were measured 3 times at each voltage, with 3 minutes under no bias between tests to allow the sample to recover. Excitation and emission bandwidths were 0 and 3 nm respectively, with a neutral density filter of O.D. 5 in the excitation pathway. A 700-850 nm range was used, with step size of 0.25 nm, 0.1 s dwell time. Presented results are an average of the three measurements.

PL and PC mapping: Measurements were performed with a Renishaw inVia Raman system (Renishaw plc., Wotton-Under-Edge, UK) in a backscattering configuration. A 532 nm laser and 50x objective were used (NA: 0.50, spot size ~ 1 µm). For the PL measurements, a laser power of 300 nW and an acquisition time of 1 s were used to measure a 0.49 cm^2 map with 576 data points.

5.3.1 Applying humidity treatments to GVL-10MeOH devices

Humidity treatments (HT) of 70% RH are essential for performance enhancement and hysteresis elimination in GBL devices and modules.[1],[3] The humidity treatment works through causing crystal realignment within the scaffold, resulting in more crystalline, highly oriented perovskite. This reduces defect driven recombination and improves bulk carrier transport.[1]

Thus far, GBL, GVL and GVL-10MeOH device data presented in chapters 3 and 4 have been from week-old settled cells, during which samples were exposed to humidity treatments and a 3-4 day period of ambient dark storage. This data is presented as this was where peak performance was generally attained for GVL and GVL-10MeOH devices. Performance increase during this time was generally ascribed to increased V_{oc} and FF.

Even initial pre-HT PCEs in GVL and GVL-MeOH cells were generally higher than those of GBL controls, with GBL devices only attaining similar performance to GVL samples after GBL HT. It was theorised that this could be a consequence of higher initial perovskite crystallinity in the GVL and GVL-10MeOH samples (presented in Chapters 3 and 4). It was however unclear whether the gradual performance enhancements observed in the week following fabrication were intrinsic or related to humidity exposure. A specific study was therefore designed to determine the true impact of HT in these cells.

To ensure that humidity treatments were having the expected impact on GBL cells fabricated in our facilities, standard GBL devices were produced, and tested before and after HT. Variations in ambient conditions between laboratories can potentially have a large impact on

perovskite crystallinity and device performance, which may not therefore reflect literature results. As shown in Figure 5.1, performance improved as presented in the literature, with HT drastically reducing hysteresis and improving J_{sc} and FF.[1]

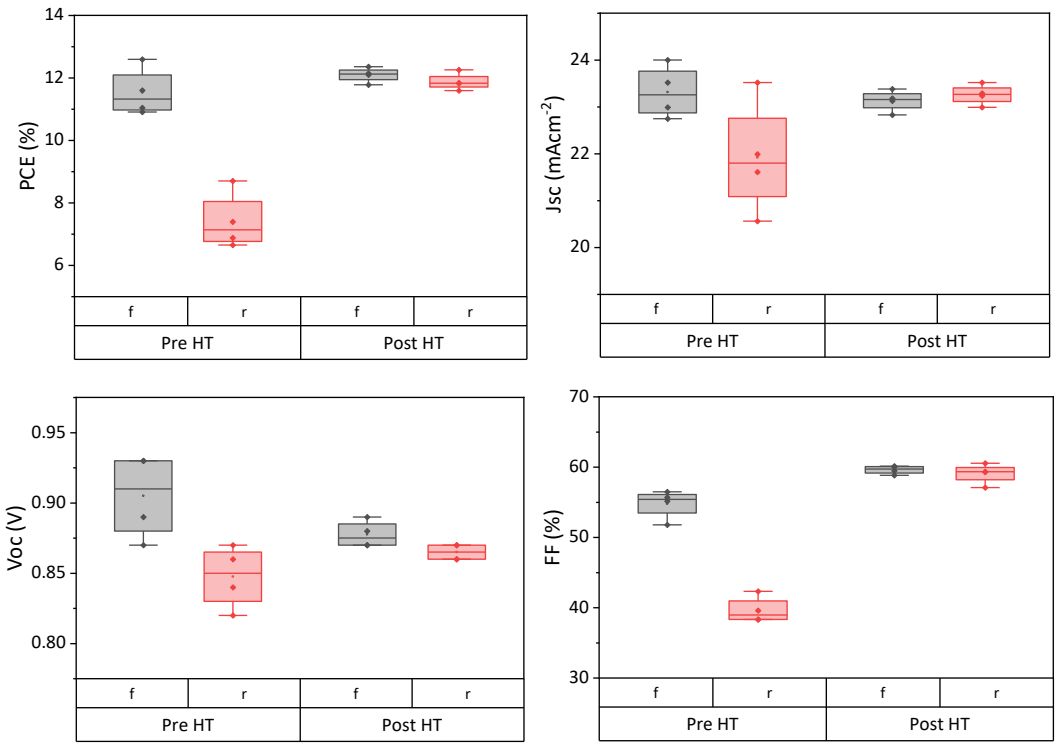

Figure 5.1: PV parameters of GBL $AVA_{0.03}MAPbI_3$ devices before and after a 70% RH HT.

To thoroughly examine the impact on GVL-10MeOH cells, four batches of devices were made. Each batch was split into two groups of similar performance following initial tests, with half exposed to HT and half stored in dry ambient conditions. After HT, these samples were placed in a dry or ambient (30% RH) environment to maintain similar storage environments. Devices were then remeasured a week after fabrication. To minimise the impact of inter-batch variation, results were normalised for comparison.

As presented in Figure 5.2, both sets of devices improved over the 7 days. These changes were similar in both the HT and dry ambient samples, with both sets experiencing large FF hysteresis reduction and slight V_{oc} and J_{sc} increases. As non-HT devices were stored in a dry ambient environment for the duration, these changes must be unrelated to humidity exposure.

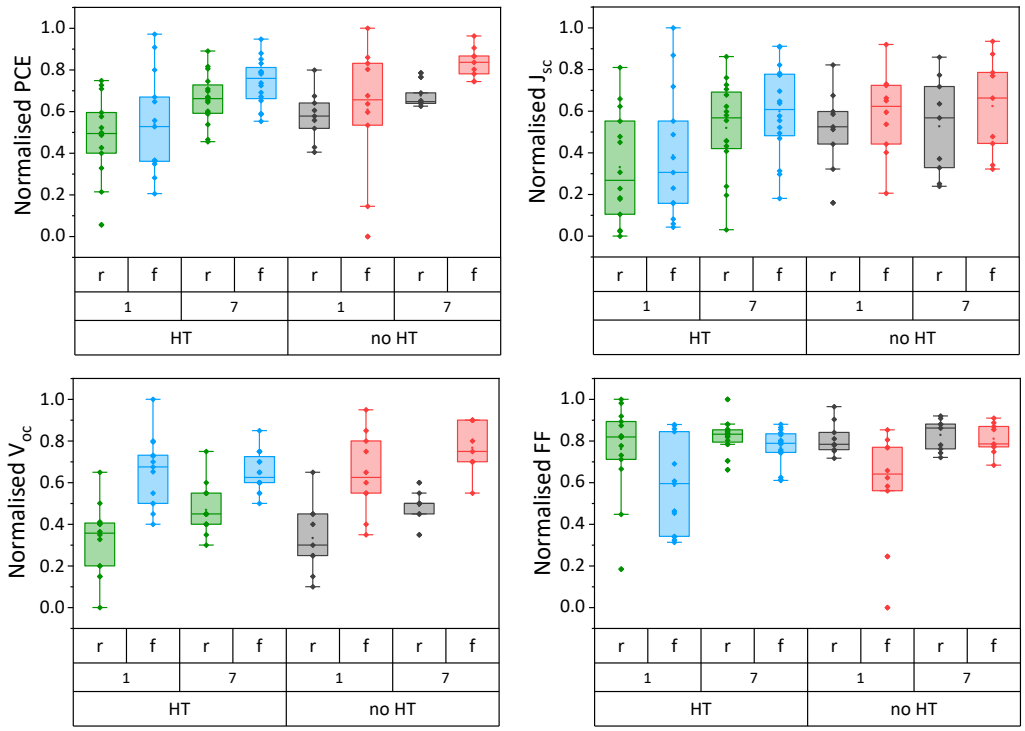

Figure 5.2: Normalised PV Data of $AVA_{0.03}MAPbI_3$ devices fabricated from GVL-MeOH precursors before and after humidity treatments (HT) or ambient dry storage. Samples were measured 1 day after fabrication and 7 days after fabrication, with HT on days 2-3. 14-18 samples in each set.

These results suggest that HT is not required for performance enhancement in GVL-10MeOH cells. In GBL samples, HT induces crystal realignment in the (110) direction, improving crystallinity and bulk carrier transport.[1] This is observable by increases in 2θ ~ 14° relative peak intensity of XRD measurements. The enhancements observed in GVL-10MeOH samples could be a consequence of a similar process, albeit one unreliant on ambient humidity. To determine whether similar crystal realignment could be occurring here, samples were analysed using XRD before and after exposure to humid or dry conditions.

As shown in Figure 5.3, GBL perovskites realigned to favour (110) orientation with HT, changing from a the initial (220) (2θ = 28°) dominant orientation. GBL samples stored in dry air showed very little change, with only small shifts in the 14° (110) peak.

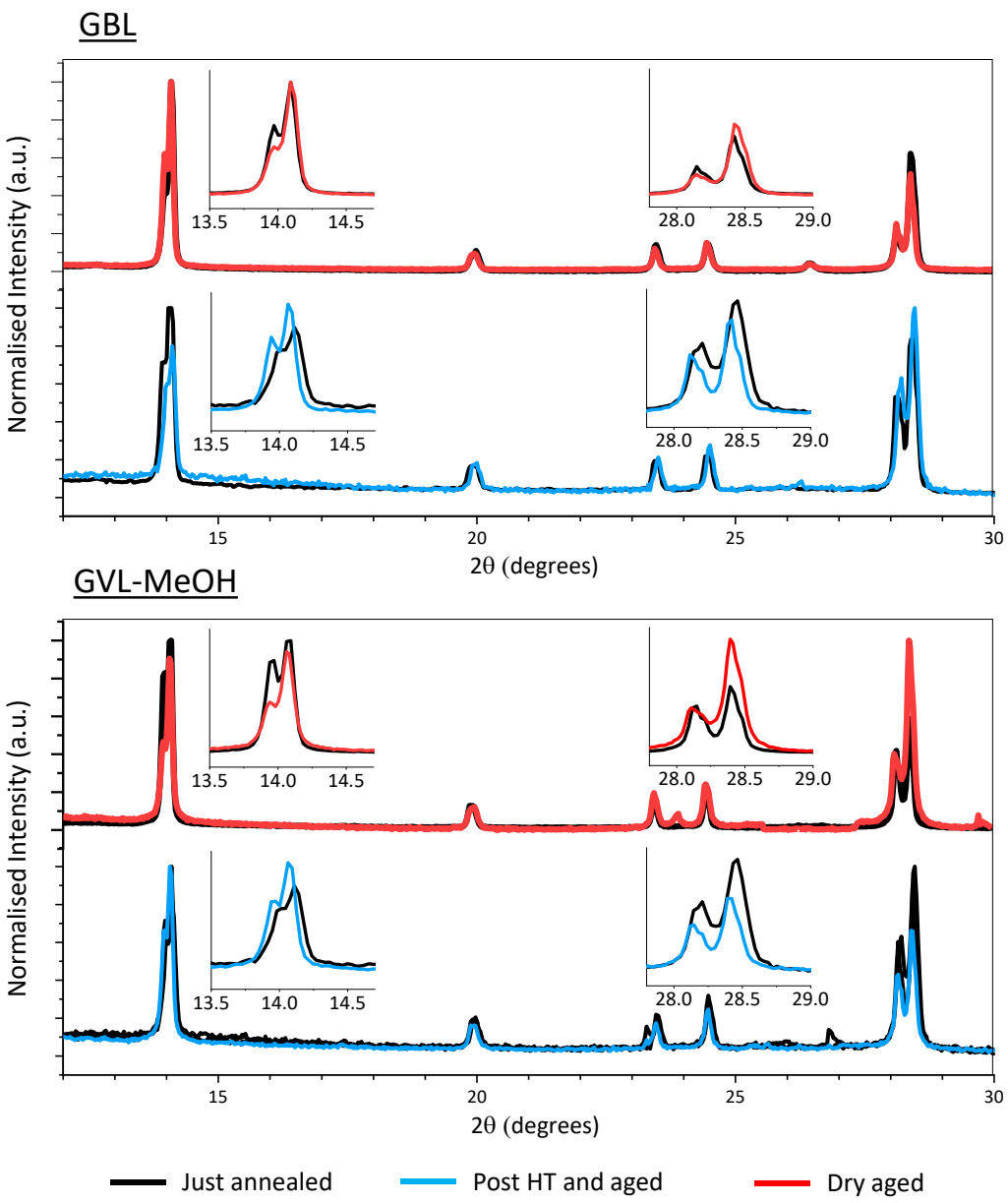

Figure 5.3: XRD traces of $AVA_{0.03}MAPbI_3$ perovskites crystallised from GBL (top) and GVL-10MeOH (bottom) precursors in mesoporous ZrO_2 scaffolds. Samples were examined directly after annealing (black) and again after exposure to dry ambient air (red) or HT (blue).

Conversely, both the HT and dry air GVL samples showed significant realignment over time. Like with GBL, the HT sample switched from a (220) orientation with a 28° high peak to a (110) favoured orientation with a 14° dominant peak. Conversely, the dry ambient sample switched from a 14° to a 28° dominant peak. It should be noted that this was not the case in every dry ambient sample- while the majority saw alignment changes after dry storage, these were not always towards a (220) orientation. Therefore, while it appears that HT favours (110) realignment, the process occurring here can induce reorganisation to favour either structure.

It was noted that realignment did not occur in every sample. If linked to performance enhancements, this may indicate that only some devices improve post-fabrication. Additionally, as the normalised device data presented in Figure 5.2 were from relatively poor devices of 10-12% PCE,[‡‡‡] they may not reflect the performance over time of high-quality cells. Optimised prints may already produce superior crystal quality, giving such devices little room for improvement. A comprehensive analysis of age-related performance changes in high-performing devices was therefore deemed necessary.

5.3.2 Age-related performance changes in high PCE devices.

In order to ascertain whether age related performance enhancements were significant in high-performing GVL-10MeOH cells, 27 standard control devices from eight different experiments were examined over the week following fabrication (Figure 5.4). Devices were tested 24 hours, and 7 days after infiltration.

The advantage of including controls from multiple batches minimises the potential for environmental fluctuations to impact observed changes. For example, should performance enhancements only occur in devices exposed to specific ambient temperatures or conditions during or after infiltration, these will represent a minority subgroup in the wider sample pool. Such an approach also therefore offers the potential to identify any such environmental factor for further examination if necessary. As such, ambient temperature and humidity were recorded during infiltration and annealing for every batch in this study. No relationship between performance enhancement and ambient annealing temperature or RH was observed, indicating that this effect is unlikely to be dependent on such variables.

[‡‡‡] This was due to print changes after a supplier paste change, discussed in detail in Chapter 6.

a)

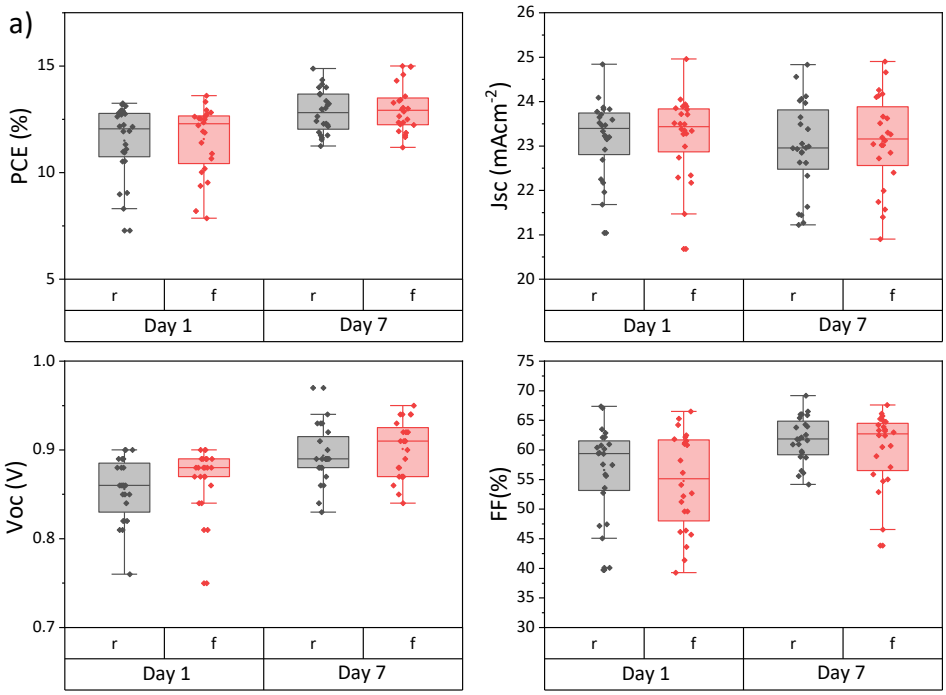

b)

		% Improved	% No change	% Fallen
PCE	**R**	77.8	11.1	11.1
	F	63.0	18.5	18.5
Voc	**R**	77.8	11.1	11.1
	F	66.7	25.9	7.4
FF	**R**	63.0	29.6	7.4
	F	63.0	25.9	11.1
Jsc	**R**	25.9	40.7	33.3
	F	22.2	55.6	22.2

Figure 5.4: a) PV parameters of 27 GVL-MeOH $AVA_{0.03}MAPbI_3$ devices from various batches, 1 and 7 days after fabrication. b) Table showing % of devices that showed improvement, no change or decreased performance after 7 days. No change was considered as within 2% of the initial measured value.[§§§]

Table 5.1: Average % change observed for each PV parameter, with maximum performance increase and decrease in bracketed italics. Change was calculated as a % of the initial measurement.

	Avg % ΔPCE *(range)*	**Avg % ΔVoc** *(range)*	**Avg % ΔFF** *(range)*	**Avg % ΔJsc** *(range)*
R	+15.5 *(-7.0, +92.2)*	4.5 *(-2.4, +17.1)*	10.60 *(-5.0, +59.0)*	-0.58 *(-4.8, +7.2)*
F	+15.26 *(7.3, +90.3)*	4.5 *(-3.4, +25.3)*	9.61 *(-6 .0, +48.0)*	-0.36 *(-4.7, +7.3)*

[§§§] The highest performing devices in this graph were fabricated using the optimised procedures detailed in Chapter 6. Improvement over time were consistent between batches regardless of print regime, hence their inclusion in this study.

As shown in Figure 5.4, device performance at 24 hours post-infiltration ranged from 7.32-13.61% PCE. A week later, the performance range was 11.25-14.96%. This is a significant increase in performance and a twofold reduction in result spread. Although result spread is still fairly high on day 7, this is likely due to the large number of different control batches used. A reduction in result spread is encouraging, as this indicates that performance enhancement is unlikely to be highly dependent on an environmental factor. Cells made during different weeks improved similarly, regardless of slight variations in ambient conditions.

To obtain a clearer view on how each individual device behaved, the % change of each photovoltaic parameter was calculated for every device (Figure 5.4b, Table 1). A change of >2% of the initial measured value was set as 'significant' and devices binned accordingly. As shown in Figure 5.4b, 78% of devices exhibited increased PCE after 7 days, ranging from 7% to 92.2% improvement on the initial performance (average 15.5%). 11% of devices showed no change, with the remaining 11% falling compared to the initial measurement. Devices that fell in performance did not show a drastic decrease, with a maximum decrease of 7% of initial PCE.

Performance increases were due to a combination of V_{oc} and FF changes: 78% of devices experiencing a V_{oc} increase (mean +5%, maximum +20%), and 63% improved FF (mean +10.6%, maximum +58%). On average, J_{sc} remained statistically similar, with a mean change of well below 1% between measurements.

Increases in V_{oc} and FF are respectively indicative of improved carrier lifetime and better charge extraction.[5],[6] As shown in section 5.2, perovskites crystallised from GVL-10MeOH precursors showed significant crystal realignment during dry storage. This could account for the observed changes in device behaviour: Higher V_{oc} is to be expected where crystallinity improves, as fewer crystal defects will reduce the recombination rate and increase carrier lifetime.[5],[7],[8] FF enhancement suggests that improved electrode contact is also occurring, improving interfacial charge transfer.[6]

However, the XRD measurements in section 5.2 only probe perovskite near the surface and may not therefore be representative of crystals deep within the TiO_2. Crystal quality through the glass electrode can be examined using electroluminescence (EL), which increases with realignment and improved crystallinity.[9],[10] Devices were therefore examined using EL to see if time dependent luminescence increases could be observed and whether these correlated with performance evolution.

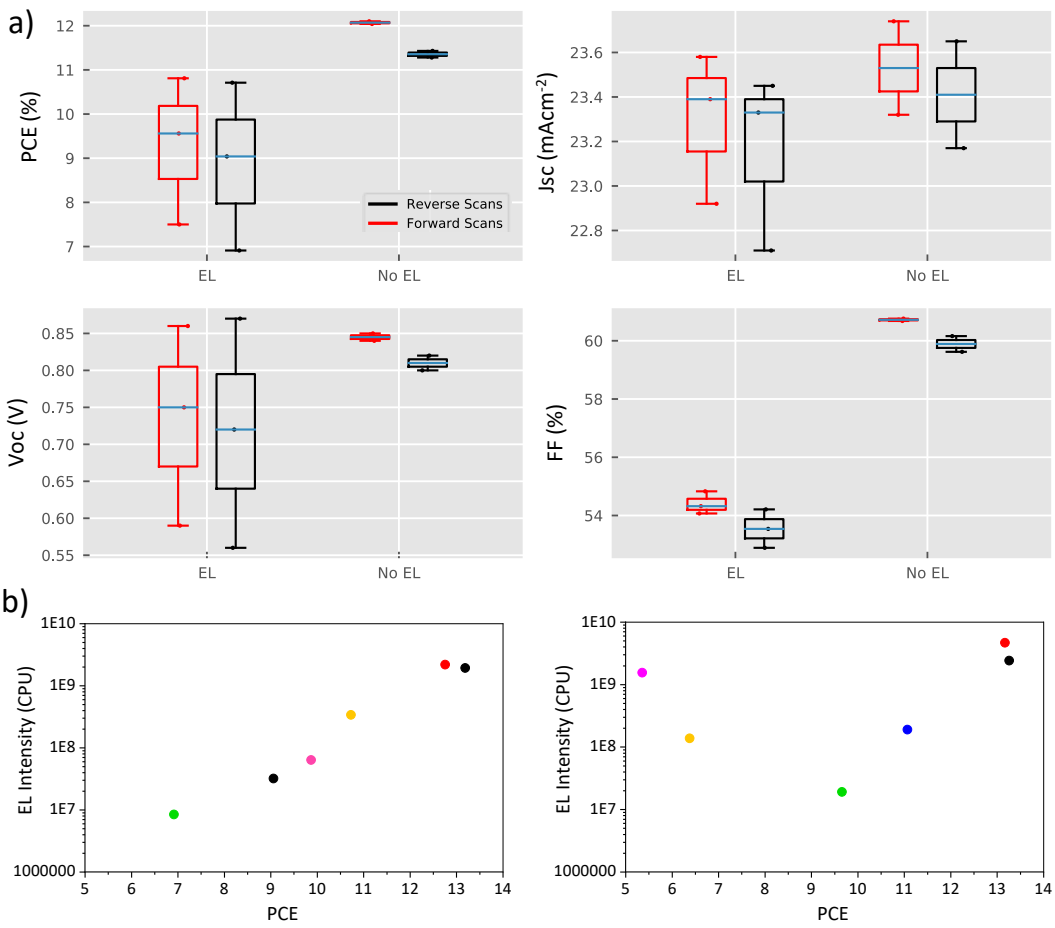

Figure 5.5: a) Impact of performing 3V EL measurements on PV parameters of devices 1 day after fabrication. Non El devices were kept back from the same batch of cells. b) relationship between EL intensity and PCE on Days 1 vs 8 after fabrication.

Unfortunately, as shown in Figure 5.5, the bias voltage required for EL measurements negatively impacted fresh cells, drastically reducing V_{oc} and FF. Devices were still measured over time and exhibited some small performance enhancements over time. However, the EL exposed devices improved much less than the non-measured controls. Additionally, although initial EL intensity was found to logarithmically correspond to performance in fresh cells, this was not the case in the aged devices. Neither raw performance nor the % enhancement correlated with raw EL intensity or % EL change. As the measurements appeared to significantly impact devices, it was decided that no clear conclusions can be drawn from this data.

PL and photocurrent mapping can also be used to compare crystal quality within the TiO_2 layer.[11] PL intensity correlates positively with crystal quality, with larger more crystalline samples producing more intense emission due to lower levels of recombination.[12]–[14] Such

samples also have less PL blue-shifting, due to smaller population of shallow traps.[15] As there are fewer shallow traps to fill during initial light exposure this can therefore accompanied by faster photocurrent evolution.[15]

PL and PC mapping were therefore performed on a sample before and after ageing, with IV analysis on each day to correlate any differences with performance evolution (Figure 5.6).

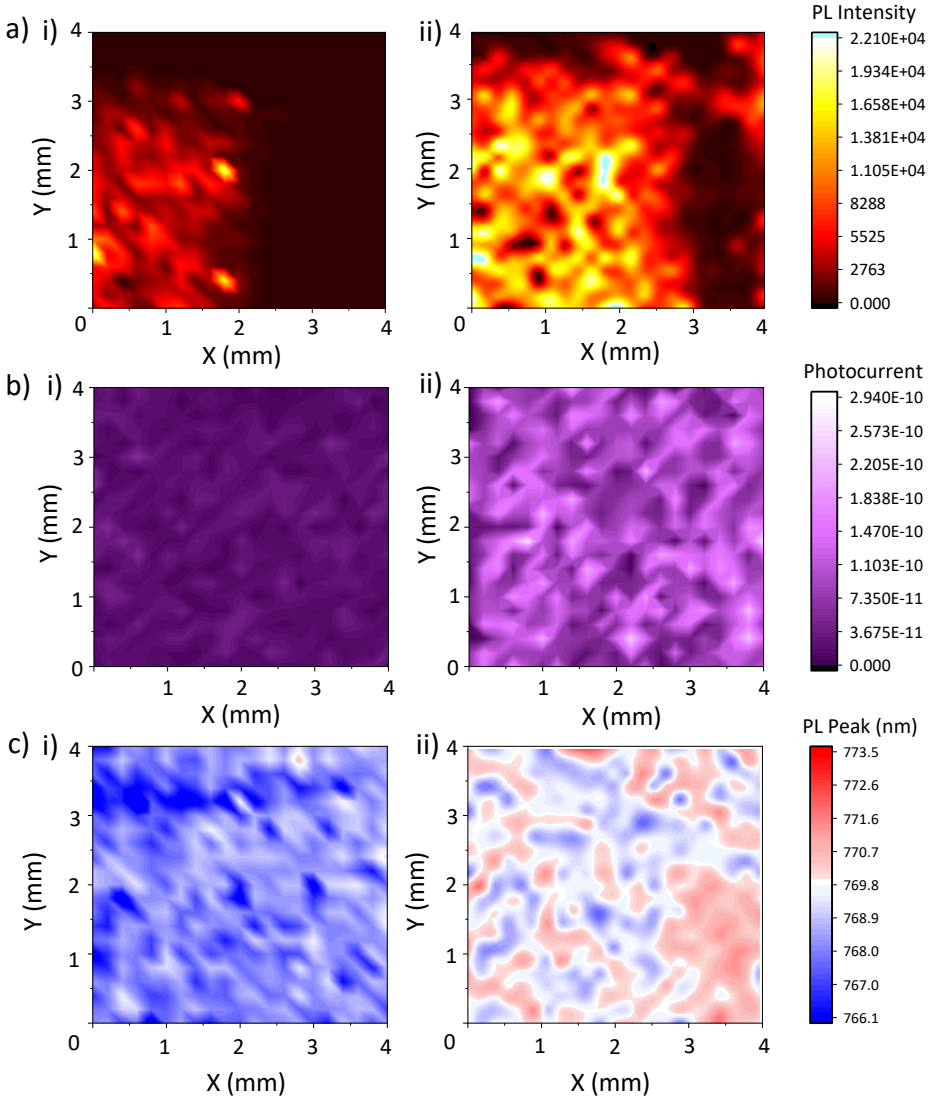

d)

	Scan	PCE (%)	V_{oc} (V)	FF (%)	J_{sc} (mA/cm^{-2})
(i)	r	11.00	0.80	61.4	22.31
	f	11.97	0.85	62.16	22.62
(ii)	r	12.00	0.82	62.19	23.58
	f	13.26	0.87	63.64	23.87

Figure 5.6: a) Photoluminescence maps, b) Photocurrent maps, c) PL peak position maps, and d) PV performance parameters of a device 1 (i) and 8 (ii) days after fabrication. Pixel size 0.085 mm^2 (576 data points per graph).

As shown in Figure 5.6 PL improved significantly over a week of ageing, with the average intensity rising from 1620 counts on day 1 to 8064 on day 7. This was accompanied by PL redshifts across the area, shifting the average peak from 768 nm to 770 nm. This was accompanied by a 10.8% increase from the initial PCE.[****] These data indicate that crystal realignment also occurs in the base TiO_2, suggesting that it takes place throughout the stack.

A tenfold increase in photocurrent response was also observed. Such a result was unexpected, as although device J_{sc} improved the change was not particularly drastic. As opposed to being an indicator that current generation has hugely increased, this may instead be due to faster device response due to fewer shallow traps and increase charge mobility. CPSCs are extremely thick, contain small-grained perovskite and have a non-selective charge transport layer. This produces an extremely slow-responding device: cells need 3-10 minutes of light soaking prior to IV testing to achieve peak performance.[16],[17] Such light soaking is not possible with the low intensity, small spot size laser used for these measurements. As such, measured photocurrent is low. A device with more crystalline perovskite, fewer shallow traps and improved charge transport is likely to respond faster during measurement conditions, thus generating a much higher photocurrent during the short time frame.

5.3.3 Elucidating age-related performance enhancements

It is clear in section 5.3 that device performance improved over the week following fabrication. When examining device EL, it became apparent that applied bias could impact performance evolution- in the case of EL, performance was negatively affected. It was therefore posited that some element of the device testing process could be driving the observed performance increases. Indeed, previous works have shown that light exposure can positively affect performance evolution beyond the normal light soaking effect in newly fabricated devices.[16],[18]

An experiment was therefore devised to determine whether IV testing was driving performance evolution. After annealing, devices were split into four groups, with one group tested as usual, one exposed only to light, one to testing bias sweeps and the last to dark storage. This was repeated on days 1 and 7. Should PCE gains be related to any element of

[****] It should be noted that while this sample experienced a significant increase in Jsc, this occurs only in 33% of devices. Voc and FF improvements are more common overall. (Figure 5.4)

testing, the dark storage samples should reflect the day 1 pre enhanced performance of the tested samples.

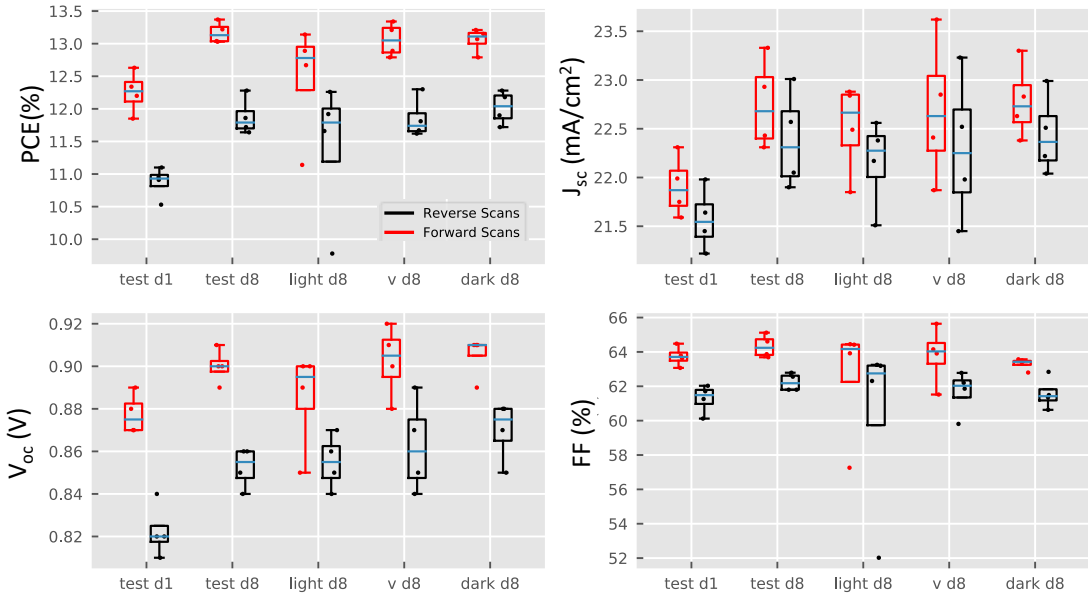

Figure 5.7: PV parameters of GVL-MeOH $AVA_{0.03}MAPbI_3$ devices exposed to testing (test d8), 1 sun illumination (light d8), bias (v d8), and dark storage. Initial performance of control devices (test d1) is provided for comparison.

As shown in Figure 5.7, test samples improved as usual, from an average 12.3% PCE on day 1 to 13.1% after ageing. Upon testing, performance of all other device sets aligned with that of the aged samples, indicating that performance enhancements were occurring independently of any testing variables. Interestingly, despite previous works showing light induced performance increases, these samples showed the lowest post-ageing performance. Although this could be an indication of stymied performance evolution, averages in this case appear to have been affected by a single sample exhibiting minimal improvement. During larger scale analysis, around 11% of devices did not improve over time. At least one such device in this experiment is therefore not unreasonable.

All the data presented thus far were from unencapsulated devices stored in ambient or dry ambient environments. Although humidity was not found to significantly impact performance (with HT and dry ambient cells exhibiting similar performance), keeping devices unencapsulated allows potential ingress of environmental species, as well as egress of internal components such as residual solvent or volatile MAI.

Encapsulated devices were therefore prepared and monitored for performance changes.

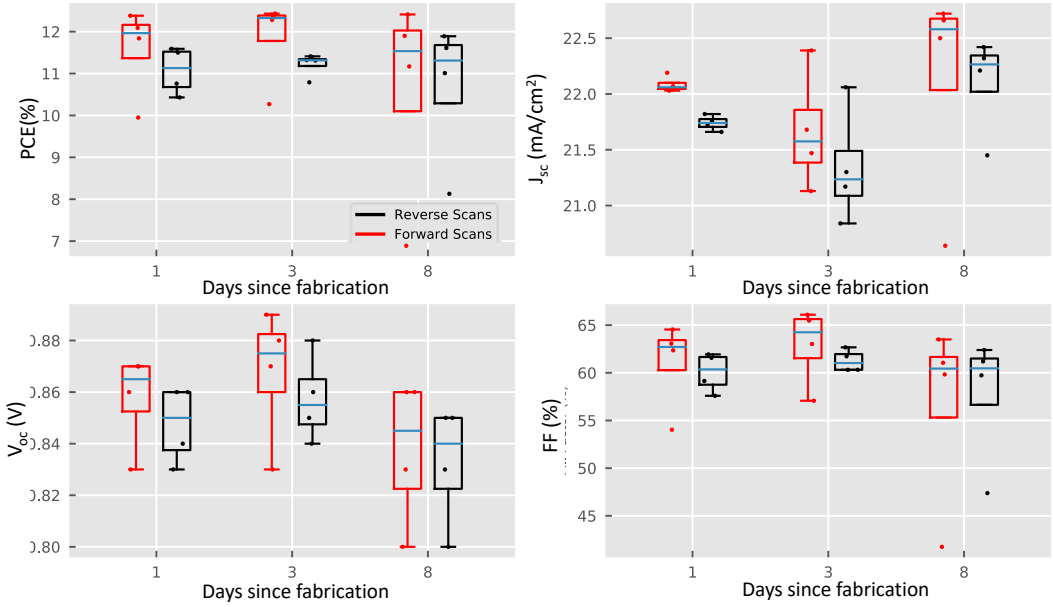

Figure 5.8: PV parameters of GVL-MeOH $AVA_{0.03}MAPbI_3$ devices after fabrication (Day 1), after encapsulation (day 3) and after 8 days (5 days encapsulated). Devices were encapsulated immediately after initial tests, but required 24 hours for full epoxy setting before tests. 4-5 devices in each set.

As shown in Figure 5.8, encapsulated devices did not improve over time, remaining the same after encapsulation before falling in performance by day 7 due to losses in J_{sc}, V_{oc} and FF. Each individual encapsulated device suffered some loss in performance between days 3 and 8, while unencapsulated controls improved as observed in previous batches. Most interestingly, those cells that tested best on day 1 exhibited the smallest performance losses on day 7. It appears that not allowing environmental exposure following fabrication was in fact detrimental to device performance.

This suggests that to achieve peak performance, something must enter or exit the stack during the week following fabrication. Preventing this is detrimental to device performance, causing significant V_{oc} and FF issues. Therefore, although these devices do not benefit from HT, an ageing period where devices are left unencapsulated is important in achieving high performance. This could be a critical consideration in potential scale-up settings, where completed devices are typically encapsulated immediately following fabrication. These results suggest that such procedures would significantly hinder module performance.

As the performance increases appear consistent across batches, they are unlikely to be caused by variable environmental factors such as temperature or RH. While airborne O_2 is likely to enter the stack, its influence on performance is generally negative, accelerating

degradation to PbI_2.[19] Similarly, MAI loss is linked to degradation and associated performance losses.[20]

Previous work on perovskites crystallised from DMF and DMSO have revealed that significant amounts of solvent can remain in perovskite films after annealing, even in planar devices with no evaporation-limiting scaffold.[21]–[23] Additionally, recent works on CPSC additives showed that ethylene carbonate (EC) additives remain in $AVA_{0.03}MAPbI_3$ perovskites after annealing. Coordination of EC to Pb centres via carbonyl groups was found to passivate surface defects and improve ambient stability.[24] As a structurally similar compound with an electron rich C=O group (Figure 5.9), GVL could also potentially interact with Pb centres and grain boundary defects.

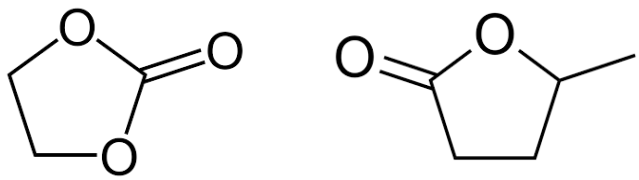

EC **GVL**

Figure 5.9: Chemical structures of ethylene carbonate (EC) and GVL

Additionally, the annealing temperature of 45°C used for perovskite crystallisation is relatively low considering the boiling point of GVL (208°C).[25] GVL is clearly removed at this temperature, as crystallisation to the black phase occurs. However, residual solvent may still remain- especially deep in the base TiO_2 layer where microns of scaffold restrict solvent escape.

To observe whether GVL could remain after annealing and examine whether coordination to Pb centres may be occurring, Fourier transform infrared (FTIR) spectroscopy was performed. Figure 5.10 shows FTIR spectra of pure GVL, pure PbI_2 and PbI_2 dried from a GVL suspension for an hour at 45°C. FTIR comparisons of perovskites were not performed, as the organic groups and AVA COOH sections would likely mask any signals due to residual GVL.

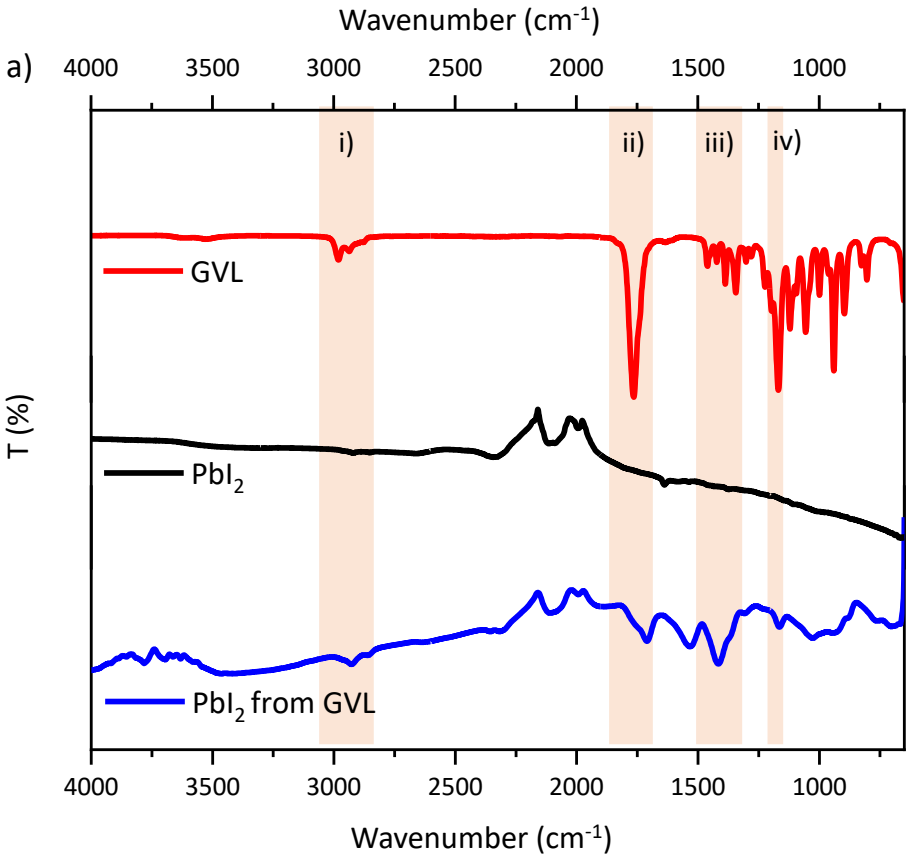

b)

	Absorption (cm^{-1})	Features	Group
i)	3012-2840	Decreasing triplet	C-H stretch
ii)	1762	Large sharp singlet	C=O lactone stretch
iii)	1466-1305	Many small sharp peaks	C-H bends
iv)	1173	Sharp narrow peak	C-O lactone stretch

Figure 5.10: a) FTIR of pure GVL, pure PbI_2 and PbI_2 after drying from GVL at 45°C. Highlighted sections show notable characteristic GVL peaks. b) Table assigning identified FTIR peaks.

The pure GVL sample shows a clear sharp symmetric C=O stretch at 1762 cm^{-1}, as well as a group of C-H stretches at 2800-3000 cm^{-1}. These peaks are also present in the annealed PbI_2 sample. In this case, the C=O is shifted to 1710 cm^{-1} and presents with shoulder towards higher wavenumbers. This peak shift is indicative of some interaction with the metal centre, although the presence of a shoulder suggests that some uncoordinated GVL may also reside in the film.[24] Interestingly, a significant OH stretch at ~3000-3500 cm^{-1} is also present in the annealed sample. While this could also be evidence of some GVL ring opening to form diols during annealing, this was considered unlikely as annealing was performed in a low humidity environment and such reactions generally occur in the presence of water and a catalyst.[26]

Samples were stored briefly in ambient air (~55% RH) prior to measuring, so this was considered more likely due to ambient water adsorption.

GVL can clearly remain on PbI_2 dried at 45°C. To determine whether this is also the case for perovskite, GVL $AVA_{0.03}MAPbI_3$ precursors were cast onto ZrO_2 scaffolds and annealed. Thermogravimetric analysis (TGA) and differential scanning calorimetry (DSC) were then run after 24 hours and 1 week. Little detailed TGA or DSC data are presented in the literature for AVA-containing perovskites. A perovskite-only sample annealed on glass for 3 hours was therefore run to 400°C to check relevant MA and AVA mass loss temperatures before analysing samples for evidence of retained solvent. Figure 5.11a) shows the thermal degradation of $AVA_{0.03}MAPbI_3$ freshly annealed on glass. A mass loss of ~25% is present from 200-300°C, corresponding with loss of the MAI portion of the perovskite.

A prior, very slight mass loss may also have occurred at 150-200°C. This may be evidence of retained solvent even in the absence of a scaffold. The derivative shows that the large loss from 200-300°C comprised of two separate events- a smaller loss from 225-250°C followed by a much larger fall. This is likely due to AVA followed by MAI loss, as the % losses and temperatures correspond with those expected for these species.[21], [22]

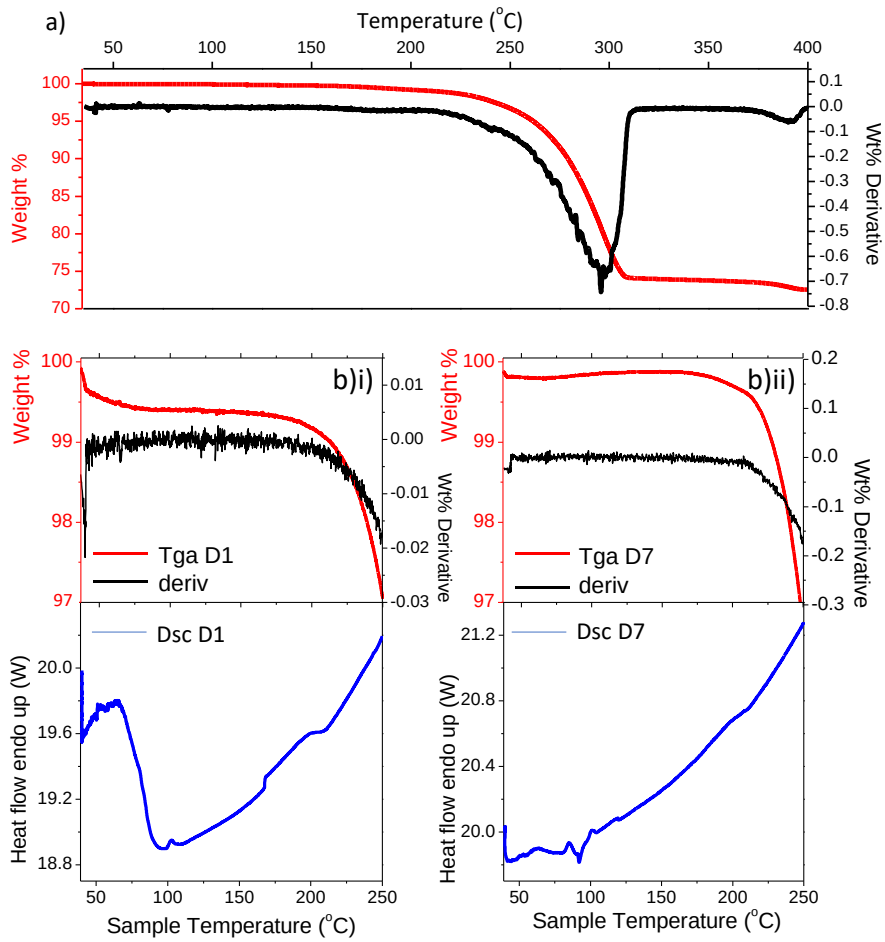

Figure 5.11: a) TGA and derivative of $AVA_{0.03}MAPbI_3$ annealed on glass. b) TGA, derivative weight % and DSC traces of $AVA_{0.03}MAPbI_3$ in ZrO_2 samples 24 h (i) and 7 days (ii) after annealing.

Despite high boiling points of over 150°C, previous works have shown that residual DMF and DMSO are removed between 0-100°C before MAI loss begins.[21],[22] GVL has a slightly higher boiling point (208°C) and may be adsorbed. This may elevate the removal temperature. However, above 250°C temperature, large MAI losses would likely mask any small change due to residual solvent removal. Samples of perovskite annealed in ZrO_2 scaffolds were therefore measured from 40-250°C. The first measurement was performed on the same day as annealing. Half of the annealed film was scraped into the pan, and the remaining film placed in a dry box for storage before removal and measurement on day 7. Figure 5.11a shows the degradation of $AVA_{0.03}MAPbI_3$ on glass.

As shown in Figure 5.11b(i), the day 1 sample experiences a 0.5% mass loss from 50-100°C, accompanied by an endothermic DSC peak in the same temperature range. This is typical of solvent removal and likely due to retained, non-adsorbed GVL. [21], [22] Both samples show a DSC phase transition at ~100°C. Interestingly, an endothermic step feature can also be

observed from 175-200°C, although as this precedes apparent MAI loss it may be AVA related as opposed to adsorbed GVL.

No early endothermic peak is observed in the aged sample (Figure 5.11 b(ii)), indicating that the retained solvent is no longer present. Additionally, the 175°C feature is much reduced, which may indicate that any adsorbed GVL also leaves the stack during this time.

A long ageing period to allow slow recrystallisation over several days is not practical, especially from a commercial standpoint. Higher annealing temperatures risk detrimentally fast crystallisation (discussed in Chapter 6). It was posited that simply increasing the annealing time may allow for complete crystallisation without requiring a long ageing step. Samples were therefore fabricated with longer annealing times of 2.5 hours.

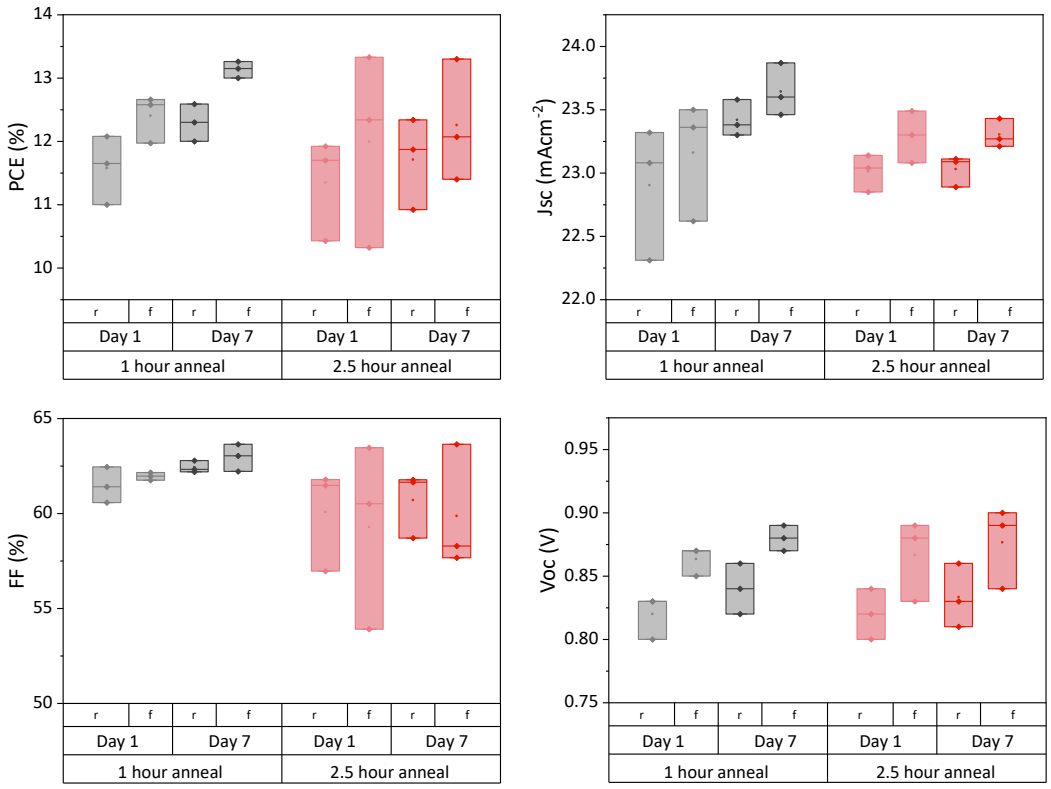

Figure 5.12: Performance of GVL-MeOH $AVA_{0.03}MAPbI_3$ devices annealed for 1 or 2.5 hours at 45°C 1 and 7 days after fabrications. Four samples in each set.

Presented in Figure 5.12, long annealed samples did not exhibit higher initial performance, and also displayed limited performance enhancement over the week when compared to standard devices. It would appear that removing a greater proportion of solvent at the outset did not produce enhanced crystallinity, and furthermore limited the capacity for crystal

reorganisation following fabrication. It seems that the slow loss of solvent over time is key to maximising performance in this case.

5.4 Conclusion

This work examines the performance evolution of $AVA_{0.03}MAPbI_3$ cells crystallised from GVL-10MeOH precursors. GBL cells are known to benefit from 70% RH humidity treatments, which acts to improve absorber crystallinity, connectivity and electrode contact. However, it was found that GVL-10MeOH devices improve over time regardless of humidity application, most commonly due to increases in FF and V_{oc}. The magnitude of performance enhancement was extremely variable, with increases of +2-98% of initial PCE (average 15%). Over the week following fabrication, 78% of devices were found to experience performance increases >2% initial PCE, experiencing an average improvement of 15.5% on the initial measurement. Peak performance was generally observed ~7 days after fabrication, although some devices peaked at four days.

This is a consequence of crystal reorientation, as evidenced by XRD peak ratio changes, PL red-shifting and increases in PL intensity with device ageing. These effects are bought about by slow removal of residual solvent from the perovskite layer. Such enhancements were not observed in long-annealed devices, suggesting that the slow removal is key for crystal realignment and related performance increases.

Crucially, early device encapsulation was found to hinder initial performance and PCE improvements, preventing solvent egress and thus recrystallisation during the ageing period. To achieve peak cell or module performance, 4-7 days of storage is therefore recommended prior to encapsulation. This work may help inform future work designing scaled-up processes for fabricating high performing modules.

5.5 References

[1] S. G. Hashmi, D. Martineau, M. I. Dar, T. T. T. Myllymäki, T. Sarikka, V. Ulla, S. M. Zakeeruddin and M. Grätzel, J. Mater. Chem. A, 2017, **5**, 12060–12067

[2] A. Karavioti, E. Vitoratos and E. Stathatos, J. Mater. Sci. Mater. Electron., 2020, 1–9

[3] F. De Rossi, J. A. Baker, D. Beynon, K. E. A. Hooper, S. M. P. Meroni, D. Williams, Z. Wei, A. Yasin, C. Charbonneau, E. H. Jewell and T. M. Watson, Adv. Mater. Technol., 2018, **3**, 1800156

[4] S. G. Hashmi, D. Martineau, X. Li, M. Ozkan, A. Tiihonen, M. I. Dar, T. Sarikka, S. M. Zakeeruddin, J. Paltakari, P. D. Lund and M. Grätzel, Adv. Mater. Technol., 2017, **2**, 1600183

[5] T. Du, J. Kim, J. Ngiam, S. Xu, P. R. F. Barnes, J. R. Durrant and M. A. McLachlan, Adv. Funct. Mater., 2018, **28**, 1801808

[6] A. Bashir, J. H. Lew, S. Shukla, D. Gupta, T. Baikie, S. Chakraborty, R. Patidar, A. Bruno, S. Mhaisalkar and Z. Akhter, Sol. Energy, 2019, **182**, 225–236

[7] J. Wu, W. Zhang, Q. Wang, S. Liu, J. Du, A. Mei, Y. Rong, Y. Hu and H. Han, J. Mater. Chem. A, 2020, **8**, 11148-11154

[8] C. M. Tsai, G. W. Wu, S. Narra, H. M. Chang, N. Mohanta, H. P. Wu, C. L. Wang and E. W. G. Diau, J. Mater. Chem. A, 2017, **5**, 739–747

[9] Z. Hameiri, A. Mahboubi Soufiani, M. K. Juhl, L. Jiang, F. Huang, Y. B. Cheng, H. Kampwerth, J. W. Weber, M. A. Green and T. Trupke, Prog. Photovoltaics Res. Appl., 2015, **23**, 1697–1705

[10] W. Feng, K. Lin, W. Li, X. Xiao, J. Lu, C. Yan, X. Liu, L. Xie, C. Tian, D. Wu, K. Wang and Z. Wei, J. Mater. Chem. A, 2021, **9**, 11064–11072

[11] H. Lakhiani, T. Dunlop, F. De Rossi, S. Dimitrov, R. Kerremans, C. Charbonneau, T. Watson, J. Barbé and W. C. Tsoi, Adv. Funct. Mater., 2019, **29**, 1900885

[12] E. V. Péan, C. S. De Castro and M. L. Davies, Mater. Lett., 2019, **243**, 191–194

[13] K. P. Goetz, A. D. Taylor, F. Paulus and Y. Vaynzof, Adv. Funct. Mater., 2020, **30**, 1910004

[14] M. Abdi-Jalebi, Z. Andaji-Garmaroudi, S. Cacovich, C. Stavrakas, B. Philippe, J. M. Richter, M. Alsari, E. P. Booker, E. M. Hutter, A. J. Pearson, S. Lilliu, T. J. Savenije, H. Rensmo, G. Divitini, C. Ducati, R. H. Friend and S. D. Stranks, Nature, 2018, **555**, 497–501

[15] T. Zhang, M. Long, K. Yan, X. Zeng, F. Zhou, Z. Chen, X. Wan, K. Chen, P. Liu, F. Li, T. Yu, W. Xie and J. Xu, ACS Appl. Mater. Interfaces, 2016, **8**, 32366–32375

[16] A. Schneider, S. Alon and L. Etgar, Energy Technol., 2019, 1900481

[17] A. Pockett, D. Raptis, S. M. P. Meroni, J. Baker, T. Watson and M. Carnie, J. Phys. Chem. C, 2019, **123**, 11414–11421

[18] E. Kobayashi, R. Tsuji, D. Martineau, A. Hinsch and S. Ito, Cell Reports Phys. Sci., 2021, **2**, 100648

[19] D. Bryant, N. Aristidou, S. Pont, I. Sanchez-Molina, T. Chotchunangatchaval, S. Wheeler, J. R. Durrant and S. A. Haque, Energy Environ. Sci., 2016, **9**, 1655–1660

[20] B. Yang, O. Dyck, W. Ming, M. H. Du, S. Das, C. M. Rouleau, G. Duscher, D. B. Geohegan and K. Xiao, ACS Appl. Mater. Interfaces, 2016, **8**, 32333–32340

[21] A. E. Williams, P. J. Holliman, M. J. Carnie, M. L. Davies, D. A. Worsley and T. M. Watson, J. Mater. Chem. A, 2014, **2**, 19338–19346

[22] Y. K. Ren, S. D. Liu, B. Duan, Y. F. Xu, Z. Q. Li, Y. Huang, L. H. Hu, J. Zhu and S. Y. Dai, J. Alloys Compd., 2017, 705, 205–210

[23] Y. Zhou, A. Najar, J. Zhang, J. Feng, Y. Cao, Z. Li, X. Zhu, D. Yang and S. F. Liu, ACS Appl.

Mater. Interfaces, 2022, **14**, 28729-28737

[24] K. Chen, Z. Zhang, J. Liu, Y. Huang, D. Wang, B. She, B. Liu, X. Zhang and J. Zhang, Adv. Mater. Interfaces, 2022, **9**, 2100395

[25] GVL MSDS, https://www.sigmaaldrich.com/MSDS/MSDS/DisplayMSDSPage.do?country=GB&language=en&productNumber=V403&brand=ALDRICH, (accessed 14 January 2021)

[26] R. Pothu, R. Gundeboyina, R. Boddula, V. Perugopu and J. Ma, New J. Chem., 2022, **4**

Chapter 6

Performance and infiltration enhancement in CPSCs

Unless specified, optical microscopy images, analysis and infiltration modeling obtained by Dr. Tom Dunlop using samples prepared by C. Worsley. Unless specified, all other measurement and data analysis was performed by C. Worsley.

6.1 Introduction

The previous chapter examined incorporating MeOH to GVL-based precursors as a targeted approach to improving CPSC infiltration and performance. Optimised systems incorporating 10% MeOH were found to consistently enhance infiltration, performance, and stability, recording up to 13.8% PCE using a 0.49 cm^2 mask. However, variations in batch infiltration and performance were still apparent.

There are many potential factors influencing performance and infiltration changes between batches.[1] Standard procedure for CPSC fabrication involves many manual processes, such as c-TiO_2 spraying, screen printer setup and infiltration. Additionally, these processes are carried out in ambient conditions. This makes determining the causes of slight inter-batch variation extremely difficult, and small consistency issues between batches are often assumed to be an unavoidable consequence of minor print changes and environmental fluctuation.

As such, little comprehensive work had been carried out to examine the specific causes of poor infiltration and performance changes. Consequently, when a significant drop in infiltration quality and device performance was observed, there was no standard procedure for determining the root cause.

Such issues in performance tend to worsen as active area increases. A thorough understanding of the factors influencing infiltration and PCE is therefore essential for scale-up, as well as being useful for small-scale research. Even slightly inconsistent batch data would be problematic in a commercial setting, and large-scale benchmark performance losses would be catastrophic to production.

The following sections will provide an analysis on the potential factors influencing performance and infiltration, with the aim of creating a reference resource of methods for targeted problem solving and performance enhancement. A facile and non-destructive method for quantitative infiltration comparison is also introduced.

6.2 Experimental

Unless covered below, all measurements and sample preparation steps were performed as detailed in Chapter 2.

White light interferometry

White light interferometry was performed on ZrO_2 layers printed on FTO with the specified regime. Layers were annealed for 30 minutes at 400°C after a slow ramp and cooled to room temperature before white light measurements as specified in section 2.3.9.

Five-times magnification was used, giving a measurement area of 1.2 mm by 0.93 mm (at a resolution of 736 x 480 pixels with sampling at 1.67 µm intervals). Average surface roughness measurements (Sa and Sz) over the printed area were taken away from the edges. A total of 9 measurements were taken for each setting.

Electroluminescence measurements

EL was performed on fully fabricated unencapsulated devices after a 7-day settling period to attain peak performance. An FS5 Spectrofluorometer (Edinburgh Instruments) with Keithley 2401 Source Meter Unit were used for all measurements. All samples were measured under 3 V applied bias to obtain high emission. Excitation and emission bandwidths were 0 and 3 nm respectively, with a neutral density filter of O.D. 5 in the excitation pathway. A 700-850 nm range was used, with step size of 0.25 nm, 0.1 s dwell time. Images were obtained every 30s after bias application to monitor EL evolution. For current samples, a constant device current of 0.1A was maintained for 30 s before EL was measured.

6.3 Analysing the problem and identifying potential causes

Following the work in Chapter 4 on GVL-10MeOH precursors, batch performance was relatively reproducible, with average batch PCEs of 12-13.5%. Although slight variation was observed between batches and lab users, this was considered an unavoidable consequence of manual processes and ambient fabrication steps.

In March 2021, a significant drop in CPSC performance was observed in all precursor formulations across different lab users at two university sites (henceforth site 1 and 2). Both sites were using the same standard method and materials for CPSC fabrication presented in Chapter 2. Although all samples experienced a drop in device performance, devices fabricated at site 1 were particularly impacted, exhibiting the visually poor infiltration shown in Figure 6.1.

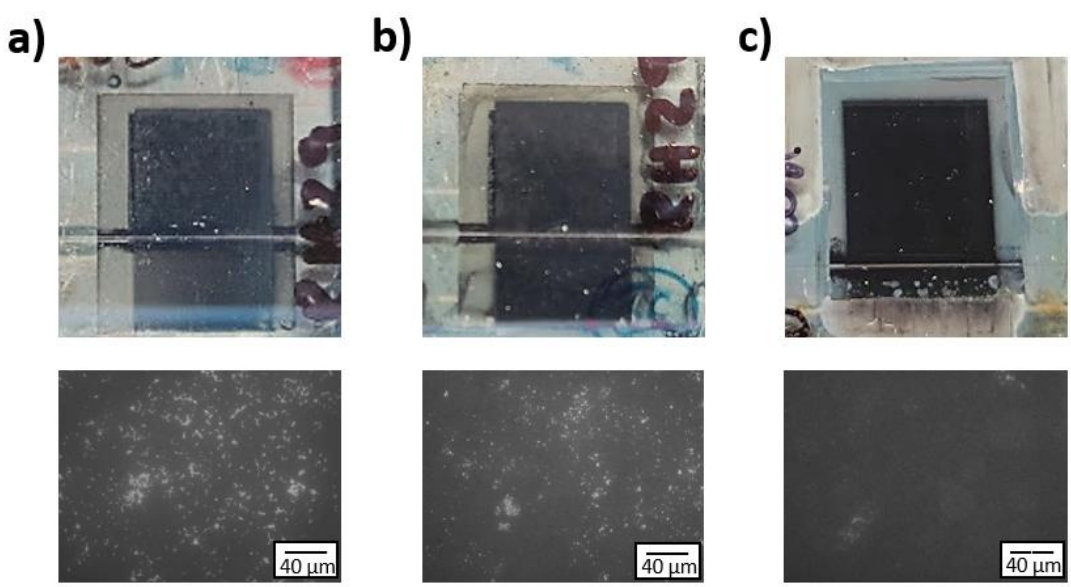

Figure 6.1: Photos and optical microscopy images of GVL-10MeOH devices infiltrated at sites 1 (LHS) and 2 (RHS) showing significant infiltration differences. a) GBL device fabricated at site 1, b) GVL-10MeOH device fabricated at site 1, c) GVL-10MeOH device fabricated at site 2.

Device performance at site 1 before and after problems began is shown in Figure 6.1, which shows a drop in all PV parameters. The performance drop was accompanied by a significant increase in hysteresis and batch variability. While some batches produced relatively reproducible PCEs of around 10%, others had visibly poor infiltration and average PCEs of ~5% with an extremely wide result spread. This chapter will examine the factors behind these changes to better understand the variables affecting infiltration and develop targeted strategies for infiltration enhancement.

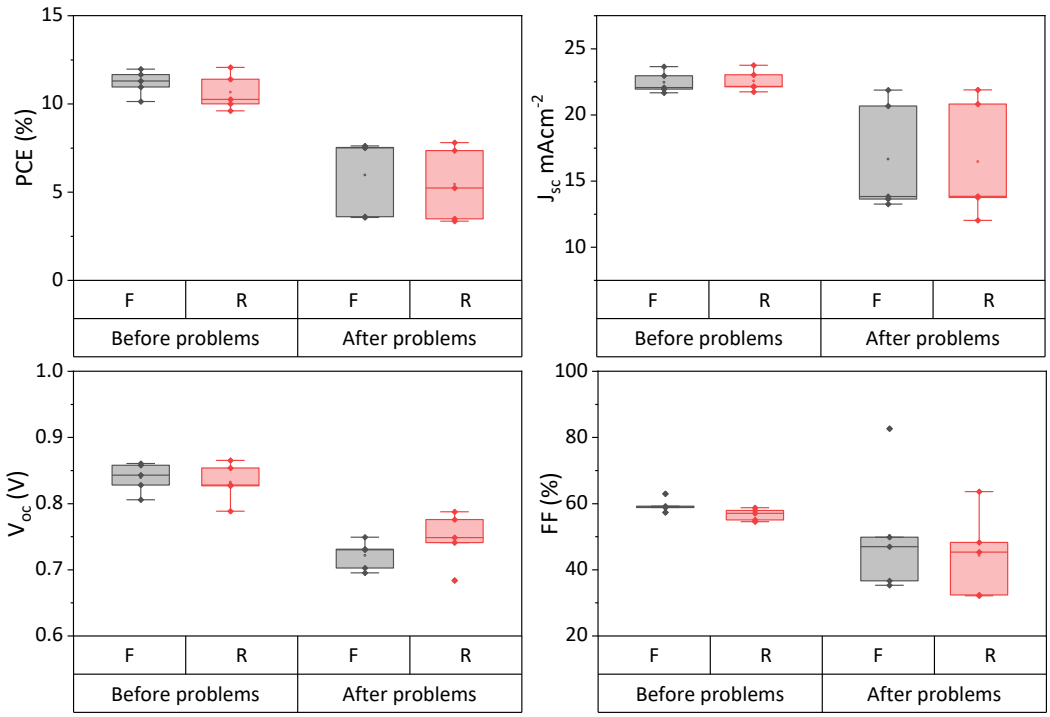

Figure 6.2: Box plots showing an example of photovoltaic parameters of standard stacks infiltrated with 1.1 M $AVA_{0.03}MAPbI_3$ in GVL-10MeOH before and after issues began at site 1.

To directly compare devices printed at different sites and ensure site 1 infiltration issues were not due to the infiltration environment, empty stacks were prepared at each site before concurrent infiltration at site 1. As in the previous batches shown in Figure 6.1, the site 1 devices exhibited both visually poor infiltration and performance loss, while the site 2 cells showed better infiltration and slightly improved performance. As shown in Figure 6.3, site 1 devices performed at 9.25% average PCE compared to 10.3% for the site 2 cells. However, all devices were significantly below the previous benchmark of 12.5-14% achieved in Chapter 4.

Consistent benchmark performance drops between batches, precursor formulations and group members is suggestive of a consistent change in one or more variables during fabrication. The isolation of infiltration issues to one site indicates that either the common problem is more severe at one site, or that several variables are contributing. Differences such as equipment calibration and cleanliness or environmental fluctuations may then exacerbate the issue to cause the poorer site 1 infiltration.

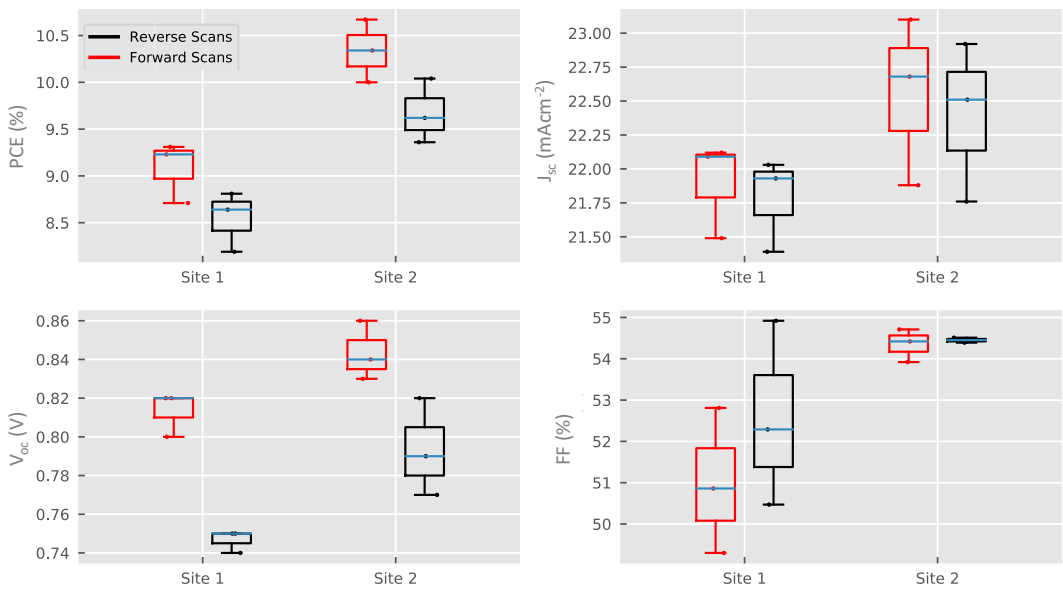

Figure 6.3: PV parameters obtained from devices printed at different university sites. Batches were infiltrated concurrently with the same 1.1M GVL-10MeOH precursor in the same environment.

The multiple ambient manual processes involved in CPSC fabrication introduce many potential causes. To thoroughly examine all factors, variables were split into three separate categories: precursor issues, environmental changes, and intrinsic stack issues, depicted in Figure 6.4.

Precursor issues

- Chemical contaminants
- Scale and stoichiometry issues

Environmental changes

- Humidity fluctuation
- Consistent annealing temperatures
- Airflow during infiltration

Intrinsic stack issues

- Contamination of equipment or damage of screens
- Paste issues
  - New ZrO_2 paste formulation: change in porosity or printing requirements.
  - Contaminants
  - Old Carbon paste- flake agglomeration, solvent loss.
  - Poor printer calibration producing sub-optimal prints

Figure 6.4: Separated bullet lists of the factors that could impact on stack infiltration and device performance.

Most simply, perovskite precursors could be causing problems. Slight changes in stoichiometry or concentration can impact on precursor viscosity or perovskite formation.[2]–[4] Therefore, poor scale calibration could easily disrupt infiltration and correct phase formation. Alternatively, chemical contaminants or degraded precursor components could affect percolation- for example, AVAI is essential to enable effective precursor wetting.[5]

Environmental impacts include anything that could change in the external environment during stack preparation, annealing or infiltration. This involves humidity, external temperature, hot plate consistency and airflow (section 6.3.1).

Finally, there may be an intrinsic issue within the stacks. Changes in paste age, formulation or the presence of contaminants could all affect printed layers, in turn impacting device function.

The prevalence and locational nature of the infiltration issues immediately discounts some of the above causes. For example, as shown previously in Figure 6.1, identical precursor batches applied to device stacks created at sites 1 and 2 produced very different results. Additionally, GBL and GVL-MeOH optimised systems produced devices of similarly poor visual infiltration (Figure 6.1), indicating that the issue is not linked to the solvent. This leaves environmental humidity fluctuations and intrinsic stack issues as the most likely contributing factors.

6.3.1 Determining the mechanisms behind poor infiltration

As shown in Figure 6.5, poor infiltration can be the result of two distinct mechanisms. In the first scenario (Figure 6.5b), some attribute of the stack, precursor or infiltration conditions must be slowing or preventing precursor access to the stack, leaving a large amount of uninfiltrated precursor at the surface. This layer would be exposed, leaving devices more sensitive to environmental changes. For example, increased airflow or ambient temperature could experience fast crystallisation of precursor atop the stack, preventing continued percolation during initial heating stages.

Alternatively, changes in carbon topology or precursor crystallisation pathways may favour surface crystal growth (Figure 6.5c). In this scenario, precursor is drawn up from the depths of the stack as surface crystals grow, to produce uninfiltrated voids.

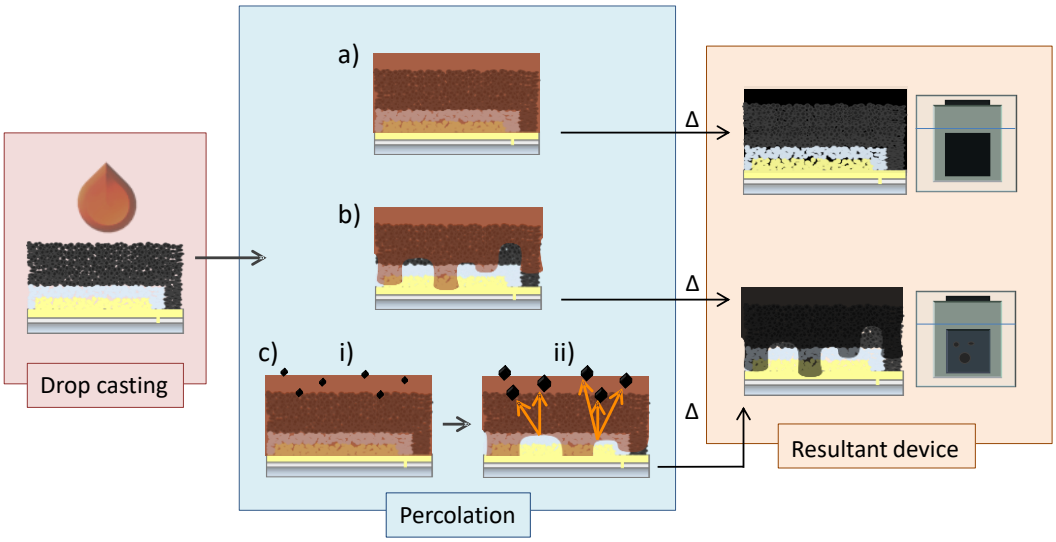

Figure 6.5: Diagrammatic representation of a) ideal infiltration, b) impeded infiltration and c) preferential surface crystallisation, with corresponding diagrams showing resultant device filling and visual appearance.

Determining which mechanism is at play could help diagnose whether the issue is related intrinsically to the stack. If problems are related to slow TiO_2 filling, increasing percolation time or slowing perovskite annealing may mitigate the issue. Conversely, samples experiencing preferential surface growth would likely not benefit from such changes. In this case, faster crystallisation may be beneficial, limiting the time in which precursor can leave the base layer. Here, longer percolation times would make little difference and slowly annealed devices would likely show no infiltration improvement. Such tests may also reveal a condition wherein these stacks can be well infiltrated. A set of experiments was therefore designed to examine the impact of crystallisation speed on infiltration.

Firstly, the annealing hot plate was set at 50°C and examined with thermocouples to examine surface temperature variation. As shown in Figure 6.6, a temperature variation of 1.5°C from front to back was observed, with all recorded temperatures lower than the set value of 50°C. As the hotplate was situated in a fume hood for perovskite annealing (with the cooler side towards the front), airflow was also likely different across the hotplate.

To ascertain that the infiltration issues were not exacerbated with the new GVL-10MeOH solvent mixes, this was performed first for GBL precursors. Infiltrated devices were placed on the hot plate and monitored to note the order of perovskite crystallisation (a 75% visual change from yellow to black in the mesoporous layers). After complete annealing, TiO_2 filling was examined with an optical microscope. Resultant images are presented in Figure 6.6.

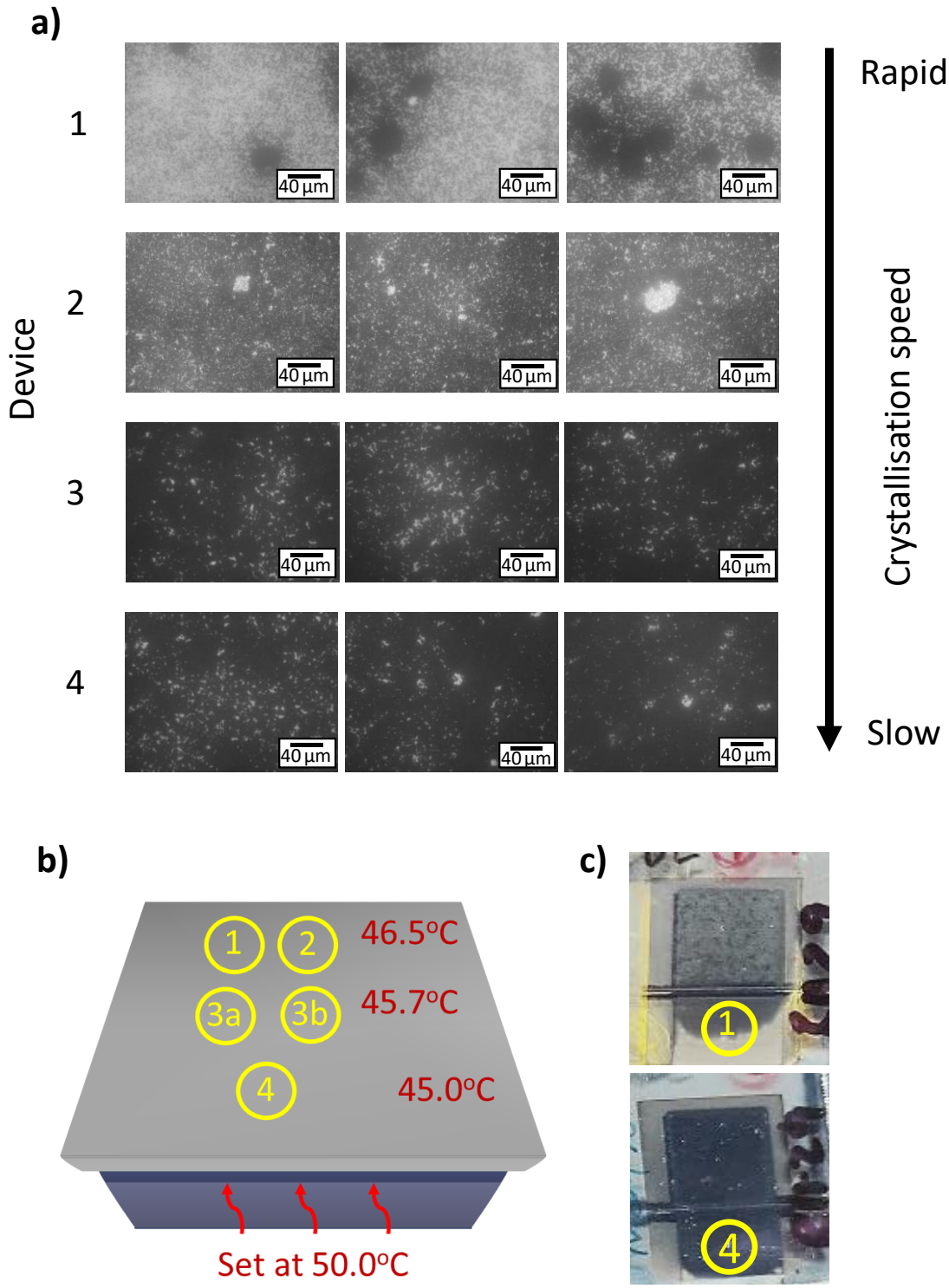

Figure 6.6: a) Optical microscopy images of devices from the same printing batch infiltrated with 0.95 M $AVA_{0.03}MAPbI_3$ in GBL (3 images for each device). Labels 1-4 refer to the order of device crystallisation. b) Diagrammatic representation of hot plate and device positions with corresponding measured surface temperatures. c) Photographs through the glass substrate of devices 1 and 4.

It is clear from these images that relative device crystallisation times corresponded to the hotplate temperature gradient, with those at higher temperature annealing significantly

faster.[14] These faster-annealed samples in turn exhibited significantly poorer infiltration, in agreement with literature observations (Figure 6.6, Figure 6.7).[6]

This was then repeated for the GVL-10MeOH precursors, to examine whether this system experienced worse issues. Conditions were the same, apart from a slight reduction of the GVL-MeOH annealing temperature (45°C) to correspond with the optimum conditions (Chapter 3). To attempt to slow crystallisation and better infiltration, a sample was also annealed at 35°C. Optical microscopy images of device TiO_2 layers are presented in Figure 6.7.

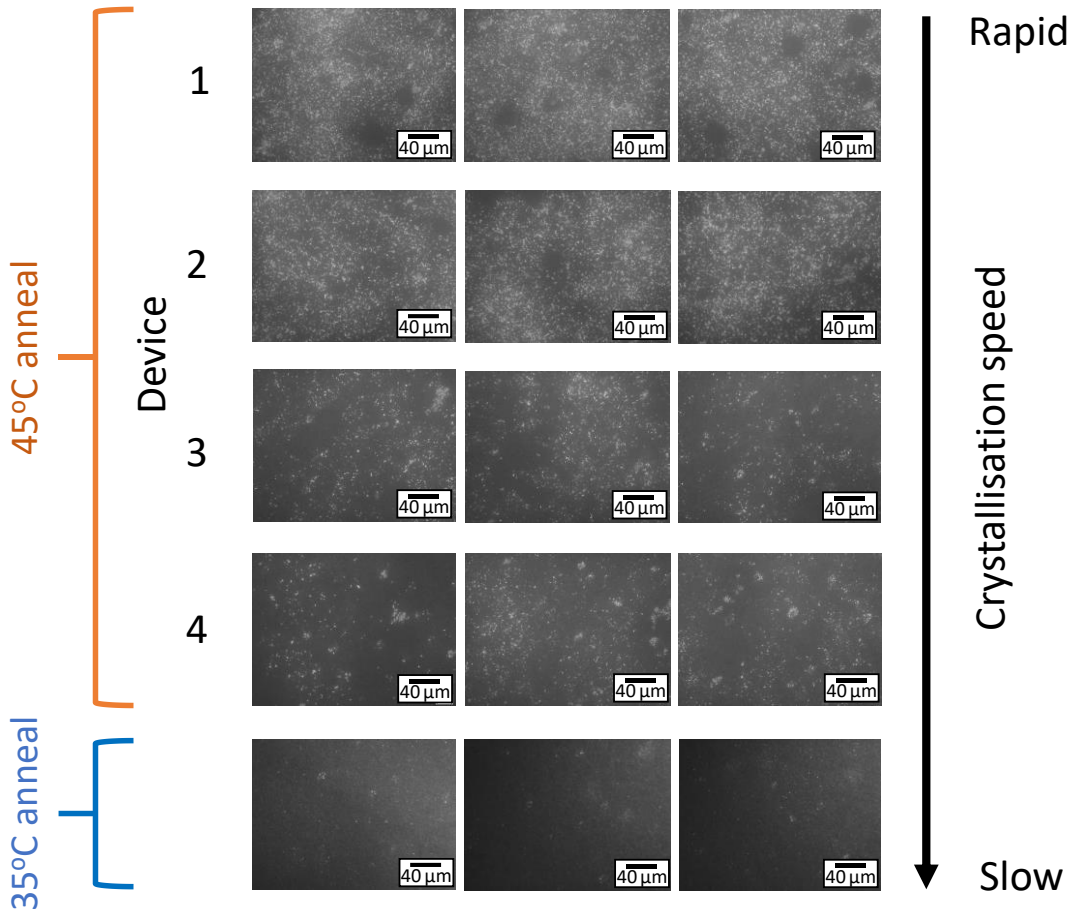

Figure 6.7: Optical microscopy images of the TiO_2 layer in devices from the same printing batch infiltrated with 1.1 M $AVA_{0.03}MAPbI_3$ in GVL-10MeOH and ordered according to crystallisation speed (3 images for each device). Devices 1-4 annealed together at 45°C according to optimised procedures (Chapter 3). The bottom device was annealed separately at 35°C.

[14] This represents an extremely narrow process window, not previously observed before problems began batches. It was later hypothesised that poor-quality prints produce samples more sensitive toward environmental fluctuation, thereby narrowing the process window and producing high variability at a low temperature differential. Print quality is discussed in section 6.6.

Once again, crystallisation speed correlated with the extent of TiO_2 filling. Only the 35°C sample came close to complete infiltration. This suggests that room temperature TiO_2 percolation is being considerably slowed or entirely prevented in these samples, implying an intrinsic stack issue is present. Encouragingly, infiltration was similar to the GBL samples in Figure 6.6, indicating that the new solvent system was not causing or exacerbating these problems. As the GVL-10MeOH solvent mix was found to be superior to GBL in Chapter 4, all devices presented henceforth were fabricated using this system.

To see if extending room temperature percolation times could improve TiO_2 filling, devices were left for different room temperature percolation periods before annealing at 45°C. If surface crystallisation is also impacting infiltration, longer room temperature percolation step should worsen the samples by providing more time for surface growth.

However, the PV parameters presented in Figure 6.8 show no significant impact on performance. PCEs and V_{oc} values were low across the batch, with significant hysteresis. It is therefore likely that room temperature percolation is being prevented, not simply slowed. Fast crystallisation at heat onset may then prevent further penetration during initial heating stages.

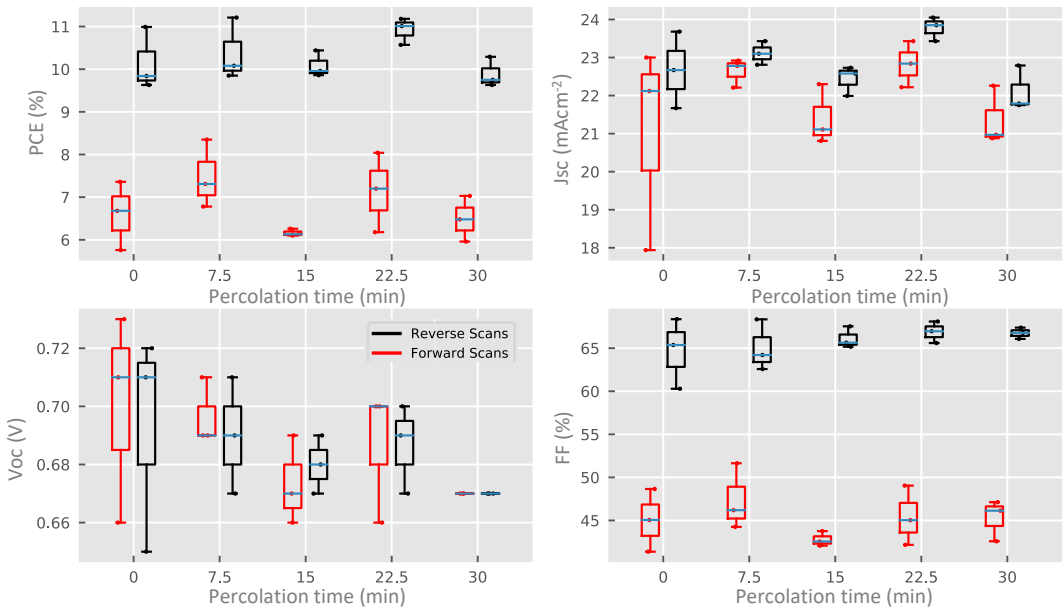

Figure 6.8: Photovoltaic parameters of devices left for different percolation periods (Forward: black, reverse: red). All stacks were from the same printing batch (fabricated at site 1). Three devices in each set.

Nucleation and growth can be slowed by limiting airflow or annealing in a solvent vapour environment. So-called 'solvent evaporation-assisted crystallisation' (SEC) processes have

been used to improve infiltration of a variety of poorly wetting non-AVA-based precursors.[7],[8]

However, annealing GVL devices in this way was found to reduce infiltration and thus performance in Chapter 2. A modified SEC procedure with a partial cover, depicted in Figure 6.9a, was therefore applied with the aim of limiting surface airflow while allowing solvent removal.

Photographs of resultant devices from sites 1 and 2 are presented in Figure 6.9b, where it is clear that site 1 devices experienced extremely poor infiltration regardless of the partial cover. Note that clear horizontal ZrO_2 printing inconsistencies were also present in these site 1 samples, indicating that site 1 printing procedures, inks, or equipment were producing uneven layers. Layer quality, printing parameters and ink behaviour are examined in sections 6.4 and 6.5. These cells exhibited such poor visual TiO_2 filling that devices were not subjected to further IV testing.

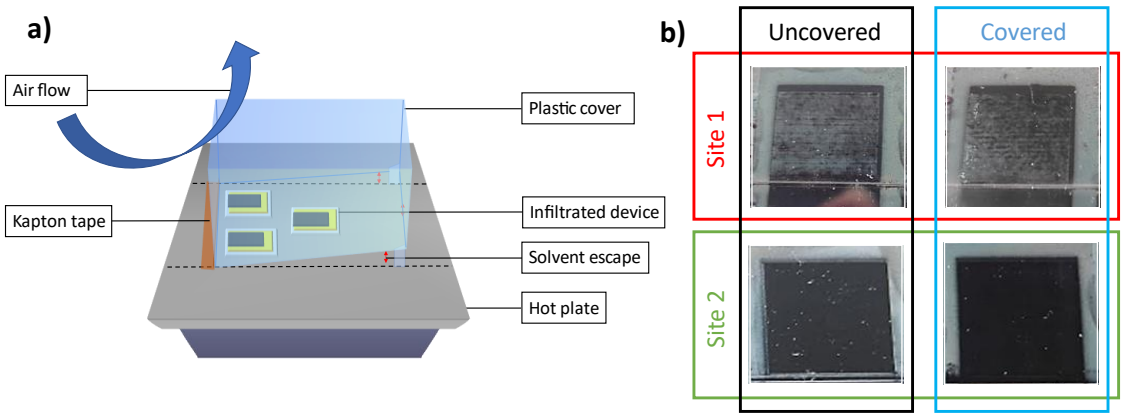

Figure 6.9: a) Diagrammatic representation of the modified SEC method with a partial cover. b) Representative photographs of devices from sites 1 and 2, annealed with and without the partial cover. Images were taken under 1 sun illumination and cropped from the same larger photograph to ensure comparable lighting.

Site 2 devices appeared well infiltrated and were therefore IV tested to determine whether limiting surface airflow had impacted performance (Figure 6.10). Higher and more reproducible PCEs were attained with partial covering due to increased J_{sc} and FF. This is suggestive of improved light absorption and perovskite-electrode contact, typical of superior infiltration.[9]

Limiting surface airflow was beneficial in site 2 devices, improving performance and reproducibility despite having limited impact in Site 1 devices. It should be noted that despite

improvements in benchmark performance, like performance to previous batches in Chapter 4 was not attained. Clearly, there existed some further variable limiting performance in these cells. However, as partial covering clearly had a positive impact in some cases, it was applied to all further batches. All devices presented henceforth were infiltrated using the partial cover unless specified. The specific impact of partial covers on more optimised stacks and a larger module is presented in section 6.7.

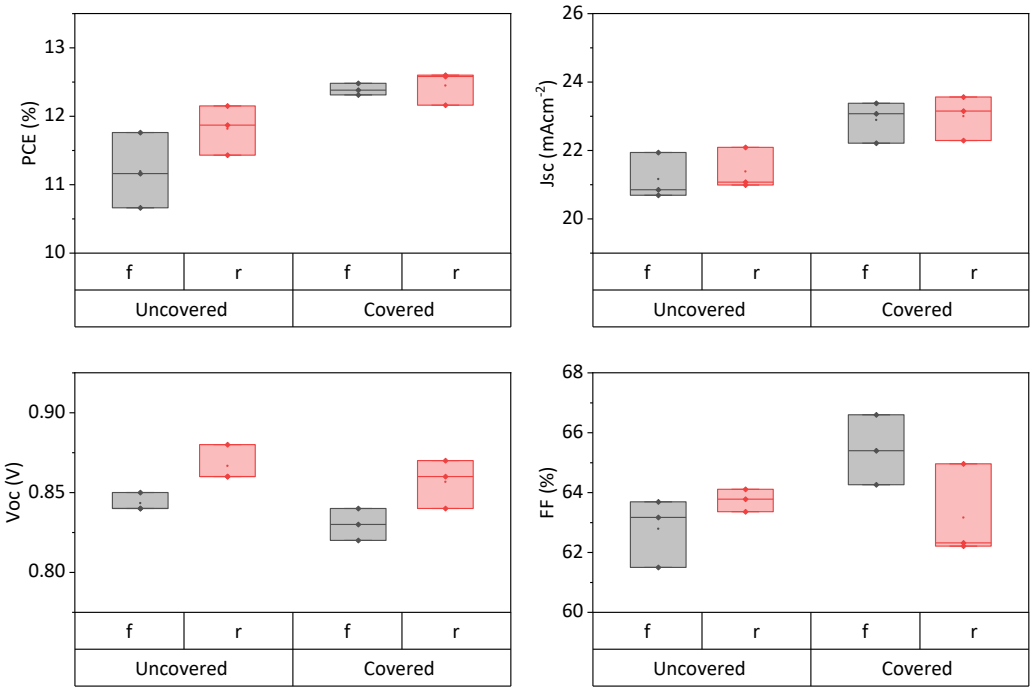

Figure 6.10: PV parameters of uncovered vs partially covered (modified SEC) devices printed at site 2.

The different effects of limiting surface airflow suggest that two different problems may be occurring, one causing benchmark performance loss at both sites and another producing severe infiltration issues at site 1. As site 1 devices exhibited some clear imperfections in the ZrO_2 prints, it was hypothesised that printing defects may be the cause of some of these issues. This is explored in detail in section 6.6. First, the following section establishes optical microscopy and paired image analysis as a method for quantifying infiltration, so as to enable more comprehensive infiltration comparisons moving forward.

6.3.2 Quantifying stack filling: the relationship between infiltration and performance.

It is clear in the preceding section that variable infiltration was causing significant performance issues in site 1 devices, with site 2 devices also experiencing benchmark performance and reproducibility issues. Poor infiltration causing low PCE is well established in the literature, where many publications on additive and solvent engineering cite superior infiltration as a main contributor to PCE and stability improvements.[1],[10],[11]

It is logical that devices with a greater uninfiltrated proportion of the base TiO_2 have low PCE, as uninfiltrated areas will reduce light absorption and have poor perovskite-electrode contact. Perovskite quality is also affected, with small inhomogeneous crystals reducing bulk transport, and increasing defect density and associated recombination. Previous work on multi mapping techniques has proven that TiO_2 infiltration directly impacts charge extraction, defect density and non-radiative recombination.[9]

Infiltration comparisons are generally presented in the form of qualitative images, using either cross sectional SEM or optical photographs through the glass substrate. While these methods can provide useful insight into stack filling, particularly where devices exhibit varied levels of infiltration, there are also significant drawbacks. [9],[12],[13]

For example, samples that appear visually similar in large scale optical images may present very differently when examined more closely using a microscope. For example, in this thesis, the site 1 infiltration issues detailed in the previous section were clearly visible to the naked eye. However, it is possible that the more subtle site 2 PCE losses were also a consequence of poor infiltration at a much smaller scale, something that would likely be missed without a more thorough high-magnification examination of devices. Performance differences due to slight infiltration changes may therefore be missed in many cases, potentially leading to erroneous conclusions as to the cause of PCE increases.

While changes in very small voids within the stack may be more closely examined with cross-sectional SEM, this is time consuming, destructive to the sample, requires specialist equipment and can be technically difficult. They also represent an extremely small portion of the sample: any given SEM cross section provides information about one linear micron long section of the device. In samples where infiltration varies significantly across microns or even centimetres, such images may not provide useful and representative data.

In an optimised industrial setting, infiltration variation between samples will likely be slight, requiring detailed, non-destructive analysis over large areas. These techniques would not be applicable in this case. Clearly, a fast, larger-scale, non-destructive method for infiltration comparison could benefit both lab scale research and larger-scale initiatives. With increasing academic and industrial focus on CPSC module manufacture such a technique could be essential for batch monitoring and quality control.

Optical microscopy and paired image analysis allows fast, large scale and non-destructive TiO_2 infiltration comparison via the glass substrate. Additionally, different size voids may be easily examined by altering magnification, potentially capturing information about multiple types of defect across a wide area. A method was therefore developed wherein optical microscopy images of the tested area were stitched and examined. As uninfiltrated areas are easily identifiable as white or light sections in the acquired image, percentage uninfiltrated area (UA) was easily calculated using image analysis and pixel binning (depicted in Figure 6.11). [15]

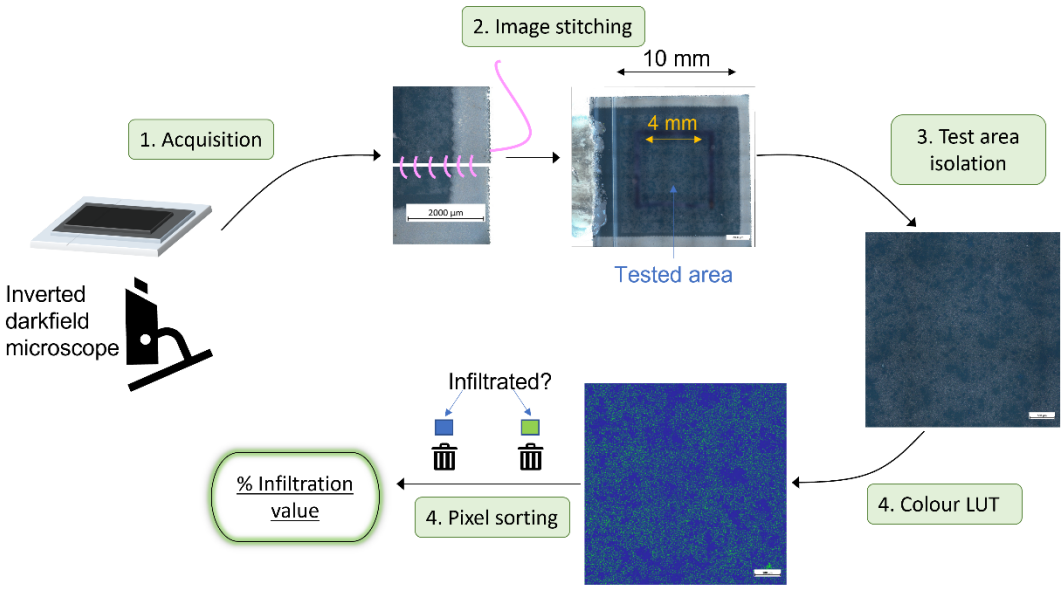

Figure 6.11: Diagrammatic representation of the process used for calculating %UA.

[15] It should be noted that % uninfiltrated areas presented here represent an average obtained from multiple images for each cell (unless stated). The image with the closest % uninfiltrated area to the device average has been chosen in each case to representatively display the optical characteristics of each sample.

Figure 6.12 shows optical microscopy devices of varied infiltration from the same print batch arranged in order of PCE, with the calculated %UA inset in each image (method used presented in Figure 6.11). It is clear from these images that PCE and TiO_2 filling are positively correlated, with better devices exhibiting less %UA. Remarkably even a device with >25% UA achieved 10.44% PCE. This result highlights how resilient CPSCs are towards changes in perovskite coverage: in classic sandwich architectures such poor coverage would drastically impact performance and lifetime.[14]

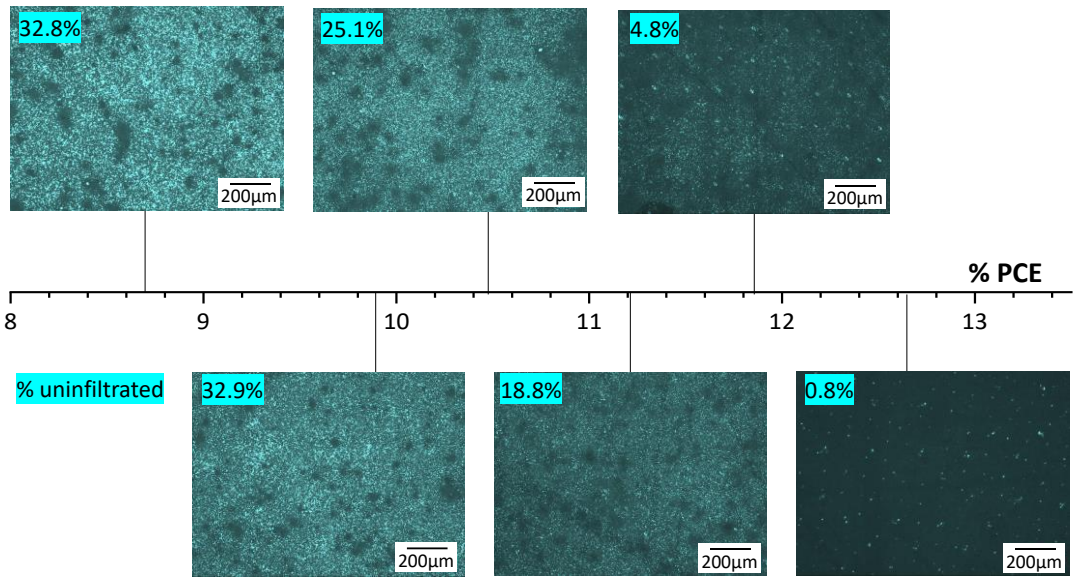

Figure 6.12: Optical microscopy images of filled TiO_2 of devices from a single print batch. PCE is indicated via the number line, %UA on each image. Image contrast-equalized and recoloured for easy comparison (image acquisition by Dr T. Dunlop, sample preparation, image editing and compilation by C.Worsley).

However, multiple other factors can impact performance: differences in ZrO_2 thickness and filling, alignment of graphite flakes, and perovskite contact with the top electrode may all impact performance, and would not be visible using this method.[13],[15]–[17] Additionally, observed filling at the base of the TiO_2 may not be representative of that deeper in the stack. Considering these factors, it was unknown whether uninfiltrated area calculated with this method would quantitatively correlate with performance- especially across multiple batches.

A more comprehensive analysis was therefore undertaken, calculating %UA for the entire tested area (4x4 mm) using the method outlined in Figure 6.12. Devices from multiple different print and infiltration batches were included, with samples from every section of this chapter. The materials and device composition are identical in all cases. Variations between batches include ambient humidity during infiltration (30-70% RH), ZrO_2 mesh size (130-34 vs

90-48), carbon ink dilution (0%, 5%, 10%), ZrO_2 thickness (1-2.6 µm) and ZrO_2 printing regimes (print print vs flood print).

As shown in Figure 6.13, plotting % uninfiltrated (inactive) area against PCE revealed a clear relationship. As % uninfiltrated decreases, PCE initially increases sharply up to 11.5% (~3% uninfiltrated), after which the rate of improvement is less marked. A non-linear Boltzmann fit gives an R^2 value of 0.995% for PCE values of 7.5-15%.)

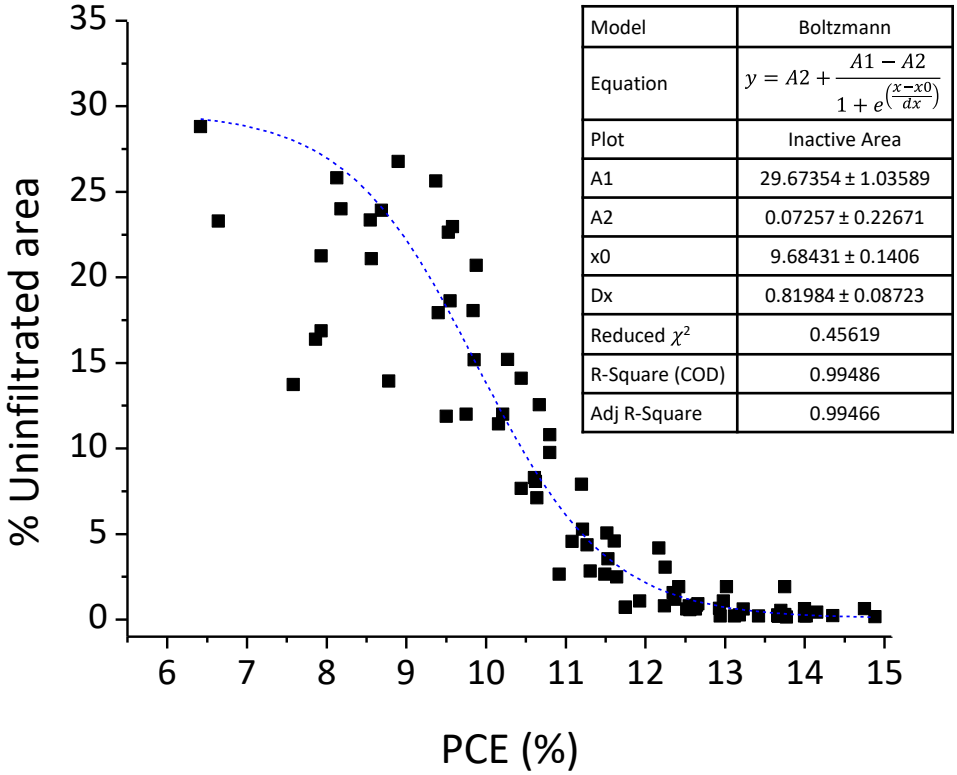

Model	Boltzmann
Equation	$y = A2 + \frac{A1 - A2}{1 + e^{\left(\frac{x - x0}{dx}\right)}}$
Plot	Inactive Area
A1	29.67354 ± 1.03589
A2	0.07257 ± 0.22671
x0	9.68431 ± 0.1406
Dx	0.81984 ± 0.08723
Reduced χ^2	0.45619
R-Square (COD)	0.99486
Adj R-Square	0.99466

Figure 6.13: PCE (%) vs % uninfiltrated area. Data for 72 devices are presented to maximise infiltration variation and observe whether different variables produced different trends. Variations between batches include ambient humidity during infiltration (30-70% RH), ZrO_2 mesh size (130-34 and 90-48), carbon ink dilution (0,5, 10%) and ZrO_2 thickness (1-2.6 um) and printing regimes (Flood print and print print), representing devices from all sections of this Chapter.

The greatest variance is present at above 5% uninfiltrated area (PCE<11%). This may be due to variations in infiltration pattern: a sample with small, dispersed crystals throughout the TiO_2 can provide the same overall uninfiltrated area as one with larger, interconnected grains confined to one section. However, performance may be quite different in such samples: Small, isolated crystals likely have a greater impact on charge transport and recombination due to poor interconnectivity and increased surface area. Refining the model to account for

crystal spread may allow improved PCE predictions at higher percentage uninfiltrated area, providing a basis for future work.

The appearance of a common trend between different batches is extremely interesting. Variables such as ZrO_2 thickness, graphite alignment and carbon thickness have all been shown to affect PCE, and are likely to vary between manually printed batches, particularly where differing print regimes are used.[13],[17]–[19] It was therefore expected that samples from different batches would produce distinct separate trendlines, for example samples with thicker ZrO_2 producing higher PCEs at given low levels of infiltration.

Instead, alignment of most samples with the general trend suggests that TiO_2 infiltration quality is the major predictor of performance here. It's possible that ZrO_2 thickness and other variables become important contributors to PCE once high-quality filling is achieved, producing different trends in such sets- although improved alignment with the trend at high infiltration % implies that this may not occur. In this case, these data suggest that for a given variable (e.g. interlayer thickness or perovskite formulation), infiltration should first be optimised before representative comparisons can be made. Alternatively, the sample differences in these sets may simply be minor enough not to induce significant deviation from the trend. A systematic comparison of %UA and performance of multiple batches with large ZrO_2 or carbon thickness variations, or different perovskite compositions provide a good opportunity for future work.

It is evident that in these samples, a significant trend exists between %UA and device performance. Infiltration can impact light absorption, bulk charge transport, recombination rate and charge extraction. Therefore, cells with low infiltration may perform poorly because of poor perovskite quality, low current generation, poor perovskite-electrode contact, or a combination of the above. The extent to which these variables contribute to performance losses here is unclear.

Perovskite quality at the base of the stack can be examined using electroluminescence (EL) imaging. On application of a bias voltage or constant current, higher quality perovskite layers will produce increased electroluminescence due to lower levels of recombination.[9],[20],[21] Additionally, bias or current application result in trap filling and ion movement, reducing non-radiative recombination and enhancing charge extraction and EL.[22]–[24] Samples with higher trap density and poor perovskite-electrode contact will therefore likely exhibit slower EL evolution.[23]–[26] Therefore, in the case of improved crystal quality, samples should achieve

high EL intensity quickly. Where poor quality crystals or low electrode contact is present, EL evolution will be slow and of lesser intensity.[23]–[26]

Three devices of visually varied infiltration were chosen for EL analysis. Relevant photographs, optical microscopy and magnified images of their infiltration quality, calculated uninfiltrated area and corresponding photovoltaic parameters are shown in Figure 6.14.

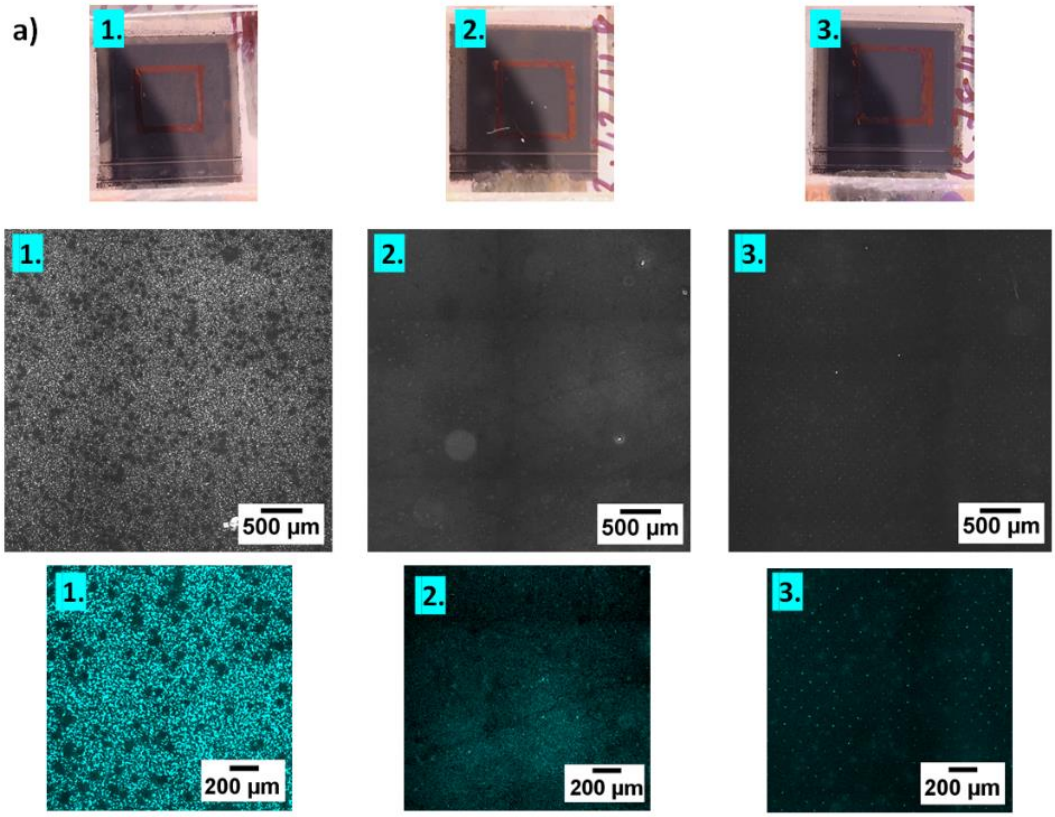

b)

Cell	PCE (%)	Voc (V)	Jsc (mAcm^{-1})	FF(%)	% Uninfiltrated
1	8.18	0.89	20.8	44.0	24.0
2	12.24	0.90	24.1	55.8	4.18
3	14.05	0.92	24.5	62.3	0.63

Figure 6.14: a) Photographs (upper), optical microscopy images (mid) and colour enhanced magnified images of three devices with varied infiltration. Mid-tier images show the entire tested area and were used to calculate the %UA in Table b). PV parameters are also shown in Table b). (Microscopy by Dr T. Dunlop, sample preparation, testing and image editing by C. Worsley).

Previous work has shown EL peak intensity to positively correlate with device V_{oc}- although this is not always the case in cells with non-selective contacts, where V_{oc} is generally

reduced.[20],[21] Based on the measured device performance (Figure 6.14), the highest EL intensity was expected from well-infiltrated sample 3.

Figure 6.15 shows the EL evolution at constant 3V bias and comparative images after 30s of holding a 0.1A of constant current. As expected, final EL intensity was highest in device 3, which is suggestive of more crystalline perovskite with less non-radiative recombination.[21]

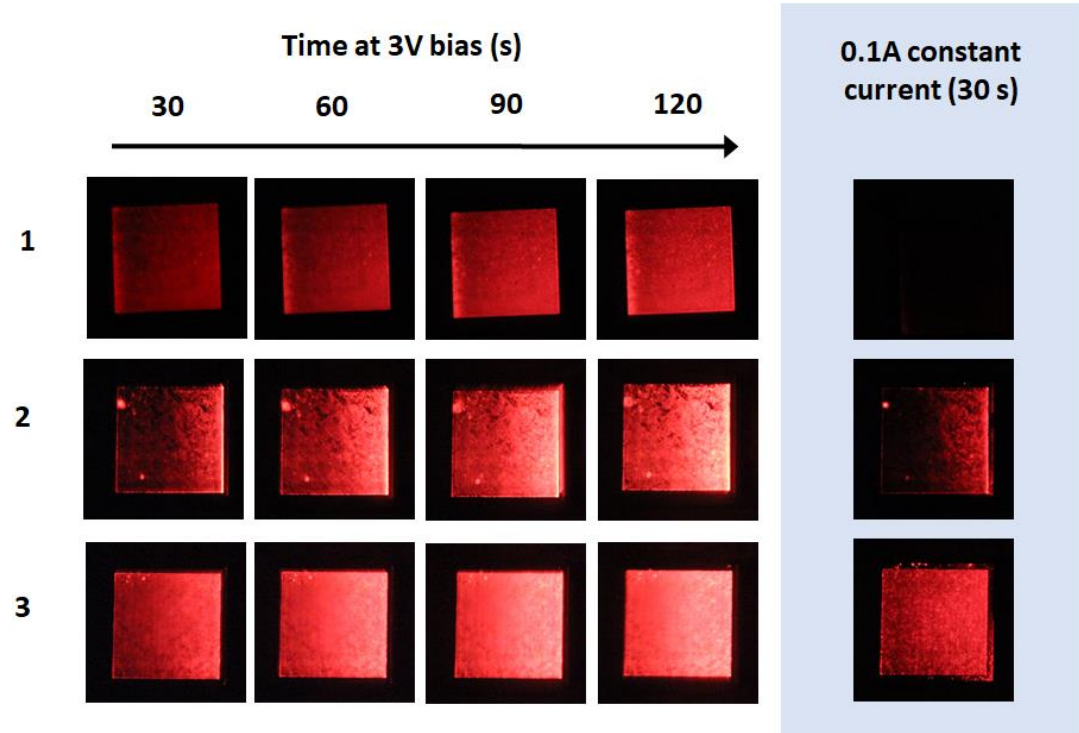

Figure 6.15: Electroluminescence images from devices 1, 2 and 3 of Figure 6.14, showing EL signal evolution with time at 3V bias (as this produced good response in all devices). EL emissions obtained after 30 s under 0.1 A constant current. EL measurements by Dr. R. Garciarodruigez, sample and image preparation by C.Worsley.

The well infiltrated device also exhibited faster EL evolution: cell 3 is bright at 30 s and shows little change after 60 s, while cell 1 changes throughout without reaching significant intensity. The difference in response time and signal intensity is even more marked under constant current, where sample 1 failed to produce any significant emission after 30 s at 0.1 A. Coupled with the drop in device FF, this result indicates that interfacial charge transfer is significantly impacted perovskite as infiltration decreases.

It should be noted that all devices showed brighter emission near the carbon electrode during initial measurements. This could be a consequence of charge accumulation and thus faster trap filling at the relatively resistive and poorly selective carbon contact.

Interestingly, comparison of optical images revealed very little correlation between uninfiltrated areas and low EL. Even in the poorly infiltrated sample, where uninfiltrated areas were clearly visible to the naked eye, surprisingly homogeneous emission was observed (Figure 6.14). This may be due to bare TiO_2 reflecting EL from surrounding perovskite. Alternatively, observed signals may originate from perovskite deeper in the ZrO_2 layer. Determining which is the cause here would require a higher resolution EL imaging capability (such as a microscope).[27]

These EL results indicate that poor infiltration impacts performance and slows device response through increasing non-radiative recombination, likely driven by limited electrode contact and higher trap density in high %UA samples. This explains the loss of V_{oc} and J_{sc} in cells of limited infiltration

This section has established that base TiO_2 infiltration can be quantitively linked to device performance. Critically, this samples from different batches were shown to follow a general trend, suggesting that some variables known to impact device performance (such as ZrO_2 thickness) have a much lower impact when infiltration is sub-optimal. This implies that for meaningful comparison between other variables (eg. Perovskite composition or layer doping), infiltration should first be optimised for a given system.

The following sections will focus on how infiltration is impacted by various environmental and fabrication procedures during device production, using qualitative and quantitative optical analysis as a tool for monitoring device quality.

6.4 The impact of ambient humidity during infiltration

Infiltration changes between sites using identical equipment and materials suggest that environmental variation could be contributing to performance differences. This is especially relevant to CPSCs, as all printing, annealing and infiltration steps are carried out in ambient conditions. Devices may therefore be significantly impacted by changes in ambient temperature, airflow or humidity. Although previous observations of uneven site 1 ZrO_2 prints (as presented in section 6.2) were indicative of potential printing issues, an initial study into the potential contribution of environmental changes was performed to confirm whether this could also be contributing to batch inconsistency.

Ambient laboratory temperatures were found to be consistent during the relevant timeframe (18 ± 2°C in the lab) and were therefore deemed unlikely to have impacted the devices.

However, humidity was particularly inconsistent on both sites, frequently fluctuating between 25% and 75% during each week. Figure 6.16 shows the indoor and outdoor humidity variation over a two-week period at site 1 (where all small-scale devices presented in this thesis were infiltrated).

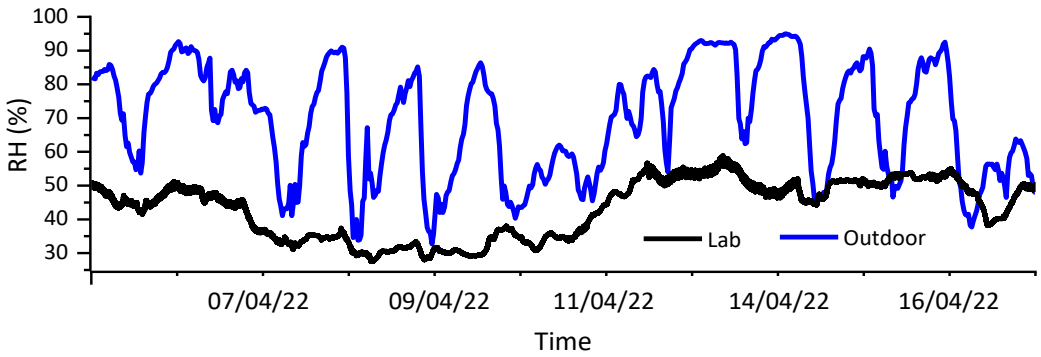

Figure 6.16: Outside humidity variation at a university site over a two-week period in April 2022. Tick lines marking dates correspond to time 00:00:00 of the relevant date.

In GBL-based $AVA_{0.03}MAPbI_3$ devices, ambient humidity exposure is known to recrystallise perovskite within the stack: many groups employ 70% RH treatments to improve PCE and reduce hysteresis.[1],[28],[29] In separate work on the impact of NH_4Cl precursor additives in CPSCs, increased ambient humidity was found to be essential for conversion of the solid intermediate to $MAPbI_3$.[30]

These prior works focus on humidity exposure post-perovskite crystallisation. However, devices are also exposed to ambient humidity throughout printing, annealing and stack infiltration. Although the high temperature annealing steps for binder removal (≥400°C) will remove adsorbed water between prints and after storage, impactful exposure to water vapour could still occur when devices are cooled to room temperature prior to infiltration.

To test whether this could impact devices, cells were cooled in ambient conditions (29% RH, 18-20°C) or a humidity oven (70%, 25°C) directly after carbon annealing prior to infiltration. After 5-10 minutes at each humidity, devices were removed to ambient conditions and immediately infiltrated and annealed. This was performed separately on uninfiltrated devices from both sites 1 and 2. The experimental regime is depicted in Figure 6.16.

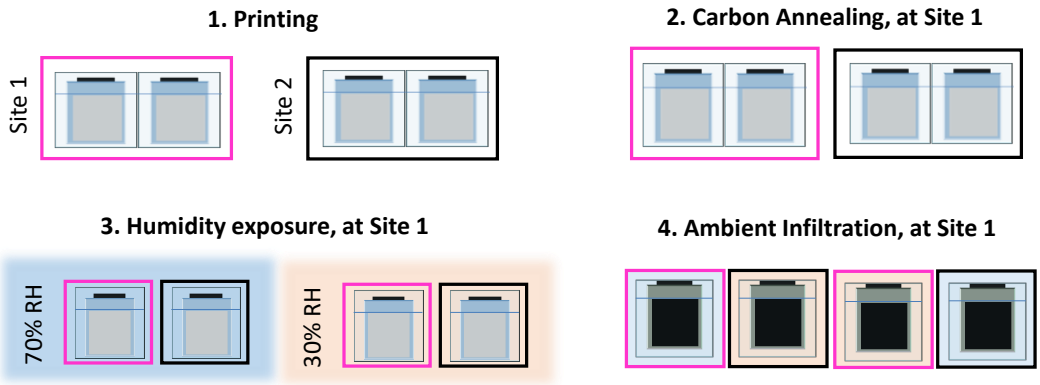

Figure 6.17: Schematic of the experimental regime for pre-infiltration humidity exposure.

As shown in Figure 6.18, both ambient and high-humidity exposed stacks from site 1 demonstrated similarly poor infiltration to prior batches. Ambient humidity variation prior to infiltration is therefore unlikely to be behind the site-specific problems discussed in sections 6.1 and 6.3, and infiltration was so visually poor in all samples that devices were not progressed for IV testing. However, humidity variation prior to infiltration may well be contributing to minor inter-batch variations in higher quality devices.

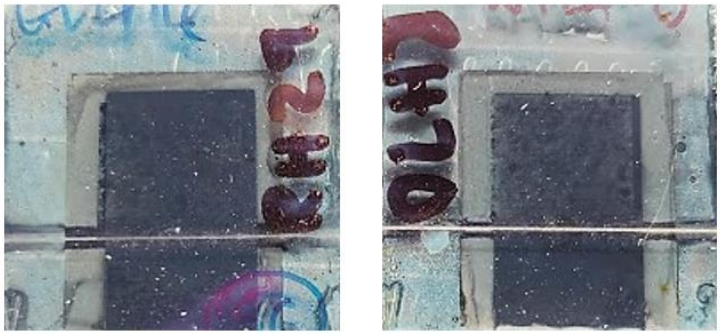

Figure 6.18: Poorly infiltrated devices printed at site 1. Devices were infiltrated with 1.1 M $AVA_{0.03}MAPbI_3$ in GVL-10MeOH after cooling for five minutes in 29% RH (ambient) or 70% RH (humidity oven).

This appears to be the case in Figure 6.19, which shows PV parameters of the site 2 samples. 70% RH exposure prior to infiltration proved beneficial in site 2 cells, with ambient (36%) devices exhibiting an average PCE of 10.32% compared to 9.90% for ambient controls. Slight J_{sc} and V_{oc} improvements were present, as well as significantly more reproducible FF.

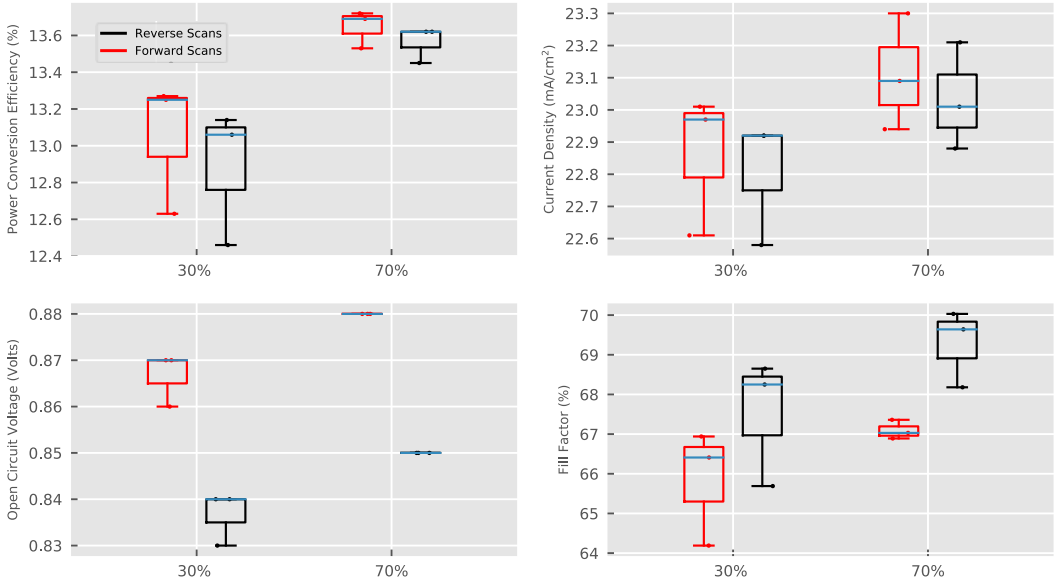

Figure 6.19: PV performance of $AVA_{0.03}MAPbI_3$ GVL-10MeOH devices from the same printing batch (fabricated at site 2), cooled at 36% RH (ambient) or 70% RH (humidity oven). Four devices in each set.

Figure 6.20 shows optical microscopy images and calculated %UA for two devices from this batch. Although TiO_2 filling appeared visually similar to the naked eye, optical analysis revealed superior infiltration at the micron scale in the 70% devices, explaining the improved performance seen in Figure 6.19.

This infiltration improvement suggests that ambient water vapour can enter the stack prior to infiltration, potentially adsorbing on the hydrophilic metal oxide surface. As GVL is hygroscopic, this may enhance precursor wetting of these layers, improving small pore filling in the site 2 devices.

a)

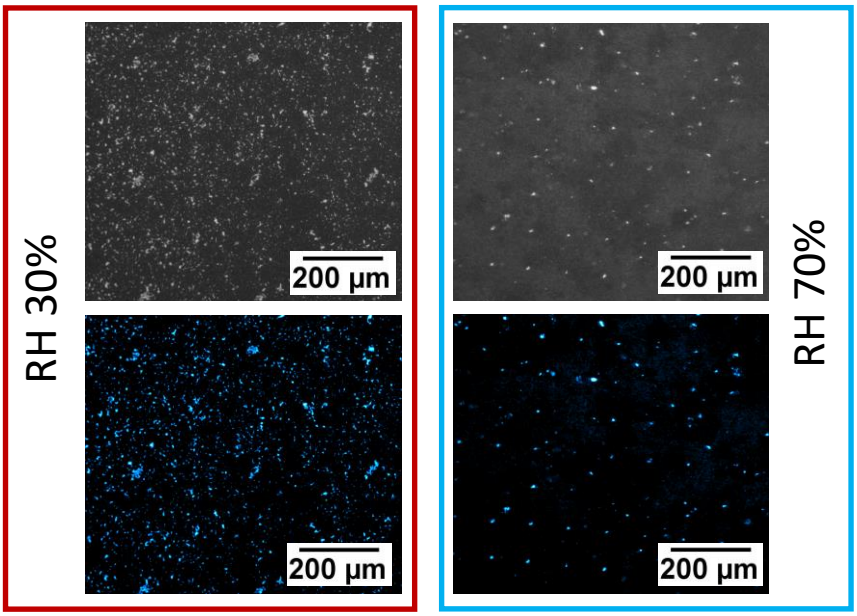

b)

%RH	Average %UA	Max %UA	Min %UA
30	10.15	25.00	2.94
70	2.32	11.54	0.81

Figure 6.20: a) Optical microscopy images showing devices infiltrated after cooling at 30% or 70% RH. Colour images shown for improved clarity. b) Table showing the average, minimum and maximum %UA across devices infiltrated after cooling in 30% (ambient) and 70% (humidity oven) RH. [16]

However, despite performance enhancement with increased RH, device performance was far below the previous benchmark of 12-13% PCE. Therefore, while humidity changes may account for some performance variation between normal batches, it is not likely the root cause of the problems under investigation here- hence why no significant improvement was observed in the site 1 batch.

After several weeks of ambient dark storage, it was noted that the 70% devices consistently exhibited significant yellowing in the ZrO_2 interlayer, while no PbI_2 formation was observed in the ambient 30% devices (Figure 6.21).

Ambient water vapour is well known to cause significant degradation in PSCs.[31] Although the hydrophobic carbon electrode AVA grain boundary passivation improves $AVA_{0.03}MAPbI_3$ CPSC stability towards ambient humidity, exposure to water vapour can still accelerate degradation.[31],[32] The annealing temperature of 45°C is not high enough to remove potential

[16] The cause of the characteristic spaced infiltration defects is examined in section 6.6.

water adsorbed prior to infiltration. Therefore, the 70% RH devices may have experienced faster degradation due to water retained in the infiltrated device.

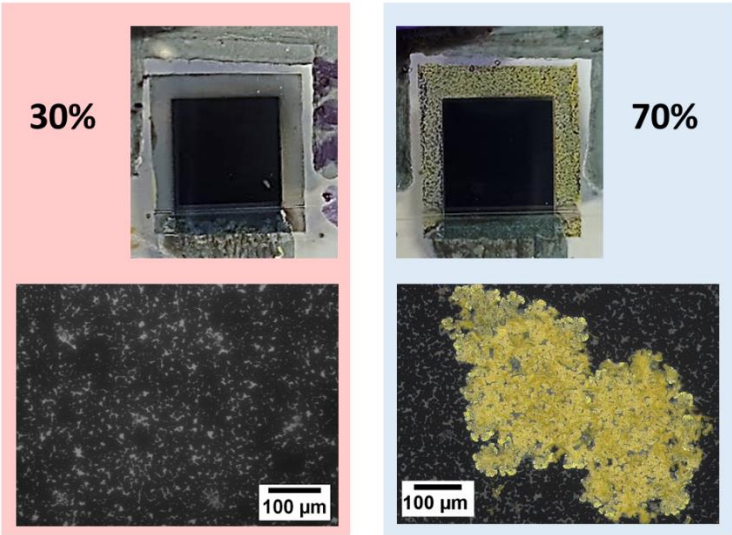

Figure 6.21: Representative photographs and optical microscopy images of devices infiltrated after cooling at 30% or 70% RH after several weeks of ambient storage.

Increasing RH prior to infiltration may therefore improve short term performance to the detriment of stability and should be applied with caution. Possibly, there exists an intermediate RH that can offer improved infiltration without accelerated degradation. Although not relevant to solving the particular issues explored in this Chapter, this provides a potential basis for future work.

This work eliminates humidity fluctuation as the cause of the benchmark performance losses and infiltration issues under investigation here. As humidity represents the only significantly variable environmental factor identified outside the stack, it follows that the cause must be related to an intrinsic change within the printed device. This will be examined in the following sections.

6.5 Paste batches and formulations

As discussed in the previous sections, a significant drop in benchmark performance was observed across two university sites, with devices from site 1 experiencing significant infiltration problems.

During investigations into these performance issues, it was noted that some site 1 devices were exhibiting printing flaws not observed before problems began. This is suggestive of a

materials or processing change. [1],[17] As no such change had occurred in the printing method, the paste supplier was contacted for information about possible paste formulation changes.

It emerged that a nanoparticle supplier change had been made to the Solaronix Zr-Nanoxide ZT-SP paste although it was claimed that paste binders and solvent formulations remained the same. However, as nanoparticle shape and surface charge can have a significant impact on paste viscosity, this could still have impacted paste rheology enough to impact printing requirements.[33]

Such changes could also make the new paste more sensitive to small differences in printer calibration or setup, resulting in the site-specific infiltration issues. For example, should the new paste be more elastic, it would be more susceptible to filamentation during printing, causing increased mesh marking and rougher layers. Filamentation occurs when printed ink adheres to the separating screen, producing strings of ink that then snap as the screen departs to leave inconsistent layers. This frequently occurs at mesh crossover points, leaving characteristic spaced peaks or troughs in the layer, referred to as mesh marks.

Paste rheology can be compared using viscosity profiles, where viscosity is measured during paste exposure to shear force. Additionally, elasticity (and thus susceptibility to filamentation) can be compared by examining the phase angle and shear modulus, which examine the responsiveness of the paste to applied shear forces. Figure 6.22a shows the viscosity profile of the old and new inks, with accompanying phase angle (b) and shear modulus (c) data.

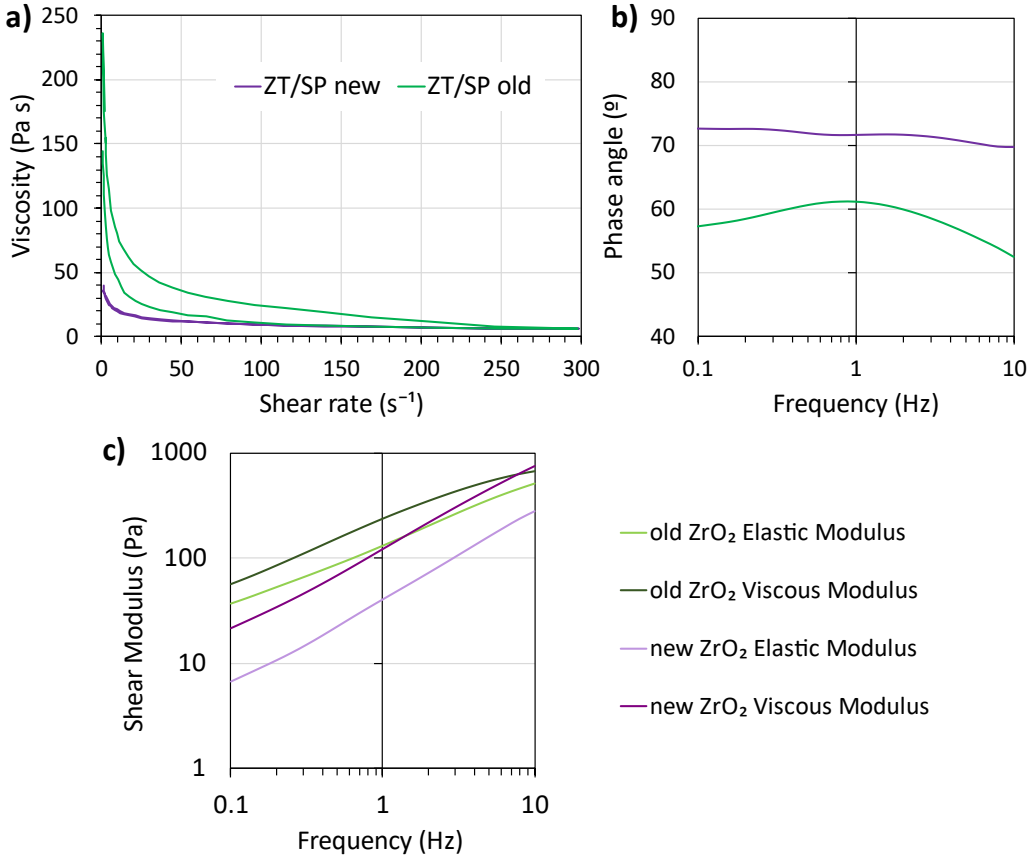

Figure 6.22: (a) Viscosity profiles of the new and old ZrO_2 paste formulations, with accompanying viscoelastic profiles, examining the change in phase angle (b), storage modulus and loss modulus (c) of the new and old ZrO_2 paste formulations. Measurements by Dr. S. Potts.

There is a clear difference in the viscosity profiles, with the new ink rest viscosity around 200 Pas lower than the older ink. The original ZrO_2 paste had a rest viscosity of around 230 Pas, which reduced to around 6 Pas at a shear rate of 300 s^{-1}. During testing, the most significant viscosity reduction for both inks occurred between rest and 60 s^{-1}, falling by around 200 Pas. This continued to drop at a lower rate until 300 s^{-1}, where final viscosity was comparable for both inks at ~6 Pas. Significant hysteresis was observed when reducing viscosity back to rest for the old ink, due a long ink recovery time.

Ink viscosities were only comparable after significant shear force. Therefore, if the older ink was pre-sheared at very high speeds, it would produce similar film thickness and roughness to the new formulation. However, in practice neither manual stirring, nor printing are conducted at high enough speeds for this to occur. The formulations therefore likely exhibit extremely different viscosities during lab-based prints and may thus produce very different printed layers.

The phase angle of the original ink varied between 52° and 61° with changes in frequency, whilst that of the new formulation varied between 70° and 73° (Figure 6.22b). Higher phase angles are indicative of a reduced elastic response and are associated with less filamentation during printing. [34] The variation in phase angle with frequency was also less significant for the newer ink, so changes in printing conditions would have a less significant impact on elastic response than with the older formulation. This indicates that, when deposited with an appropriate printing regime, the newer ink should be less prone to mesh marking and show better reproducibility between batches. [34]

However, crucially, the change in elastic response and rest viscosity likely render the previous standard printing regime (two print passes, each with a hard squeegee using a fine (130-34) mesh)[17] unsuitable. Tailored for a much more viscous paste, this may produce rougher, thinner films when applied to the new ink. As detailed in Chapter 1, thick ZrO_2 layers of up to 4 µm are reported as optimal in the literature, so a drop in thickness could explain the drop in benchmark performance observed at site 2.

It was suggested that nanoparticle changes could also have impacted layer porosity. Drops in ZrO_2 pore diameters or surface area could affect precursor penetrating the interlayer and accessing underlying TiO_2. Annealed films were therefore subjected to Brunauer-Emmett-Teller (BET) surface area analysis.

Pore distribution plots, shown in Figure 6.23 show highly variable results between samples. This is likely due to the nature of the samples: films must be scraped off to form a powder prior to analysis. The way the powder settles can then skew pore distribution data at the macro scale, with close sitting particles acting as large mesopores during adsorption, skewing distribution data. Surface area values should however remain comparable, as this will not change depending on particle alignment within the powder.

[17] The numerical nomenclature for screen designs refers respectively to the density and diameter of threads used to form the mesh. For example, a '130-34' screen will have 130 strings per cm mesh, each with a diameter of 31 µm.

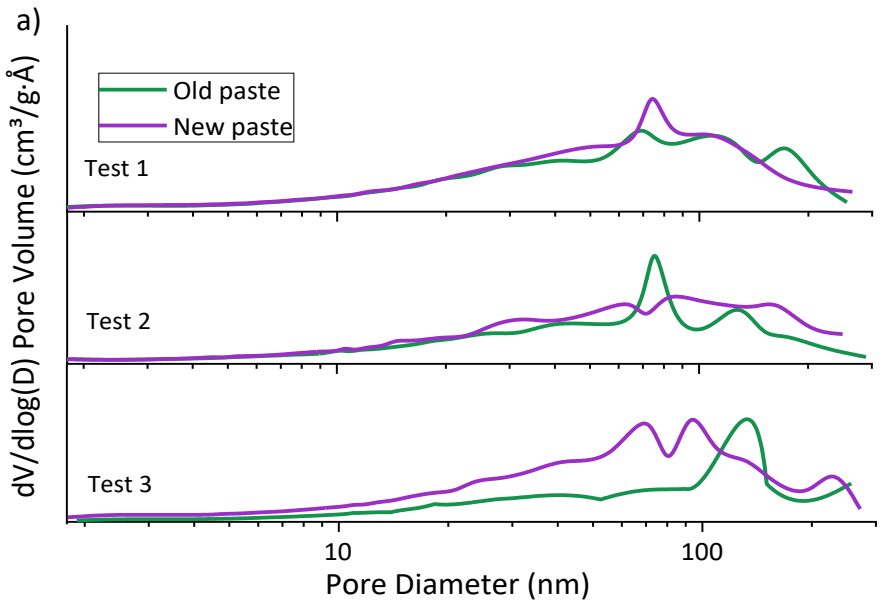

b)

Paste	Avg BET surface area m^2g^{-1}	Mean average pore width (nm)
old	42.55 ± 0.70	16.06 ± 0.97
new	39.41 ± 0.76	16.30 ± 0.74

Figure 6.23: a) BET pore distribution plots of solid annealed old and new ZrO_2 films from different samples on three separate days. b) Table with average calculated BET surface areas and mean average pore widths.

Presented in the underlying table, average ZrO_2 BET surface areas of powders from the old paste were consistently higher than those fabricated of the new ink. However, this difference accounts for less than a 1.5% change in surface area and mean average pore widths were not significantly changed. This suggests that the paste nanoparticle composition has not changed significantly: much larger or smaller particles would likely have obvious impact on pore size and surface area. Observed infiltration issues are therefore not likely due to significant changes in film porosity.

Additionally, the drastic differences in viscosity and elastic response are more typical of a binder or solvent change. This could easily impact both print quality and film annealing requirements, respectively resulting in poor quality layers or problematic residual binder.[35] Thermogravimetric analysis was therefore performed on each paste.

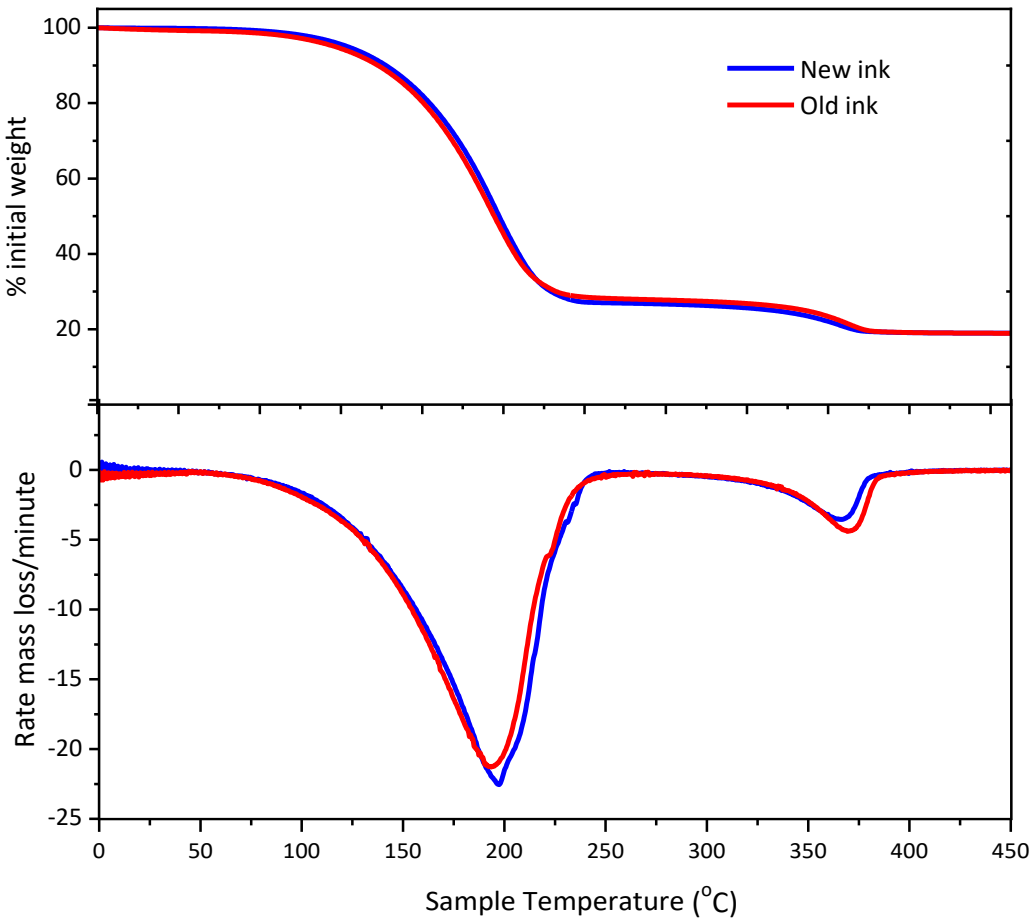

Figure 6.24: Thermogravimetric mass loss from new and old ZrO_2 formulations (top) with accompanying derivative plots (bottom). Scan rate 20°Cmin^{-1} Note that the sharp peak at ~240°C is likely an artefact related to equipment disturbance during measurements.

As shown in Figure 6.24, overall % mass loss from both samples was identical, indicating that overall non-ZrO_2 content is the same in both pastes.

Solvent and binder percentages were alike between the samples, with each paste showing ~70% solvent mass and ~10% binder. There may be very slightly less mass % binder in the new ink, as the binder peak at ~375°C was marginally lower than that of the old pot. However, this difference is very small, and thus unlikely to have caused any significant change in paste rheology. Additionally, no mass loss occurred after ~390°C in either paste, suggesting that binder removal was complete by this temperature. The current annealing process (400°C hold for 30 minutes) should therefore be sufficient to ensure complete binder removal in cells.

The change in nanoparticle supplier must therefore have caused the observed rheological differences. In Al_2O_3 nanofluids, less spherical nanoparticles have been shown to produce

more viscous solutions, while partial aggregation to form low concentrations of high aspect-ratio aggregates have low concentrations of high aspect-ratio aggregates have a similar impact.[33] Potentially, changes in nanoparticle shape with the new supplier, or partial agglomeration within the old paste may have affected viscosity.

As the annealed ZrO_2 samples did not exhibit significantly different BET surface areas or paste composition, the infiltration and performance issues are likely due to changes in print quality. This is likely a consequence of the rheological data presented in this section, which show significant viscosity and elasticity changes in the new ink. The next section will compare the impact of different print regimes on film thicknesses, topologies and performance in devices fabricated with the new ink.

6.6 Changing printing parameters

6.6.1 The influence of layer thickness and mesh selection

As detailed in section 6.5, the newer ZrO_2 ink has much lower initial viscosity, is less elastic, and is less susceptible to change in shear rate. Although this should make prints with the new ink more reproducible, the printing requirements are also likely very different. Due to lower viscosity, printed layers of the new formulation are likely thinner and may exhibit different topology.[34] Of particular concern was the potential for mesh marking, characteristic spaced peaks or troughs across the film left by the screen mesh on the print surface. This can potentially impact device performance and infiltration by reducing precursor wetting. Observed marks will correspond with the mesh dimensions of the relevant screen. Therefore, if different screens have been used for TiO_2, ZrO_2 and carbon, mark spacing can be measured to conclude in which layer the problematic marks reside.

Devices fabricated with each paste were therefore optically examined for evidence of mesh mark related infiltration defects. As shown in Figure 6.25, devices fabricated with the new formulation exhibited poorer infiltration across the general area, as well as at regularly spaced intervals. Aligning with the dimensions of the 130-34 TiO_2 and ZrO_2 screens, these voids are likely a consequence of mesh marking. As both these layers were deposited with a similar 130-34[18] mesh, it is not possible to identify specific ZrO_2 marks in either sample.

[18] This numerical format refers respectively to thread density and diameter. So, a 130-34 mesh will have 130 threads per cm^2, each with a diameter of 34 µm. This is finer than a 60-64 mesh, as the threads are of lower diameter.

However, the new formulation device exhibits two distinct sets of significantly larger marks, proving that ZrO_2 marking has more severely impacted infiltration.

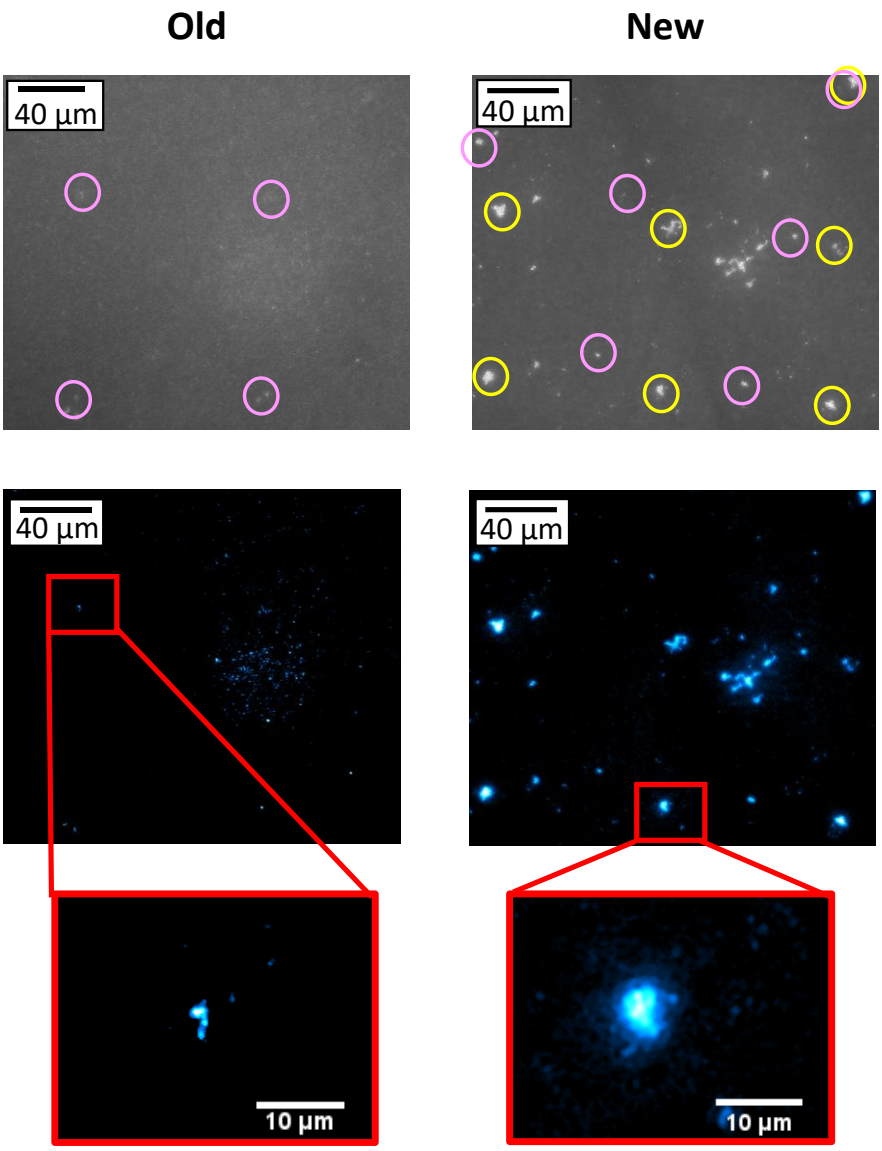

Figure 6.25: Optical microscopy images of infiltrated device showing clear infiltration defects caused by mesh marking. Top images show original photos, with flaws due to mesh marking circled yellow. Mid-tier shows coloured image, with mesh marks infiltration defects magnified in the bottom images.

Infiltration problems across the general area often occur due to increased ZrO_2 thickness, as the precursor must travel further to fill the base TiO_2 electrode. However, the rheological analysis presented in section 6.5 suggested that the new formulation would likely produce thinner layers, which are generally considered easier to infiltrate. However, this can also be problematic for performance, as thin ZrO_2 can decrease performance through increasing minority carrier populations at electrodes.[18],[24] Profilometry data were therefore obtained

for films produced using both formulations and average roughness values (R_a) calculated (Table 2).

Table 6.2: Table comparing average thickness of annealed ZrO_2 printed with the old vs new formulation. RaAverages were obtained from 3-5 measurements across different prints.

ZrO_2 formulation	Layers printed	Thickness (mean, µm)	Ra (mean, a.u.)
Old	1	1.62 ± 0.11	0.121 ± 0.011
New	1	1.05 ± 0.04	0.126 ± 0.011
	2	2.61 ± 0.14	0.155 ± 0.013

As predicted by rheological analysis, single print thickness decreased over 35% with the new ink. This could easily contribute to the observed benchmark performance drop in otherwise well-infiltrated site 2 devices.[17],[36] A double print produced a more suitable thickness of ~2.6 µm and may therefore be necessary to produce high-performing devices with the new formulation. Similar R_a values were obtained for both pastes, although it should be noted that widely spaced mesh marks can be missed during by single line profilometry scans and may not therefore have significantly impacted this data.

Relying on a double print is impractical, adding extra printing and drying steps to the manufacturing process. The current screen was a 130-34 fine mesh, which allows a relatively low amount of ink through the mesh. Test layers were therefore deposited with a larger mesh (90-48) in an attempt to produce a thicker single print with the new ink (Table 3). This was successful, with a single large mesh print producing similar thickness (2.53 ± 0.05 µm) to two layers with the fine mesh (2.61 ± 0.14 µm). R_a values were also comparable. Having achieved appropriate thicknesses with each mesh, devices were made using either a single, large mesh print or double, fine mesh print (henceforth '1L' and '2F' respectively).

Table 6.3: Table comparing the average thickness of annealed ZrO_2 layers printed with the new paste using 90-48 mesh screens (1L). Thickness and roughness averages were obtained from 3-5 measurements across different prints.

ZrO_2 formulation	Layers printed	Thickness (mean, µm)	Ra (mean, a.u.)
New	1	2.53 ± 0.05	0.157 ± 0.014

As shown in Figure 6.26, the adjusted ZrO_2 thickness drastically improved device performance, producing average PCEs of 11.5% and 12.0% for the 1L and 2F samples respectively. However, performance was still highly variable, with PCEs ranging from 9.0-13.8% PCE for 1L and 10.0-14.0% for 2F. There were also marked differences between sets: The 2F exhibited a greater proportion of samples in the upper J_{sc} range, as well as significantly higher and more reproducible V_{oc} values.

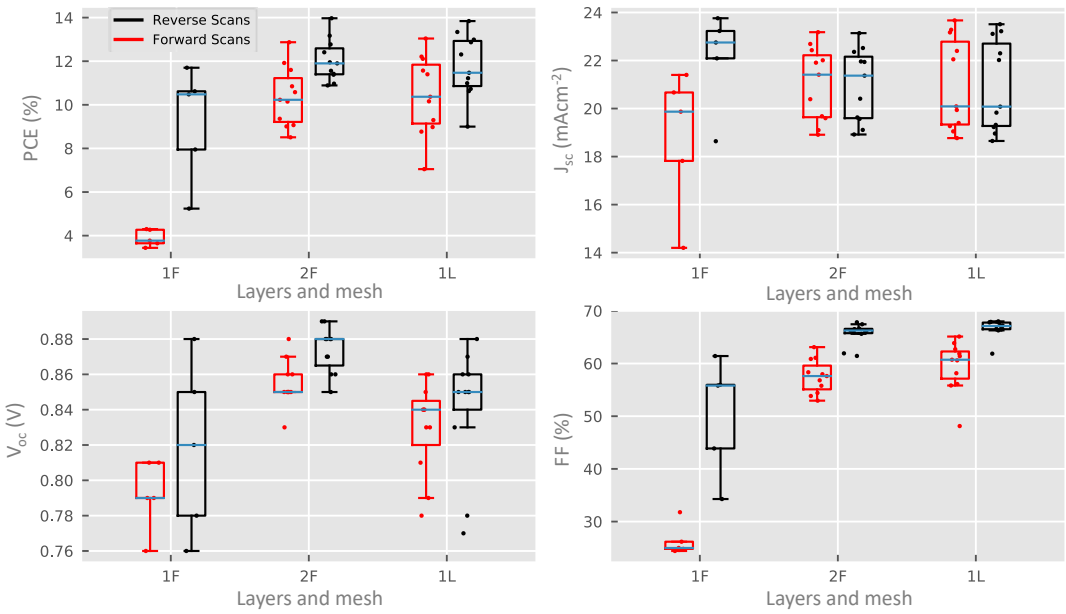

Figure 6.26: Photovoltaic parameters of devices produced using a single layer and fine mesh (1F), double layer and fine mesh (2F) or single layer and large mesh (1L) for the ZrO_2, printed with the new paste. Six 1F devices, and eleven 2F and 1L devices.

These results that show that adjusting ZrO_2 thickness using the 2F and 1L prints enabled a return to the Chapter 4 baseline of 12-14% PCE in many devices. However, significant performance variation still presented a problem.

As the only variable in these sets was the ZrO_2 deposition, this must be due some irreproducibility in this layer. The wider performance spread in 1L devices indicates that this issue is worse in 1L prints. However, earlier profilometry results indicated similar thickness and roughness between 1L and 2F ZrO_2 prints. It was hypothesised that either profilometry scans were not providing representative data, or that slight ZrO_2 topology changes in 1L samples were somehow causing issues in the subsequent carbon print. As linear profilometry data represents but a single line along a print, isolated, spaced or macroscopic printing inconsistencies may easily be missed. White light interferometry (WLI) was therefore

performed on stacks produced using 2F and 1L ZrO_2 for a more representative comparison of topology (Figure 6.27).

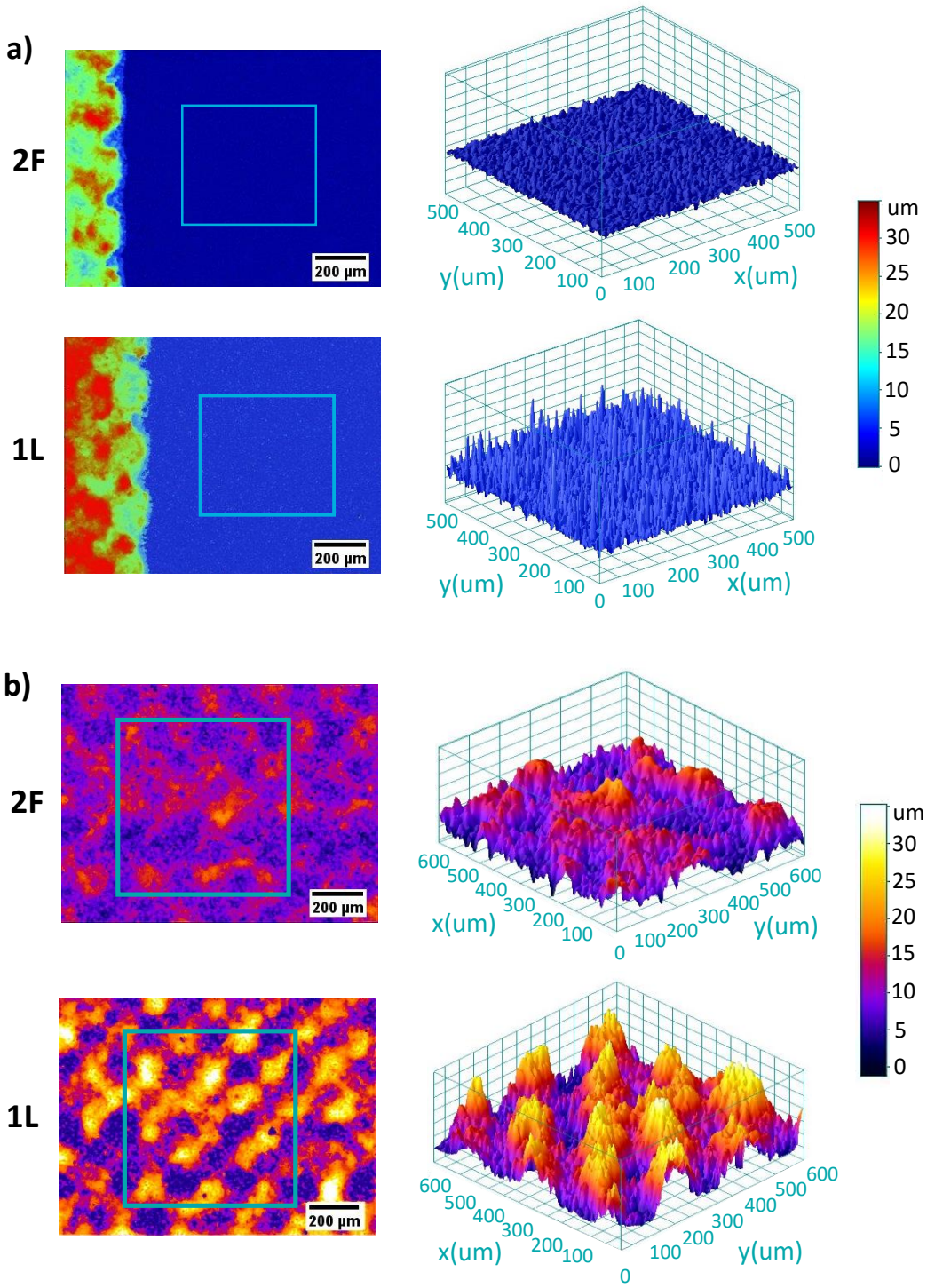

Figure 6.27: WLI of a) ZrO_2 and b) Carbon layers in cells with ZrO_2 deposited using i) 2F or ii) 1L prints. Images are presented in both 2D and 3D with similar scales for ease of comparison. The section of the 2D image used for 3D analysis is highlighted on each image with a square. Measurements by Dr. S. Potts, sample preparation and image analysis by C. Worsley.

Unlike the single line profilometry scans, the WLI results show a clear increase in ZrO_2 roughness with the 1L print (Figure 6.27a). It should be noted that this roughness increase was present despite a lack of obvious mesh marking in either case. Therefore, even in a high-quality print with no mesh marking, the 2F regime produces smoother and more consistent prints. Critically, this may not be the case with every batch- small differences in printer setup such as squeegee tension can alter mesh mark prevalence and severity from batch to batch.

To provide quantitative layer comparisons S_z and S_a values were calculated. S_z, a measure of maximum roughness, is most impacted by severe large surface peaks and troughs. S_a is less impacted by large single defects and thus provides more insight into overall layer quality.

2F layers exhibited an average S_a of 171.31 ± 6.06 nm, compared to 341.44 ± 24.22 nm for 1L. The average S_z of the 2F sample was also approximately three times lower, 4.57 ± 0.27 µm versus 7.34 ± 0.35 µm for 1L. Both S_z and S_a will be higher in a layer with mesh marking. As mark diameter is usually correlated with mesh thread diameter, any mesh marks are likely to be more severe in a non-ideal 1L print.[34]

Even without significant mesh marking, changes in ZrO_2 topology significantly impacted that of the subsequent carbon print, with greater ZrO_2 roughness drastically increasing the prevalence and severity of marks in the top electrode. This is likely even more pronounced in samples with ZrO_2 mesh marking.

Such marks could change affect precursor wetting and thus infiltration. However, as the carbon surface is many microns away from base of the stack it was unclear as to what extent its topology would impact TiO_2 filling. A 1L device was therefore optically examined for evidence of mesh mark-related infiltration issues.

Figure 6.28a shows a contrast enhanced optical image of the infiltrated TiO_2 in a 1L device. It is clear in this device that mesh marking has had a significant impact on infiltration. As discussed in section 6.3.2, perovskite-free voids are easily identified as light sections on the image. Two sets of regularly spaced voids are distinguishable, the smaller identified in red and the larger in green.

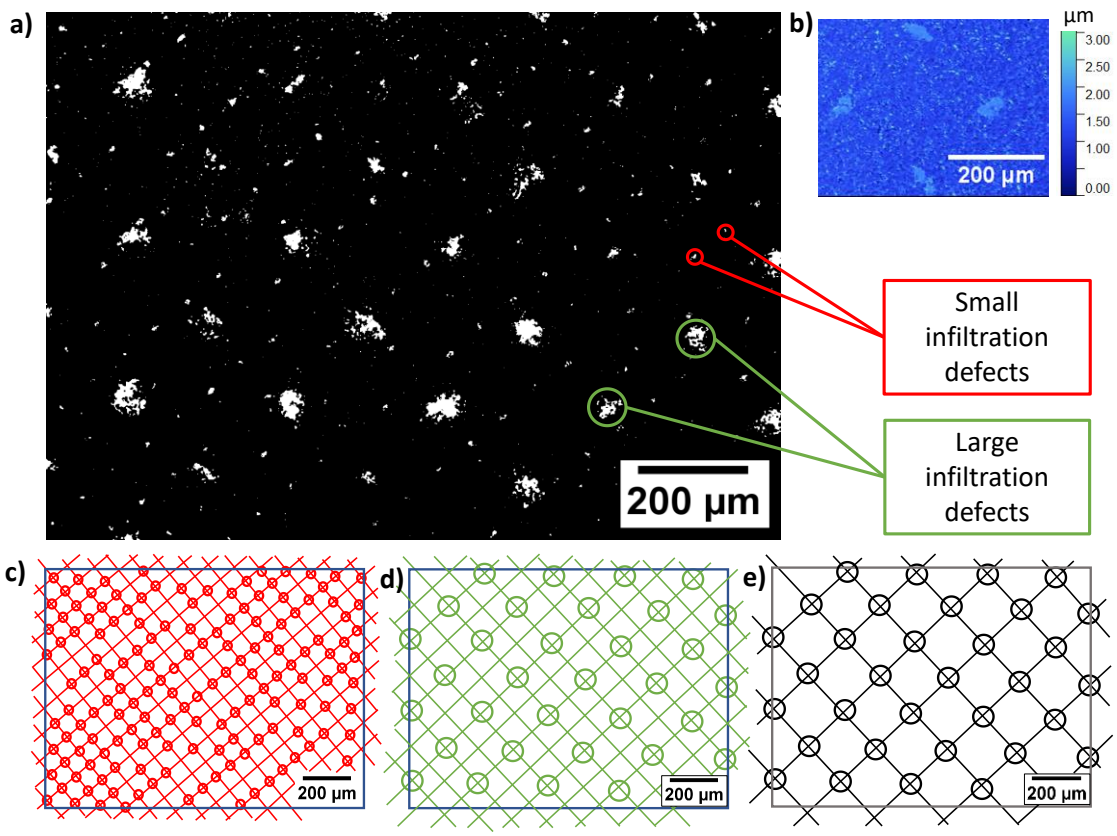

Figure 6.28: a) Contrast enhanced optical image of an infiltrated TiO_2 in a 1L device, with examples of spaced defects highlighted. b) WLI of mesh marks observed on printed, uninfiltrated 1L ZrO_2 films. c), d) and e), show diagrams of mesh dimensions of TiO_2, ZrO_2 and Carbon screens respectively. The circles represent cross sections where an infiltration issue is present on the optical image. Image Acquisition by Dr. T. Dunlop, sample preparation and image analysis by C.Worsley.

The smaller set are less severe and represent a small overall % uninfiltrated area (%UA). They are thus unlikely to produce a significant performance loss. However, the larger set produce a sum uninfiltrated area of ~6.8% (calculated by image analysis). According to the trend between infiltration and performance presented in section 6.3.2, this could correspond to over 0.5% PCE loss.

As highlighted by Figure 6.28c, the spacing of these infiltration defects corresponds to that of the 130-34 TiO_2 mesh. Interestingly, these defects are larger and more common at alternate mesh crossover points. In other words, every other thread appears to cause worse infiltration defects.

This makes identifying the cause of the larger set more difficult: the spacings correspond to the carbon mesh, but also to that of alternate crossover points on the IL ZrO_2 mesh (Figure 6.28c, d). Indeed, when examined with WLI, 1L ZrO_2 films exhibited very similar mesh markings (Figure 6.28b).

However, the ZrO_2 defects observed via WLI present as slightly raised smooth areas not much higher than the bulk print. Conversely, the carbon marks on 1L samples (presented in Figure 6.27) were proportionally large: twice the height of the bulk layer some cases. It is therefore more likely that the infiltration defects in Figure 6.28 are a consequence of **carbon** mesh marks, caused by increased general roughness in the underlying ZrO_2.

In 1L samples even ZrO_2 without mesh marks caused a very uneven carbon print (Figure 6.27). 1L prints with ZrO_2 mesh marking will be rougher still, and likely produce even rougher carbon prints. Therefore, IL samples are more prone to large, carbon mesh mark-related defects and higher overall %UA. This explains the slightly lower average performance and greater result spread in the 1L samples.

Even if 2F samples should experience ZrO_2 mesh marks, these will be of similar size to the TiO_2 defects, as a 130-34 mesh screen was used for both. Therefore, even in the case of 2F mesh marks, the resultant carbon mesh marks may be less severe due to lower overall ZrO_2 roughness.

In this section, ZrO_2 ink changes were found to have reduced print thickness to ~1 µm, badly impacting baseline performance. Adjusting the thickness to ~2 µm improved performance, with some devices attaining PCEs of 12.5-14%, in line with the previous baseline. This was most apparent with a 2F regime, which produced consistently higher V_{oc} than a 1L print of similar thickness due to smoother ZrO_2 prints. Consequently, 2F prints were used for all devices henceforth (unless specified). Critically, small changes in ZrO_2 roughness were found to drastically impact that of the subsequent carbon print.

Clearly, the quality of both ZrO_2 and carbon depositions can contribute significantly to infiltration issues. The next section will therefore focus on improving ZrO_2 print quality, while a strategy for reducing carbon marking will be explored in section 6.6.3.

6.6.2 ZrO_2 printing regimes

As shown in the previous section, the roughness of the ZrO_2 layer can significantly impact that of the subsequent carbon print. Rheological changes in the ZrO_2 ink were also discovered, with the new ink exhibiting lower initial viscosity and less elastic behaviour. This section will therefore aim to reduce ZrO_2 roughness and improve print reproducibility with the new ink. Unless stated, all samples presented through chapters 1-4 were prepared using a print-print (PP) deposition method for the ZrO_2 layer. Depicted in Figure 6.29, this method

involves two high tension passes with hard squeegees. This was required for the old viscous ZrO_2 ink, which required a significant amount of force to pass through the screen mesh.

However, as the new ink is less viscous it may pass through the screen with a single, lower tension squeegee pass. The PP method may be unsuitable in this case: after significant ink deposition with the first pass, the screen is likely to stick to the underlying ink during the second pass. This can produce filamentation and mesh marking, increasing overall roughness.[34]

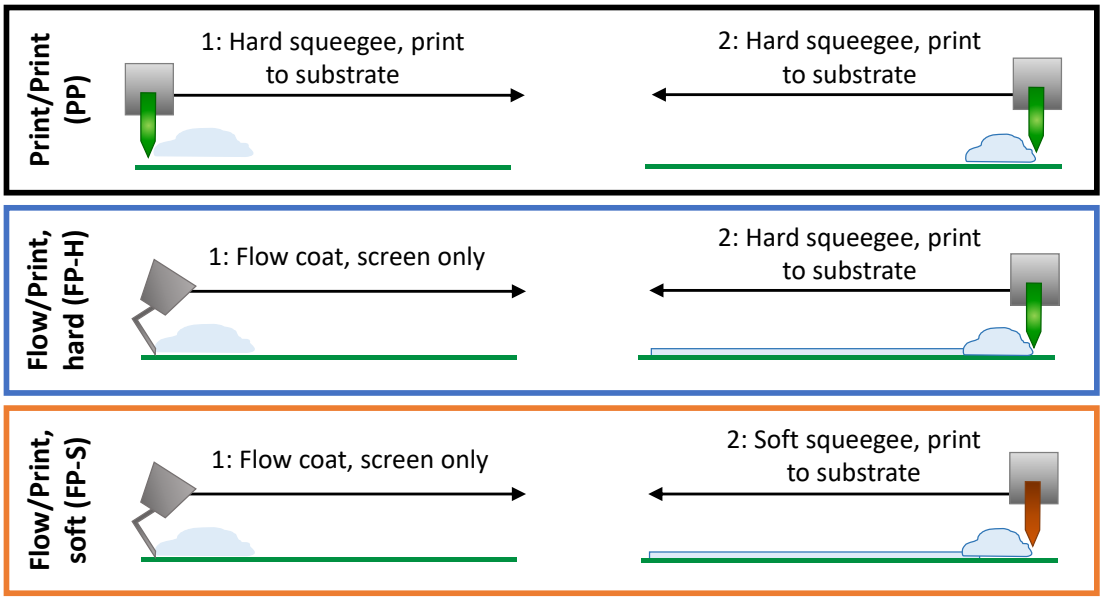

Figure 6.29: Diagrammatic representation of the different printing regimes.

A method known as flow coating can be used when an ink is of low enough viscosity to pass through the mesh with minimal force. Here paste is first spread across the screen to fill the mesh before a single squeegee pass to coat the underlying substrate. This allows mesh filling and even ink distribution while minimising contact time between the screen and the deposited layer. Fewer contacts between screen and substrate produces less opportunity for ink filamentation and thus mesh marking.[34],[37]

Two flow coat printing methods were therefore trialled in an attempt to produce reproducibly smooth layers and reduce mesh marks, which were shown to reduce infiltration. Figure 6.29 depicts the chosen methods, one with a hard squeegee (FP-H), and the other with a soft squeegee (FP-S). The FP-S method was trialled in an attempt to increase single layer thickness. It was hoped that this would produce thick enough films to use only one print, reducing the number of steps required for CPSC production. As the purpose of

trialling a soft squeegee was to obtain increased single layer thickness, only single prints were examined.

As single PP prints of the new paste were found in section 6.6.1 to produce films of ~1 µm with the 130-34 fine mesh, PP and FP-H samples were prepared with two ZrO_2 layers to ensure adequate thickness (the 2F method).[24],[38] Produced films were annealed, before profilometry to compare film thickness (Table 6.4).

Table 6.4: Average profilometry thickness and roughness (R_a) values of 2F and 1F ZrO_2 layers deposited with different PP, FP-H and FP-S printing regimes. Averages were calculated from 6 measurements (profiles taken from three different samples, all results averaged).

Print Regime	Layers printed	Thickness (mean, µm)	Ra (mean, µm)
Print/Print (PP)	2	2.61 ± 0.14	0.202 ± 0.059
Flood/Print, hard (FP-H)	2	2.55 ± 0.13	0.162 ± 0.036
Flood/Print, soft (FP-S)	1	1.27 ± 0.13	0.145 ± 0.058

As presented in Table 4, the PP and FP-H double layer prints exhibited similar thicknesses of 2.5-2.7 µm.[19] Although FP-S produced thicker layers than single prints with the PP method, average layers were still quite thin, at 1.27 ± 0.13 µm. This may cause increased hysteresis and decreased V_{oc} in devices, due to higher levels of recombination at electrode interfaces.[1],[17],[24]

Figure 6.30 shows three of the profilometry scans obtained for the FP-H and PP regimes, wherein mesh marking can be observed in both cases (visible as downward lines along the scan). As well as affecting infiltration through increasing roughness, these deep trough marks could act as pinhole defects, producing short circuits in completed devices.

[19] This value is higher than that previously obtained for the 2F prints in section 6.6.2. This was due to a printer recalibration during servicing, after which layer thicknesses increased somewhat. This did not negatively impact performance or infiltration

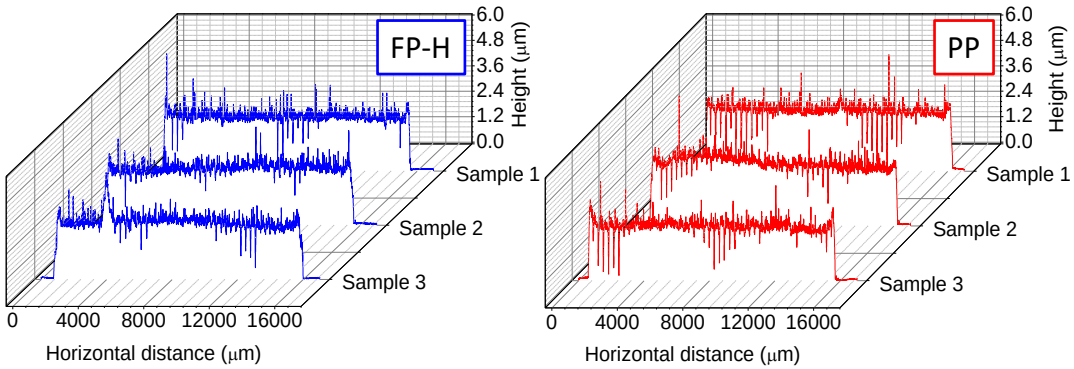

Figure 6.30: Profilometer measurements of three different 2F samples produced using FP-H and PP printing regimes.

From these scans, it appeared that the mesh marks in the FP-H film were fewer and less deep. To provide a more accurate and representative comparison of film topology, prints were examined with WLI to compare mesh mark severity (Table 6.5, Figure 6.31). For this analysis 1L layers (single prints with a large mesh screen) were prepared, as these was previously found to produce larger and more easily identifiable marks (section 6.6.1).

As shown in Table 5, PP and FP-H regimes produced similar average S_a and S_z values (~220 nm and ~6 µm respectively), while those of FP-S films were much lower (~100 nm) due to decreased thickness. The similarity of PP and FP-H values could suggest that the films exhibit similar topology. However, the processed images of surface topology therefore provide a better comparison in this case (Figure 6.31).

Table 6.5: WLI surface profiles of ZrO_2 films printed with different regimes. A single S_z value provides the sum of the greatest peak and trough present in a measured area, while Sa is the mean of the average height difference across the measured area. Average values were calculated from 9 measurements over a 1.2 mm x 0.93 µm area.

Settings	Avg surface roughness (Sa, nm)	Avg maximum surface roughness (Sz, µm)
Print/Print (PP)	218.14 ± 6.99	5.85 ± 1.36
Flow/Print, hard (FP-H)	221.99 ± 12.63	6.62 ± 2.02
Flow/Print, soft (FP-S)	105.65 ± 6.07	3.89 ± 0.87

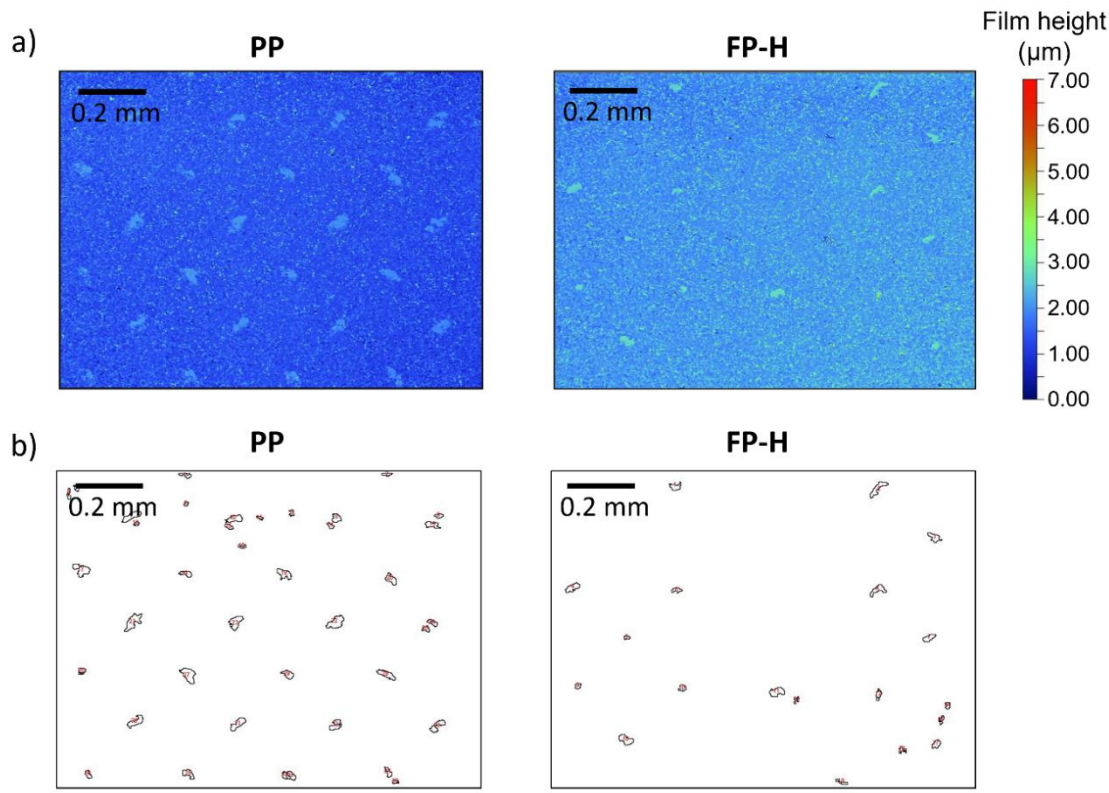

Figure 6.31: WLI of 1L ZrO_2 films on FTO/glass substrates, deposited with PP and FP-H printing regimes. Data coloured by a) height, b) artefacts identified via image analysis. WLI measurements by Dr S. Potts. Sample preparation and image analysis by C. Worsley.

Figure 6.31 reveals 26 large, regular mesh-marks across the examined area on the PP sample, while the same analysis identified ~14 such marks on the FP-H film. Additionally, marks observed in the FP-H sample were generally smaller. These correspond with alternate mesh cross sections of the 60-64 ZrO_2 mesh. This corroborates the single line profilometry results in Figure 6.31. Therefore, the FP-H regime produces less severe mesh marking whether using a fine mesh double layer (as for profilometry in Figure 6.30) or a large mesh single layer (as in Figure 6.31).

As shown in section 6.6.1, lower ZrO_2 roughness can significantly improve subsequent carbon prints and perovskite infiltration. Devices were therefore fabricated with the PP and FP-H regimes and optically examined (Figure 6.32). These cells were produced using the optimal 2F (130-34 mesh, two layers), as this was found in section 6.6.2 to produce better devices.

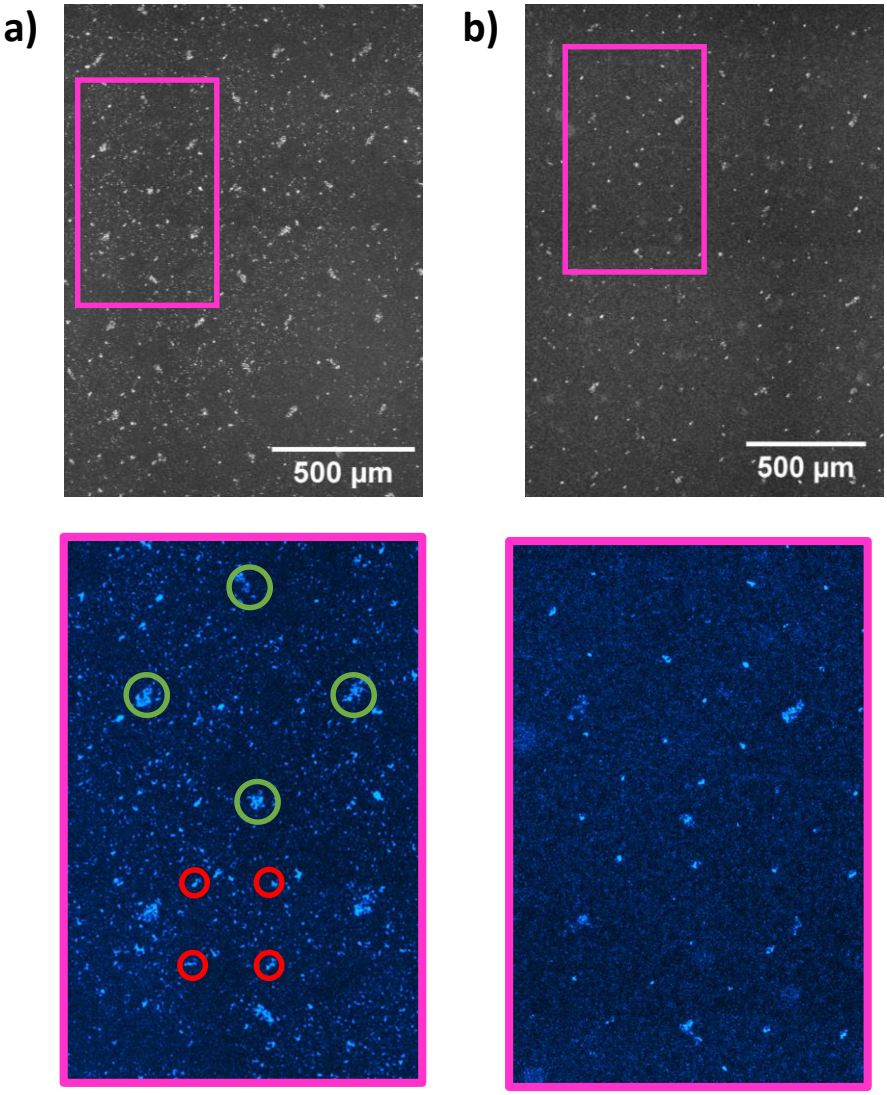

Figure 6.32: Optical images of the infiltrated TiO_2 in devices with 2F ZrO_2 deposited using a) PP and b) FP-H regimes. Lighter areas represent uninfiltrated sections, as discussed in section 6.3.2). Pink boxes highlight the areas presented in higher magnification (adjusted for improved clarity).

The larger set of mesh marking related defects at ~200 µm intervals (green circle) correspond with 60-64 carbon mesh crossover points and are likely due to increased ZrO_2 roughness (section 6.1, Figure 6.30). Both samples also showed a smaller set with ~120 µm spacing (red circles), which align with alternate 130-34 mesh crossover points. As this screen was used for both ZrO_2 and TiO_2, these marks could be associated with either layer.

Although these defects were present in both cells, the PP device (Figure 6.32a) exhibited larger carbon mesh mark infiltration defects. Improved PCE was therefore expected for devices produced using the FP regime.

Photovoltaic parameters from devices with PP, FP-H and FP-S ZrO_2 layers are presented in Figure 6.33. FP-H layers produced the best devices, with a champion PCE of 13.34% (average 13.09 ± 0.25%) compared to 12.60% for PP and 11.00% for FP-S (average PCEs of 12.45 ± 0.25% and 10.51 ± 0.57% respectively). This was due to higher V_{oc} and J_{sc} in FP-H devices, a result of superior infiltration. FP-S devices suffered from low V_{oc} and much greater hysteresis, likely a consequence of thinner ZrO_2.[24] Stabilised PCEs reflected the same trend, with the FP-H devices attaining the highest PCE at 11.8%.

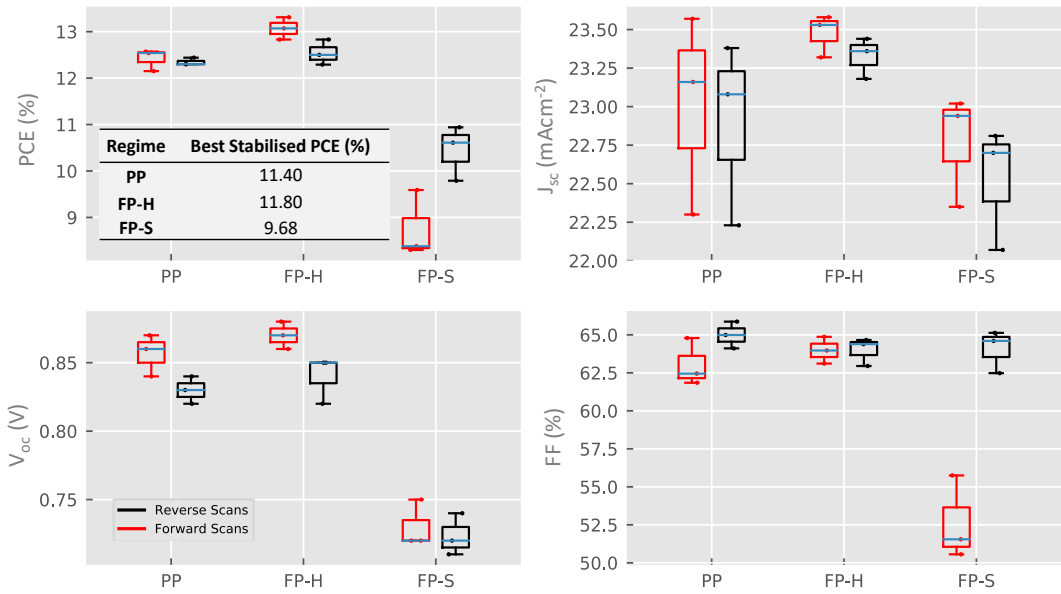

Figure 6.33: Photovoltaic parameters of a batch of devices with 2F ZrO_2 layers deposited with three different printing regimes. Three devices in each batch. Inlaid table shows the stabilised PCEs obtained for the best performing device from each batch.

Although the results presented in section 6.6.1 indicate that double prints are superior for PP regimes, the improved layer quality attained with the FP-H 2F regime could remove the requirement for such thick interlayers. This would be advantageous in reducing device fabrication time. Devices were therefore produced with single and double prints, to check that a double layer was still necessary.

Presented in Figure 6.34, single layers produced extremely high hysteresis, with average forward PCEs nearly half that of the reverse. Although these devices were better than those with a single PP layer (8-10% PCE, Figure 6.19, section 6.6.1), they were still inferior to those with a double print.

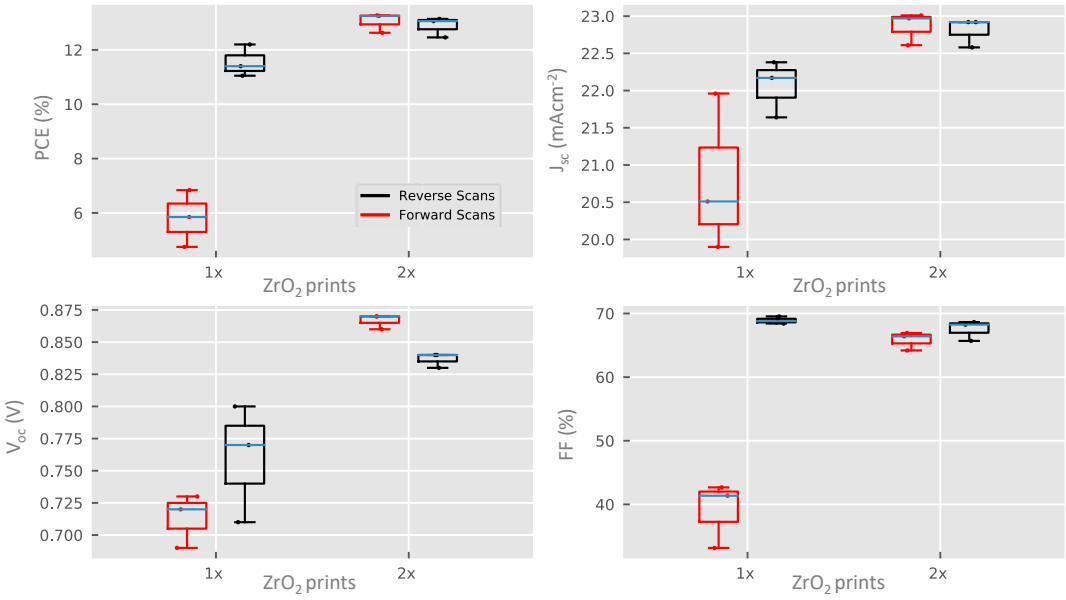

Figure 6.34: Photovoltaic parameters of devices produced with one (1x) or 2 (2x) ZrO_2 layers, deposited via the FP-H regime.

Despite the increase in production time introduced by an additional print, the results in this section indicate that a 2F ZrO_2 layer deposited with an FP-H printing regime is the best option for quality infiltration and device performance. Henceforth, all presented devices were fabricated with a 2F ZrO_2 layer with an FP-H printing regime.

The next section will focus on improving carbon layer topology to enhance infiltration.

6.6.3 Adjusting the carbon layer

As presented in section 6.6.1 (Figure 6.28), slight increases in ZrO_2 roughness can severely impact the quality of the subsequent carbon layer even in the absence of mesh marking. Although improvements obtained by changing the printing regime (section 6.6.2) should help mitigate this, slight changes in ZrO_2 quality between batches could still lead to carbon defects and associated performance variation.

Previous work has shown that dilution with 5-10% 1-methoxy-2-propanol can reduce mesh marking and overall roughness in this particular carbon paste, by enabling more effective ink separation. This leads to less filamentation during printing, resulting in smoother layers.[34] This method was therefore employed to produce stacks with pastes using 0, 5 and 10% dilutions.

a)

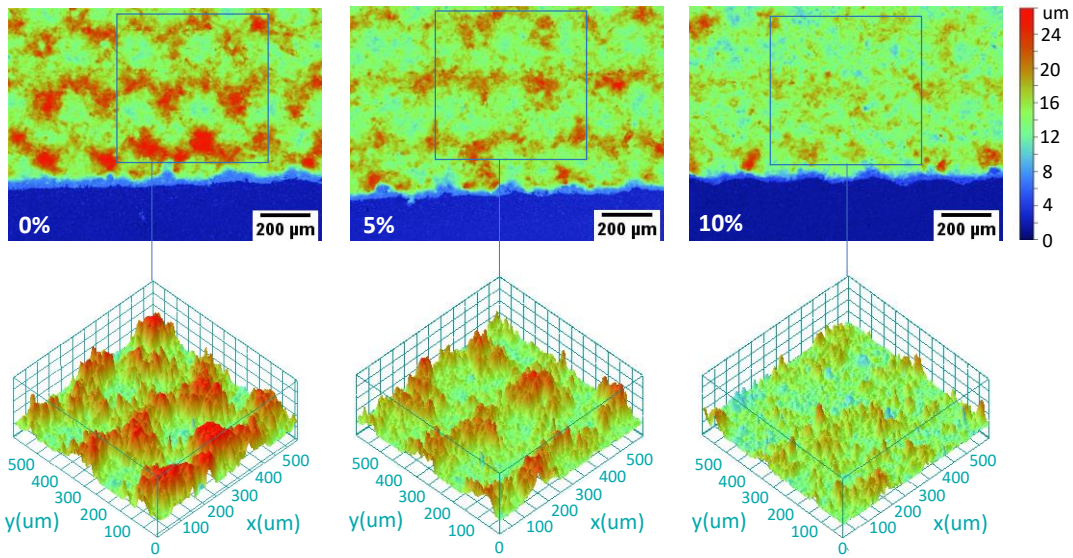

b)

% Dilution	Average thickness (µm)	Average (Sz) (µm)	Average Sa (nm)
0	12.41 ± 2.58	2.16 ± 0.08	20.13 ± 0.44
5	10.6 ± 2.24	1.78 ± 0.07	18.4 ± 1.25
10	11.93 ± 1.63	1.67 ± 0.06	17.55 ± 0.47

Figure 6.35: a) 2D and 2D WLI images of carbon (green/red) layers on complete devices, printed from inks of 0, 5 or 10% dilution with 1-methoxy-2-propanol. Blue areas show the underlying ZrO_2. b) Numerical data from WLI analysis, averages from 9 measurements for each sample. WLI measurements by Dr.S. Potts, image analysis by C. Worsley.

As shown in Figure 6.35, dilution caused a significant visible decrease in carbon roughness and mesh marking. This caused average S_z to drop from 2.16 ± 0.08 µm with the standard paste to 1.78 ± 0.07 µm and 1.67 ± 0.06 µm for the 5% and 10% dilutions respectively. S_a values also decreased in both samples. Despite statistically similar S_a values for the 5 and 10% samples, the 3D image data show a clear reduction in mesh marking with extra dilution. The 10% may therefore produce the best device infiltration.

Such changes in layer thickness and topology can also impact conductivity. Rough samples contain areas of high and low carbon concentration, changing conductivity across the sample and leading to an overall decrease. Thin layers or low carbon loading can also negatively affect the electrode, leading to low device FF.[19]

As thickness did not significantly fall with dilution, significant conductivity loss was considered unlikely (Figure 6.35). However, the decrease in carbon load with dilution could still theoretically have a negative impact. Sheet resistances were therefore obtained for different ink dilutions on plain glass.

Table 6.6: Average sheet resistance of carbon layers printed using GEM ink of 0, 5 or 10% dilution with 1-methoxy-2-propanol. The 10x10 cm² layers were screen printed using a standard 61-64 carbon mesh onto plain glass. 4 measurements for each average value.

% Dilution	Average sheet resistance (Ω)
0	21.85 ± 0.48
5	17.44 ± 0.23
10	16.45 ± 0.56

As shown in Table 6, sheet resistance decreased significantly with dilution: 5% solvent addition caused a >20% reduction, with a further 4% drop in resistance at 10%. These changes could have a significant impact on device performance: the decrease in mesh marking may improve TiO_2 infiltration, while reduced sheet resistances enhance back electrode charge extraction. Resultant devices may therefore exhibit improved J_{sc} and FF due to improved light absorbance and electrode contact.

Figure 6.36 shows cell performance of devices produced using these pastes. As expected, 5% devices presented improved average J_{sc} (24.1 ± 0.7 mAcm^{-2}) and FF (62.7 ± 4.4%) compared to the undiluted controls (23.4 ± 0.6 mAcm^{-2} and 52.8 ± 5.7% respectively). Corresponding PCE gains were also observed, increasing from 11.57 ± 1.18% at 0% to 14.05 ± 1.36% at 5% (champion device 15.00% PCE).

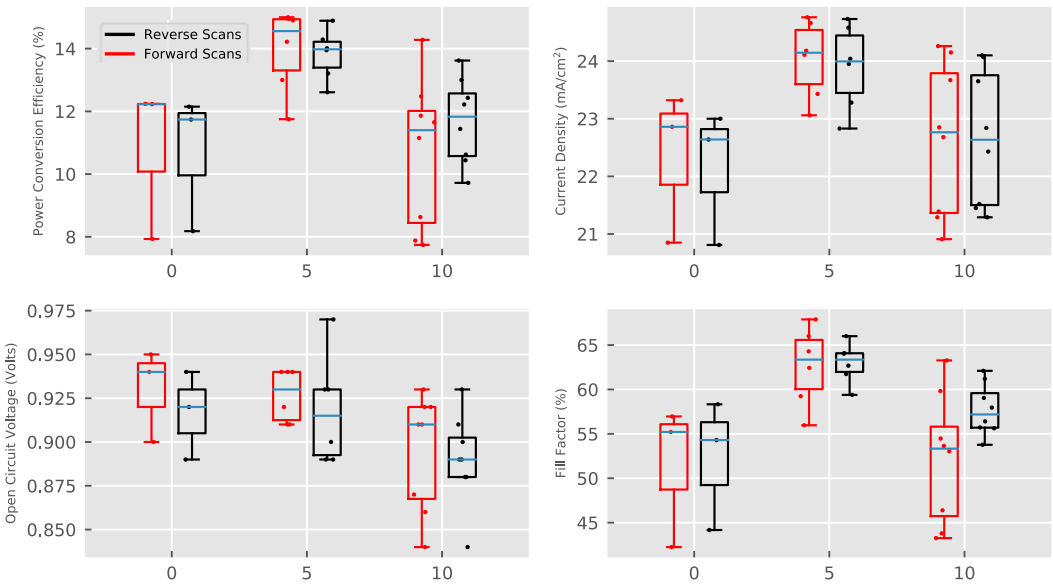

Figure 6.36: PV parameters of devices made using GEM carbon paste diluted with 0, 5, or 10% of 1-methoxy-2-propanol. Other prints were deposited in the same run, and all were infiltrated at the same time in identical conditions.

Interestingly, the 10% devices exhibited much greater result spread, ranging from 8.65% - 14.31% PCE (average 12.55 ± 2.45%). This is somewhat unexpected, as prints of 10%

diluted inks on glass demonstrated statistically similar thickness to 5% films, with around 4% lower sheet resistance. Considering this, similar FF and J_{sc} enhancements were expected.

Optical examination (Figure 6.37) revealed that the 10% samples varied widely in infiltration quality, ranging from 0.71% to 14.09% uninfiltrated area. This accounts for the large result spread. Although examples of extremely good infiltration (<1% uninfiltrated) were observed for each set, 5% dilution produced the most consistent high TiO_2 filling. The average uninfiltrated area of six samples was 0.48 ± 0.28%, increasing to only 0.83% for the worst sample.

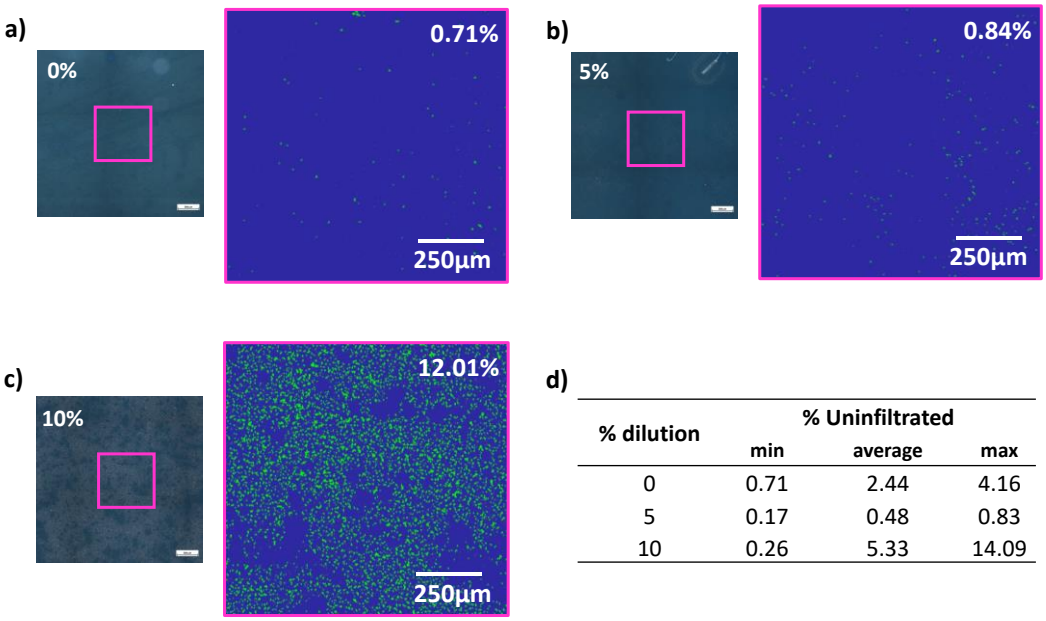

% dilution	% Uninfiltrated		
	min	average	max
0	0.71	2.44	4.16
5	0.17	0.48	0.83
10	0.26	5.33	14.09

Figure 6.37: Optical images and magnified coloured sections of filled TiO_2 layers in devices produced using diluted carbon ink. The worst performing device from each set is shown, with % uninfiltrated area labelled. Inlaid table shows the average % uninfiltrated area of all devices alongside the minimum and maximum measured uninfiltrated values.

It was theorised that higher dilution may provide greater freedom of movement to suspended graphite flakes in the carbon ink, allowing more to settle horizontally to the ZrO_2 interface. This has been shown to negatively impact infiltration by blocking access to the underlying mesoporous layers, which could in turn reduce FF and J_{sc}.[13],[27] Additionally, different prints may vary in graphite content, depending on the effectiveness of mixing prior to printing.

Beam milled cross sections of 0% and 10% devices were examined for evidence of different flake distribution. When using polarising lenses, graphite flakes with different orientations are highlighted at different degrees of polarisation (Figure 6.38).

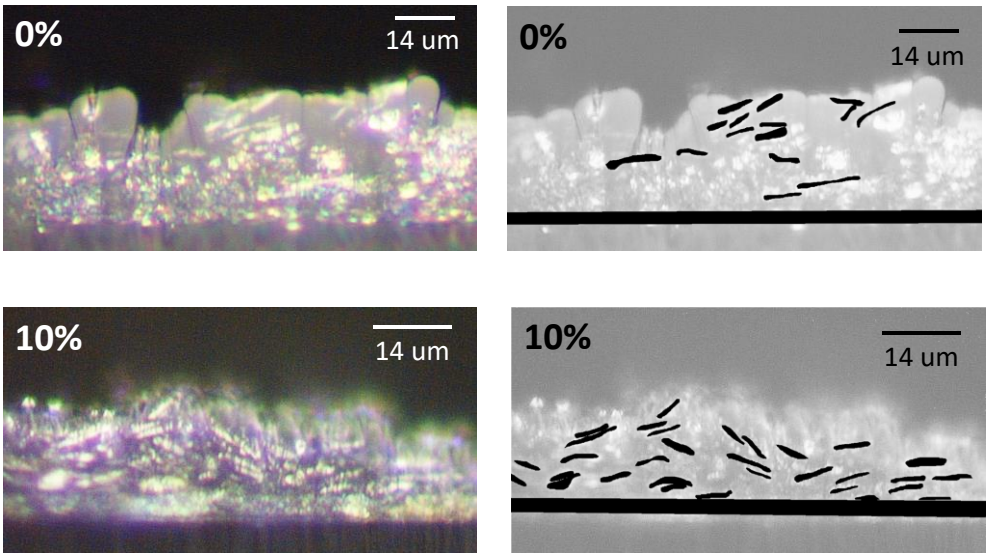

Figure 6.38: Cross sectional images of complete devices obtained using an optical microscope and polarising lens to highlight horizontally aligned graphite flakes in the carbon layer. Obvious flakes and the mesoporous TiO_2 and ZrO_2 layers are masked in the RHS images for clarity.

Much more horizontally aligned graphite is visible in the 10% sample, with nearly twice as many obvious flakes. This may account for the slight conductivity enhancement seen in the 10% films. Also, infiltration may be impacted differently in each sample depending on the relative spread of these flakes, accounting for the varied results observed.

This section has built on the previous work in optimising the ZrO_2 layer, through 5% dilution of the carbon paste to minimise mesh marking and thus improve precursor wetting and infiltration. A champion PCE of 15% was attained, surpassing that of the best devices in Chapter 4. The optimal regime combined two fine mesh ZrO_2 prints (applied with an FP-H print regime to minimise mesh marking) with the 5% carbon dilution, representing a new standard fabrication procedure.

6.7 Summary: Methods for troubleshooting infiltration and performance issues in CPSCs and modules

Many different factors are shown to influence CPSC performance and infiltration in this chapter. It is not therefore possible to present a universal solution to fix infiltration or performance issues: the underlying causes may well be different in each case. However, as specific issues were found during this work to produce characteristic effects on device presentation and behaviour, discerning the root of the problem is not impossible.

As presented in section 6.3.2, TiO_2 filling is intrinsically linked to performance. Visual inspection of this layer, both with the naked eye and using an optical microscope, can provide useful information on performance issues: The distribution and appearance of perovskite-free voids can be indicative of specific issues within the stack (Figure 6.39). For example, increased mesh marking causes even, spaced micro-scale defects, while varied stack thickness causes a gradient infiltration effect across the area. As issues can coexist on drastically different scales, a combination of macro and micro-scale inspection is advised. As this method is non-destructive, it is perhaps advisable to routinely examine devices from each batch. As well as providing a database of normal, quality devices from a given laboratory or factory, this would allow for early detection of potential problems prior to testing.

Furthermore, it may be advisable to retain an uninfiltrated device stack from each print batch; ZrO_2 and carbon topology and thickness have significant impacts on device performance and are more difficult to examine once the stack is fully prepared due to the presence of surface perovskite crystals.

Figure 6.39 presents common characteristic defects observed during this work. The following section discuss each issue, and present recommendations to assist in troubleshooting specific performance issues. Although methods will mostly be discussed in the context of devices, they are equally applicable to modules and may therefore be useful for troubleshooting in future large-scale commercial settings.

i)

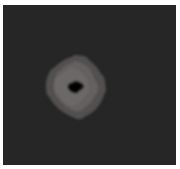

Likely cause: Contaminant or solvent droplet damage.*

Check: cleanliness of print area, pastes.

ii)

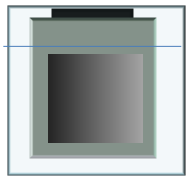

Likely cause: Uneven layer thickness, likely ZrO_2 or Carbon.

Check: Layer thickness and topology, printing settings.

iii)

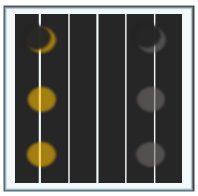

Likely cause: Uneven heating or airflow during perovskite anneal.

Check: Position of heating elements, airflow.

iv)

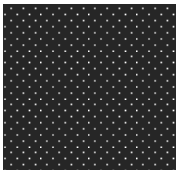

Likely cause: Mesh marking.

Check: Which mesh dimension matches your marks?

v)

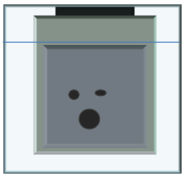

Likely cause: Impeded infiltration and/or fast surface crystallisation.

Check: All hot plate temperatures, print thicknesses and topology, airflow.

vi)

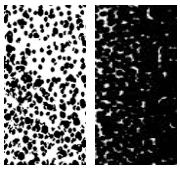

Likely cause: Impeded infiltration or fast crystallisation.*

Check: Layer thickness and topology, hot plate temperature, airflow.

vii)

No obvious infiltration issue/change (under microscope).

Check: ZrO_2 thickness, Carbon thickness and conductivity.

*Figure 6.39: Diagrams of common large (green) and small-scale (blue) infiltration issues in cells and modules, alongside likely causes and suggested checks. * May be large-scale and optically visible- extremely poor sparse infiltration can appear homogeneously grey to the naked eye, while contaminant or solvent damage depends on the size of the respective contaminant or droplet.*

Issue i) Contamination

Often (but not always) visible at the macro-scale, contaminants and solvent damage produce similar issues in completed devices, producing uneven voids of varied size, sometimes with a distinctive 'halo' or ringed surrounding pattern (Figure 6.40). In the case of physical

contaminants, a particle can be present at the defect centre, whereas solvent contamination issues are particle free.

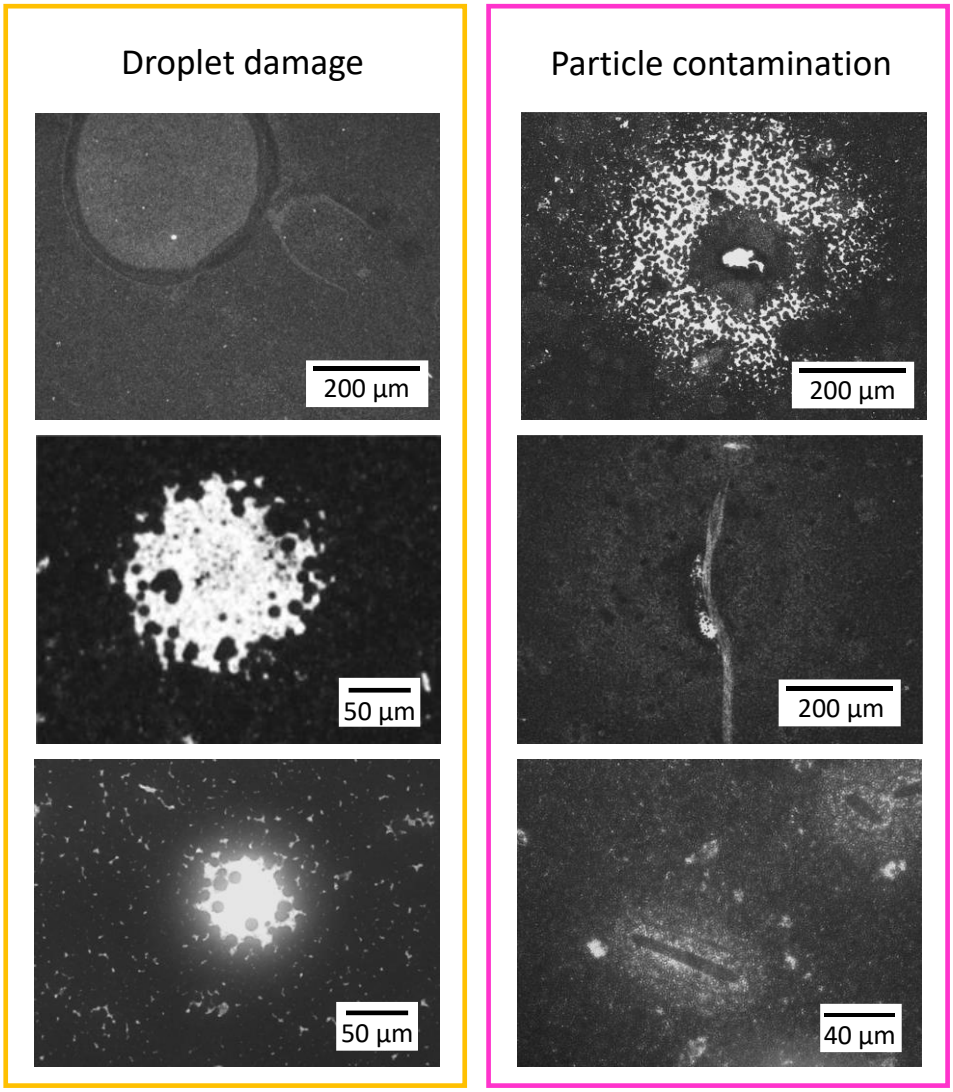

Figure 6.40: Optical images of infiltration defects caused by solvent droplet damage and particle contamination.

While solvent damage can be easily prevented through careful handling of liquids around printed stacks (especially when wet), physical contamination can be more persistent depending on the source. Wet and dry printed layers, screens and printing equipment should all be stored under covers to protect from dust and other airborne particulates.

Whenever contaminants are observed in a printed layer, pastes and screens should be carefully inspected for particles or blockages. Blocked screens require cleaning, while contaminated pastes should be disposed of. If equipment and materials appear clean, the printing, slumping, annealing and storage areas should be wiped down to eliminate the source of particles, and storage procedures reviewed where necessary.

Issue ii) Gradient infiltration

Clear gradients across the active area are indicative of printing inconsistencies such as uneven thickness or topology. This can occur across the width of a single cell or module, or across several cells when printing small-scale devices. Such films can then cause large performance variations within the device batch, or decreased power output and performance in a module.

Sub-optimal printer setup is usually the cause of these issues. As shown in Figure 6.41a), uneven squeegee or flow coat setup can produce thickness and mesh marking variation. Glass warping from high temperature annealing steps can also produce similar problems. Careful setup and pressure monitoring can help prevent squeegee related issues. Changing screen designs to limit the horizontal print width (depicted in Figure 6.41b) can also improve uniformity and batch variation.

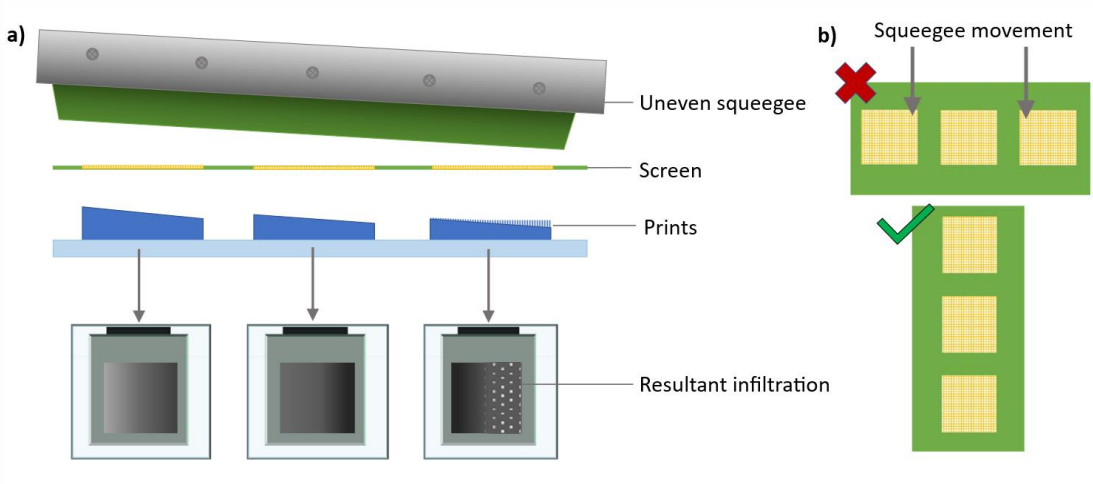

Figure 6.41: a) Diagrammatic representation of the consequences of uneven squeegee pressure and its resultant impact on device infiltration. Note that mesh marking defects in real samples will only be visible via optical microscopy. b) Screen alignment to limit horizontal print variations.

Print variation in any layer can produce infiltration issues, although the thicker ZrO_2 and carbon are more likely to cause problems. As presented in section 6.6.1, ZrO_2 variation can then introduce defects in the subsequent carbon print. Determining which layer is causing issues may therefore be difficult.

It is advisable to retain an uninfiltrated device stack from each print batch, as thickness across an uninfiltrated stack or layer can be examined with profilometry, while white light interferometry provides quick topological data. Prepared devices are more difficult: although mesh marking problems can be observed through the glass substrate, cross sectional analysis may be required to examine print quality.

Issue iii) Large grey or yellow areas in otherwise well infiltrated modules/ Extreme infiltration variation in a single print batch[20]

As presented in section 6.3.1, increased crystallisation speed can produce drastically different infiltration in devices from the same print batch. Temperature variation and airflow can both alter crystallisation time and can hence significantly affect infiltration (Figure 6.42).

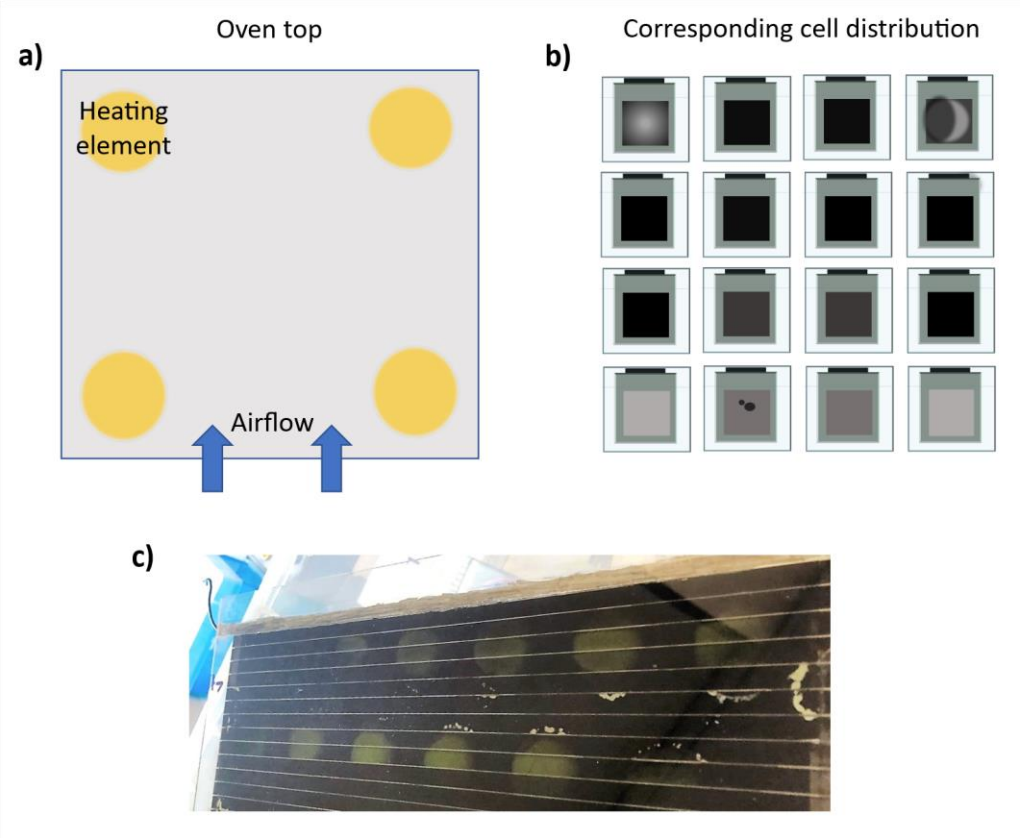

Figure 6.42: Diagrammatic representation of a) oven top and b) resultant impact on device infiltration. Depicted in c) is a photograph of damage on a 30x30 module caused by hot plate heating elements and airflow during perovskite annealing.

This was observed at larger scale during initial trials of 30x30 cm module production. Although set to a 45°C perovskite annealing temperature, initial modules showed significant evenly spaced infiltration defects across multiple cells (Figure 6.42). Through the glass substrate, these artefacts were greyish white or yellow. Grey or white perovskite free voids indicate an infiltration issue, whereas the yellow suggest accelerated degradation had occurred.

[20] Note that extreme variation between devices or across modules from a single print batch can also be due to inconsistent prints (see issue ii). If a partial cover does not help, examine the print quality.

Upon examination of equipment, it was noted that defects corresponded to the position of heating elements and air vents on the oven roof. A simple partial cover was thus applied, to protect the module surface while allowing sufficient solvent removal. This completely eliminated the defects, as shown in Figure 6.43.

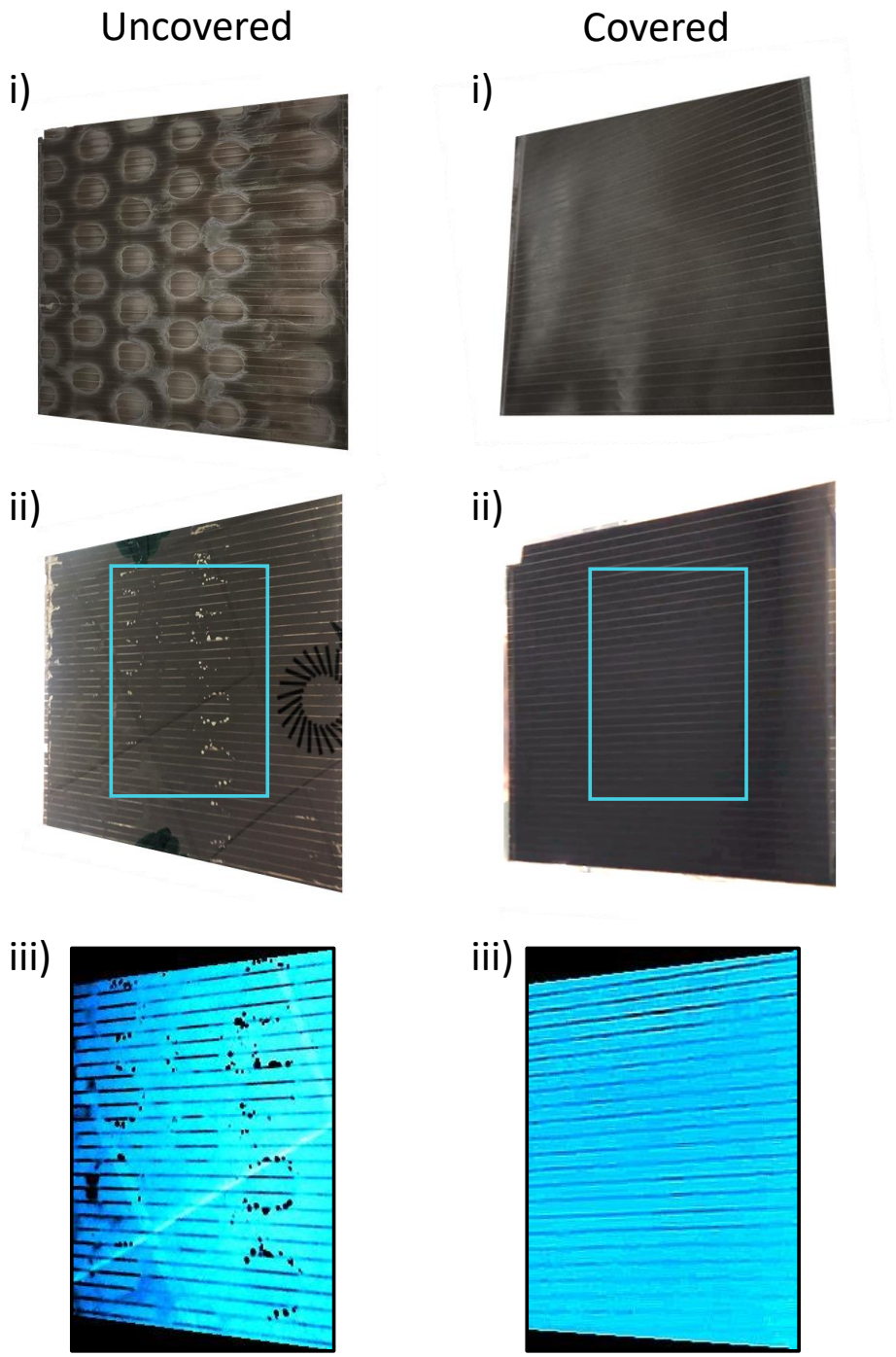

Figure 6.43: Photographs of 900 cm^2 with (RHS) and without (LHS) a cover during perovskite annealing. i) Back electrode, ii) through glass substrate, iii) magnified with applied colour filter to highlight infiltration problems.

Issue iv) Micron sized, evenly spaced perovskite free voids

Perhaps the most characteristic defects are those caused by mesh marks. Evenly spaced and present across a large area, these features are obvious when examining the infiltrated TiO_2 layer with an optical microscope (Figure 6.44).

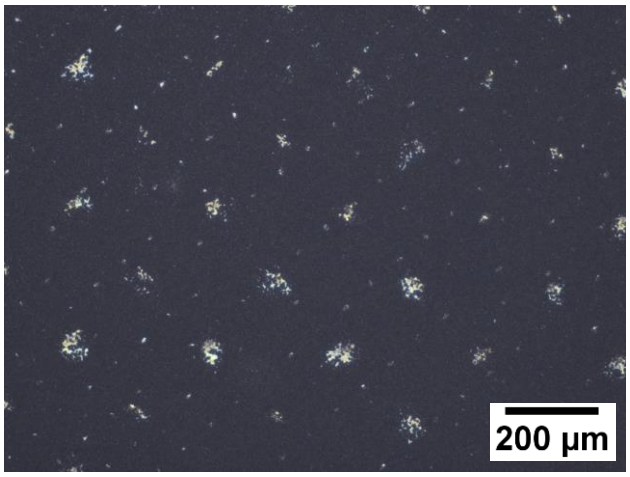

Figure 6.44: Optical microscopy of a device with two types of mesh mark- related infiltration defect.

Although occupying a smaller area than other defects discussed in this section, mesh marks can still have an impact on device performance. Especially for larger carbon related marks, the additive uninfiltrated area due to marking can still be significant (in the range of 1-6% of TiO_2 area). Additionally, marking can reduce layer effectiveness. For example, pinhole marks in the ZrO_2 interlayer can cause shorts, while severe marking on the carbon electrode was shown in section 6.6.3 to reduce conductivity. This can impact charge collection in the completed device, which becomes increasingly important at module scale.

Observed marks will correspond with the mesh dimensions of the relevant screen. Therefore, if different screens have been used for TiO_2, ZrO_2 and carbon, mark spacing can be measured to conclude in which layer the problematic marks reside. For example, the large marks in Figure 6.44 must correspond with those from the carbon layer, as this was the only deposition where a larger mesh was used. However, the smaller marks could be either ZrO_2 or TiO_2 based, as both were deposited with similar mesh screens.

Crucially, marks in a given layer are not necessarily due to printing issues in that layer. For example, it was found in section 6.6.1 that slight increases in ZrO_2 roughness could cause severe increases in marking of the subsequent carbon print. Therefore, the print topology of each layer (in an uninfiltrated device) should be examined upon observing mesh marking in devices or modules, to ascertain the root cause of the problem.

The risk of obtaining severe marks can be reduced by adjusting printer setup- using the minimum printable squeegee pressure or switching to a finer mesh can both be effective. It should be noted that not all pastes are suitable for fine meshes- for example, the large graphite flakes in carbon inks are likely to case blockages.

As shown in sections 6.3.1 and 6.3.2, adjusting the printing regime can also be minimise marking. Flow coating methods were shown to be preferable to print-print regimes for the ZrO_2 ink. Unless pastes are considerably viscous and require forcing through the mesh, print print methods unnecessarily introduce increased risk of severe marking and should perhaps be avoided. Reducing paste viscosity with dilution can be helpful (as in section 6.6.3) but should be approached cautiously to avoid detrimental losses in print thickness.

Issues v), vi) Random void or crystallite spacing at micro or macro-scale

Perhaps the most difficult to diagnose issues are those causing random infiltration. Devices can be of extremely varied infiltration quality, with macro or micro-scale defects across the entire TiO_2 layer. Consequently, such problems are not always visible to the naked eye- the most severe issues are clearly observed in complete devices, while smaller problems require evaluation with optical microscopy (Figure 6.45). Commonly, these problems arise as a consequence of multiple concurrent problems, with defects such as increased layer roughness, mesh marking and sub-optimal airflow acting in tandem. Attempts to improve infiltration may therefore uncover other problems. For example, the yellow box in Figure 6.45 surrounds two devices from the same print batch, one of which was annealed under lower airflow. The improved infiltration in this second device reveals mesh marking defects, which were otherwise unobservable in the more sparsely filled sample.

A multi-faceted problem-solving approach is therefore necessary in this case.

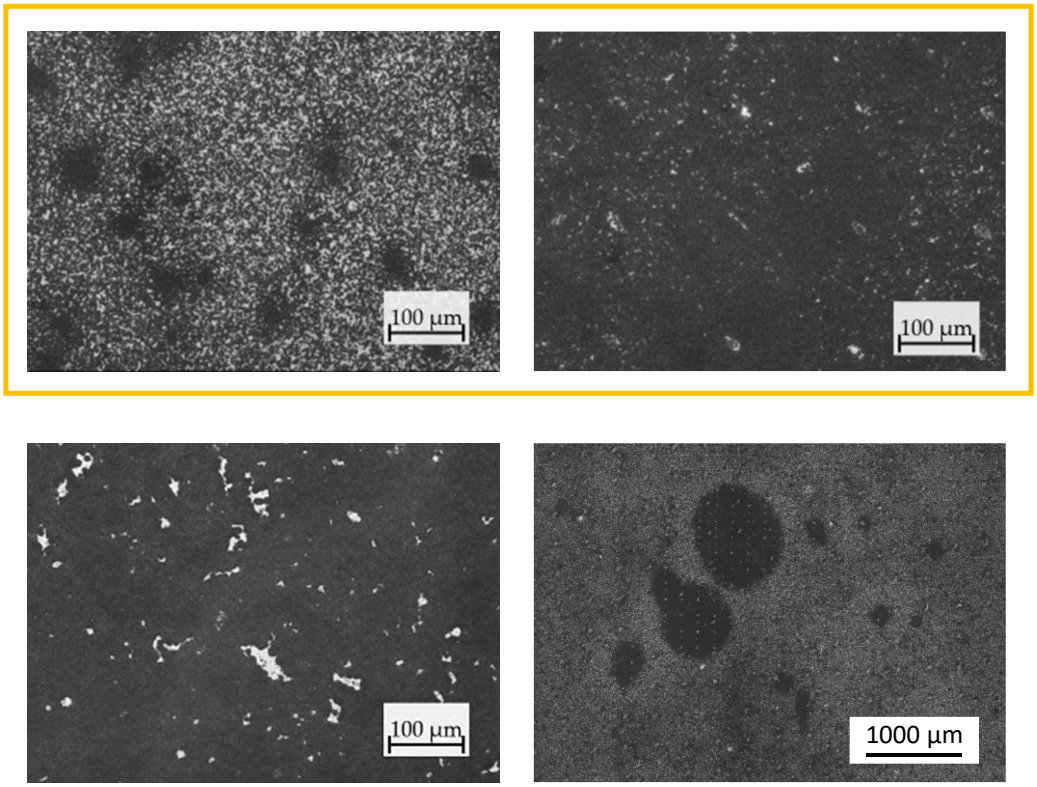

Figure 6.45: Optical microscopy images of randomly dispersed infiltration issues. The yellow box highlights images of two devices from the same printing batch, where improved infiltration in the RHS sample reveals mesh marking.

After any poor infiltration, hot plate or oven temperature should be checked immediately. As shown in section 6.3.1, temperature and airflow drastically impact crystallisation times, and hence stack filling. Airflow is perhaps more difficult to measure, although fume hood or oven extraction can potentially be checked. To minimise surface airflow while allowing adequate solvent removal, a partial cover can be applied. Even without infiltration issues, this may improve batch reproducibility by ensuring devices encounter like solvent environments and airflow during the annealing process. It should also help limit variation between batches by limiting the impact of airflow variation on different days.

It should be noted that the negative impact of airflow and temperature are likely exacerbated in stacks with sub-optimal prints where infiltration is already impeded. Therefore, upon experiencing poor infiltration in a given batch any remaining uninfiltrated stacks should be examined for evidence of increased roughness, mesh marking or film thickness. Where significant changes have occurred, printer setup and regime should be reviewed. Note that minor mesh marking (especially in the ZrO_2 layer) should not cause extreme infiltration issues by itself, so evidence of minor mesh marking in any layer is unlikely to be the cause. If no

uninfiltrated stacks from the relevant printing batches remain, cross sectional imaging and optical imaging of the infiltrated TiO_2 may provide some insight.

In the absence of any significant stack issues, high temperature annealing and infiltration equipment should be examined. Previous works have found that residual binder in the carbon or ZrO_2 electrodes can inhibit stack filling.[35] Therefore, if equipment is not achieving the requisite temperature for effective binder removal, poor infiltration may follow. Too high an annealing temperature can also cause problems through inducing peeling or graphitisation of the top electrode.[39] Completely graphitised layers present as silvery and reflective (compared to the usual matte black), while round silvery marks on the layer indicate partial conversion.

If no obvious issues with the stacks, equipment or annealing environment are discovered, modifying the precursor composition or perovskite annealing procedure may be necessary. Slight changes in precursor wetting, viscosity or crystallisation can have significant impacts on infiltration. Different solvents, precursor formulations, concentrations or additives may all therefore require slightly different conditions for optimal stack filling- especially in the absence of a wetting agent such as AVAI. Although exposure to increased relative humidity was shown in section 6.4 to aid infiltration, it also caused accelerated PbI_2 formation. RH adjustments for infiltration enhancements should therefore be applied with caution and are nor recommended as a preferred method for improving stack filling. Further work is required to determine whether this accelerated degradation can be prevented with encapsulation or improved storage methods.

In principle, modifications that slow crystallisation or speed up stack filling should improve infiltration. Options include adjusting precursor concentration, introducing solvent additives and reducing annealing temperatures or airflow. The impact of these changes will be highly dependent on the precise precursor formulation and device structure, and effectiveness may therefore be highly variable. A universal solution for preventing this infiltration issue in all CPSCs cannot therefore be presented.

Issue vii) Performance drops and hysteresis changes without infiltration problems

Upon experiencing benchmark performance drops without obvious infiltration issues, layer thickness in the relevant print batch should be examined either using device cross sections or profilometry of uninfiltrated stacks. As shown in section 6.6.1 and 6.6.2, sub optimally thin ZrO_2 layers lower benchmark performance and dramatically increase hysteresis. Other work

has shown that thin carbon layers can cause similar performance losses: thinner layers are more resistive and resultant devices suffer from poor charge extraction and increased recombination.[19]

Low quality blocking layers can produce similar issues. Although $TiCl_4$ treatments were shown to help, simply adjusting the deposition method is an easier and more time efficient way of ensuring optimal layer thickness and preventing pinholes.[40]

6.9 Conclusion

This work has examined the many factors influencing infiltration in CPSCs, presenting a facile non-destructive method for quantifying TiO_2 filling. It was found that % uninfiltrated area correlated well with device performance, which could enable accurate PCE prediction in devices and modules.

Both intrinsic and extrinsic factors were found to impact infiltration. Print quality in the ZrO_2 and carbon layers proved highly influential- even slight variation in ZrO_2 roughness was found to drastically increase carbon mesh marking, reducing infiltration, carbon conductivity and device V_{oc} and FF. Optimising interlayer printing, diluting carbon inks to minimise mesh marking and applying partial covers during annealing resulted in improved GVL-MeOH device performance, reaching a champion PCE of 15%.

Uneven heating and airflow also contributed significantly resulting in intra-batch variation between small devices. In modules, distinctive large infiltration defects with accelerated degradation were observed. Introducing partial covers to ensure even heating and minimise surface airflow during perovskite annealing drastically improved module homogeneity and device reproducibility. Problems such as paste contamination, mesh marking, uneven printing and irregular heating and airflow were also found to cause characteristic infiltration defects.

Optical examination can thus reveal the root cause of many infiltration problems, enabling quick identification of manufacturing issues. Such methods could therefore be extremely useful for batch monitoring and troubleshooting in large-scale commercial settings.

6.8 References

[1] S. M. P. Meroni, C. Worsley, D. Raptis and T. M. Watson, *Energies*, 2021, **14**, 386

[2] V. Kapoor, A. Bashir, L. J. Haur, A. Bruno, S. Shukla, A. Priyadarshi, N. Mathews and S. Mhaisalkar, *Energy Technol.*, 2017, **5**, 1880–1886

[3] C. Worsley, D. Raptis, S. Meroni, A. Doolin, R. Garcia, M. Davies and T. Watson, *Energy Technol.*, 2021, **9**, 2100312

[4] S. M. P. Meroni, Y. Mouhamad, F. De Rossi, A. Pockett, J. Baker, R. Escalante, J. Searle, M. J. Carnie, E. Jewell, G. Oskam and T. M. Watson, *Sci. Technol. Adv. Mater.*, 2018, **19**, 1–9

[5] A. Mei, X. Li, L. Liu, Z. Ku, T. Liu, Y. Rong, M. Xu, M. Hu, J. Chen, Y. Yang, M. Grätzel and H. Han, *Science*, 2014, **345**, 295–298

[6] S. Liu, Y. Sheng, D. Zhang, W. Zhang, Z. Qin, M. Qin, S. Li, Y. Wang, C. Gao, Q. Wang, Y. Ming, C. Liu, K. Yang, Q. Huang, J. Qi, Q. Gao, K. Chen, Y. Hu, Y. Rong, X. Lu, A. Mei and H. Han, *Fundam. Res.*, 2022, **2**, 276-283

[7] Q. Wang, W. Zhang, Z. Zhang, S. Liu, J. Wu, Y. Guan, A. Mei, Y. Rong, Y. Hu and H. Han, *Adv. Energy Mater.*, 2020, **10**, 1–7

[8] X. Hou, M. Xu, C. Tong, W. Ji, Z. Fu, Z. Wan, F. Hao, Y. Ming, S. Liu, Y. Hu, H. Han, Y. Rong and Y. Yao, *J. Power Sources*, 2019, *415*, 105–111

[9] H. Lakhiani, T. Dunlop, F. De Rossi, S. Dimitrov, R. Kerremans, C. Charbonneau, T. Watson, J. Barbé and W. C. Tsoi, *Adv. Funct. Mater.*, 2019, **29**, 1900885

[10] Z. Liu, S. Bi, G. Hou, C. Ying and X. Su, *J. Power Sources*, 2019, **430**, 12–19

[11] Y. Hu, Z. Zhang, A. Mei, Y. Jiang, X. Hou, Q. Wang, K. Du, Y. Rong, Y. Zhou, G. Xu and H. Han, *Adv. Mater.*, 2018, **30**, 1705786

[12] N. G. Park and K. Zhu, *Nat. Rev. Mater.*, 2020, 1–18

[13] T. Dunlop, O. Kesteven, F. De Rossi, P. Davies, T. Watson and C. Charbonneau, *Materials (Basel).*, 2021, **14**, 5852

[14] G. E. Eperon, V. M. Burlakov, P. Docampo, A. Goriely and H. J. Snaith, *Adv. Funct. Mater.*, 2014, **24**, 151–157

[15] Q. Wang, S. Liu, Y. Ming, Y. Guan, D. Li, C. Zhang, Z. Wang, Y. Rong, Y. Hu and H. Han, *Sustain. Energy Fuels*, 2018, **2**, 2412–2418

[16] A. Priyadarshi, A. Bashir, J. T. Gunawan, L. J. Haur, A. Bruno, Z. Akhter, N. Mathews and S. G. Mhaisalkar, *Energy Technol.*, 2017, **5**, 1866–1872

[17] G. Syrrokostas, G. Leftheriotis, S. N. Yannopoulos and Jianbo Yin, *J. Nanomater.*, 2019, 8348237

[18] L. Wagner, C. Qiu, M. Unmüssig, D. Bogachuk, S. Mastroianni, U. Würfel, Y. Hu, H. Han and A. Hinsch, *Sol. RRL*, 2021, **5**, 2000595

[19] K. Li, H. Chen, H. Liu, Y. Yuan, Y. Gao, B. Yang and C. Zhou, *Org. Electron.*, 2018, **62**, 298–303

[20] W. Tress, N. Marinova, O. Inganäs, M. K. Nazeeruddin, S. M. Zakeeruddin, M. W. Graetzel Tress, N. Marinova, M. K. Nazeeruddin, S. M. Zakeeruddin, M. Graetzel, W. Tress and O. Inganäs, *Adv. Energy Mater.*, 2015, **5**, 1400812

[21] Z. Hameiri, A. Mahboubi Soufiani, M. K. Juhl, L. Jiang, F. Huang, Y. B. Cheng, H. Kampwerth, J. W. Weber, M. A. Green and T. Trupke, *Prog. Photovoltaics Res. Appl.*, 2015, **23**, 1697–1705

[22] A. Schneider, S. Alon and L. Etgar, *Energy Technol.*, 2019, 1900481

[23] A. Pockett, D. Raptis, S. M. P. Meroni, J. Baker, T. Watson and M. Carnie, *J. Phys. Chem. C*, 2019,

123, 11414–11421

[24] R. Kerremans, O. J. Sandberg, S. Meroni, T. Watson, A. Armin and P. Meredith, *Sol. RRL*, 2019, 1900221

[25] P. Fassl, V. Lami, A. Bausch, Z. Wang, M. T. Klug, H. J. Snaith and Y. Vaynzof, *Energy Environ. Sci.*, 2018, **11**, 3380–3391

[26] S. Ham, Y. J. Choi, J. W. Lee, N. G. Park and D. Kim, *J. Phys. Chem. C*, 2017, **121**, 3143–3148

[27] H. Lakhiani, T. Dunlop, F. De Rossi, S. Dimitrov, R. Kerremans, C. Charbonneau, T. Watson, J. Barbé and W. C. Tsoi, *Adv. Funct. Mater.*, 2019, 1900885

[28] S. G. Hashmi, D. Martineau, M. I. Dar, T. T. T. Myllymäki, T. Sarikka, V. Ulla, S. M. Zakeeruddin and M. Grätzel, *J. Mater. Chem. A*, 2017, **5**, 12060–12067

[29] A. Bashir, S. Shukla, J. H. Lew, S. Shukla, A. Bruno, D. Gupta, T. Baikie, R. Patidar, Z. Akhter, A. Priyadarshi, N. Mathews and S. G. Mhaisalkar, *Nanoscale*, 2018, **10**, 2341–2350

[30] Y. Rong, X. Hou, Y. Hu, A. Mei, L. Liu, P. Wang and H. Han, *Nat. Commun.*, 2017, **8**, 14555

[31] Y. H. Kye, C. J. Yu, U. G. Jong, Y. Chen and A. Walsh, *J. Phys. Chem. Lett.*, 2018, **9**, 2196–2201

[32] A. Mei, Y. Sheng, Y. Ming, Y. Hu, Y. Rong, W. Zhang, S. Luo, G. Na, C. Tian, X. Hou, Y. Xiong, Z. Zhang, S. Liu, S. Uchida, T.-W. Kim, Y. Yuan, L. Zhang, Y. Zhou and H. Han, *Joule*, 2020, **4**, 2646–2660

[33] E. V. Timofeeva, J. L. Routbort and D. Singh, *J. Appl. Phys.*, 2009, **106**, 014304

[34] S. J. Potts, C. Phillips, T. Claypole and E. Jewell, *Coatings*, 2020, **10**, 1–17

[35] J. Baker, K. Hooper, S. Meroni, A. Pockett, J. McGettrick, Z. Wei, R. Escalante, G. Oskam, M. Carnie and T. Watson, *J. Mater. Chem. A*, 2017, **5**, 18643–18650

[36] T. Liu, L. Liu, M. Hu, Y. Yang, L. Zhang, A. Mei and H. Han, *J. Power Sources*, 2015, **293**, 533–538

[37] Z. Wan, M. Xu, Z. Fu, D. Li, A. Mei, Y. Hu, Y. Rong and H. Han, *Front. Optoelectron.*, 2019, 1–8

[38] I. Zimmermann, P. Gratia, D. Martineau, G. Grancini, J.-N. N. Audinot, T. Wirtz and M. K. Nazeeruddin, *J. Mater. Chem. A*, 2019, **7**, 8073–8077

[39] A. Mishra, Z. Ahmad, I. Zimmermann, D. Martineau, R. A. Shakoor, F. Touati, K. Riaz, S. A. Al-Muhtaseb and M. K. Nazeeruddin, *Org. Electron.*, 2019, **65**, 375–380

[40] D. Raptis, C. A. Worsley, S. M. P. Meroni, A. Pockett, M. Carnie and T. Watson, *Sol. 2022, Vol.* **2***, Pages 293-304*, 2022, **2**, 293–304

Chapter 7

Future work and perspectives

7.1 Discussion

This thesis has examined GVL as a replacement for GBL in CPSC devices and modules. GVL is shown not only to be a viable replacement to GBL, producing similar PCEs in 1 cm^2 devices, but superior when combined with 10% methanol to tune the viscosity. Perhaps most significantly, the GVL precursors offer significant advantages at scale due to increased stability towards precipitation. This enabled successful fabrication of 517.7 cm^2 active area modules, which were placed outside for weathering. Clearly, the GVL-MeOH precursors are very promising for potential scale-up.

Considering its similarity to the GBL molecule, differing only in an additional methyl group, the observed differences in GVL and GBL precursor behaviour are unexpected. Unlike with GBL, there appears to be no colloidal formation in the GVL or GVL-MeOH systems, as evidenced by the lack of laser scattering in Chapters 3 and 4. Despite this, perovskite was found to crystallise much more rapidly from the GVL precursors upon heating.

This suggests that solvent-solute coordination is very different between the two systems, which could mean different crystallisation pathways are favoured in each system. Controlling crystal growth and nucleation using specialised annealing covers has been a key in achieving high CPSC PCEs of 17-18**%.**[1],[2] A deeper understanding of solvent-solute coordination and perovskite crystal growth in GVL precursors could therefore offer a pathway to improved PCE in these devices.

Such work could also enable the application of alternative cations such as Cs or FA into the GVL system. Mixed cation perovskites are generally deposited using DMF/DMSO mixtures and have experienced significant phase instability when dissolved in GBL in our laboratory. Increasing the versatility of the GVL system to more than one perovskite formulation would significantly enhance its commercial viability, while reducing the toxicity and improving scalability in mixed cation CPSCs.

As discussed in Chapter 5, the GVL devices require a week of unencapsulated ambient storage to reach peak performance due to slow residual solvent loss. Over the week following infiltration, PCE improved significantly in >78% of devices. This was not seen in devices

annealed for longer, or where encapsulation was performed early. In fact, early encapsulation was detrimental to long term performance. While it is important for other research groups or future scaled initiatives to learn how to achieve peak performance , a seven-day waiting period between infiltration and encapsulation is far from practical. Further work into methods to accelerate performance evolution would therefore be beneficial.

Finally, while there was a significant correlation between % uninfiltrated area (UA) and performance for the $AVA_{0.03}MAPbI_3$ cells examined in Chapter 6, scope exists for further study into this relationship. While this work presents a clear general trend in this case, it is possible that the trend varies in devices with different properties: for example, different perovskite compositions or layer thicknesses. While devices of different layer thicknesses (e.g., ZrO_2 layers of 1 and 2 µm are present) were used in the analysis, the variations were slight compared to those present in the literature, which can reach up to 4 µm. At extremes, the trends presented here may not apply. A more rigorous study including devices of multiple layer thicknesses or different perovskite compositions may therefore be necessary to determine the extent of the trend and improve the potential for this technique to accurately predict PCE.

7.2 References

[1] S. Liu, Y. Sheng, D. Zhang, W. Zhang, Z. Qin, M. Qin, S. Li, Y. Wang, C. Gao, Q. Wang, Y. Ming, C. Liu, K. Yang, Q. Huang, J. Qi, Q. Gao, K. Chen, Y. Hu, Y. Rong, X. Lu, A. Mei and H. Han, *Fundam. Res.*, 2022, **2**, 276-283

[2] C. Ling, Y. Xia, X. Xiao, X. Chen, Z. Zheng, M. Xia, Y. Hu, A. Mei, Y. Rong and H. Han, *Small Methods*, 2022, **6**, 2200161

[3] S. M. P. Meroni, C. Worsley, D. Raptis and T. M. Watson, *Energies*, 2021, **14**, 386

[4] C. Tong, W. Ji, D. Li, A. Mei, Y. Hu, Y. Rong and H. Han, *J. Mater. Chem. A*, 2019, **7**, 10942–10948